

Piezoelectric and Dielectric Properties of LiNbO₃, PMN-PT, and PZT-5A Materials
at Cryogenic Temperatures

by

Md Shahidul Islam

A thesis submitted in partial fulfillment of the requirements for the degree of
Doctor of Philosophy

Department of Physics
University of Alberta

Abstract

The piezoelectric coefficients d_{ij} , dielectric constant K_{ij}^{σ} , dielectric loss, creep and hysteresis were measured for 41° X-cut lithium niobate (LiNbO_3), single crystal lead magnesium niobate-lead titanate (PMN-PT) and ceramic lead zirconium titanate (PZT-5A) transducers. The measurements were made between room temperature and 78 mK. The magnitude and temperature dependence of the three materials' properties can be understood in terms of intrinsic and extrinsic mechanisms in single crystals and ceramics. Several new features were observed, including a direct connection between creep and hysteresis, a unique region of negative creep in PMN-PT, and a surprisingly strong low-temperature dependence of d_{15} for PMN-PT and PZT, that extends well below 1 K. The strong low-temperature dependence of d_{15} PMN-PT and PZT suggests that there must be a wide range of small energy scales involved in domain wall motion. The hysteresis and creep in PMN-PT extend to temperatures below 10 K, which is consistent with weakly pinned domain walls. The dielectric loss does not show unusual behavior in the negative creep region of the temperature range, suggesting that the negative creep mechanism does not affect the behavior. In PZT, the hysteresis disappears below 30 K, as expected if its domain walls are pinned by grain boundaries. The implication for selecting the best material for positioning actuators that need large displacement involve d_{15} . At cryogenic temperatures, one can use a LiNbO_3 transducer/stack to achieve this. All three materials would be effective cryogenic ultrasonics sensors, but it would be challenging to use any of them as voltage sensors at frequencies below 1 kHz, since high input impedance would be needed. Given its nearly constant sensitivity for g_{15} and dielectric constant, LiNbO_3 is probably the best sensor choice for precise measurements that cover a wide temperature range.

I would like to dedicate this thesis to my late parents, Md Abul Quashem and Anjuman Ara Begum, and my wife, Rokeshana Afroz.

Acknowledgements

I would like to thank my supervisor, John Beamish, for his generous guidance, patience, and encouragement throughout my degree. He was a true mentor, friend, and colleague.

I want to express my sincere thank to my supervisory committee members, Doug Schmitt, and John Davis for conveying their knowledge and expertise to this work. A special thanks to Frank Marsiglio, Samer Adeeb, and John Page, for participating in my final exam.

I would also like to thank Don Mullin, Greg Popowich, Steve Rogers, Paul Zimmermann, Dave Fortin, Devon Bizuk and other technical staff for their invaluable technical support. Many thanks to Zhigang Cheng for helping me to transfer helium mixture to the mini dilution fridge and Jaechun Jeon for letting me use his Sawyer-Tower Circuit. Special thanks to my friend, Biswajit Nandi, for drawing the schematic of my devices.

This long journey would not come to an end without having my family's sacrifices and continuous encouragement. I owe everything to my wife, Rokeshana Afroz and my sons, Shaukat Wasit and Safwat Islam.

I am also grateful to the Natural Sciences and Engineering Research Council of Canada (NSERC), and the University of Alberta for their financial support to this work.

Finally, I would like to thank Almighty Allah for giving me the opportunity, determination, and strength to complete the degree successfully.

Contents

1	Introduction	1
2	Background	5
2.1	Tensor definition of stress and strain	5
2.1.1	Stress	5
2.1.2	Strain	7
2.2	Tensor definitions of the dielectric, piezoelectric and elastic coefficients	9
2.2.1	Dielectric coefficients	9
2.2.2	Piezoelectric coefficients	10
2.2.3	Elastic stiffness and compliance:	10
2.2.4	Matrix notation:	11
2.2.5	Crystal symmetry and crystal systems	12
2.2.6	The effects of crystal symmetry on piezoelectric materials . . .	13
2.2.7	Transformation of vectors and tensors	13
2.2.8	Transformation for rotation	14
2.2.9	Transformation of third-rank tensors	14
2.3	Ferroelectric domains and poling of ferroelectric single crystals and ceramics	20
2.4	Piezoelectric and dielectric properties of single crystal LiNbO_3 , PMN-PT and ceramic PZT	23
2.4.1	Single crystal LiNbO_3	23
2.4.2	Single crystal PMN-PT	27
2.4.3	Polycrystalline PZT ceramics	28
2.5	Review of the temperature dependence of piezoelectric and dielectric properties	30
2.6	Non-linearity, hysteresis and creep properties of piezoelectric materials	37
2.6.1	Non-linearity	37
2.6.2	Hysteresis	37
2.6.3	Creep	38

2.7	Depolarization of piezoelectric crystals	40
2.8	Multilayer piezoelectric stack actuators	40
2.9	Dielectric properties	43
2.10	Different types of dielectric constants	47
3	Experiment	48
3.1	Experimental Apparatus	48
3.1.1	Dilution Refrigerators	48
3.1.2	Gas Handling System and Leak Testing	50
3.1.3	Thermometry and Temperature Control	51
3.1.4	Capacitance Measurements	52
3.2	Experimental Techniques	54
3.2.1	Experimental design and analysis of capacitance measurements to measure shear piezoelectric displacement	54
3.2.2	Longitudinal d_{33} measurements and effects of magnetic clamping	60
3.2.3	Procedure to measure piezoelectric coefficients, hysteresis and creep	66
3.2.4	Piezoelectric Polarization Measurements	69
3.2.5	Experimental design and procedure to measure dielectric constant, K	71
4	Temperature Dependence of Piezoelectric and Dielectric Properties	73
4.1	Introduction	73
4.2	The shear piezoelectric coefficient (d_{15})	74
4.2.1	LiNbO ₃ single crystal	74
4.2.2	PMN-PT single crystal	76
4.2.3	PZT-5A ceramic	79
4.3	The longitudinal piezoelectric coefficient (d_{33})	80
4.3.1	PMN-PT single crystal	80
4.3.2	PZT-5A ceramic	80
4.4	The dielectric constant and loss conductance	83
4.4.1	LiNbO ₃ single crystal	83
4.4.2	PMN-PT single crystal	84
4.4.3	PZT-5A ceramics	86
4.5	The voltage constants g_{15} and g_{33}	87
4.5.1	LiNbO ₃ single crystal	87
4.5.2	PMN-PT single crystal	88

4.5.3	PZT-5A ceramic	88
4.6	Discussion	90
5	Hysteresis and Creep Properties of Piezoelectric Materials	105
5.1	Introduction	105
5.2	LiNbO ₃ single crystal	106
5.2.1	Hysteresis measurements	106
5.2.2	Creep measurements	110
5.3	PMN-PT single crystal	112
5.3.1	Hysteresis measurements	113
5.3.2	P-E hysteresis loop	119
5.3.3	Creep measurements	121
5.4	Polycrystalline PZT-5A	136
5.4.1	Hysteresis measurements	136
5.4.2	Creep measurements	141
5.5	Discussion	144
6	Conclusion	150
7	Bibliography	154

List of Tables

4.1	Experimental values of the shear and longitudinal piezoelectric coefficients and voltage constants of the three materials at room temperature and at their lowest temperatures	97
4.2	Experimental values of the dielectric constant of the three materials at room temperature and at their lowest temperatures	104

List of Figures

2.1	Normal and shear components of stress on a cubic element (Figure reproduced from Ney, 1985)	5
2.2	The forces on the faces parallel to the x_1 axis (Figure reproduced from Ney, 1985)	6
2.3	(a) Before stretching and (b) after stretching of a thin wire	8
2.4	(a) Pure shear, (b) pure rotation and (c) simple shear in the x_1x_2 plane of a rectangular block	8
2.5	Polarization direction with the forces affecting a piezoelectric element	12
2.6	Transformation of two sets of coordinate axes, Ox_i and Ox'_i where $i = 1, 2, 3$	15
2.7	Crystal structure of a perovskite piezoelectric (a) cubic lattice with no dipole above the Curie temperature and (b) tetragonal (orthorhombic) lattice with dipole moment below the Curie temperature	21
2.8	(a) a 180° domain wall separating anti-parallel ferroelectric domains, and (b) a non- 180° domain wall separating mutually perpendicular domains	22
2.9	(a) Unpoled and (b) poled single crystal (Figure reproduced from Bukhari M.Sc. thesis, 2014)	22
2.10	A typical hysteresis loop (or switchery) in a ferroelectric ceramic and corresponding domain reversal (Figure reproduced from Jin <i>et al.</i>) . Switching during poling shows the (a) non-polarized state, b) under an applied electric field, c) a polarized state.	23
2.11	Positions of the lithium atoms (Li) and the niobium atoms (Nb) with respect to the oxygen (O) octahedra in the paraelectric (left) and ferroelectric (right) phase of lithium niobate single crystal (Figure reproduced from Weis <i>et al.</i> , 1985)	24
2.12	Schematic phase diagram of the $\text{Li}_2\text{ONb}_2\text{O}_5$ pseudobinary system (Figure reproduced from Volk <i>et al.</i> , 2008)	25

2.13	(a) X-cut and Y-cut, (b) 41° X-cut and (c) 36° Y-cut of LiNbO ₃ single crystal	26
2.14	The accepted phase diagram of PMN-PT crystals as proposed by Guo <i>et al.</i> C, T, R, O, and M refer to cubic, tetragonal, rhombohedral, orthorhombic and monoclinic phase regions, respectively.	28
2.15	(a) Phase diagram of PZT and (b) the piezoelectric coefficients, d_{ij} , as a function of composition	29
2.16	Weak temperature dependence of the piezoelectric coefficient d_{15} for LiNbO ₃ (Figure reproduced from G. Gautschi <i>et al.</i> , 2002) . . .	31
2.17	Temperature dependence of the dielectric constant for LiNbO ₃ single crystal (Figure reproduced from Yamada <i>et al.</i> , 1967)	32
2.18	Large piezoelectric displacements for a stack of 36° Y-cut LiNbO ₃ single crystals for applied voltage between -700 V and + 700 V (Figure reproduced from Kawamata <i>et al.</i> , 2007)	32
2.19	Three temperature dependence regions of d_{33} for PMN-28PT (Figure reproduced from Martin <i>et al.</i> , 2012)	33
2.20	Temperature dependence of the shear piezoelectric constant d_{15} (black dots) and the shear voltage constant g_{15} (white dots) for a PMN-PT single crystal (Figure reproduced from Wang <i>et al.</i> , 2011)	34
2.21	Temperature dependence of the transverse piezoelectric constant d_{31} for a PMN-PT single crystal (Figure reproduced from Wang <i>et al.</i> , 2011)	34
2.22	The variation of temperature dependence of the dielectric constant (white dots) and loss tangent (black dots) for a PMN-PT single crystal (Figure reproduced from Wang <i>et al.</i> , 2011)	35
2.23	Temperature dependence of piezoelectric coefficients for PZT-5H (Figure reproduced from Wang <i>et al.</i> , 1998)	36
2.24	The temperature dependence of the dielectric constant for PZT-500 (●) and PZT-52/48 (○) at 1 kHz (Figure reproduced from Zhang <i>et al.</i> , 1998)	36
2.25	Displacement vs. applied voltage, showing the non-linearity.	37
2.26	Displacement (x) vs. voltage (V) hysteresis loop.	38
2.27	Displacement vs. time showing piezoelectric jump and creep.	39
2.28	Shear stack actuators with shear displacement, ΔL_{shear} ,	41
2.29	Longitudinal stack actuators with longitudinal displacement, ΔL_{long} ,	42
2.30	Transverse stack actuators with transverse displacement, ΔL_{trans} ,	42

2.31	Longitudinal stack actuator using 36° Y-cut LiNbO ₃ single crystals (Figure reproduced from Kawamata <i>et al.</i> , 2007)	42
2.32	A DC voltage applied to a piezoelectric transducer	43
2.33	(a) AC voltage applied to a piezoelectric transducer and (b) corre- sponding parallel equivalent circuit of capacitor for the transducer	44
2.34	(a) Parallel equivalent circuit of capacitor and (b) Phase diagram between charging current and applied voltage of the parallel equivalent circuit	45
2.35	Transducer to measure dielectric constant (a) K_{11} and (b) K_{33} , under constant stress or strain.	47
3.1	The main components and flow diagram of a ³ He- ⁴ He dilution refriger- erator (Figure reproduced from Pobell, 1992)	49
3.2	Schematic of our gas handling system to operate a ³ He- ⁴ He dilution refrigerator.	50
3.3	Sample of the 4-wires thermometer and a 2-wires configured heater (Figure reproduced from Bukhari M.Sc. thesis, 2014)	52
3.4	Regular two-terminal capacitor (C_m) measurement with stray capac- itance (C_s) between the leads.	53
3.5	The shielded standard three terminal capacitor arrangement used by the AH2500A capacitance bridge.	53
3.6	Typical series of individual capacitance measurements over time, il- lustrating the noise for our capacitance measurements at 30 K.	54
3.7	Schematic diagram of the capacitive displacement technique used to measure d_{15} , creep and hysteresis properties of shear piezoelectric transducers.	55
3.8	Parallel block capacitor with its electric fields. The right figure shows the strong electric fields (black arrows) inside the gap, and compara- tively weak stray fields (green lines) surrounding the blocks. The small black circle blows up the fringe fields (red line) at the edges of the gap in the left figure.	56
3.9	Stray capacitance calculation for the LiNbO ₃ device at room temper- ature.	58
3.10	Stray capacitance calculation for the PZT-5A device at room temper- ature.	59
3.11	(a) Shear mode and (b) longitudinal and transverse modes of the transducers with respect to applied voltage and the polarization direction.	61

3.12	Schematic diagram of the capacitive displacement technique used to measure d_{33} of longitudinal piezoelectric transducers.	61
3.13	(a) Capacitance vs. time graph for a LiNbO ₃ single crystal at 6 K under an applied voltage ± 20 V. (b) best fit line is to find the average capacitance and change in capacitance with respect to applied voltage.	67
3.14	Hysteresis in a PMN-PT crystal at 70 K during cycling of the applied voltage from -50 to +50 V.	68
3.15	Creep for applied voltage ± 50 V at 70 K of the shear PMN-PT transducer.	68
3.16	The polarization hysteresis loop measurement.	70
3.17	Schematic diagram for dielectric measurements.	71
4.1	Temperature dependence of the measured (uncorrected for stray capacitance) shear piezoelectric coefficient d_{15} of a LiNbO ₃ transducer.	75
4.2	Temperature dependence of the measured uncorrected (black dots) and corrected (blue dots) shear piezoelectric coefficient d_{15} of a LiNbO ₃ transducer.	75
4.3	Temperature dependence of corrected d_{15} of a single LiNbO ₃ transducer (blue dots) and a stack of three transducers (open blue dots).	76
4.4	The shear PMN-PT single crystal with Cr/Au electrodes from TRS Ceramics, Inc.	77
4.5	Temperature dependence of the measured uncorrected (dark red dots) and corrected (red dots) piezoelectric strain coefficient, d_{15} , for a PMN-PT single crystal.	78
4.6	Temperature dependence of the corrected piezoelectric strain coefficient, d_{15} , below 10 K for a PMN-PT single crystal.	78
4.7	The uncorrected (dark green dots and open circles) and corrected (green dots and open circles) piezoelectric strain coefficient d_{15} of a PZT-5A ceramic.	79
4.8	Temperature dependence of the piezoelectric coefficient d_{15} of a PZT-5A ceramic below 10 K.	80
4.9	Temperature dependence of the corrected longitudinal coefficient d_{33} for a PMN-PT single crystal.	81
4.10	Temperature dependence of the longitudinal piezoelectric coefficient d_{33} of a PZT-5A ceramic.	82
4.11	Temperature dependence of d_{33} below 50 K.	82

4.12	Temperature dependence of the dielectric constant and loss conductance for shear LiNbO ₃	83
4.13	Temperature dependence of the dielectric constant and loss conductance at 1 kHz for a shear PMN-PT single crystal.	84
4.14	Temperature dependence of the dielectric constant and loss conductance at 1 kHz for a longitudinal PMN-PT single crystal from APC international, Ltd.	85
4.15	Temperature dependence of the dielectric constant and loss conductance at 1 kHz for a longitudinal PMN-PT single crystal from TRS ceramics, Inc.	85
4.16	Temperature dependence of the dielectric constant and loss conductance for a shear PZT-5A crystal at 1 kHz, from room temperature to 1.4 K.	86
4.17	Temperature dependence of the dielectric constant and loss conductance for a longitudinal PZT-5A crystal at 1 kHz, from room temperature to 1.4 K.	87
4.18	Temperature dependence of the shear piezoelectric voltage coefficient g_{15} of a LiNbO ₃ transducer.	88
4.19	Temperature dependence of the piezoelectric voltage constants g_{15} and g_{33} of PMN-PT transducers.	89
4.20	Temperature dependence of the piezoelectric voltage constants g_{15} and g_{33} of PZT-5A transducers.	89
4.21	Comparison of shear piezoelectric displacement per volt for different transducers, on logarithmic scales.	90
4.22	Comparison of shear piezoelectric displacement per volt for different transducers, on linear scales.	91
4.23	Comparison of the longitudinal piezoelectric coefficient d_{33} of PMN-PT and PZT-5A transducers on logarithmic scales.	93
4.24	Comparison of the longitudinal piezoelectric coefficient d_{33} of PMN-PT and PZT-5A transducers on linear scales.	94
4.25	Comparison of temperature dependence of the shear piezoelectric voltage coefficient g_{15} of LiNbO ₃ PMN-PT and PZT-5A transducers.	94
4.26	Comparison of temperature dependence of longitudinal piezoelectric voltage coefficient g_{33} of PMN-PT and PZT-5A transducers.	95
4.27	Comparison of the temperature dependence of the dielectric constant and loss tangent for shear LiNbO ₃ , PMN-PT and PZT-5A crystals on linear scales.	99

4.28	Comparison of the temperature dependence of the dielectric constant and loss tangent for shear LiNbO ₃ , PMN-PT and PZT-5A crystals on logarithmic scales.	100
4.29	Comparison of the temperature dependence of the dielectric constant and loss tangent for longitudinal PMN-PT and PZT-5A crystals on linear scales.	102
4.30	Comparison of the temperature dependence of the dielectric constant and loss tangent for longitudinal PMN-PT and PZT-5A crystals on logarithmic scales.	103
5.1	Displacement vs. applied voltage for the LiNbO ₃ single crystal at 10 K. The left axis is displacement, with the corresponding measured capacitance on the right axis.	107
5.2	Displacement vs. applied voltage for the LiNbO ₃ single crystal at 70 K.	108
5.3	Displacement vs. applied voltage for the LiNbO ₃ single crystal at 150 K.	108
5.4	Displacement vs. applied voltage for the LiNbO ₃ single crystal at 200 K.	109
5.5	Displacement vs. applied voltage for the LiNbO ₃ single crystal at 295 K.	109
5.6	Displacement vs. time for a constant applied voltage of 150 V at 10 K.	110
5.7	Displacement vs. time for a constant applied voltage of 150 V at 70 K. A small negative thermal drift is visible.	111
5.8	Displacement vs. time for a constant applied voltage of 150 V at 150 K. A small positive thermal drift is visible.	111
5.9	The applied voltage sequence for creep, d_{15} and hysteresis measurements on a shear PMN-PT single crystal.	112
5.10	Hysteresis between displacement/capacitance and applied voltage for a PMN-PT single crystal at 70 K. Black points correspond to increasing voltages; red points to subsequent decreasing voltages.	113
5.11	Hysteresis at 5 K (a) and 30 K (b).	114
5.12	Hysteresis at 60 K (a) and 90 K (b).	114
5.13	Hysteresis at 150 K (a) and 210 K (b).	115
5.14	Hysteresis at 240 K (a) and 310 K (b).	115
5.15	Temperature dependence of the hysteresis width determined from hysteresis loops like these in Figure 5.11 to 5.14.	116

5.16	Temperature dependence of the average hysteresis width. Error bars are standard deviations of all measured data at each point.	116
5.17	Temperature dependence of the hysteresis width normalized by d_{15}	117
5.18	Hysteresis loops at 20 K, for ± 50 and ± 75 V maximum applied voltages.	118
5.19	Hysteresis loops at 20 K, for ± 50 and ± 75 V maximum applied voltages.	118
5.20	The voltage dependence of the hysteresis width for a PMN-PT single crystal at 20 K.	119
5.21	P-E hysteresis loop for a PMN-PT single crystal at 295 K.	120
5.22	Temperature dependence of the P-E hysteresis width for a PMN-PT single crystal.	120
5.23	Temperature dependence of the P-E hysteresis loops for a PMN-PT single crystal measured at 1 kHz.	121
5.24	Shear displacement vs. time following changes to the applied voltage for a PMN-PT single crystal at 70 K.	122
5.25	Extrapolation (red fit line) to get rid of thermal drift from the positive creep and (blue fit line) from the negative creep for PMN-PT crystal at 70 K.	122
5.26	Temperature dependence of the creep following a voltage change $\Delta V = +50$ V (0 V \rightarrow +50 V).	123
5.27	(a) Positive and (b) Negative creep following a voltage change $\Delta V = +50$ V (0 V \rightarrow +50 V).	124
5.28	Temperature dependence of the creep following a negative voltage change $\Delta V = -100$ V (+50 \rightarrow -50 V).	125
5.29	Temperature dependence of the creep for positive and negative voltage changes $\Delta V = +50$ V and $\Delta V = -100$ V.	125
5.30	Positive (black dots) and negative (red dots) creep at 70 K, divided by the applied voltage change.	126
5.31	Positive (black dots) and negative (red dots) creep at 270 K, divided by the applied voltage change.	127
5.32	Exponential fits of the creep data after applying a voltage change $\Delta V = +50$ V. Insert shows fits of the data for the first 300 seconds.	128
5.33	Exponential fits of the creep data after applying a negative voltage change $\Delta V = -100$ V. Insert shows fits of the data for the first 300 seconds.	128
5.34	Power law analysis of positive creep data after applying a voltage $\Delta V = +50$ V. Panels (a) to (d) have logarithmic time axes corresponding to exponents n from 0.01 to 0.5.	129

5.35	Logarithmic fit of the positive creep for 1000 seconds following an applied voltage change $\Delta V = +50$ V.	131
5.36	Logarithmic fit of the positive creep for 10000 seconds following an applied voltage change $\Delta V = +50$ V.	132
5.37	Logarithmic fit of the negative creep for 1000 seconds following an applied voltage change $\Delta V = -100$ V.	133
5.38	Logarithmic fit of the negative creep for 19000 seconds following an applied voltage change $\Delta V = -100$ V.	134
5.39	Positive and negative creep at 70 K for the shear PMN-PT single crystal. The insert shows the data for the first 50 seconds.	135
5.40	Temperature dependence of the difference between positive and negative creep displacements at 20 s (green dots left axis) and of the coefficient c (dark red dots, right axis) for the shear PMN-PT single crystal.	136
5.41	Relationship between displacement and applied voltage at 10 K for PZT-5A ceramic. Left axis is displacement with the corresponding measured capacitance on the right axis.	137
5.42	Hysteresis between displacement and applied voltage at 35 K.	138
5.43	Hysteresis between displacement and applied voltage at 100 K.	138
5.44	Hysteresis between displacement and applied voltage at 200 K.	139
5.45	Hysteresis between displacement and applied voltage at 295 K.	139
5.46	Temperature and voltage dependence of the hysteresis width of a PZT-5A ceramic.	140
5.47	Voltage dependence hysteresis width of a PZT-5A ceramic at 77 K.	140
5.48	Displacement vs. time for a constant applied voltage 150 V at 10 K.	141
5.49	Creep of the PZT-5A ceramic at 77 K, for changes in applied voltage of 150 V.	142
5.50	Temperature dependence of creep for the shear PZT-5A ceramic following a voltage change $\Delta V = 150$ V ($0 \rightarrow +150$ V).	142
5.51	Logarithmic fit of creep data for the PZT-5A ceramic following an applied voltage change $\Delta V = 150$ V.	143
5.52	Temperature dependence of the coefficient c calculated from logarithmic fits of creep data for the PZT-5A ceramic.	144
5.53	Temperature dependence of the hysteresis width (red dots) and the creep coefficients c (dark red dots) for a shear PMN-PT single crystal.	145
5.54	Temperature dependence of (a) d_{15} and hysteresis width and (b) dielectric constant and dielectric loss for the shear PMN-PT single crystal.	146

5.55	Comparison of the temperature dependence of the hysteresis width and the creep coefficient c for the PZT-5A ceramic for applied voltages between -150 and +150 V.	147
5.56	Temperature dependence of (a) d_{15} and hysteresis width for ± 150 V and (b) dielectric constant and dielectric loss for the shear PZT-5A ceramic.	148
5.57	Comparison of the temperature dependence of the hysteresis width of the three materials for applied voltages between - 50 and + 50 V. . .	149

Abbreviations

AC - Alternating Current
AH - Andeen Hagerling
AFM - Atomic Force Microscopy
CCW - Counter-Clockwise
CW - Clockwise
DC - Direct Current
GHS - Gas Handling System
LN₂ - Liquid Nitrogen
LiNbO₃ - Lithium Niobate
MPB - Morphotropic Phase Boundary
OFHC - Oxygen Free High Conductivity Copper
PT - Lead Titanate
PZ - Lead Zirconium
PMN-PT - Lead Magnesium Niobate-Lead Titanate
PZT - Lead Zirconium Titanate
P-E - Polarization - Electric field
RF - Radio Frequency
STM - Scanning Tunneling Microscopy
ST - Sawyer Tower
SAW - Surface Acoustic Wave
T_C - Curie Temperature

Chapter 1

Introduction

A piezoelectric is a material that produces an electric charge on its surface proportional to the applied mechanical force or generates a displacement when a voltage is applied across it. These two properties are known as the direct and converse (indirect) piezoelectric effects [1, 2, 3]. The direct effect is the principle used in pressure, force, acceleration and vibration sensors [1] and the converse piezoelectric effect is the basis for displacement actuators, surface acoustic waves (SAW), ultrasonic wave sensors [1]. For example, piezo-generators transform mechanical energy into electrical energy (direct piezoelectric effect), and piezo-motors change electrical energy into mechanical energy (converse piezoelectric effect) [4]. The same transducer may be used to perform both jobs by using the direct or converse piezoelectric operations.

Piezoelectric materials have been widely used as transducers, actuators, and sensors in various fields, for example, aerospace systems (vibration cancellation and optical positioning) [5, 6], industrial process control (high displacement actuators) [7, 8, 9] and biomedical (ultrasonic transducers) [10]. Single crystal lithium niobate (LiNbO_3) and lead magnesium niobate-lead titanate (PMN-PT), and polycrystalline ceramic lead zirconate titanate (PZT) are the most widely used materials. One needs to be aware of the temperature dependence of the piezoelectric materials in some applications. For example, in our lab PZT transducers were used to measure the elastic and plastic properties of solid helium [11, 12] at temperatures as low as 15 mK.

Although most applications are at room temperature, scanning tunneling microscopes (STM) are often designed to operate below 4 K, and require high sensitivity or large displacements for precise micro-positioning [13, 14, 15]. This means that large piezoelectric coefficients d_{ij} are needed, but the piezoelectric coefficients of most materials decrease significantly at cryogenic temperatures. The piezoelectric coefficients of the most commonly used material, PZT, decrease nearly linearly with temperature and the longitudinal and extensional coefficients d_{33} and d_{31} are about 5 times

smaller at 4 K than at room temperature [3, 15, 16, 17]. However, little is known about the shear coefficient d_{15} at cryogenic temperatures. The piezoelectric coefficients of LiNbO_3 single crystals are much less temperature dependent but their room temperature coefficient d_{15} is about 7 times smaller than for PZT [18, 19, 20]. Newer materials like single crystal PMN-PT have exceptionally large piezoelectric coefficients at room temperature, but limited information is available about their behavior below 75 K [14, 21, 22]. The limited information on these materials often leads people to assume that piezoelectric properties do not change below 4 K.

In micro-positioning applications like scanning tunneling microscopy (STM) [15] and atomic force microscopy (AFM) [23], time-dependent processes (creep and hysteresis) limit their performance when large voltages are applied. Single crystal PMN-PT and ceramics PZT have significant creep and hysteresis [24, 25, 26], which limits their accuracy in such applications. LiNbO_3 , which requires high voltages to generate large displacements [27] has much less creep or hysteresis, which may make them a better choice. Although creep and hysteresis are limiting features in many piezoelectric applications, the few studies of their temperature dependent properties have been limited to longitudinal transducers where the polarization is parallel to the applied electric field. For shear transducers where the polarization is perpendicular to the applied electric field, almost nothing is known, despite their potential for applications.

The temperature dependence of dielectric properties is also important for many electronics applications. The dielectric coefficients of the three piezoelectric materials decrease with temperature [18, 28, 29] but there is little information available at cryogenic temperatures, particularly for shear polarizations.

Although some of the piezoelectric and dielectric properties of single crystal LiNbO_3 , PMN-PT, and polycrystalline ceramic PZT have been investigated as function of temperature, there are two unexplored practical questions that are addressed in this thesis.

- i). How do the piezoelectric coefficients, particularly of shear transducers, behave at low temperature?
- ii). How do the creep and hysteresis depend on temperature?

We measured these low-temperature properties using a direct capacitive displacement detection technique, with high sensitivity by using a high-resolution capacitance bridge. We used this technique because it allows us to directly measure creep and hysteresis, which is not possible with the resonance method. There are very few previous studies using this technique, although in 1986, Yorke *et al.* [15] measured longitudinal piezoelectric coefficients d_{33} for PZT ceramics from room temperature down to 2 K using this method. In our research, we have studied shear and longitudi-

nal transducers of the three materials, including a stack of three LiNbO_3 transducers we assembled, and measured the temperature dependence of both piezoelectric and dielectric coefficients. We have also investigated the creep and hysteresis of shear transducers as functions of temperature and voltage.

The temperature dependence of the piezoelectric and dielectric properties of these materials arises from a combination of intrinsic and extrinsic contributions. The intrinsic contribution comes directly from the single-domain properties of the crystal, for example thermal expansion, while the extrinsic properties are the result of domain wall motion, interactions between grains or phase boundaries, and thermally induced defect motion [29, 30, 31, 32]. It is expected that the extrinsic properties may be frozen out at low temperatures since they are activated thermally.

LiNbO_3 is a single crystal with single domain. It has a very high Curie temperature, $T_C = 1210$ °C, and relatively small piezoelectric coefficients d_{ij} , which are intrinsic. PMN-PT is also a single crystal but with multi-domains. It has a low Curie temperature $T_C = 130$ °C and the piezoelectric coefficients are mostly extrinsic. PZT is a ceramic with multi-grains and each grain contains multi-domains. The Curie temperature is higher than PMN-PT, $T_C = 350$ °C. Its room temperature piezoelectric coefficients are mostly extrinsic. The much larger room temperature coefficients of both PZT-5A ceramics and PMN-PT single crystals are achieved by using materials with compositions close to a transition between tetragonal and rhombohedral structures. Their piezoelectric behavior is affected by the temperature dependence of this phase boundary and by extrinsic effects associated with grain boundaries and domain walls.

We can summarize the main results of our measurements on the different materials. LiNbO_3 has small d_{ij} at room temperature, with weak temperature dependence and no measurable creep or hysteresis at any temperature. PMN-PT has very large d_{ij} at room temperature, with a plateau between 80 and 240 K where d_{ij} is still large but nearly independent of temperature. The creep and hysteresis are large and become negative between 150 K and 300 K, but disappear at the lowest temperature. PZT-5A has intermediate d_{ij} at room temperature which decrease roughly linearly with temperature. The creep and hysteresis increase monotonically with temperature. At the lowest temperatures, none of the materials show creep or hysteresis and their d_{ij} are of similar magnitudes.

This thesis is organized as follows. Chapter 2 contains the theoretical and experimental background to the work. Chapter 3 describes the experimental apparatus and techniques for all the measurements. Chapter 4 presents measurements and analysis of the temperature dependence of piezoelectric and dielectric coefficients of the three

materials. The creep and hysteresis results and analysis of their temperature and voltage dependences are presented in Chapter 5. The essential findings of the three piezoelectric materials are summarised in Chapter 6.

Chapter 2

Background

Piezoelectric materials are widely used often over an extensive range of temperature. This Chapter reviews piezoelectric and dielectric properties of crystals, including the commonly used materials LiNbO_3 , PMN-PT and PZT-5A.

2.1 Tensor definition of stress and strain

2.1.1 Stress

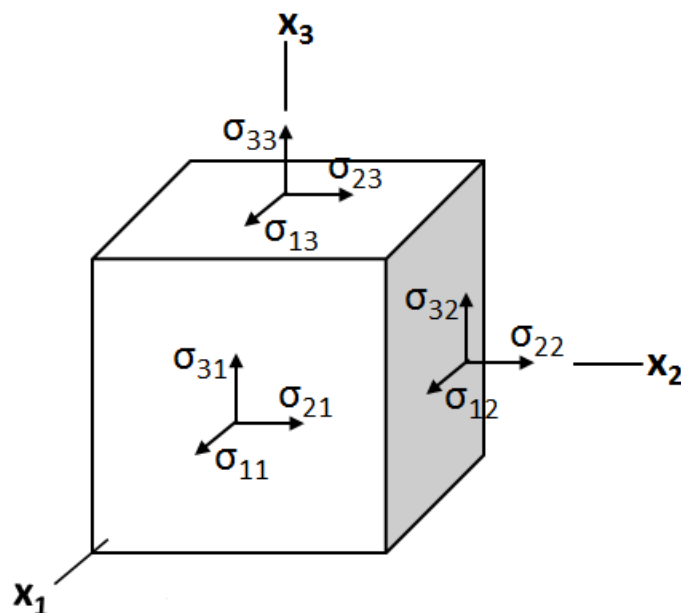


Figure 2.1: Normal and shear components of stress on a cubic element (Figure reproduced from Ney, 1985) [33].

The average force per unit area, exerted on a body when it is compressed or sheared, is called stress. To understand the effects of forces to a body, we need to understand the stress at a point. Let us consider the components of the stress tensor σ_{ij} (Nm^{-2}) acting on a cubic volume element as shown in Figure 2.1. If i is the direction in which the stress acts and j is the direction perpendicular to the face on which the stress acts in Figure 2.1, we can distinguish two types of stress. These are

- (i) Normal: σ_{ij} when $i = j$
- (ii) Shear: σ_{ij} when $i \neq j$.

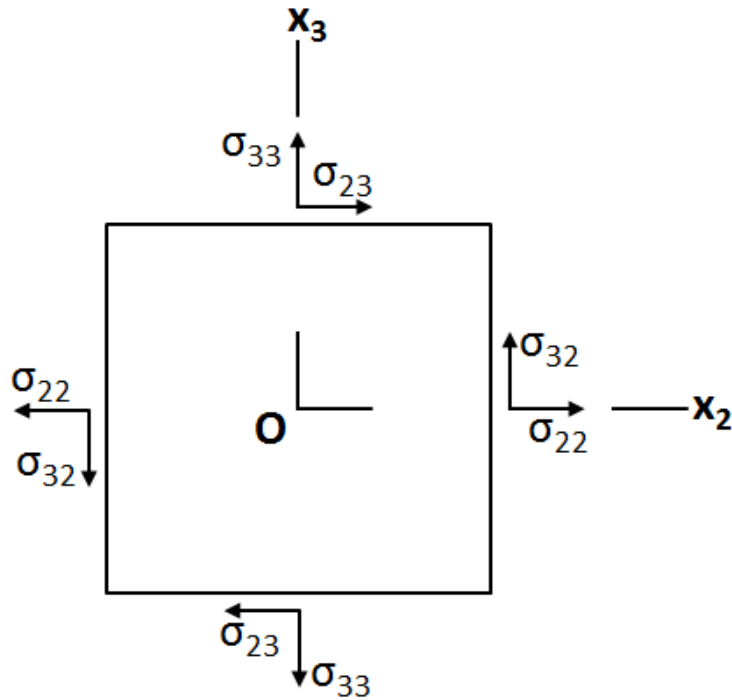


Figure 2.2: The forces on the faces parallel to the x_1 axis (Figure reproduced from Ney, 1985) [33].

(linear acceleration) or it would rotate. Stresses on opposite faces of the cube are opposite and equal which means only three faces of the cube are sufficient to explain stresses. However, a 3×3 array can describe the stress at a point as the stress tensor

$$\begin{bmatrix} \sigma_{11} & \sigma_{12} & \sigma_{13} \\ \sigma_{21} & \sigma_{22} & \sigma_{23} \\ \sigma_{31} & \sigma_{32} & \sigma_{33} \end{bmatrix}.$$

To simplify, we can consider both rotational and linear acceleration. Let consider the total moments around the x-axis which must be zero. Figure 2.2 shows only relevant stresses. Hence,

$$\sigma_{32} = \sigma_{23}.$$

In general, $\sigma_{ij} = \sigma_{ji}$ for all i, j , so σ_{ij} is a symmetric second rank tensor and there are only 6 independent elements

$$\begin{bmatrix} \sigma_{11} & \sigma_{12} & \sigma_{13} \\ \sigma_{12} & \sigma_{22} & \sigma_{23} \\ \sigma_{13} & \sigma_{23} & \sigma_{33} \end{bmatrix}.$$

2.1.2 Strain

The strain is defined as the relative change in the dimensions of a body that has undergone deformation. For simplicity, consider an extensible thin wire. From Figure 2.3, the strain in OP in one dimension is

$$e = \frac{O'P' - OP}{OP} = \frac{u}{x}.$$

More particularly, the strain at origin is defined as

$$e = \lim_{x \rightarrow 0} \left(\frac{u}{x} \right) = \frac{du}{dx}.$$

In three dimensions,

$$u_1 = e_{11}x_1 + e_{12}x_2 + e_{13}x_3$$

$$u_2 = e_{21}x_1 + e_{22}x_2 + e_{23}x_3$$

$$u_3 = e_{31}x_1 + e_{32}x_2 + e_{33}x_3$$

In general, $u_i = e_{ij}x_j$, where e_{ij} is the strain, a second rank tensor. For small deformation ∂u , the tensile strains along the axes x_1, x_2, x_3 are

$$e_{11} = \frac{\partial u_1}{\partial x_1}, \quad e_{22} = \frac{\partial u_2}{\partial x_2}, \quad e_{33} = \frac{\partial u_3}{\partial x_3}.$$

To explain the other strain components, let us consider a deformation in the x_1x_2 plane of a rectangular block, as shown in Figure 2.4 with $e_{12} \neq 0$; $e_{21} \neq 0$. It is clear that

$$e_{12} \approx \frac{\partial u_1}{\partial x_2} \approx (\text{angle}); \quad e_{21} \approx \frac{\partial u_2}{\partial x_1} \approx (\text{angle}).$$

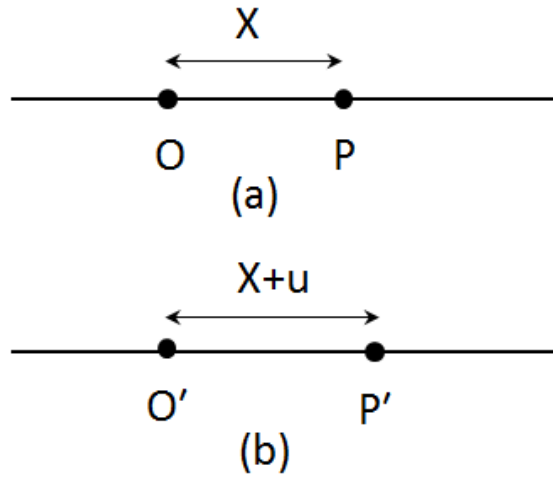


Figure 2.3: (a) Before stretching and (b) after stretching of a thin wire [34].

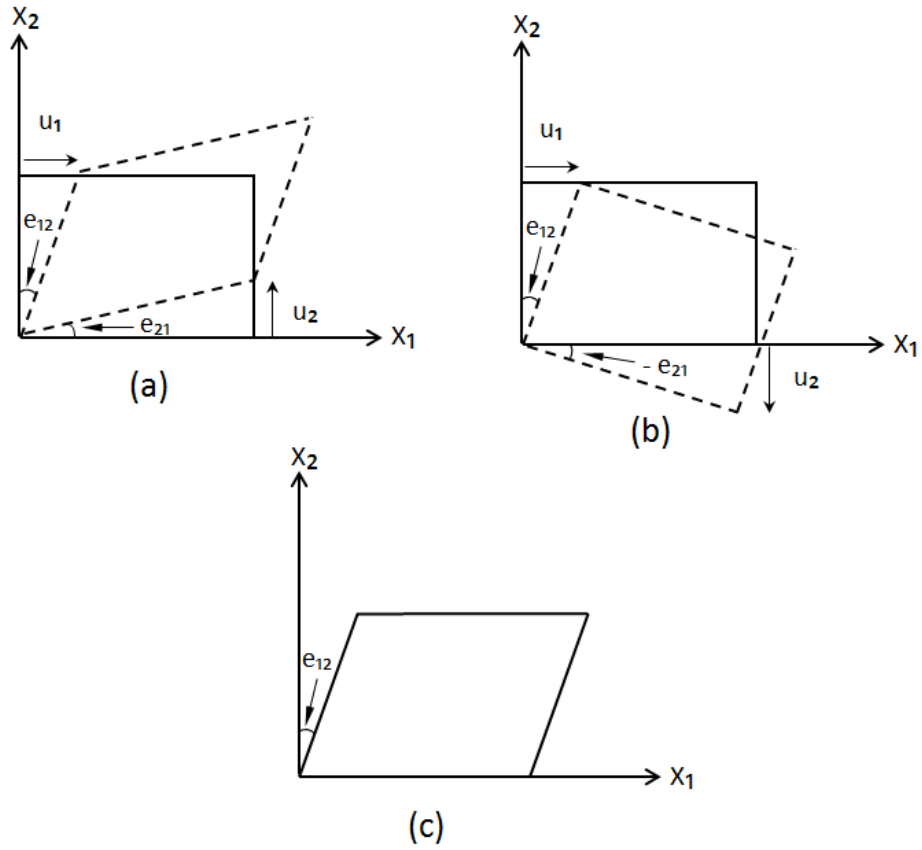


Figure 2.4: (a) Pure shear, (b) pure rotation and (c) simple shear in the x_1x_2 plane of a rectangular block [34].

Three possible combinations of e_{12} and e_{21} are very useful. These are:

- 1) $e_{12} = e_{21}$ is "pure shear" (Figure 2.4(a)),
- 2) $e_{12} = -e_{21}$ is "pure rotation" (Figure 2.4(b)),
- 3) $e_{12} \neq 0$ and $e_{21} = 0$ is "simple shear" (Figure 2.4(c)).

It is clear that e_{12} and e_{21} describe both shear and rotation. Therefore, we can write any second rank tensor as the sum of a symmetric and an anti-symmetric tensor.

$$e_{ij} = \epsilon_{ij} + \varpi_{ij}$$

where $\epsilon_{ij} = \frac{1}{2}(e_{ij} + e_{ji}) = \epsilon_{ji}$ is a symmetric tensor and $\varpi_{ij} = \frac{1}{2}(e_{ij} - e_{ji}) = -\varpi_{ji}$ is an anti-symmetric tensor. Now the symmetric strain tensor is ϵ_{ij} .

2.2 Tensor definitions of the dielectric, piezoelectric and elastic coefficients

2.2.1 Dielectric coefficients

When an electric field E_i (Vm^{-1}) (E_i is a component of the vector electric field) is applied to a dielectric material, a polarization P_i (Cm^{-2}) is induced in the material, which can be written [33]

$$P_i = \epsilon_0 \chi_{ij} E_j \quad (i, j = 1, 2, 3) \quad (2.1)$$

where the summation with respect to two letter suffix can be understood by Einstein summation convention and the dielectric susceptibility of the material χ_{ij} (Fm^{-1}) is second rank tensor. The total induced surface charge density, D_i (Cm^{-2}) can be written as

$$D_i = \epsilon_0 E_i + P_i \quad (2.2)$$

where $\epsilon_0 = 8.854 \times 10^{-12}$ (Fm^{-1}). Finally, we can write

$$D_i = \epsilon_0 E_i + \epsilon_0 \chi_{ij} E_j = \epsilon_0 (\delta_{ij} + \chi_{ij}) E_j = \epsilon_{ij} E_j \quad (2.3)$$

where ϵ_{ij} is the permittivity tensor and δ_{ij} is Kronecker's symbol ($\delta_{ij} = 1$ for $i = j$ and $\delta_{ij} = 0$ for $i \neq j$). The tensor dielectric constant is related to the permittivity tensor which is [33]

$$K_{ij} = \frac{\epsilon_{ij}}{\epsilon_0}. \quad (2.4)$$

2.2.2 Piezoelectric coefficients

When an external stress deforms or mechanically strains a piezoelectric crystal, it exhibits electric polarization which is known as the direct piezoelectric effect, and can be written as

$$P_i = d_{ijk}\sigma_{jk} \quad (2.5)$$

where the piezoelectric coefficients d_{ijk} (CN^{-1}) are a third rank tensor. In the converse piezoelectric effect, when an external electric field is applied to a crystal, it generates a strain which can be written as

$$\epsilon_{jk} = d_{ijk}E_i. \quad (2.6)$$

The units of the converse piezoelectric coefficients (d_{ijk}) are mV^{-1} (equivalent to CN^{-1}) and d_{ijk} is also a third rank tensor with 27 components. Since σ_{jk} and ϵ_{jk} are symmetric tensors with respect to their indices, the piezoelectric coefficient tensor should also be symmetric in those indices

$$d_{ijk} = d_{ikj}. \quad (2.7)$$

This reduces the number of independent components of d_{ijk} to 18 [33]. Depending on the symmetry of the material, the 18 independent components of d_{ijk} can be reduced further, as we discuss later.

Three types of piezoelectric coefficients are particularly relevant in applications. These are longitudinal (compression or expansion), transverse and shear coefficients. The coefficient measured along the direction of the applied field is known as the longitudinal coefficient, and that measured perpendicular to the direction of the applied field is known as the transverse coefficient. The rest of the coefficients are called shear coefficients.

2.2.3 Elastic stiffness and compliance:

By definition, the stress and strain are symmetric second-rank tensors, which means that $\sigma_{ij} = \sigma_{ji}$ and $\epsilon_{ij} = \epsilon_{ji}$. In accordance with Hooke's law for an anisotropic medium, we can write the general relation between stress σ_{ij} and strain ϵ_{ij} as

$$\sigma_{ij} = c_{ijkl}\epsilon_{kl} \quad (2.8)$$

and

$$\epsilon_{ij} = s_{ijkl}\sigma_{kl} \quad (2.9)$$

where the elastic stiffness c_{ijkl} (Nm^{-2}) and compliance s_{ijkl} (m^2N^{-1}) are fourth rank tensors. The number of components of both c_{ijkl} and s_{ijkl} is 81. Since both stress and strain are symmetric, however, one can easily show that

$$c_{ijkl} = c_{jikl} = c_{ijlk} = c_{jilk} \quad (2.10)$$

and

$$s_{ijkl} = s_{jikl} = s_{ijlk} = s_{jilk}. \quad (2.11)$$

Therefore, the number of independent components of both c_{ijkl} and s_{ijkl} tensors is reduced to 36. By using thermodynamics [33, 35], it can also be proved that c_{ijkl} ($c_{ijkl} = c_{klij}$) and s_{ijkl} ($s_{ijkl} = s_{klij}$) are symmetric tensors with respect to double indices. Hence, the number of components is then further reduced from 36 to 21.

2.2.4 Matrix notation:

We can simplify the writing of 3rd and 4th rank coefficients in tensor form by using the matrix or abbreviated notation form. The tensor notation is related to the matrix notation using the correspondence [35]

$$\begin{array}{l} \text{Tensor notation} \quad 11 \quad 22 \quad 33 \quad 23, 32 \quad 31, 13 \quad 12, 21 \\ \text{Matrix notation} \quad 1 \quad 2 \quad 3 \quad 4 \quad 5 \quad 6 \end{array}$$

where 11, 22 and 33 are the normal components and 23 or 32, 13 or 31 and 12 or 21 represents the shear components of stress and strain tensors. The piezoelectric and elastic coefficients can be written in matrix notation as

$$P_i = d_{im}\sigma_m \quad (2.12)$$

$$\epsilon_m = d_{im}E_i \quad (2.13)$$

$$\sigma_m = c_{mn}\epsilon_n \quad (2.14)$$

$$\epsilon_m = s_{mn}\sigma_n \quad (2.15)$$

where $i = 1, 2, 3$ and $m, n = 1, 2, \dots, 6$. Figure 2.5 shows the direction of the notation i , m , and n in terms of 1, 2, ..., 6 along the axes X, Y, and Z. The most commonly used three piezoelectric coefficients can be described in terms of the displacements induced by a given applied voltage in the axes X, Y, and Z which are:

$d_{33}.V$ = induced displacement in direction 3 due to the voltage (V) applied in direction 3.

$d_{31}.V$ = induced displacement in direction 1 due to the voltage (V) applied in direction 3.

$d_{15}.V$ = induced shear displacement in direction 2 due to the voltage (V) applied in direction 1.

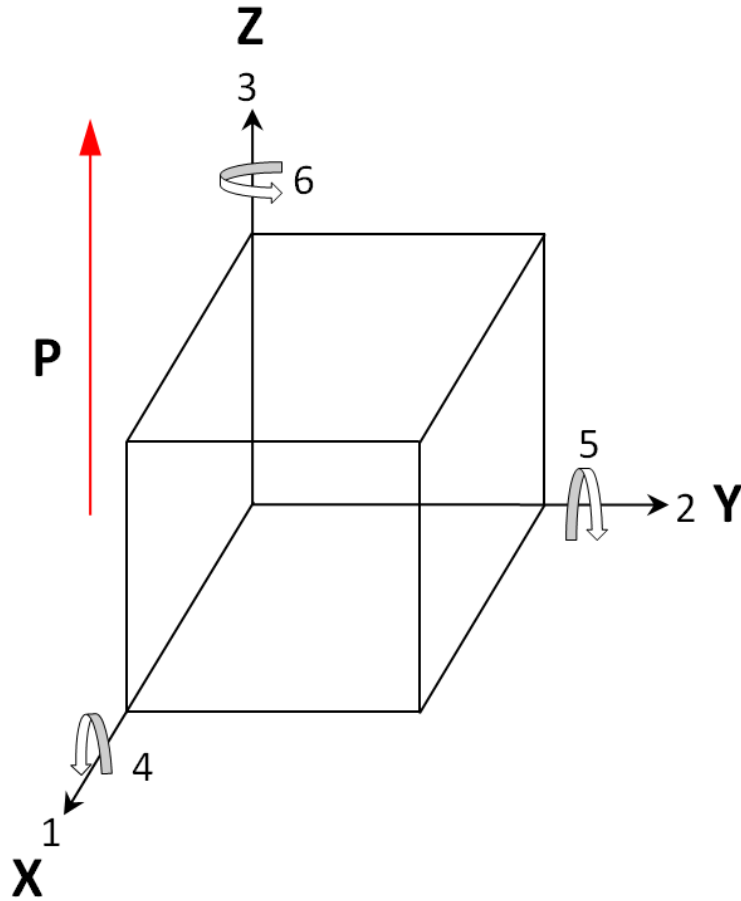


Figure 2.5: Polarization direction with the forces affecting a piezoelectric element [36, 37].

2.2.5 Crystal symmetry and crystal systems

There are three important crystal symmetry operations: rotation, reflection and inversion, which result in crystals with 32 possible combinations of symmetry elements. These 32 combinations are known as point groups or crystal classes. These 32 crystal classes can be divided into seven crystal systems. These are

- (i) Triclinic
- (ii) Monoclinic
- (iii) Orthorhombic
- (iv) Tetragonal
- (v) Cubic
- (vi) Trigonal
- (vii) Hexagonal.

2.2.6 The effects of crystal symmetry on piezoelectric materials

Depending on the crystal symmetry, the independent piezoelectric (18) and elastic (21) coefficients are reduced further in the 32 crystal point groups. According to Neumann's principle [33, 35], elastic compliance and stiffness exist in all 32 crystal point groups, but piezoelectric coefficients are non-zero only in certain crystal symmetries. The piezoelectric coefficients are zero in all centrosymmetric classes and in class 432 (international class symbol) [33]. Piezoelectric effects are found only if the crystal belongs to one of the 20 noncentrosymmetric classes [33].

2.2.7 Transformation of vectors and tensors

A tensor of first rank is known as a vector. A vector with respect to two sets of coordinate axes, Ox_i and Ox'_i can be written :

$$\begin{aligned} x_i &= a_{ji} x'_j && \text{for axes } Ox_i \\ x'_i &= a_{ij} x_j && \text{for axes } Ox'_i \end{aligned}$$

where a_{ji} and a_{ij} are transformation matrices which are described in next section. From the tensor definition, we get

$$p_i = T_{ij} q_j \quad (2.16)$$

where T_{ij} is a second rank tensor representing a physical property (e.g. the dielectric constant). Now we want to see how this will vary with the co-ordinate reference frame used. Suppose we write

$$p'_i = a_{ik} p_k, \quad (2.17)$$

$$p_k = T_{kl} q_l \quad (2.18)$$

and

$$q_l = a_{jl} q'_j. \quad (2.19)$$

If we combine these three equations, we get

$$p'_i = a_{ik} p_k = a_{ik} T_{kl} q_l = a_{ik} T_{kl} a_{jl} q'_j \quad (2.20)$$

or

$$p'_i = T'_{ij} q'_j. \quad (2.21)$$

Finally, we can write the tensor in the new set of axes as

$$T'_{ij} = a_{ik} a_{jl} T_{kl}. \quad (2.22)$$

2.2.8 Transformation for rotation

A counter-clockwise rotation about the x_3 -axis of a coordinate system by an angle θ gives the following transformation from the original coordinate position

$$x'_1 = x_1 \cos \theta + x_2 \sin \theta, \quad (2.23)$$

$$x'_2 = x_2 \cos \theta - x_1 \sin \theta \quad (2.24)$$

and

$$x'_3 = x_3. \quad (2.25)$$

In matrix notation, equation (2.23) to (2.25) can be written as

$$\begin{pmatrix} x'_1 \\ x'_2 \\ x'_3 \end{pmatrix} = \begin{pmatrix} \cos \theta & -\sin \theta & 0 \\ \sin \theta & \cos \theta & 0 \\ 0 & 0 & 1 \end{pmatrix} \begin{pmatrix} x_1 \\ x_2 \\ x_3 \end{pmatrix} \quad (2.26)$$

and the rotation matrix about x_3 is

$$a(x_3) = \begin{pmatrix} \cos \theta & -\sin \theta & 0 \\ \sin \theta & \cos \theta & 0 \\ 0 & 0 & 1 \end{pmatrix}. \quad (2.27)$$

Similarly, the rotation matrix about x_1 is

$$a(x_1) = \begin{pmatrix} 1 & 0 & 0 \\ 0 & \cos \theta & -\sin \theta \\ 0 & \sin \theta & \cos \theta \end{pmatrix} \quad (2.28)$$

and the rotation matrix about x_2 is

$$a(x_2) = \begin{pmatrix} \cos \theta & 0 & \sin \theta \\ 0 & 1 & 0 \\ -\sin \theta & 0 & \cos \theta \end{pmatrix}. \quad (2.29)$$

2.2.9 Transformation of third-rank tensors

A third rank tensor with respect to two sets of coordinate axes, ox_i and ox'_i , as shown in Figure 2.6 can be written as

$$P_i = d_{ijk} \sigma_{jk} \quad (2.30)$$

or

$$P = d\sigma \quad (2.31)$$

and

$$P'_i = d'_{lmn} \sigma'_{mn} \quad (2.32)$$

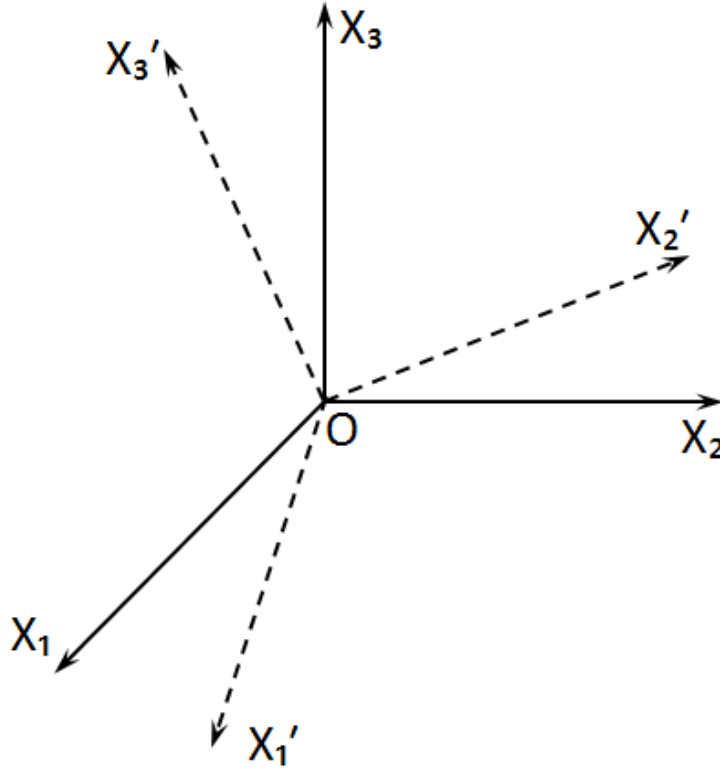


Figure 2.6: Transformation of two sets of coordinate axes, Ox_i and Ox'_i where $i = 1, 2, 3$.

or

$$P'_i = d'_{lmn} \sigma'_{mn}. \quad (2.33)$$

Since σ is a symmetric second-rank tensor, the transformations follow as [38]

$$P' = aP, \quad \sigma' = \alpha\sigma \quad \text{and} \quad \sigma = \alpha^{-1}\sigma'. \quad (2.34)$$

Hence, from equation (2.30), (2.31) and (2.32), we can write

$$P' = aP = ad\sigma = ad\alpha^{-1}\sigma' = d'\sigma'. \quad (2.35)$$

The transformation of third rank tensor can be written as

$$d' = ad\alpha^{-1} \quad (2.36)$$

where a , is the transformation matrix, which can be found by direct inspection or from rotation matrices, and its components are known as direction cosines, α^{-1} , is the inverse of the quadratic transformation matrix α , and d , is the piezoelectric coefficient matrix. The general forms of the three matrices are [33, 38]

$$a = \begin{pmatrix} a_{11} & a_{12} & a_{13} \\ a_{21} & a_{22} & a_{23} \\ a_{31} & a_{32} & a_{33} \end{pmatrix},$$

$$\alpha = \begin{pmatrix} a_{11}^2 & a_{12}^2 & a_{13}^2 & 2a_{12}a_{13} & 2a_{13}a_{11} & 2a_{11}a_{12} \\ a_{21}^2 & a_{22}^2 & a_{23}^2 & 2a_{22}a_{23} & 2a_{23}a_{21} & 2a_{21}a_{22} \\ a_{31}^2 & a_{32}^2 & a_{33}^2 & 2a_{32}a_{33} & 2a_{33}a_{31} & 2a_{31}a_{32} \\ a_{21}a_{31} & a_{22}a_{32} & a_{23}a_{33} & a_{22}a_{33} + a_{23}a_{32} & a_{22}a_{33} + a_{23}a_{32} & a_{22}a_{33} + a_{23}a_{32} \\ a_{31}a_{11} & a_{32}a_{12} & a_{33}a_{13} & a_{12}a_{33} + a_{13}a_{32} & a_{13}a_{31} + a_{11}a_{33} & a_{11}a_{32} + a_{12}a_{31} \\ a_{11}a_{21} & a_{12}a_{22} & a_{13}a_{23} & a_{12}a_{23} + a_{13}a_{22} & a_{13}a_{21} + a_{11}a_{23} & a_{11}a_{22} + a_{12}a_{21} \end{pmatrix}$$

and

$$d = \begin{pmatrix} d_{11} & d_{12} & d_{13} & d_{14} & d_{15} & d_{16} \\ d_{21} & d_{22} & d_{23} & d_{24} & d_{25} & d_{26} \\ d_{31} & d_{32} & d_{33} & d_{34} & d_{35} & d_{36} \end{pmatrix}.$$

In tensor subscript notation, the piezoelectric coefficients with respect to two sets of coordinates can be written as

$$d'_{ijk} = a_{il}a_{jm}a_{kn}d_{lmn}. \quad (2.37)$$

We can use the direct inspection method to calculate the effect of crystal symmetry on the components of tensor properties, except for the trigonal and hexagonal crystal systems. For example, the center-of-symmetry operation (inversion) corresponds to

$$x'_1 \rightarrow -x_1, \quad x'_2 \rightarrow -x_2, \quad x'_3 \rightarrow -x_3 \quad \text{or} \quad 1' \rightarrow -1, \quad 2' \rightarrow -2, \quad 3' \rightarrow -3.$$

By direct inspection, we can write the matrices corresponding to an inversion operation as,

$$a = \begin{pmatrix} -1 & 0 & 0 \\ 0 & -1 & 0 \\ 0 & 0 & -1 \end{pmatrix}$$

and

$$\alpha^{-1} = \begin{pmatrix} 1 & 0 & 0 & 0 & 0 & 0 \\ 0 & 1 & 0 & 0 & 0 & 0 \\ 0 & 0 & 1 & 0 & 0 & 0 \\ 0 & 0 & 0 & 1 & 0 & 0 \\ 0 & 0 & 0 & 0 & 1 & 0 \\ 0 & 0 & 0 & 0 & 0 & 1 \end{pmatrix}.$$

Therefore,

$$\begin{aligned}
d' &= \begin{pmatrix} -1 & 0 & 0 \\ 0 & -1 & 0 \\ 0 & 0 & -1 \end{pmatrix} \begin{pmatrix} d_{11} & d_{12} & d_{13} & d_{14} & d_{15} & d_{16} \\ d_{21} & d_{22} & d_{23} & d_{24} & d_{25} & d_{26} \\ d_{31} & d_{32} & d_{33} & d_{34} & d_{35} & d_{36} \end{pmatrix} \begin{pmatrix} 1 & 0 & 0 & 0 & 0 & 0 \\ 0 & 1 & 0 & 0 & 0 & 0 \\ 0 & 0 & 1 & 0 & 0 & 0 \\ 0 & 0 & 0 & 1 & 0 & 0 \\ 0 & 0 & 0 & 0 & 1 & 0 \\ 0 & 0 & 0 & 0 & 0 & 1 \end{pmatrix} \\
&= \begin{pmatrix} -d_{11} & -d_{12} & -d_{13} & -d_{14} & -d_{15} & -d_{16} \\ -d_{21} & -d_{22} & -d_{23} & -d_{24} & -d_{25} & -d_{26} \\ -d_{31} & -d_{32} & -d_{33} & -d_{34} & -d_{35} & -d_{36} \end{pmatrix}.
\end{aligned}$$

If inversion is a symmetry operation of a crystal, all the piezoelectric coefficients must be the same before and after the operation, i.e., $d'_{ijk} = d_{ijk}$. Comparing the components before and after the inversion operation, we see that $d_{ijk} = -d_{ijk} = 0$ which means all the piezoelectric moduli are zero for all 11 centro-symmetrical crystal groups.

Let consider another example such as the symmetry operation on point groups of cubic crystals (23). By direct inspection, we can write for 2-fold rotation about the x_3 -axis, $x'_1 \rightarrow -x_1$, $x'_2 \rightarrow -x_2$, $x'_3 \rightarrow x_3$, and after that 3-fold rotation along [111] direction, $x'_1 \rightarrow -x_2$, $x'_2 \rightarrow -x_3$, $x'_3 \rightarrow x_1$. Finally, the transformation matrices are

$$a = \begin{pmatrix} 0 & -1 & 0 \\ 0 & 0 & -1 \\ 1 & 0 & 0 \end{pmatrix}$$

and

$$\alpha^{-1} = \begin{pmatrix} 0 & 0 & 1 & 0 & 0 & 0 \\ 1 & 0 & 0 & 0 & 0 & 0 \\ 0 & 1 & 0 & 0 & 0 & 0 \\ 0 & 0 & 0 & 0 & 0 & 1 \\ 0 & 0 & 0 & -1 & 0 & 0 \\ 0 & 0 & 0 & 0 & -1 & 0 \end{pmatrix}.$$

Therefore,

$$\begin{aligned}
d' &= \begin{pmatrix} 0 & -1 & 0 \\ 0 & 0 & -1 \\ 1 & 0 & 0 \end{pmatrix} \begin{pmatrix} d_{11} & d_{12} & d_{13} & d_{14} & d_{15} & d_{16} \\ d_{21} & d_{22} & d_{23} & d_{24} & d_{25} & d_{26} \\ d_{31} & d_{32} & d_{33} & d_{34} & d_{35} & d_{36} \end{pmatrix} \begin{pmatrix} 0 & 0 & 1 & 0 & 0 & 0 \\ 1 & 0 & 0 & 0 & 0 & 0 \\ 0 & 1 & 0 & 0 & 0 & 0 \\ 0 & 0 & 0 & 0 & 0 & 1 \\ 0 & 0 & 0 & -1 & 0 & 0 \\ 0 & 0 & 0 & 0 & -1 & 0 \end{pmatrix} \\
&= \begin{pmatrix} -d_{22} & -d_{23} & -d_{21} & d_{25} & d_{26} & -d_{24} \\ -d_{32} & -d_{33} & -d_{31} & d_{35} & d_{36} & -d_{34} \\ d_{12} & d_{13} & d_{11} & -d_{15} & -d_{16} & d_{14} \end{pmatrix}.
\end{aligned}$$

Since these are symmetry operations of a cubic crystal, $d'_{ijk} = d_{ijk}$. If we compare the components before and after the cubic symmetry operations, we find

$$d_{12} = -d_{23}, \quad d_{23} = -d_{31} \quad \text{and} \quad d_{31} = d_{12}$$

so

$$d_{12} = -d_{23} = d_{31} = 0$$

and similarly,

$$\begin{aligned} d_{13} &= -d_{21} = d_{32} = 0, \\ d_{11} &= -d_{22} = -d_{33} = 0, \\ d_{16} &= -d_{24} = -d_{35} = 0, \\ d_{15} &= d_{26} = -d_{34} = 0, \\ &\text{and} \\ d_{14} &= d_{25} = d_{36} \neq 0. \end{aligned}$$

Therefore, the piezoelectric coefficients for the cubic crystal point group (23) have the form

$$\begin{pmatrix} 0 & 0 & 0 & d_{14} & 0 & 0 \\ 0 & 0 & 0 & 0 & d_{14} & 0 \\ 0 & 0 & 0 & 0 & 0 & d_{14} \end{pmatrix}.$$

On the other hand, for the trigonal and hexagonal crystal systems, the direct inspection method is not applicable. To calculate the non-zero piezoelectric coefficients of trigonal and hexagonal crystal systems, we need to use the rotational matrix about the x_3 -axis, which is

$$a(x_3) = \begin{pmatrix} \cos \theta & -\sin \theta & 0 \\ \sin \theta & \cos \theta & 0 \\ 0 & 0 & 1 \end{pmatrix}.$$

If we consider a 6-fold rotation axis parallel to x_3 for the hexagonal system, the transformation matrices are [38]

$$a = \begin{pmatrix} \frac{1}{2} & \frac{\sqrt{3}}{2} & 0 \\ -\frac{\sqrt{3}}{2} & \frac{1}{2} & 0 \\ 0 & 0 & 1 \end{pmatrix}$$

and

$$\alpha^{-1} = \begin{pmatrix} \frac{1}{4} & \frac{3}{4} & 0 & 0 & 0 & -\frac{\sqrt{3}}{2} \\ \frac{3}{4} & \frac{1}{4} & 0 & 0 & 0 & \frac{\sqrt{3}}{2} \\ 0 & 0 & 1 & 0 & 0 & 0 \\ 0 & 0 & 0 & \frac{1}{2} & \frac{\sqrt{3}}{2} & 0 \\ 0 & 0 & 0 & -\frac{\sqrt{3}}{2} & \frac{1}{2} & 0 \\ \frac{\sqrt{3}}{4} & -\frac{\sqrt{3}}{4} & 0 & 0 & 0 & \frac{1}{4} \end{pmatrix}.$$

Therefore,

$$d' = \begin{pmatrix} \frac{1}{2} & \frac{\sqrt{3}}{2} & 0 \\ -\frac{\sqrt{3}}{2} & \frac{1}{2} & 0 \\ 0 & 0 & 1 \end{pmatrix} \begin{pmatrix} d_{11} & d_{12} & d_{13} & d_{14} & d_{15} & d_{16} \\ d_{21} & d_{22} & d_{23} & d_{24} & d_{25} & d_{26} \\ d_{31} & d_{32} & d_{33} & d_{34} & d_{35} & d_{36} \end{pmatrix} \begin{pmatrix} \frac{1}{4} & \frac{3}{4} & 0 & 0 & 0 & -\frac{\sqrt{3}}{2} \\ \frac{3}{4} & \frac{1}{4} & 0 & 0 & 0 & \frac{\sqrt{3}}{2} \\ 0 & 0 & 1 & 0 & 0 & 0 \\ 0 & 0 & 0 & \frac{1}{2} & \frac{\sqrt{3}}{2} & 0 \\ 0 & 0 & 0 & -\frac{\sqrt{3}}{2} & \frac{1}{2} & 0 \\ \frac{\sqrt{3}}{4} & -\frac{\sqrt{3}}{4} & 0 & 0 & 0 & \frac{1}{4} \end{pmatrix}.$$

To simplify the calculation, we can impose a 2-fold rotation about the x_3 -axis upon the hexagonal crystal. Some of the piezoelectric moduli will be eliminated by this operation [38]. Hence,

$$d' = \begin{pmatrix} -1 & 0 & 0 \\ 0 & -1 & 0 \\ 0 & 0 & 1 \end{pmatrix} \begin{pmatrix} d_{11} & d_{12} & d_{13} & d_{14} & d_{15} & d_{16} \\ d_{21} & d_{22} & d_{23} & d_{24} & d_{25} & d_{26} \\ d_{31} & d_{32} & d_{33} & d_{34} & d_{35} & d_{36} \end{pmatrix} \begin{pmatrix} 1 & 0 & 0 & 0 & 0 & 0 \\ 0 & 1 & 0 & 0 & 0 & 0 \\ 0 & 0 & 1 & 0 & 0 & 0 \\ 0 & 0 & 0 & -1 & 0 & 0 \\ 0 & 0 & 0 & 0 & -1 & 0 \\ 0 & 0 & 0 & 0 & 0 & 1 \end{pmatrix}$$

or,

$$d' = \begin{pmatrix} 0 & 0 & 0 & d_{14} & d_{15} & 0 \\ 0 & 0 & 0 & d_{24} & d_{25} & 0 \\ d_{31} & d_{32} & d_{33} & 0 & 0 & d_{36} \end{pmatrix}.$$

Now if we apply a 6-fold symmetry operation to this hexagonal crystal, we can easily calculate the non-vanishing moduli. Therefore

$$d' = \begin{pmatrix} -\frac{1}{2} & -\frac{\sqrt{3}}{2} & 0 \\ \frac{\sqrt{3}}{2} & -\frac{1}{2} & 0 \\ 0 & 0 & 1 \end{pmatrix} \begin{pmatrix} 0 & 0 & 0 & d_{14} & d_{15} & 0 \\ 0 & 0 & 0 & d_{24} & d_{25} & 0 \\ d_{31} & d_{32} & d_{33} & 0 & 0 & d_{36} \end{pmatrix} \begin{pmatrix} \frac{1}{4} & \frac{3}{4} & 0 & 0 & 0 & -\frac{\sqrt{3}}{2} \\ \frac{3}{4} & \frac{1}{4} & 0 & 0 & 0 & \frac{\sqrt{3}}{2} \\ 0 & 0 & 1 & 0 & 0 & 0 \\ 0 & 0 & 0 & -\frac{1}{2} & -\frac{\sqrt{3}}{2} & 0 \\ 0 & 0 & 0 & \frac{\sqrt{3}}{2} & -\frac{1}{2} & 0 \\ \frac{\sqrt{3}}{4} & -\frac{\sqrt{3}}{4} & 0 & 0 & 0 & \frac{1}{4} \end{pmatrix}$$

which gives us 8 equations. These are

$$\begin{aligned} d_{14} &= \frac{1}{4}d_{14} + \frac{\sqrt{3}}{4}d_{24} - \frac{\sqrt{3}}{4}d_{15} + \frac{3}{4}d_{25}, \\ d_{15} &= \frac{\sqrt{3}}{4}d_{14} + \frac{3}{4}d_{24} + \frac{1}{4}d_{15} + \frac{\sqrt{3}}{4}d_{25}, \\ d_{24} &= -\frac{\sqrt{3}}{4}d_{14} + \frac{\sqrt{3}}{4}d_{24} - \frac{\sqrt{3}}{4}d_{15} + \frac{3}{4}d_{25}, \\ d_{25} &= \frac{1}{4}d_{14} + \frac{1}{4}d_{24} + \frac{3}{4}d_{15} - \frac{\sqrt{3}}{4}d_{25}, \\ d_{31} &= \frac{1}{4}d_{31} + \frac{3}{4}d_{32} + \frac{\sqrt{3}}{4}d_{36}, \\ d_{32} &= \frac{3}{4}d_{31} + \frac{1}{4}d_{32} - \frac{\sqrt{3}}{4}d_{36}, \\ d_{33} &= d_{33}, \end{aligned}$$

and

$$d_{36} = -\frac{\sqrt{3}}{2}d_{31} + \frac{\sqrt{3}}{2}d_{32} + \frac{1}{4}d_{36}.$$

After solving these 8 equations, we find that the non-vanishing piezoelectric moduli for hexagonal class 6 crystal are

$$= \begin{pmatrix} 0 & 0 & 0 & d_{14} & d_{15} & 0 \\ 0 & 0 & 0 & d_{15} & -d_{14} & 0 \\ d_{31} & d_{31} & d_{33} & 0 & 0 & 0 \end{pmatrix}.$$

2.3 Ferroelectric domains and poling of ferroelectric single crystals and ceramics

When a ferroelectric material is cooled through a phase transition from para-electric to ferroelectric, its crystal structure changes [39, 40, 41, 42] and the temperature at the phase transition is called Curie temperature (T_C). During the transformation, the crystal structure is distorted which produces an electric dipole moment (the spontaneous polarization). The ferroelectric materials of the most practical interest are perovskite-type crystal structures with a general formula ABO_3 . The most widely used are grown from a solid solution of lead titanate, $PbTiO_3$.

To discuss ferroelectric domains, consider a perovskite crystal $PbTiO_3$. It transforms from a paraelectric cubic to a ferroelectric tetragonal phase at a Curie temperature 490 °C. At the transition O and Ti/Zr ions move along the c-axis relative to the large Pb ions, as shown in Figure 2.7. The movement of the ions along the c-axis produces a permanent electric dipole moment which leads to a net polarization at the crystal. A small area of the crystal with uniformly oriented dipole moments is referred to as a ferroelectric domain, and the thin layer which separates two domains is called a domain wall. Domain walls that separate anti-parallel ferroelectric domains are known as 180° domain walls and the walls between mutually perpendicular domains are known as non-180° domain walls [43]. Figure 2.8 schematically illustrates both 180° domain walls and non-180° domain walls. In ceramics, the material consists of small crystallites (grains) with different orientations. These are separated by grain boundaries and may contain several ferroelectric domains.

The spontaneous polarization (dipole moments) may be randomly oriented throughout a ferroelectric single crystal or inside grains in ferroelectric ceramics, with no net polarization of the material. To align these, a large DC electric field is applied to the material slightly below its Curie temperature (T_C) [36]. The direction of the applied DC electric field determines the direction of the polarization. This process known as poling the material.

Consider a ferroelectric single crystal consisting of a random orientation of domains with no net polarization of the crystal, as shown in Figure 2.9(a). When the

Perovskite-Type Structure

General formula: ABO_3

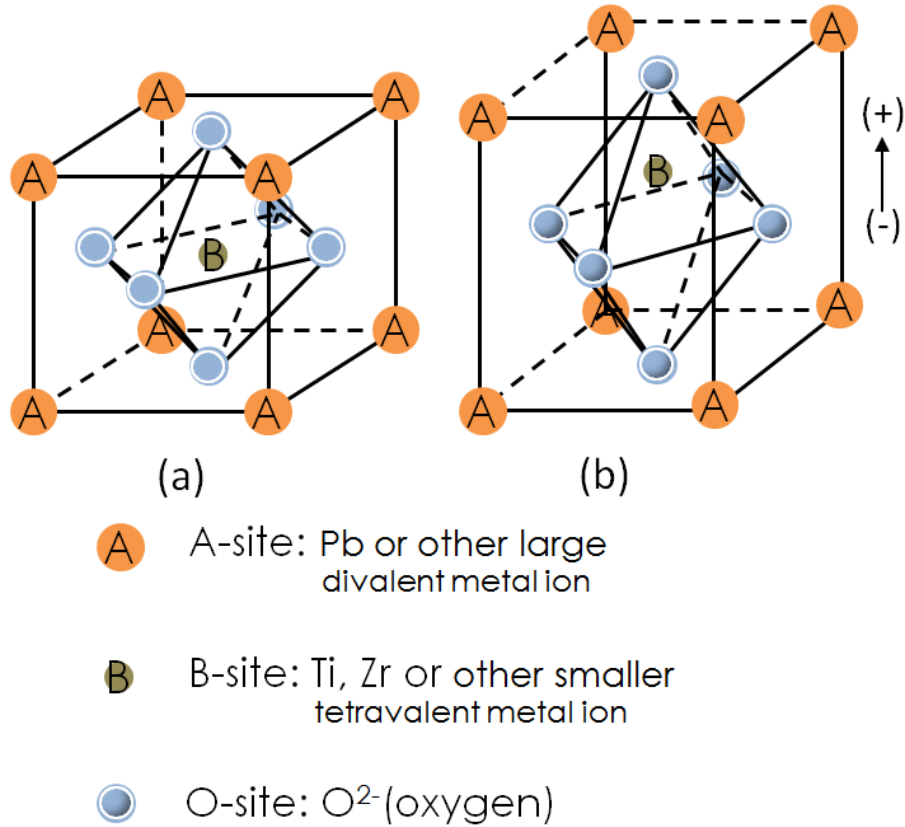


Figure 2.7: Crystal structure of a perovskite piezoelectric (a) cubic lattice with no dipole above the Curie temperature and (b) tetragonal (orthorhombic) lattice with dipole moment below the Curie temperature [36].

material is exposed to the poling field, some domains get bigger due to the motion of domain walls, as shown in Figure 2.9(b). As a result, a net polarization is produced in the single crystal, in the direction of the poling field. Sometimes, for example in lithium niobate, a single domain or monodomain can be produced by poling a single crystal.

In a ferroelectric ceramic, randomly oriented domains inside the grains can make the net polarization zero as shown in Figure 2.10(a). If the piezoelectric ceramic is exposed to a large poling field, the dipole moments will align in the direction nearest to the poling field. It is impossible to have perfectly aligned dipole moments along the poling field due to the random orientation of grains. However, a reasonable degree of alignment can be achieved since each grain can have several allowed directions. Because of the domain alignment, the material also elongates in the same direction

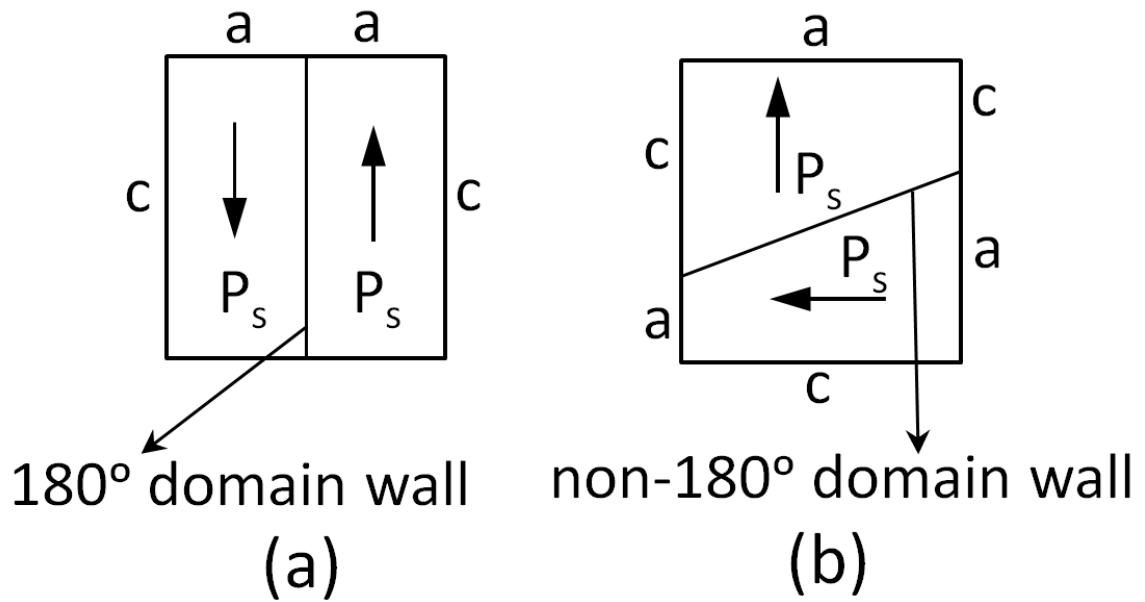


Figure 2.8: (a) a 180° domain wall separating anti-parallel ferroelectric domains, and (b) a non-180° domain wall separating mutually perpendicular domains [43, 44].

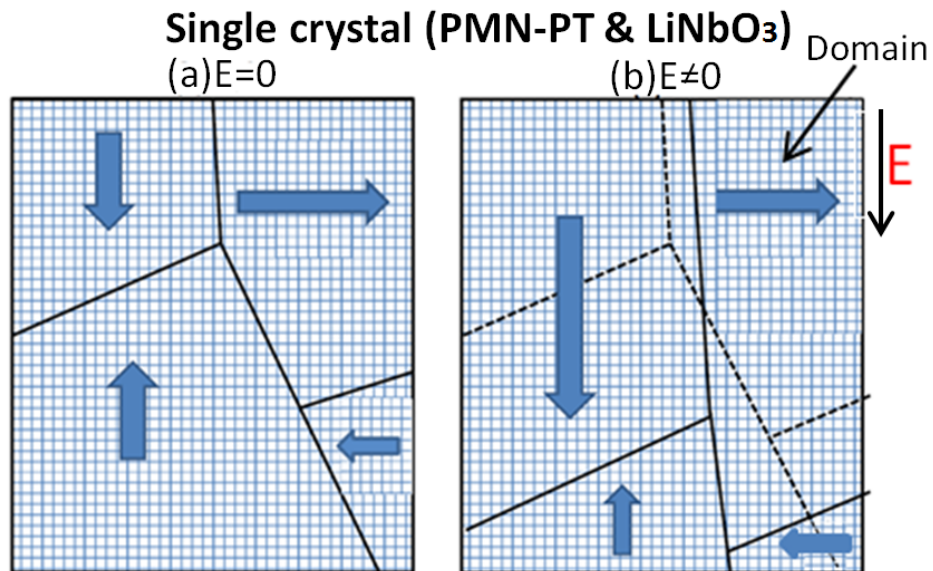


Figure 2.9: (a) Unpoled and (b) poled single crystal (Figure reproduced from Bukhari M.Sc. thesis, 2014) [45].

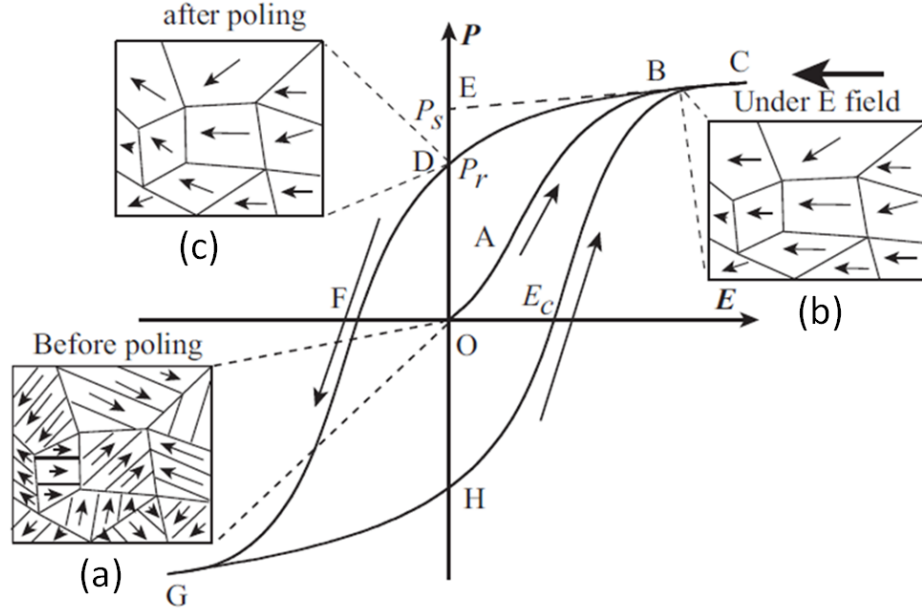


Figure 2.10: A typical hysteresis loop (or switchery) in a ferroelectric ceramic and corresponding domain reversal (Figure reproduced from Jin *et al.*) [46]. Switching during poling shows the (a) non-polarized state, (b) under an applied electric field, (c) a polarized state.

as shown in Figure 2.10(b). When the poling field is removed, the spontaneous polarization does not entirely return to its original position, and the crystal remains partially polarized as shown in Figure 2.10(c). The partial polarization is called a remnant polarization. Due to such poling, the material has become permanently piezoelectric. When the poled material is then subjected to a DC electric field in the poling direction, the material elongates further in the direction of the field [36, 47].

2.4 Piezoelectric and dielectric properties of single crystal LiNbO_3 , PMN-PT and ceramic PZT

These three piezoelectric materials are widely investigated because of their large piezoelectric and dielectric properties. We discuss these three materials' temperature dependence, composition, crystal structure, and symmetry which are responsible for their larger piezoelectric and dielectric properties.

2.4.1 Single crystal LiNbO_3

Lithium niobate (LiNbO_3) crystals are not naturally occurring. In 1949, Matthias and Remeika synthesized single crystals of LiNbO_3 for the first time and discovered

their ferroelectric properties [48]. After that, several papers were published about the properties and structure of the material. This single crystal belongs to a trigonal crystal system where it can have either a rhombohedral or hexagonal unit cell [20]. It has been widely used in various devices because of its piezoelectric, pyroelectric, electro-optic, photo-elastic and dielectric properties [18, 19, 20, 49]. It is also used in surface acoustic wave (SAW) devices for its low acoustic losses [27]. The Curie temperature of LiNbO_3 is 1210°C . Above the Curie temperature, it has a paraelectric phase. In the paraelectric phase, the Li atoms, which are $c/4$ away from Nb atoms, stay in an oxygen layer and the Nb atoms lie in the center between nearest oxygen layers. This orientation produces no net polarization [50]. Below the Curie temperature, it forms planar sheets of oxygen atoms in a ferroelectric distorted hexagonal closed packed configuration, where the elastic forces of the crystal shift the lithium and niobium ions into new position which induces spontaneous polarization [20]. Both the paraelectric and ferroelectric crystal structures of LiNbO_3 are shown in Figure 2.11.

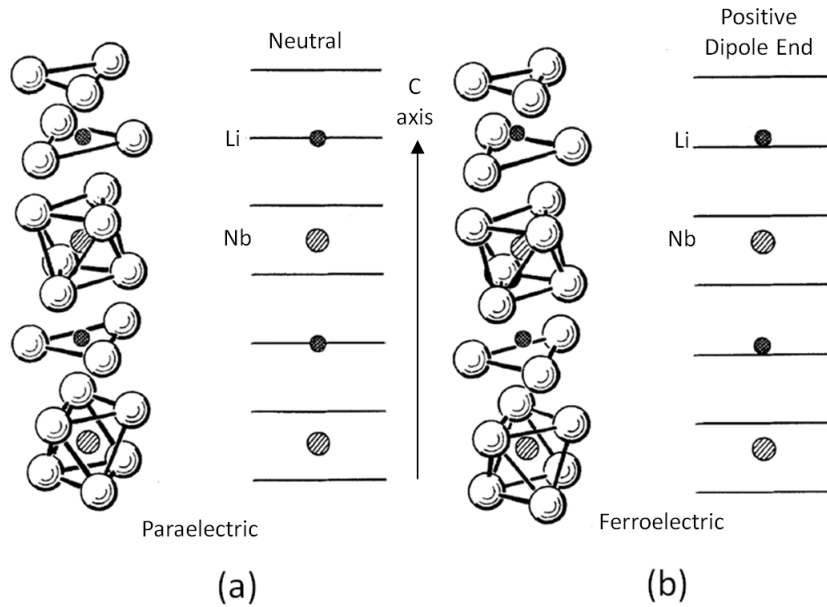


Figure 2.11: Positions of the lithium atoms (Li) and the niobium atoms (Nb) with respect to the oxygen (O) octahedra in the paraelectric (left) and ferroelectric (right) phase of lithium niobate single crystal (Figure reproduced from Weis *et al.*, 1985) [20, 50].

The ferroelectric phase of the crystal has three-fold rotation symmetry about its c axis and three mirror symmetry planes which are 60° apart. The LiNbO_3 crystal is classified as a member of point group $3m$ with those two crystal symmetry operations

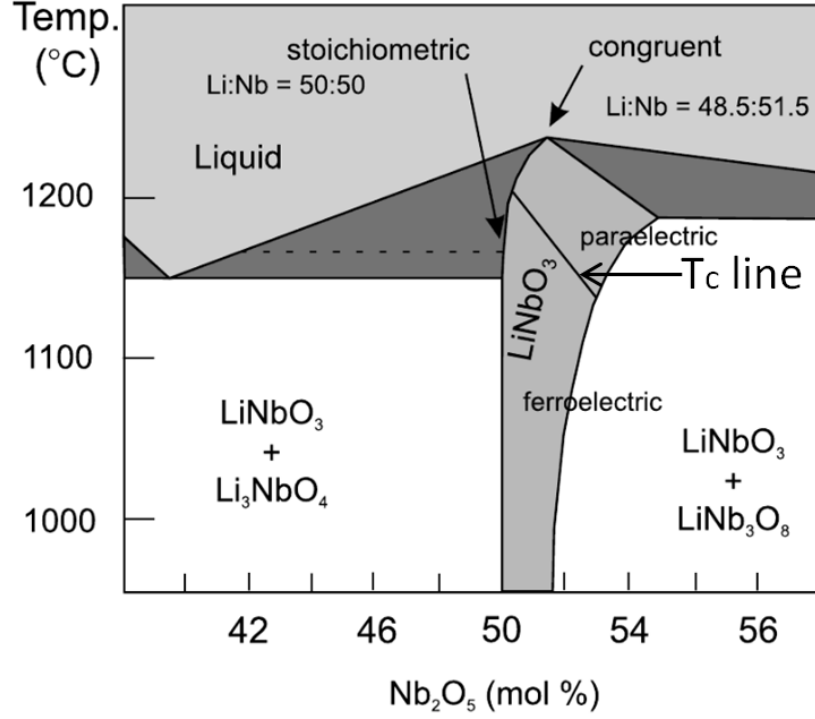


Figure 2.12: Schematic phase diagram of the $\text{Li}_2\text{ONb}_2\text{O}_5$ pseudobinary system (Figure reproduced from Volk *et al.*, 2008) [51].

[52]. Figure 2.12 shows the phase diagram of the $\text{Li}_2\text{ONb}_2\text{O}_5$ pseudobinary system. LiNbO_3 is one of the important compounds of this system. LiNbO_3 crystals are grown near the stoichiometric and congruent composition to get a larger piezoelectric effect. The line between the paraelectric and ferroelectric phases in Figure 2.12 is the Curie temperature (T_c) line. It is clear that T_c is strongly composition dependent. Since LiNbO_3 crystals are point group $3m$ classes, the non-vanishing piezoelectric and dielectric coefficients [18] have the following form

$$\begin{pmatrix} 0 & 0 & 0 & 0 & d_{15} & -2d_{22} \\ -d_{22} & d_{22} & 0 & d_{15} & 0 & 0 \\ d_{31} & d_{31} & d_{33} & 0 & 0 & 0 \end{pmatrix}$$

and

$$\begin{pmatrix} K_{11} & 0 & 0 \\ 0 & K_{11} & 0 \\ 0 & 0 & K_{33} \end{pmatrix}.$$

So the piezoelectric and dielectric properties of LiNbO_3 crystal can be described by four independent piezoelectric coefficients d_{15} , d_{22} , d_{31} , d_{33} and two independent dielectric coefficients K_{11} , K_{33} , respectively.

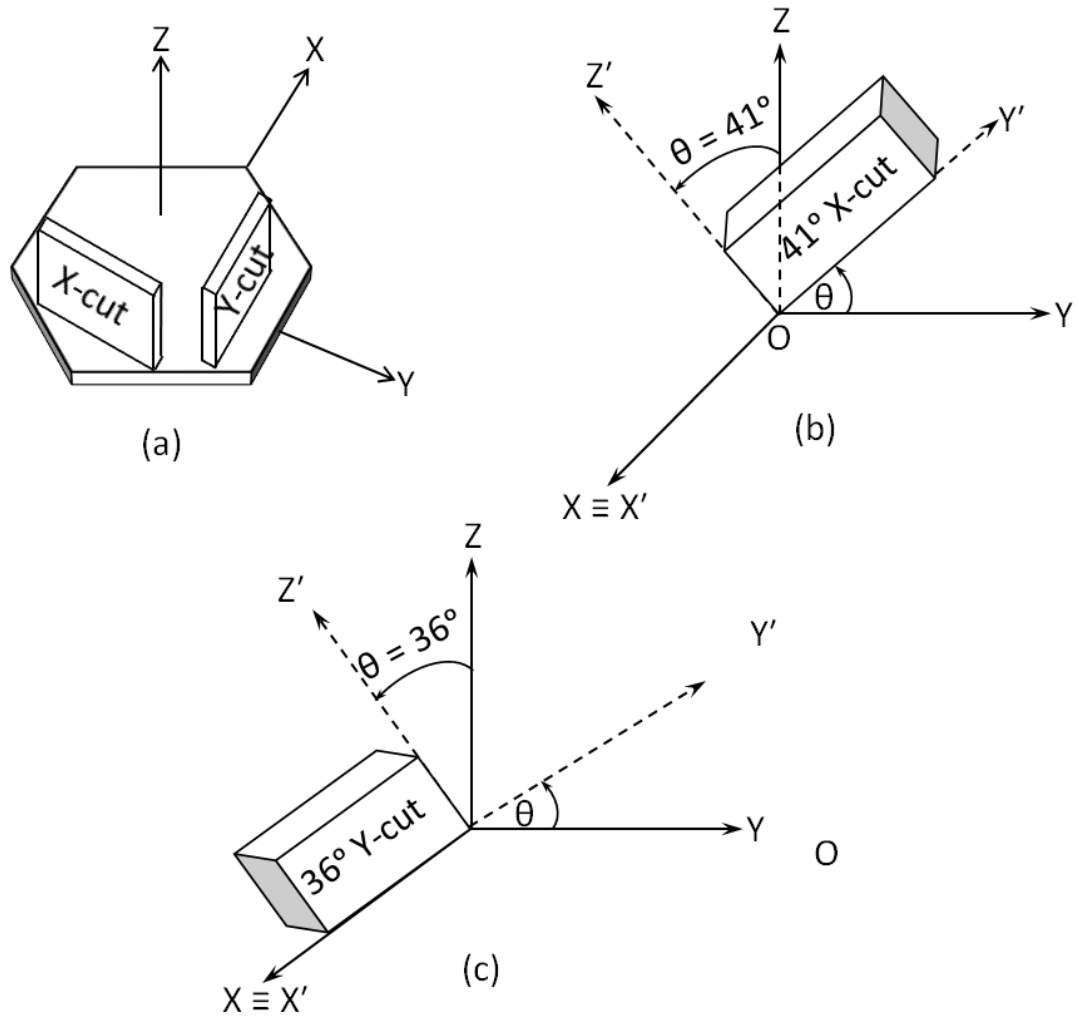


Figure 2.13: (a) X-cut and Y-cut, (b) 41° X-cut and (c) 36° Y-cut of LiNbO₃ single crystal [1, 27].

Depending on which piezoelectric coefficients need to be measured, LiNbO₃ crystals are commonly cut in a number of useful ways perpendicular to the X, Y, and Z axes. Shear cuts such as 41° X-cut, 163° rotated Y-cut and longitudinal cuts like Z-cut and 36° Y-cut (quasi longitudinal) are very popular. X-cut and Y-cut orientations of LiNbO₃ single crystals are shown in Figure 2.13(a) and a 41° X-cut is shown in Figure 2.13(b). The 41° X-cut has pure shear modes because it is perpendicular to the X-axis. In our lab, we used 41° X-cut and 36° Y-cut LiNbO₃ transducers to measure the shear and longitudinal piezoelectric and dielectric coefficients.

2.4.2 Single crystal PMN-PT

During the last couple of decades, relaxor ferroelectric materials have been widely investigated, with an extensive and increasing range of applications. Conventional piezoelectric crystals have either tetragonal or rhombohedral symmetry and a dipole moment below the Curie temperature (T_C) that produces piezoelectric properties. Above the Curie temperature, piezoelectric properties sharply disappear because the crystal has a simple cubic symmetry with no dipole moment. In relaxor materials, the phase transition from para-electric to ferroelectric phase does not occur at a specific temperature, but the change occurs over a temperature range known as the Curie range.

Lead magnesium niobate-lead titanate (PMN-PT) is one of the best known relaxor ferroelectric crystals. Its chemical composition is $(1-x)\text{Pb}(\text{Mg}_{1/3}\text{Nb}_{2/3})\text{O}_3-x\text{PbTiO}_3$. It can be grown either as a single crystal or as a polycrystalline ceramic from a solid solution of relaxor ferroelectric PMN and a normal ferroelectric PT. Technologically, single crystals are more important because of their larger electromechanical coupling coefficients, piezoelectric coefficients and dielectric constants, with low dielectric losses, compared to those of polycrystalline ceramics. This crystal (PMN-PT) has complex phase boundaries in the region ($0.3 < x < 0.35$) at room temperature, referred to as the morphotropic phase boundary (MPB). Crystals are usually grown near the MPB because larger piezoelectric and dielectric properties are observed in this region. In 2003, Guo *et al.* grew PMN-PT single crystals using a modified Bridgeman technique and introduced a modified MPB as shown in Figure 2.14 [53]. They mainly determined that the MPB boundary region ($0.3 < x < 0.35$) involves two-phase boundaries between rhombohedral - monoclinic (orthorhombic O_1) and monoclinic - tetragonal (orthorhombic O_2), where abnormal dielectric and piezoelectric properties are observed. Their proposed MPB is widely accepted in the community.

Above T_C PMN-PT crystals have a para-electric phase with a cubic $m3m$ symmetry for all compositions [53, 54, 55, 56] so far studied. Below T_C , their structure depends on the composition x . The MPB of PMN-PT is between $x=0.33$ to $x=0.35$ and separates rhombohedral $3m$ symmetry below $x \leq 0.33$ and tetragonal $4mm$ symmetry above ≥ 0.35 . Within the MPB, PMN-PT has a monoclinic m symmetry, and an orthorhombic $mm2$ symmetry is observed on both side of the MPB.

Piezoelectric properties of this material also depend on the poling direction. Poling along $\langle 001 \rangle$ directions in PMN-PT creates a symmetrical multi-domain configuration with macroscopic tetragonal symmetry ($4mm$) and only three independent piezoelectric coefficients, $d_{15} = d_{24}$, $d_{31} = d_{32}$, and d_{33} [57]. Poling along $\langle 111 \rangle$

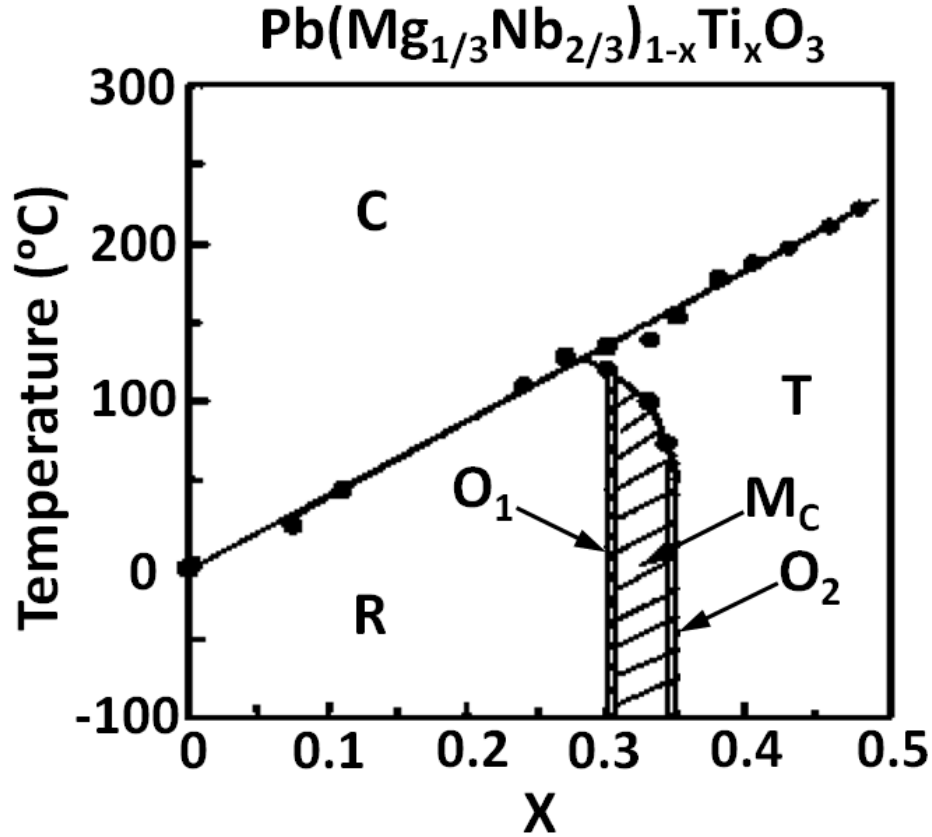


Figure 2.14: The accepted phase diagram of PMN-PT crystals as proposed by Guo *et al.* [53]. C, T, R, O, and M refer to cubic, tetragonal, rhombohedral, orthorhombic and monoclinic phase regions, respectively.

PMN-PT creates a single domain rhombohedral ($3m$) symmetry with four independent piezoelectric coefficients, $d_{15} = d_{14}$, $d_{16} = \frac{d_{21}}{2} = -\frac{d_{22}}{2}$, $d_{31} = d_{32}$ and d_{33} [57]. Poling along $\langle 011 \rangle$ of PMN-PT creates a symmetrical multi-domain configuration with macroscopic orthorhombic symmetry ($mm2$). These crystals have five independent piezoelectric coefficients, d_{15} , d_{24} , d_{31} , d_{32} , and d_{33} [57]. The PMN-PT crystal has a lower Curie temperature ($(130-170)^\circ\text{C}$) than LiNbO_3 (1210°C) and PZT (350°C) crystals, which limits its applications at higher temperatures.

2.4.3 Polycrystalline PZT ceramics

PZT ($\text{PbZr}_x\text{Ti}_{1-x}\text{O}_3$) ceramics were first discovered in the 1950s and they are now the most used piezoelectric materials. PZT is grown from a solid solution of lead zirconate (PbZrO_3) and lead titanate (PbTiO_3). It has a perovskite (ABO_3) crystalline structure, where Pb atoms fill the A-sites at the corners of the unit cell, and O_2 atoms are at the face centers. Ti or Zr atoms are positioned at the center of the unit cell to

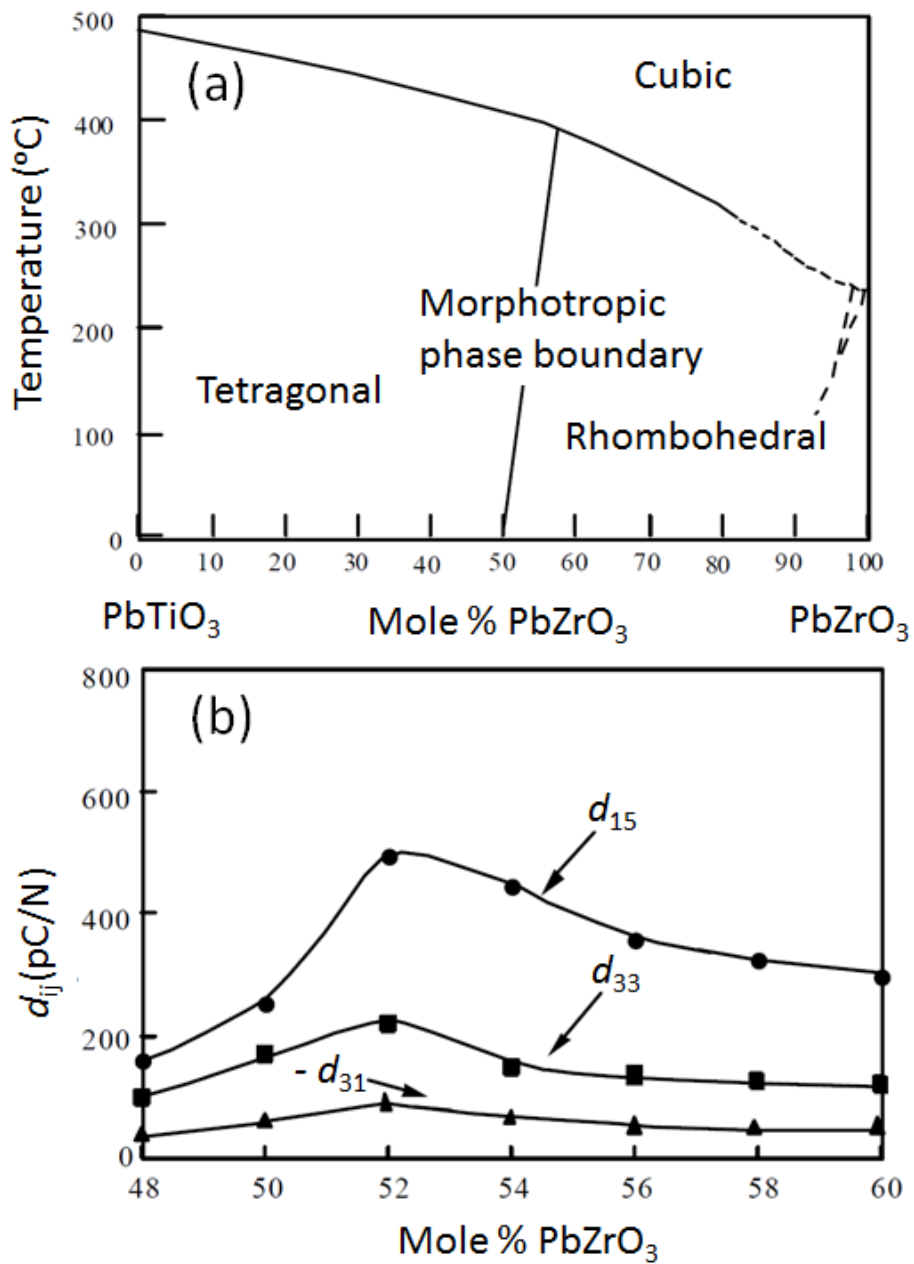


Figure 2.15: (a) Phase diagram of PZT and (b) the piezoelectric coefficients, d_{ij} , as a function of composition [58].

fill B-sites where they are octahedrally coordinated. The Curie temperature (T_C) of the material is 350°C . Above T_C , it shows a para-electric simple cubic (m3m) symmetry with no dipole moment. Below T_C , it has a ferroelectric tetragonal (4mm) or rhombohedral (3m) crystal structure. Pure PT (PbTiO_3) is tetragonal ferroelectric (4mm) and pure PZ (PbZrO_3) is antiferroelectric orthorhombic at room temperature. The boundary between the ferroelectric tetragonal (4mm) and rhombohedral (3m) phases is called the morphotropic phase boundary (MPB). Figure 2.15 shows the MPB of PZT. PZT is mainly grown near the MPB because larger piezoelectric and dielectric properties are achieved in these region [58].

The 32 point groups that are described in section 3, do not apply to polycrystalline ceramics such as PZT, which consist of randomly oriented of grains in all directions. They can be described by a symmetry axis of infinite order (∞) [59]. A symmetry axis of infinite order means that its physical properties are unchanged when the material is rotated by any angle around such an axis. Before poling, PZT ceramics have spherical symmetry ($\infty\infty m$) [43], with randomly oriented grains are separated by grain boundaries. Individual grains have spontaneously polarized domain, but produce no net polarization of the ceramic until it is poled by an external electric field. After poling, it has a cylindrical symmetry (∞m) [43]. The non-zero matrix elements of the dielectric, piezoelectric, and elastic compliance coefficients of poled PZT ceramics are the same as for crystals that belong to point group 6mm. Hence, the symmetry of the poled PZT ceramics can be described by three piezoelectric coefficients d_{33} , d_{31} and d_{15} [59] which are described in section 2.2.4.

2.5 Review of the temperature dependence of piezoelectric and dielectric properties

LiNbO_3 transducers have been used at cryogenic temperatures [60] but there do not appear to be published measurements of d_{15} or d_{33} below room temperature. The piezoelectric coefficients of LiNbO_3 single crystals are weakly temperature dependent. The shear coefficient d_{15} drops by about 5% between 200°C and 20°C . Figure 2.16 shows the temperature dependence of the piezoelectric shear coefficient d_{15} [1, 61] between 20°C and 200°C .

Figure 2.17 shows the temperature dependence of the shear and longitudinal dielectric constants [18] for LiNbO_3 in a temperature range from 20°C to 200°C . They decrease gradually with temperature and the maximum value drops by about 5% over the whole temperature.

Thin single crystals of LiNbO_3 can tolerate high voltages and generate large dis-

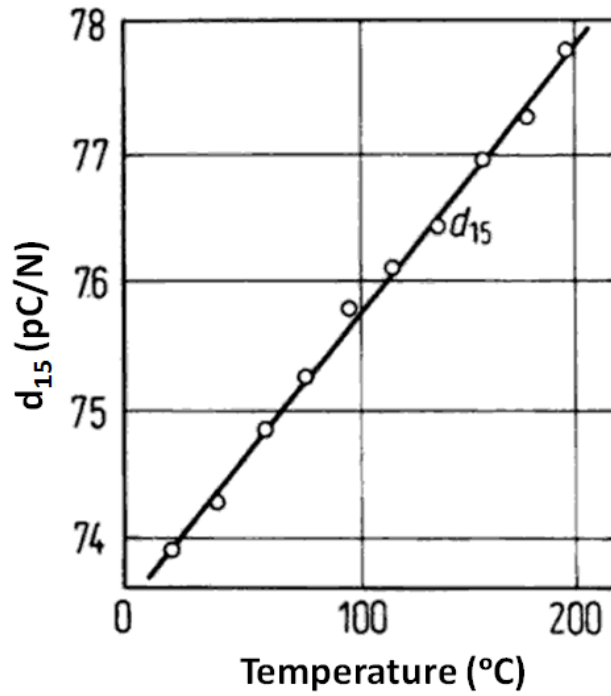


Figure 2.16: Weak temperature dependence of the piezoelectric coefficient d_{15} for LiNbO_3 (Figure reproduced from G. Gautschi *et al.*, 2002) [1, 61].

placements. Figure 2.18 shows the displacement for applied voltages up to 700 V applied to a stack of 36° Y-cut LiNbO_3 transducer [27]. Over this voltage range, there was no measurable hysteresis.

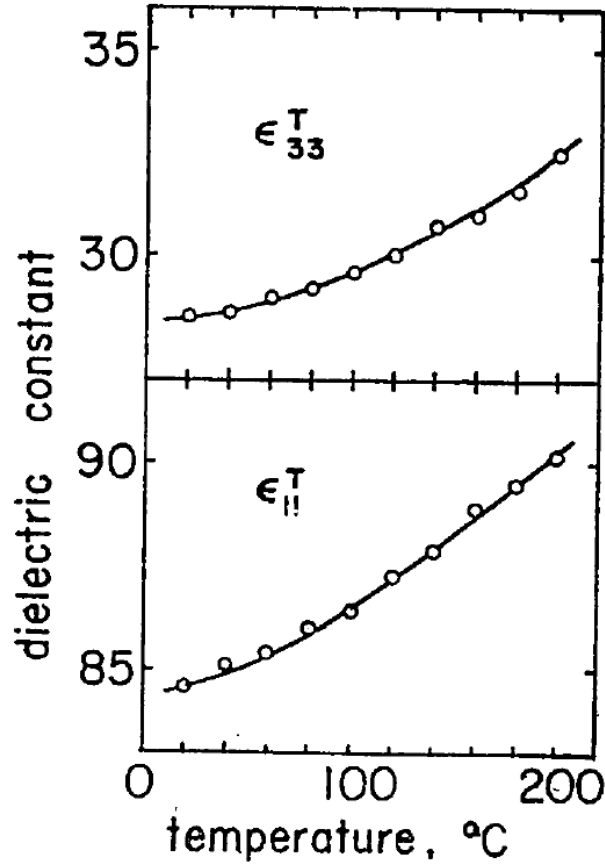


Figure 2.17: Temperature dependence of the dielectric constant for LiNbO₃ single crystal (Figure reproduced from Yamada *et al.*, 1967) [18].

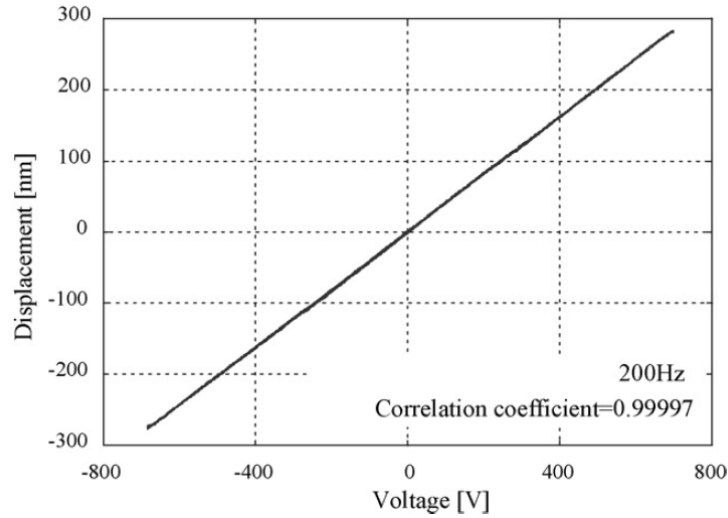


Figure 2.18: Large piezoelectric displacements for a stack of 36° Y-cut LiNbO₃ single crystals for applied voltage between -700 V and + 700 V (Figure reproduced from Kawamata *et al.*, 2007) [27].

Single crystal PMN-PT has exceptionally large piezoelectric coefficients at room temperature but limited information is available about its behaviour below 75 K, and none at all for the shear coefficients d_{15} below 75 K [14, 21]. Its piezoelectric coefficients have three temperature dependence regions between room temperature and 5 K [14, 21]. In 2012, Martin *et al.* reported d_{33} is strongly temperature dependent below 100 °C and above 250 °C, but it is weakly temperature dependent in a plateau region between 100 °C and 250 °C, as shown in Figure 2.19. In 2011, Wang *et al.* observed similar temperature behavior of the shear d_{15} and transverse d_{31} piezoelectric coefficients between room temperature and 77 K as shown in Figures 2.20 and 2.21 [14] with a plateau that is even less temperature dependent.

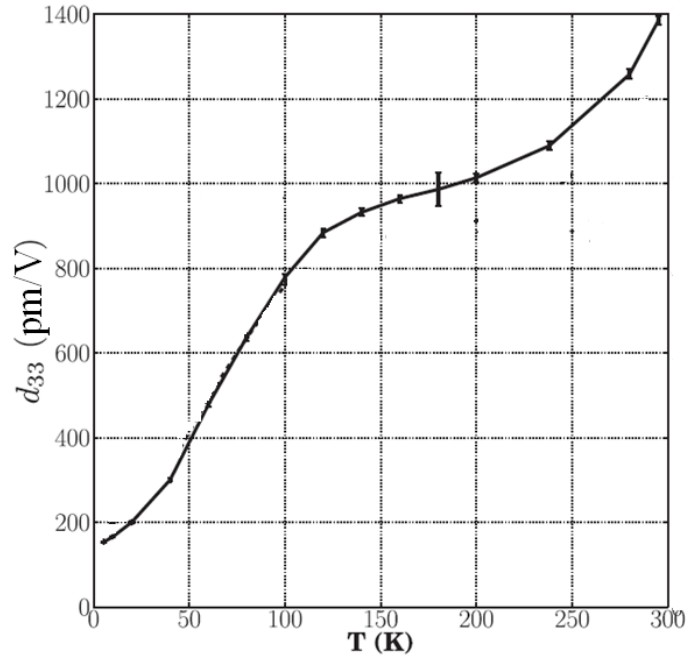


Figure 2.19: Three temperature dependence regions of d_{33} for PMN-28PT (Figure reproduced from Martin *et al.*, 2012) [21].

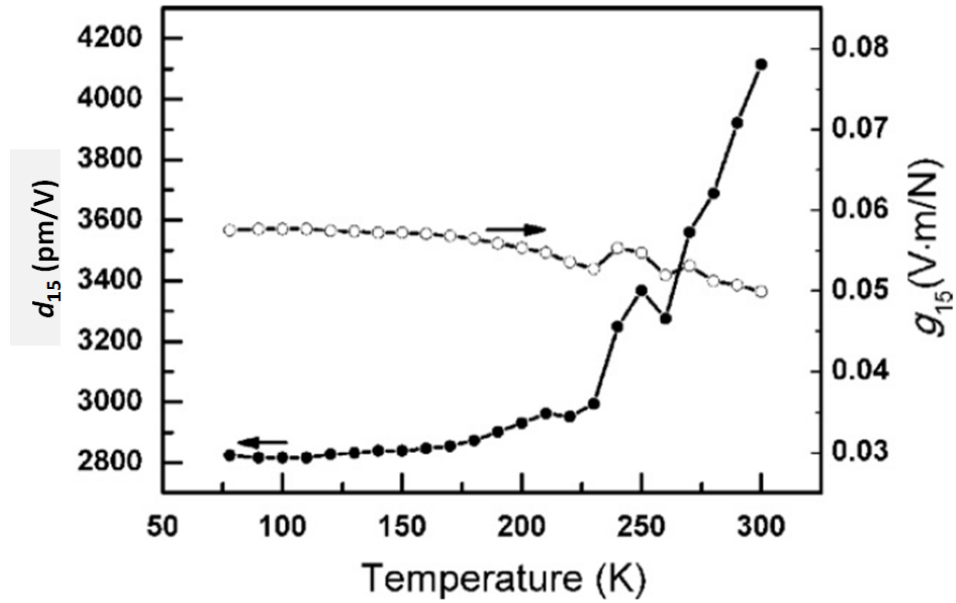


Figure 2.20: Temperature dependence of the shear piezoelectric constant d_{15} (black dots) and the shear voltage constant g_{15} (white dots) for a PMN-PT single crystal (Figure reproduced from Wang *et al.*, 2011) [14].

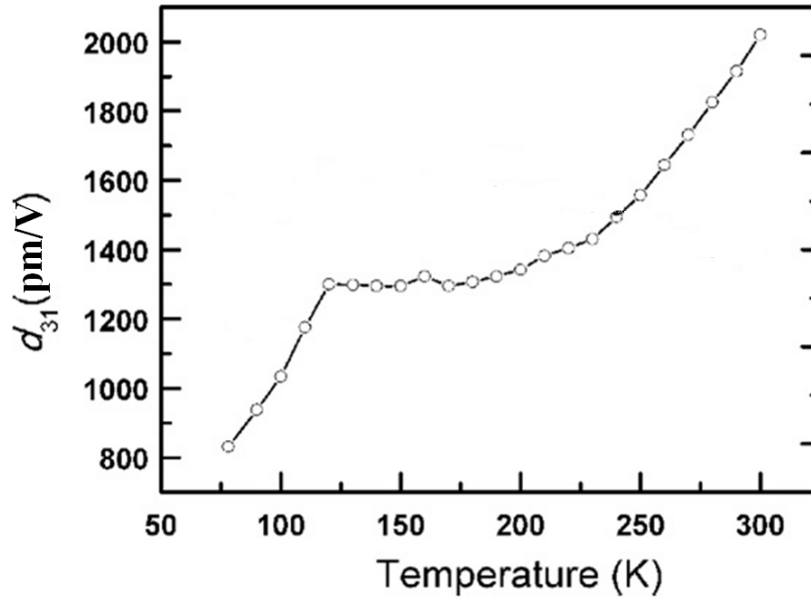


Figure 2.21: Temperature dependence of the transverse piezoelectric constant d_{31} for a PMN-PT single crystal (Figure reproduced from Wang *et al.*, 2011) [14].

The dielectric constant of this material has a temperature dependence much like that of piezoelectric coefficients. Wang *et al.* measured the temperature dependence of the dielectric constant and loss tangent for PMN-PT single crystal as shown in Figure 2.22 [14].

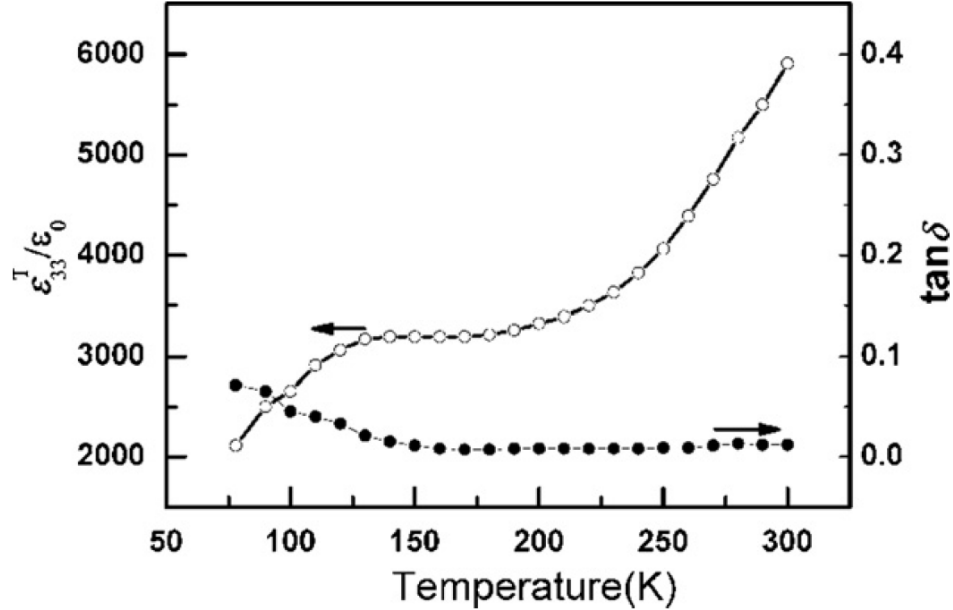


Figure 2.22: The variation of temperature dependence of the dielectric constant (white dots) and loss tangent (black dots) for a PMN-PT single crystal (Figure reproduced from Wang *et al.*, 2011) [14].

The piezoelectric coefficients of the most commonly used material, PZT, change roughly linearly with temperature [17]. Its room temperature piezoelectric coefficients d_{33} and d_{31} become about 5 times smaller at 4 K [15, 17] but little is known about the shear coefficient d_{15} at cryogenic temperatures. Figure 2.23 shows the temperature dependence of the piezoelectric coefficients d_{ij} for PZT-5H ceramics at temperatures between $-150\text{ }^\circ\text{C}$ and $100\text{ }^\circ\text{C}$ [62].

The dielectric coefficients of this material are also roughly linearly temperature dependent below room temperature. Zhang *et al.* measured the temperature dependence of the dielectric constant for both PZT 52/48 and PZT-500, as shown in Figure 2.24 from 15 to 300 K [29].

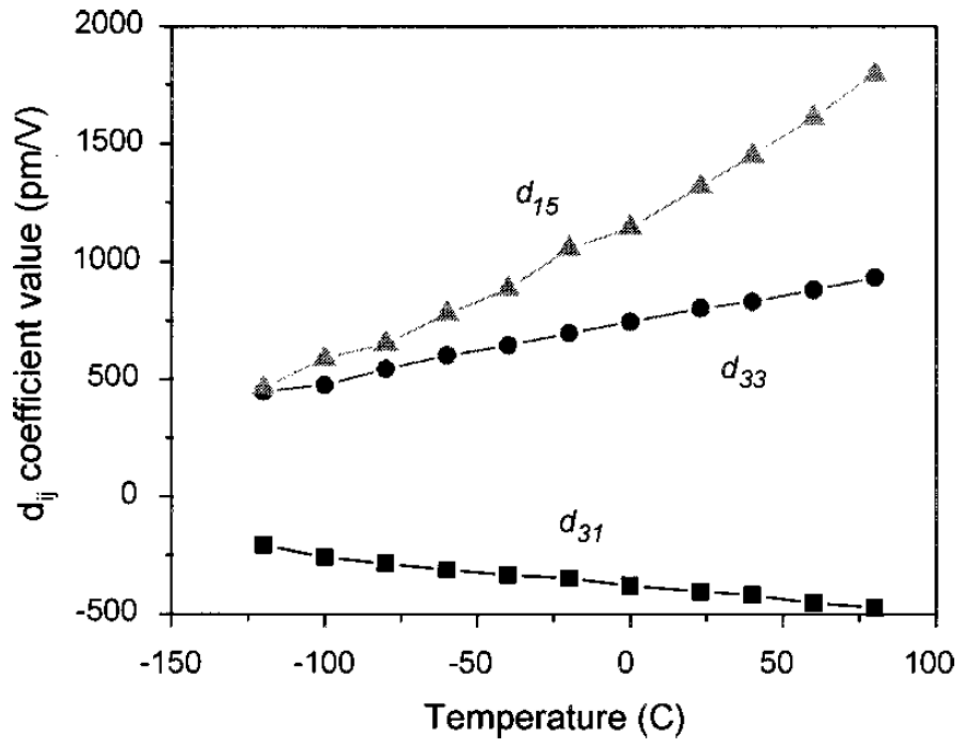


Figure 2.23: Temperature dependence of piezoelectric coefficients for PZT-5H (Figure reproduced from Wang *et al.*, 1998) [62].

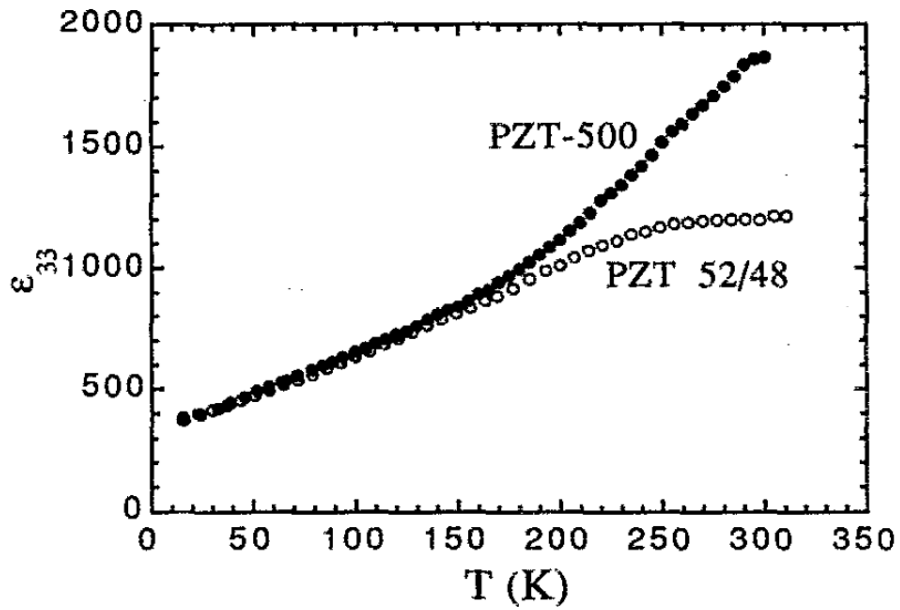


Figure 2.24: The temperature dependence of the dielectric constant for PZT-500 (\bullet) and PZT-52/48 (\circ) at 1 kHz (Figure reproduced from Zhang *et al.*, 1998) [29].

2.6 Non-linearity, hysteresis and creep properties of piezoelectric materials

2.6.1 Non-linearity

A displacement-voltage curve may show linearity (displacement proportional to applied voltage) and non-linearity, as illustrated in Figure 2.25. Linear piezoelectric behavior is usually observed at small voltages and temperatures but most piezoelectrics are non-linear at large voltages. For many practical applications of piezoelectric materials, large displacements are needed, which requires large voltages.

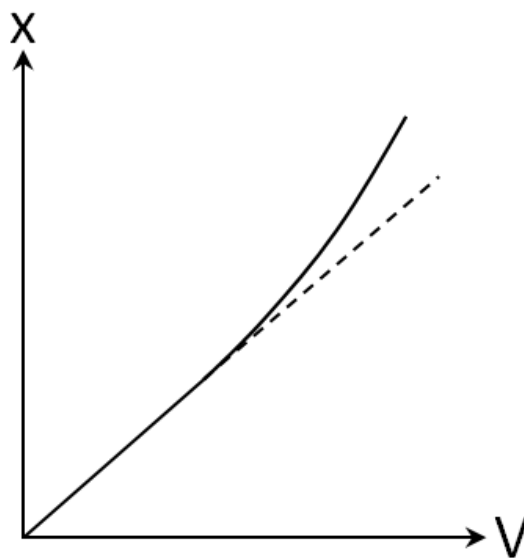


Figure 2.25: Displacement vs. applied voltage, showing the non-linearity.

2.6.2 Hysteresis

To discuss hysteresis and loss, let us consider a schematic piezoelectric displacement (x) vs. voltage (V) curve, as shown in Figure 2.26. If the displacement traces an open path during voltage cycling, it is called hysteresis. It can also be described as a dissipation, loss tangent or loss conductance, which occurs when there is a phase lag between the applied voltage and the displacement. In a single crystal, the geometry and dynamics of changes in the domain configuration produce hysteresis between the induced polarization and electric field [63]. The behavior of ceramics is even more

complicated because of the crystallite structure. In ceramics, the hysteresis loop depends on both structure and composition [63].

The piezoelectric losses occur in both dielectric (polarization-electric field hysteresis) and piezoelectric (displacement-voltage hysteresis) behavior. Domain-wall motion, lattice distortion, micro-structural evolution and internal friction (molecular friction) all play a role in these losses [64, 65, 66]. Piezoelectric loss can be calculated from the area or width of the hysteresis. Molecular friction is important in the low electric-field losses [67] in PZT materials while the higher electric-field losses are primarily due to increased motion of non-180° domain wall [64].

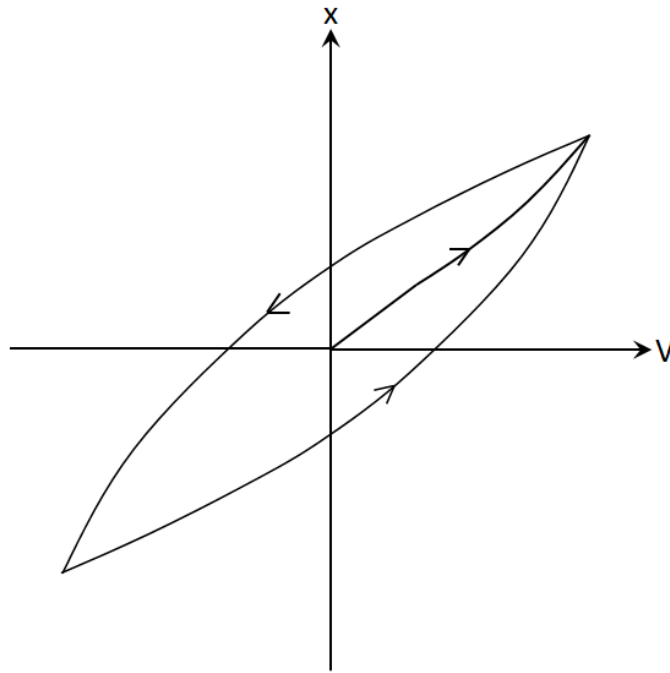


Figure 2.26: Displacement (x) vs. voltage (V) hysteresis loop.

2.6.3 Creep

When a constant voltage is applied to a piezoelectric material its piezoelectric displacement changes immediately (y_0), followed by a much slower time-dependent displacement. The slow displacement may reduce domain wall mobility through the gradual build-up of hindering domain structures [63]. This time-dependent property is known as relaxation aftereffect or creep. Figure 2.27 illustrates the initial piezoelectric displacement followed by creep. The creep rate usually follows a logarithmic

relation $a \log_{10}\left(\frac{t}{t_0}\right)$ [25, 68, 69]. The choice of t_0 is a bit arbitrary because

$$\lim_{t \rightarrow 0} \log_{10}(t) = -\infty,$$

making creep hard to separate from the immediate jump y_0 . Such a total piezoelectric displacement can be written as

$$\Delta x = y_0 + a \log_{10}\left(\frac{t}{t_0}\right) \quad (2.38)$$

where the parameters y_0 and a may be temperature and voltage dependent and t is the time.

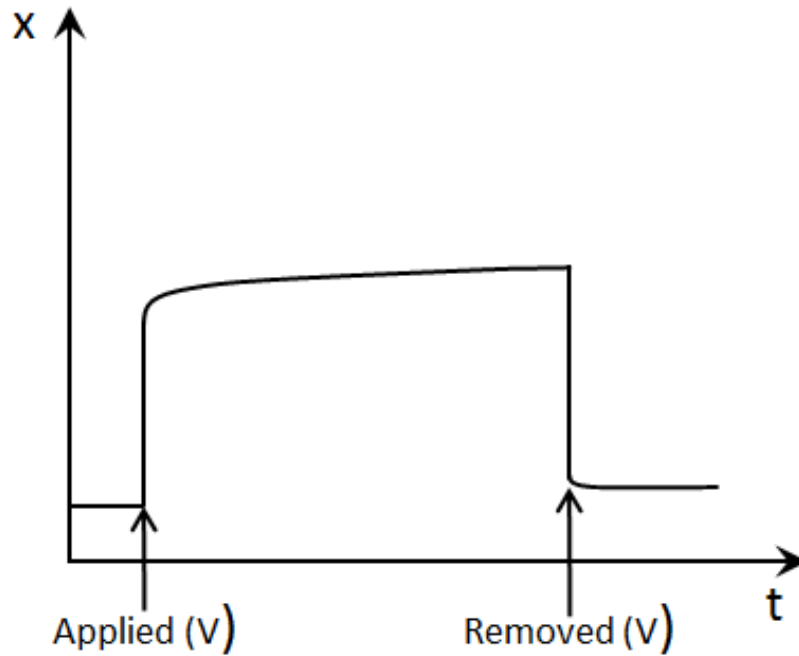


Figure 2.27: Displacement vs. time showing piezoelectric jump and creep.

If we assume that creep is directly proportional to the applied voltage change ΔV , then the creep displacement can be written as

$$\Delta x_1 = c \Delta V \log_{10}\left(\frac{t}{t_0}\right). \quad (2.39)$$

where the parameter c may be temperature dependent. By comparing equation 2.38 and 2.39, one can write $c = a/\Delta V$. If we assume the creep displacements due to successive voltage changes are independent of each other, they can be added to get the total creep displacement for the successive voltage changes. This creep produces hysteresis in displacement vs. voltage curves.

2.7 Depolarization of piezoelectric crystals

Piezoelectric materials may be depolarized by exceeding their electrical, mechanical, or thermal limitations. Their piezoelectric properties can be destroyed or diminished by depolarization. A strong electric field of opposite polarity or perpendicular to the polarization can depolarize piezoelectric materials. The depolarization depends on several factors such as the temperature, the exposure time and the field strength [36]. Electrical fields of 150 V/mm for PMN-PT, (200-500) V/mm for PZT and (1-5) kV/mm for LiNbO₃ may depolarize these materials. An AC current will also have a depolarization effect since the polarity during half of the cycle is opposite to the polarization field. Large mechanical stresses may also destroy the orientation of the dipoles. The degree of depolarization depends on the manufacturing process and material composition. Materials are also depolarized when heated above the Curie temperature. The maximum operating temperature of materials should not exceed about half of the Curie temperature [36], roughly 210 °C for PZT, 80 °C for PMN-PT and 600 °C for LiNbO₃ crystals.

2.8 Multilayer piezoelectric stack actuators

A single thick transducer needs high voltages to produce the large electric fields for large displacements but application of large voltages may depolarize the transducer. Although the applied fields have to be kept below depolarization fields, the voltages involved are still quite large for single thick transducers. A multilayer piezoelectric stack can overcome this problem. It is made from several thin transducers where adjacent transducers, have opposite polarizations, with thin metallic electrodes separating them. When a voltage is applied to the stack, the same voltage will be applied to each transducer. The displacements of the individual transducers will add up, creating large displacements with comparatively low operating voltages. Since the stack is made from thin transducers, the lower applied voltages produce large electric fields in each transducer.

Consider a stack which contains a number n of thin transducers. If the individual displacement of each transducer is δl , the total displacement (ΔL) of the stack can be written as

$$\Delta L = n \times \delta l \quad (2.40)$$

where $\delta l = d_{15}V$ for a shear transducer. For a longitudinal transducer, the thickness change $\delta t = d_{33}V$ and for a transverse transducer $\delta l = d_{31}\frac{l}{t}V$. Figures 2.28, 2.29

and 2.30 show shear, longitudinal and transverse stacks. In our lab, we made a shear stack of 3 single 41° X-cut LiNbO_3 transducers and obtained the expected shear displacements, as discussed in Chapter 4. Kawamata *et al.* [27] developed a longitudinal stack actuator of 36° Y-cut LiNbO_3 transducers (shown in Figure 2.31) and achieved (760 ± 380) nm displacements with an applied voltage of ± 1 kV. It would require impracticably large voltages to generate such large displacements with a single thick transducer. They suggested that their stack could be used in AFM and STM applications because of its large piezoelectric displacement compared to a single transducer [27].

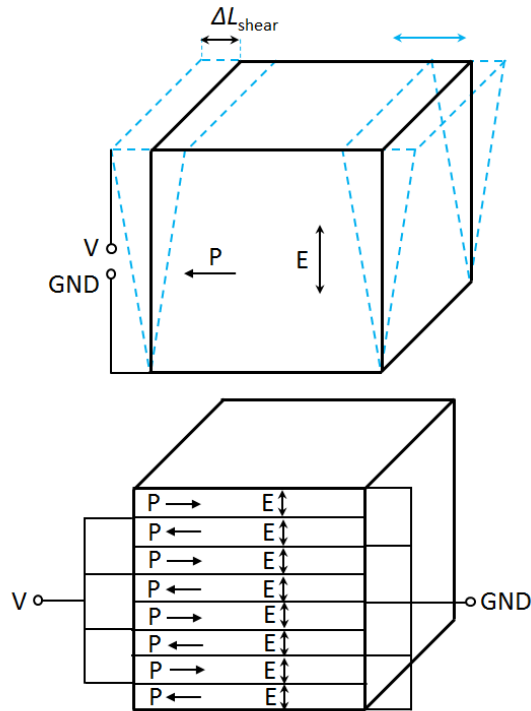


Figure 2.28: Shear stack actuators with shear displacement, ΔL_{shear} , [69].

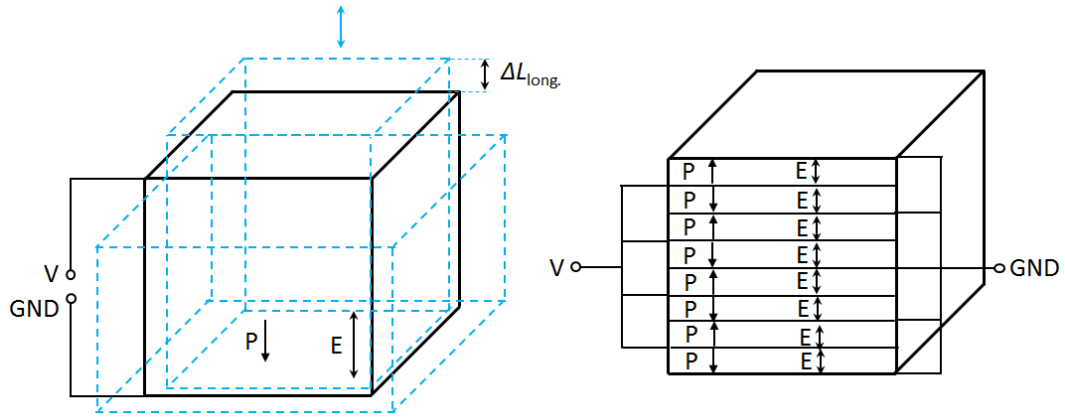


Figure 2.29: Longitudinal stack actuators with longitudinal displacement, ΔL_{long} , [69].

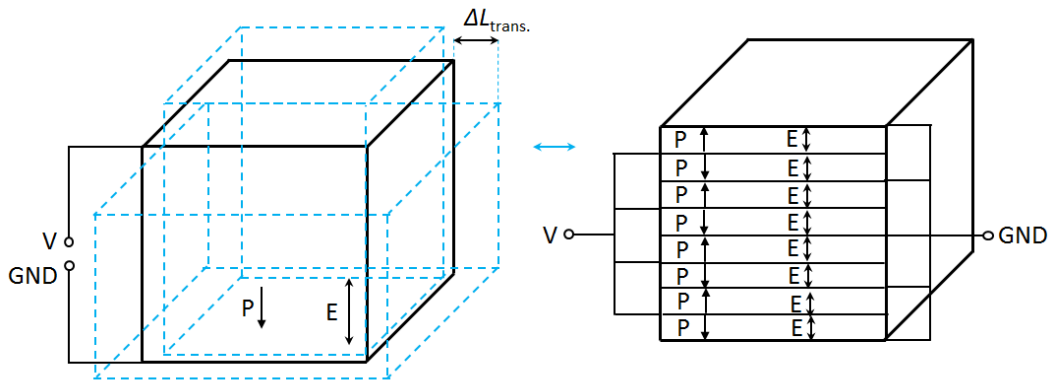


Figure 2.30: Transverse stack actuators with transverse displacement, ΔL_{trans} , [69].

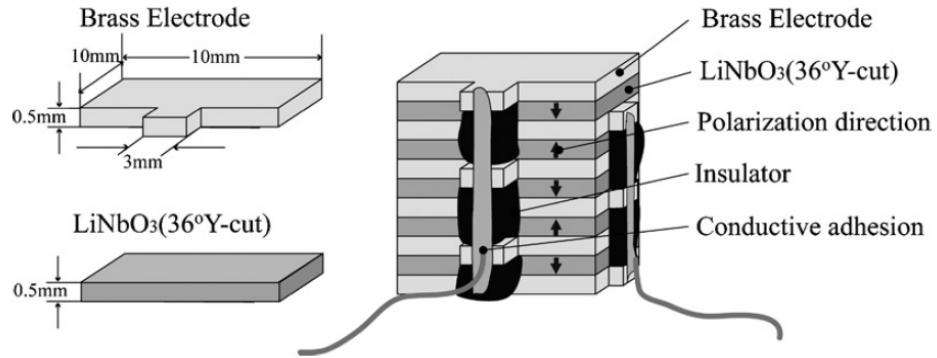


Figure 2.31: Longitudinal stack actuator using 36° Y-cut LiNbO_3 single crystals (Figure reproduced from Kawamata *et al.*, 2007) [27].

2.9 Dielectric properties

The dielectric coefficient of piezoelectric materials can change with temperature, frequency, chemical composition, pressure and molecular structure of the materials. A dielectric is a material that can store electrical energy when an external voltage is applied. For example, if a DC voltage is applied across a parallel plate capacitor, it can store more charge with a dielectric material rather than a vacuum between the plates, as shown in Figure 2.32. With vacuum between the plates, a voltage across the plates will produce a electric displacement (D) which can be written as

$$D = \varepsilon_0 E. \quad (2.41)$$

Neglecting the edge effect from the fringing fields outside of the area between the plates, the capacitance is

$$C_0 = \frac{Q_0}{V} = \frac{\varepsilon_0 EA}{Et} = \frac{\varepsilon_0 A}{t} \quad (2.42)$$

where $Q_0 = \varepsilon_0 EA$ is the stored charge , $V = Et$ is the applied voltage , A is the area of the plates, t is the separation between the plates and $\varepsilon_0 = 8.85 \times 10^{-12}$ (Fm⁻¹) is the permittivity of free space. If the space between the plates is filled with a dielectric

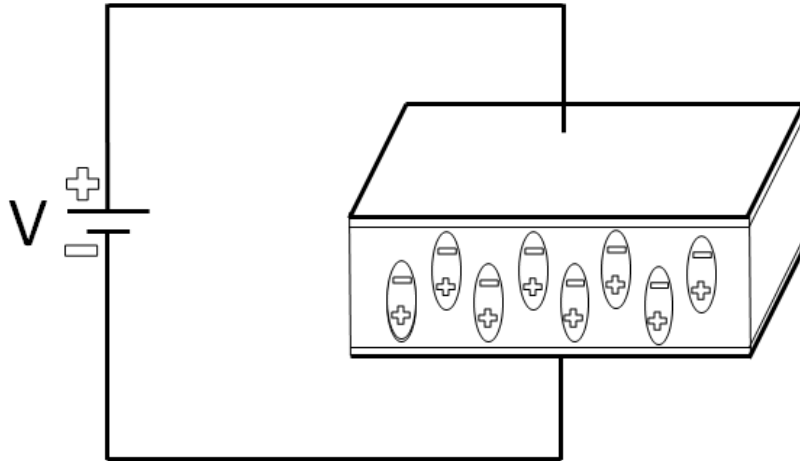


Figure 2.32: A DC voltage applied to a piezoelectric transducer [70].

material, it produces an additional charge density, P , from the polarization of charges within the material. The total electric displacement, D , can be written as

$$D = \varepsilon_0 E + P = K\varepsilon_0 E. \quad (2.43)$$

The capacitance then can be written as

$$C = \frac{Q}{V} = \frac{K\varepsilon_0 EA}{Et} = \frac{K\varepsilon_0 A}{t} = KC_0 \quad (2.44)$$

where K is the relative permittivity (or dielectric constant).

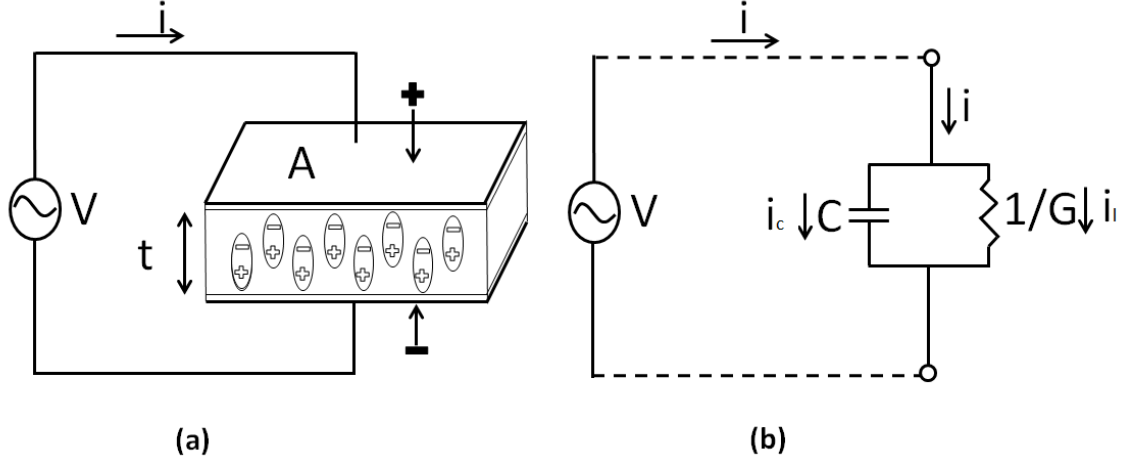


Figure 2.33: (a) AC voltage applied to a piezoelectric transducer and (b) corresponding parallel equivalent circuit of capacitor for the transducer [70].

For an AC sinusoidal voltage across the capacitor shown in Figure 2.33, the current (i) can be divided into a charging current (i_c) and a loss current (i_l). Those currents are related to the capacitance, C , and loss conductance, G , (or loss tangent). If the capacitor filled by a lossy dielectric material then the relative permittivity K^* is a complex number which can be written as [70]

$$K^* = \frac{\varepsilon}{\varepsilon_0} = \varepsilon_r^* = \varepsilon_r' - j\varepsilon_r'' \quad (2.45)$$

where $j^2 = -1$. From equation 2.44, the capacitance can be written as

$$C^* = \frac{K^* \cdot \varepsilon_0 A}{t} = \frac{\varepsilon_0 \varepsilon_r^* A}{t} \quad (2.46)$$

and the impedance of the circuit is

$$Z = \frac{1}{j\omega C^*} \quad (2.47)$$

where ω ($= 2\pi f$) is the angular frequency of the AC sinusoidal voltage. The admittance of the circuit is

$$Y = \frac{1}{Z} = j\omega C^* = \frac{j\omega \varepsilon_0 \varepsilon_r A}{t} = \frac{j\omega \varepsilon_0 (\varepsilon_r' - j\varepsilon_r'') A}{t} \quad (2.48)$$

or,

$$Y = j\omega C + G \quad (2.49)$$

where $C = \frac{\epsilon_0 \epsilon_r' A}{t}$ and $G = \frac{\omega \epsilon_0 \epsilon_r'' A}{t}$. The circuit current can be written as

$$i = YV = (j\omega C + G)V \quad (2.50)$$

or,

$$i = i_c + i_l. \quad (2.51)$$

If the material is lossy, there must be a component of current in phase with voltage [63]. Figure 2.34 shows the parallel equivalent circuit with the phase of the charging current and loss current with respect to the applied voltage in a lossy dielectric material (θ is the phase angle and δ is the loss angle). The loss tangent or dissipation can be written as a ratio of the loss conductance, G , and the magnitude of the capacitive susceptance, B ,

$$\tan \delta = \frac{G}{B} = \frac{G}{\omega C} = \frac{\epsilon_r''}{\epsilon_r'} \quad (2.52)$$

where $B = \omega C$.

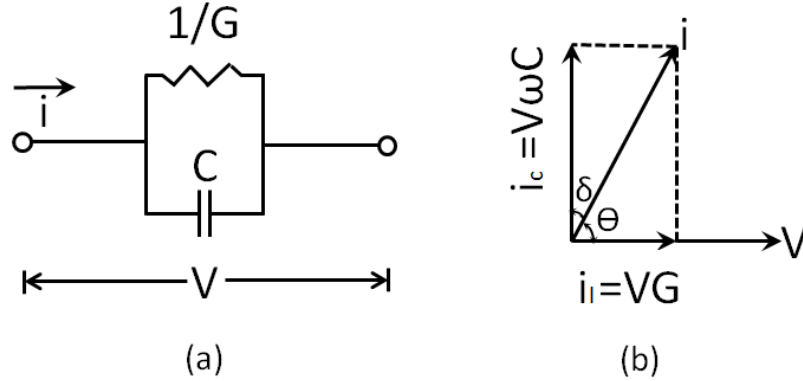


Figure 2.34: (a) Parallel equivalent circuit of capacitor and (b) Phase diagram between charging current and applied voltage of the parallel equivalent circuit [70].

The average input power delivered to the circuit is

$$\frac{1}{2} Y V^2 = \frac{j\omega C V^2}{2} + \frac{G V^2}{2} \quad (2.53)$$

where the first term represents the storage energy and the second term represent loss energy. The average power dissipated in a lossy capacitor is

$$U_T = \frac{G V^2}{2} = \frac{1}{2} \frac{\omega \epsilon_0 \epsilon_r'' A}{t} V^2 = \frac{1}{2} \omega C V^2 \tan \delta. \quad (2.54)$$

The hysteresis loss in terms of the area enclosed within the P-E loop [71] can be written as

$$U = \int_{t_1}^{t_2} P dE \quad (2.55)$$

where $P^* = \varepsilon_0 \varepsilon_r^* E^*$. The average P-E hysteresis loss can be obtained from

$$U_H = \frac{1}{T} \int_0^T P dE \quad (2.56)$$

where $T = \frac{2\pi}{\omega}$. If we consider a polarization, P , with a phase lag from the applied electric field, E , we can obtain the average hysteresis loss

$$U_H = \frac{1}{2} \omega C V^2 \tan \delta \quad (2.57)$$

which is identical with equation 2.54.

2.10 Different types of dielectric constants

The relative dielectric constant K is the ratio of capacitance C of a transducer filled with a dielectric material and C_0 of the same transducer's top and bottom plates separated by a vacuum. The two independent dielectric constants for these crystals are $K_{11}^\sigma = K_{22}^\sigma$ and K_{33}^σ or $K_{11}^\epsilon = K_{22}^\epsilon$ and K_{33}^ϵ . The superscript σ or ϵ means that the dielectric constants are measured under constant stress or strain. The subscript 11 means that the dielectric displacement is perpendicular to the polarization direction i.e. the applied electric field and the dielectric displacement in direction 1 and 33 indicates the dielectric displacement is parallel to the direction of polarization i.e. the applied electric field and the dielectric displacement in direction 3 [36, 69].

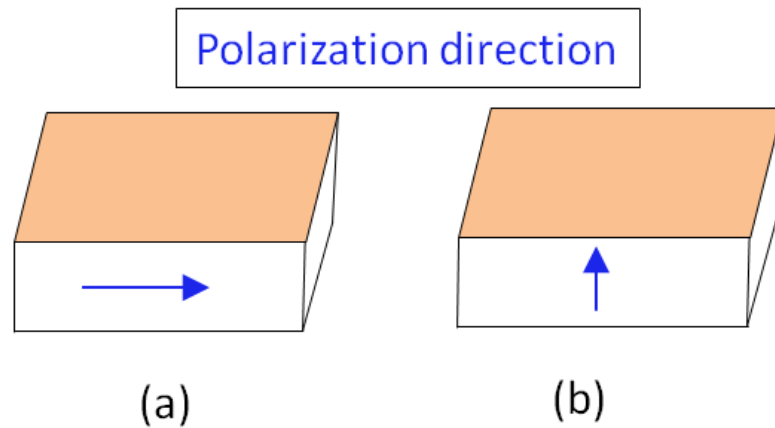


Figure 2.35: Transducer to measure dielectric constant (a) K_{11} and (b) K_{33} , under constant stress or strain.

Chapter 3

Experiment

This Chapter is divided into two sections: experimental apparatus and experimental techniques. The relevant information on all instruments, cryogenic and vacuum techniques, thermometry and temperature control and capacitance measurements is provided in the experimental apparatus section. The drawings of the cell, procedures for data acquisition and analysis, and procedures to measure the temperature and voltage dependence properties of piezoelectric coefficients, dielectric constants and losses, hysteresis and creep are discussed in experimental techniques section.

3.1 Experimental Apparatus

3.1.1 Dilution Refrigerators

We used an SHE mini dilution refrigerator and a 1 K cryostat to perform all these experiments. The SHE mini dilution refrigerator was used to measure piezoelectric coefficients such as d_{15} and d_{33} , creep and hysteresis properties of the samples. The 1 K cryostat was used to measure dielectric coefficients, loss tangent and polarization of the samples.

The lowest temperature stage of the SHE mini dilution refrigerator is called the mixing chamber, where the experimental cell, built with oxygen-free copper (OFHC), was mounted. A ^4He pot which provides the 1 K stage, needed to be refilled once a day from the helium bath. Figure 3.1 shows the schematic of a ^3He - ^4He dilution refrigerator with its main components and the flow diagram for its liquid mixture. Six (6) stainless steel coaxial cables were installed to replace the old two stainless steel coaxial cables in order to perform these experiments. This new system gave us the ability to measure two samples in every cool down. All the coaxial cables from room temperature to the experimental cell were thermally anchored to the 4 K, 1 K and mixing chamber stages. The lowest temperature achieved with the fridge was

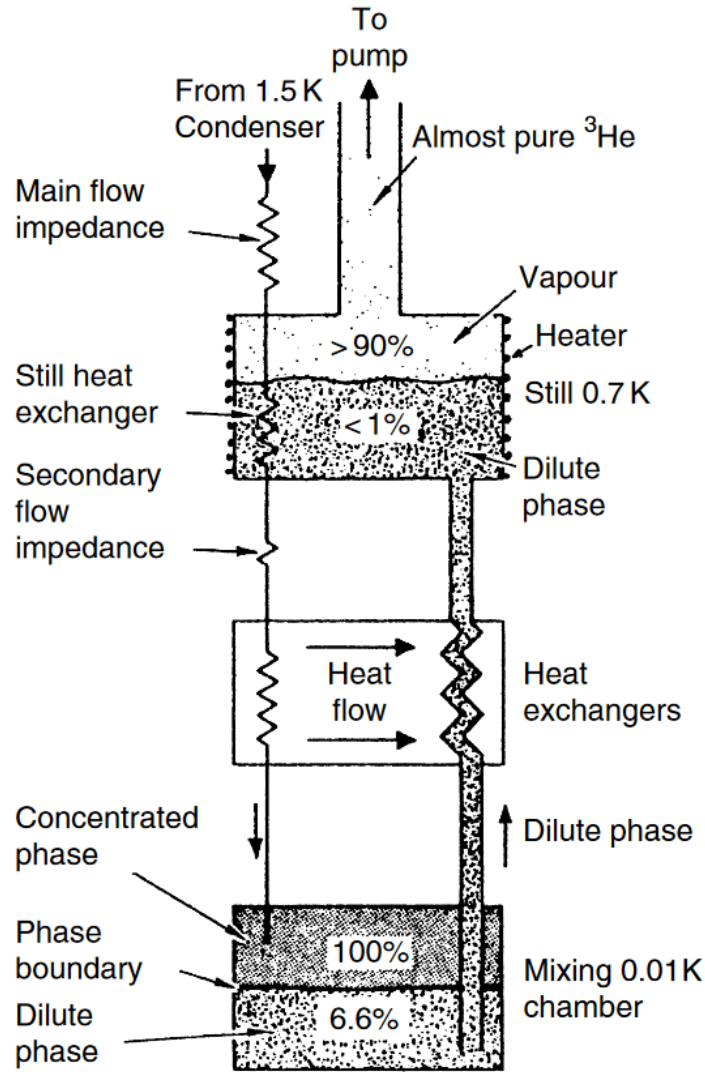


Figure 3.1: The main components and flow diagram of a ^3He - ^4He dilution refrigerator (Figure reproduced from Pobell, 1992) [72].

about 75 mK, higher than the limit of 40 mK quoted by the manufacturer indicating that heat leaks due to radiation, coaxial cables, thermometers and heater leads were about $5 \mu\text{W}$.

The measurements were done in two steps. In the first step, a copper strip thermally connected the 4 K flange to the mixing chamber, to make measurements from room temperature down to 4 K. In this way we were able to control the temperature very precisely, with only a few mK fluctuation. In the second step, we removed the copper strip and ran the dilution fridge. We used vibration reducers to minimise the vibration from the ^3He mechanical pump and the 1 K pot pump. In this way, we measured data from 10 K to 78 mK. We mounted two thermometers and a 200Ω

heater on the cell to measure and control the cell temperature precisely.

The lowest temperature stage in the 1 K cryostat was a ^4He pot where the experimental cell, built from brass, was mounted along with a $200\ \Omega$ heater, a carbon glass and a platinum thermometer. The lowest temperature achieved with the 1 K cryostat was 1.3 K. In this cryostat we measured the capacitance and dielectric loss conductance of transducers during temperature cycling between room temperature and 1.3 K, using an AH 2550A 1 kHz ultra-precision capacitance bridge. The dielectric constant was then calculated from the capacitance data.

3.1.2 Gas Handling System and Leak Testing

The gas handling system (GHS) was built to provide vacuum for the fridge, the desired pressures for storage tanks and fill lines, and to admit the clean gas to the dilution fridge in a controlled way. Figure 3.2 shows the schematic of the GHS. We modified an

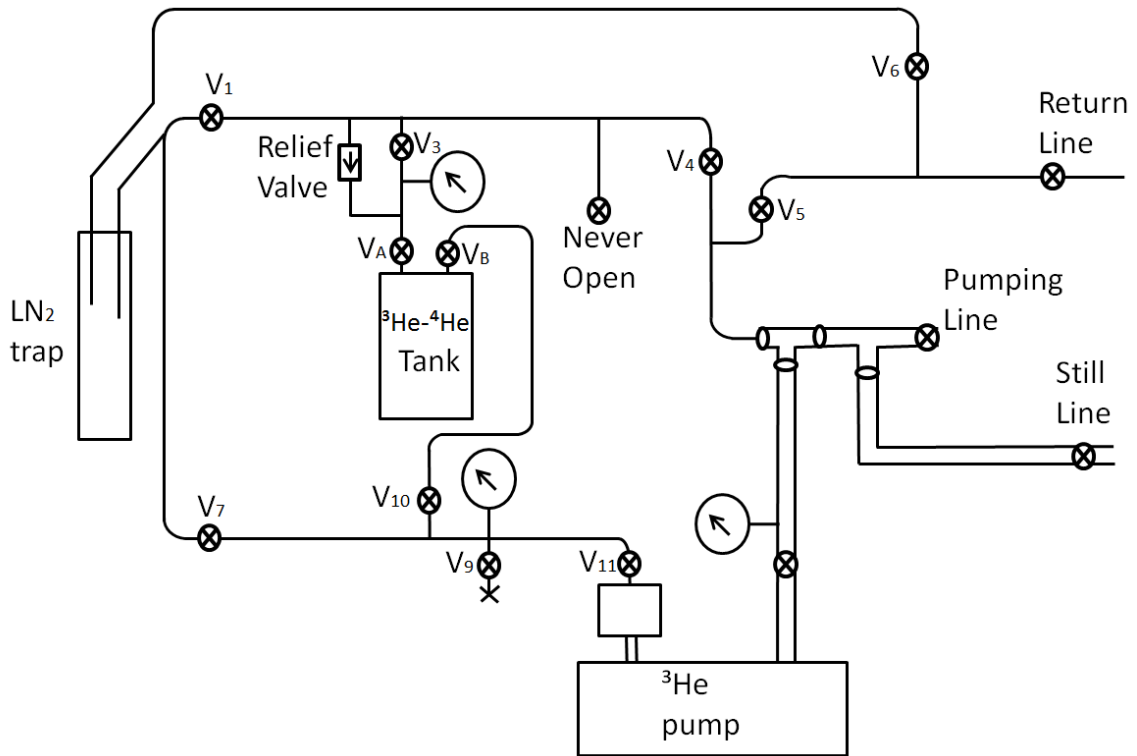


Figure 3.2: Schematic of our gas handling system to operate a ^3He - ^4He dilution refrigerator.

existing system by installing an adjustable safety valve across V_3 to protect against explosion of the important parts of the system. The basic operation is described below.

An important part of the GHS is a liquid nitrogen (LN_2) cold trap. It is filled with molecular sieve (Union Carbide: Type 13X) which cleans the mixture of ^3He - ^4He circulating through it by removing condensable gases at liquid nitrogen temperature before they reach the coldest parts of the fridge and plug its capillaries. The system is equipped with several room temperature pressure gauges, a ^3He - ^4He mixture tank and a hermetically ^3He sealed pump.

A turbopump (Agilent Technologies with V 81-AG rack controller, backed by a DS-102 Agilent roughing pump) was used to pump out the fridge, LN_2 trap and vacuum can and a mechanical pump was used to pump on the ^4He pot. Once everything was evacuated, an ASM-110 Alcatel leak detector was used for leak testing at room temperature, liquid nitrogen temperature, and liquid helium temperature. If no leak was observed at those temperatures, we filled and ran the fridge to achieve the lowest temperature.

3.1.3 Thermometry and Temperature Control

In order to perform dielectric and piezoelectric measurements over the entire temperature range, we used five thermometers to control temperature. Between 12 and 300 K we used calibrated platinum thermometers (Lake Shore Cryotronics [73] model P1935). Carbon glass thermometers (Lake Shore Cryotronics [73] model CGR-1-2000 and model-CGR-1-1500) were used down to 1.5 K and a calibrated ruthenium oxide thermometer (Lake Shore Cryotronics [73] model RX-102A-CD) was used at the lowest temperatures. All thermometers were calibrated and allowed temperatures to be controlled accurately. There were no problems encountered in making thermal contact with the thermometers.

All thermometers were mounted inside round copper blocks which were then screwed to the fridge or cell or 1K pot. Thermal contact was made with Apiezon grease and by varnishing the electrical leads to copper posts screwed into the mounting blocks. All the heater and thermometer leads were thermally anchored to the 1K pot and mixing chamber to minimize the heat load on the fridge.

We used one 200 Ω and one 151.2 Ω heater on the mixing chamber, one 200 Ω heater on the cell and one 132 Ω heater on the still to make sure that if one was damaged we could still continue our experiments. We used a ruthenium oxide thermometer for our low-temperature measurements below 4 K because it had an estimated accuracy of ± 1 mK below 0.5 K and ± 2 mK above 0.5 K. All the thermometers were used in a four wire configuration and the heaters in a two wire configuration. Figure 3.3 shows examples of thermometers and heaters. Neocera temperature controllers

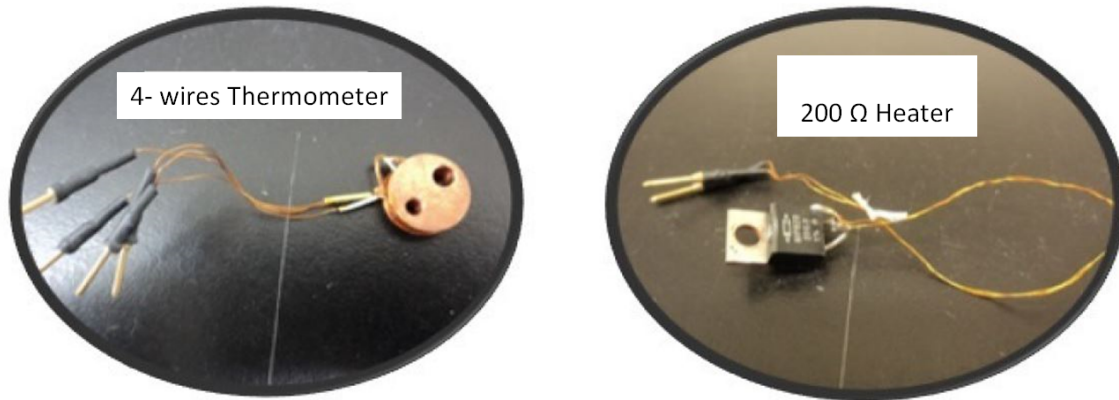


Figure 3.3: Sample of the 4-wires thermometer and a 2-wires configured heater (Figure reproduced from Bukhari M.Sc. thesis, 2014) [45].

LTC-11 and LTC-21 used to control the thermometers and heaters. The control temperature was usually very stable with only a few mK fluctuations.

3.1.4 Capacitance Measurements

All displacements were measured capacitively, using polished copper blocks of cm size. The AH2500A 1 kHz capacitance bridge [74] provides excellent accuracy and resolution for the precise measurement of capacitance and loss. It uses a three terminal measurement technique. In ordinary two terminal capacitor measurement, the stray capacitances between the HIGH (H) and LOW (L) terminals, due to surrounding objects such as the capacitor case and ground are impossible to avoid. Figure 3.4 illustrates the regular two terminal capacitor measurement with a total stray capacitance C_s . In a three terminal capacitor measurement, the third terminal works as a shield to eliminate effects of the surrounding stray capacitance, as shown in Figure 3.5.

The capacitance bridge can also reduce the random noise in a single measurement by internally averaging the noise over a time period. The averaging time for each single measurement was 4 seconds in our experiments. The maximum excitation voltage of the bridge, used in all our measurements, is 15 VAC for capacitance measurement ranges (-11 to + 110 pF and loss ranges 0.8 to + 8 nS). Our capacitance values were within this range (3.5 pF for PZT/PMN-PT and 3.3 pF for LiNbO₃/stack of LiNbO₃). The resolution of the bridge for a single measurement with these settings was $\frac{\delta C}{C} \approx 4.1 \times 10^{-7}$. Figure 3.6 shows a typical series of single capacitance

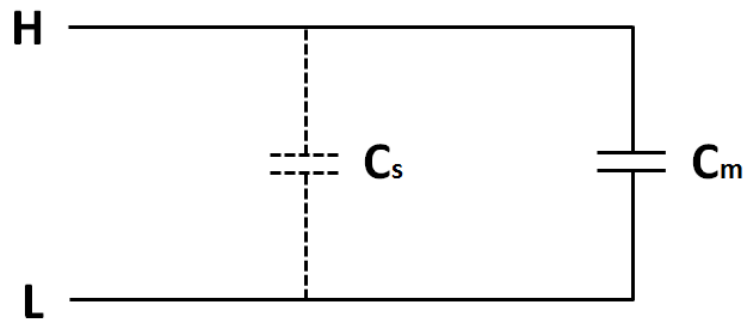


Figure 3.4: Regular two-terminal capacitor (C_m) measurement with stray capacitance (C_s) between the leads.

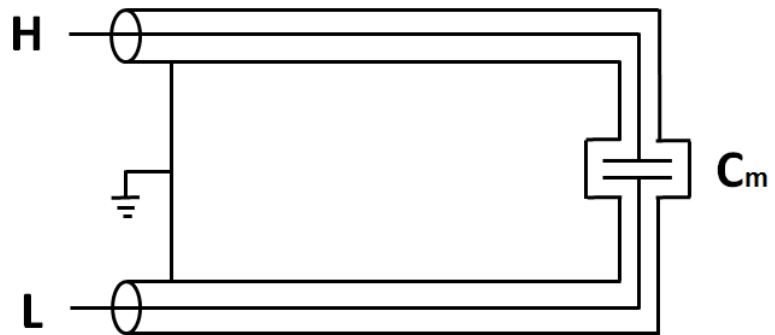


Figure 3.5: The shielded standard three terminal capacitor arrangement used by the AH2500A capacitance bridge.

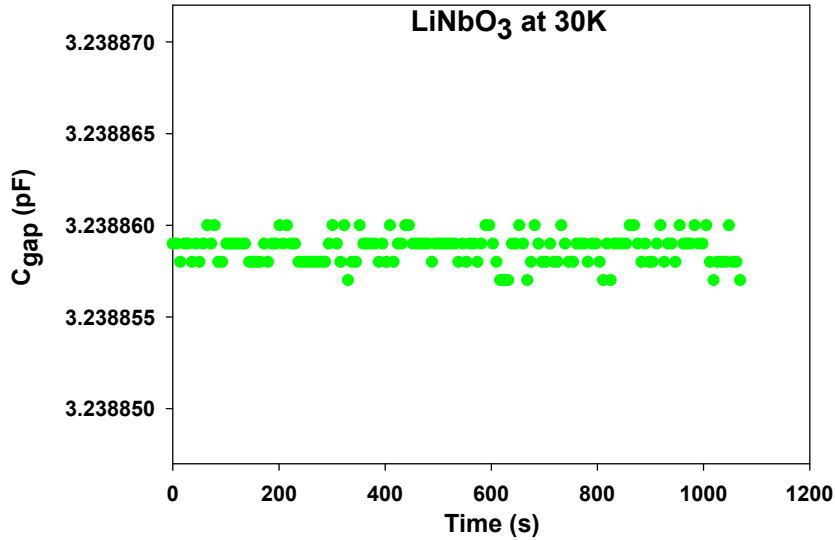


Figure 3.6: Typical series of individual capacitance measurements over time, illustrating the noise for our capacitance measurements at 30 K.

measurements at 30 K with no voltage applied to the LiNbO₃ transducer, where noise $\frac{\delta C}{C} = 3.0 \times 10^{-7}$. This noise corresponds to a displacement δl equal to 0.09 nm for a typical parallel plate spacing $l = 0.3$ mm (0.06 nm for $l = 0.2$ mm).

3.2 Experimental Techniques

3.2.1 Experimental design and analysis of capacitance measurements to measure shear piezoelectric displacement

In order to measure the shear piezoelectric coefficient d_{15} from room temperature down to 78 mK, we used a capacitive displacement detection technique. We machined a large ($14 \times 14 \times 16$ mm³) and a small ($10 \times 10 \times 8$ mm³) block and polished their faces with 20, 12, 9, 5, 3 and 1-micron polishing sheets. The copper blocks and the L shaped copper base (20 mm surface width) were cleaned ultrasonically, followed by washing with methanol. The small polished block was then permanently attached to the base, and the large polished block was attached to one of the brass electrodes using epoxy (Hysol TRA-BOND 2151(3g), BIPAX) for electrical insulation. The device was mounted on the mixing chamber of a dilution refrigerator. Stainless steel coaxial cables connected a capacitance bridge to the fixed copper block and to the block clamped on top of the transducer, to measure the capacitance between the blocks. An AH2550A [74] 1 kHz ultra-precision digital capacitance bridge was used

to measure the capacitance between the blocks. In this technique, we used a magnetic clamp instead of soldering a wire to the transducer. The magnetic clamp helped to ensure the transducer's temperature was the same as the mixing chamber temperature and allowed us to reuse the transducer in other experiments.

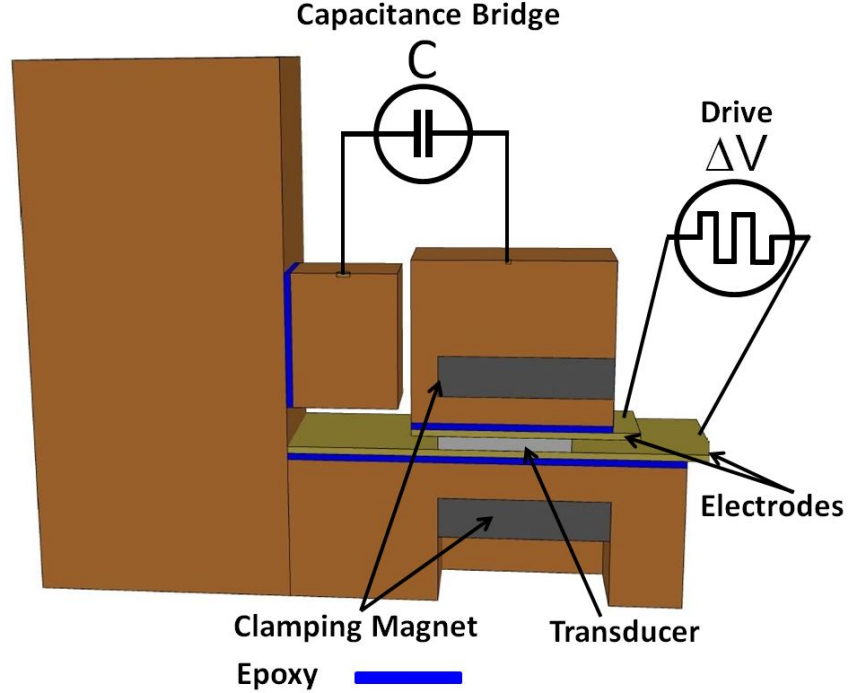


Figure 3.7: Schematic diagram of the capacitive displacement technique used to measure d_{15} , creep and hysteresis properties of shear piezoelectric transducers.

Figure 3.7 shows a schematic of the cell used to measure d_{15} , creep and hysteresis properties. The piezoelectric shear transducer was magnetically clamped between one of the blocks and the base of the cell. A voltage change (ΔV) applied across the shear transducer using two thin brass electrodes produced a transverse displacement $\Delta x = d_{15}\Delta V$. This then produced a capacitance change ΔC proportional to the change in spacing $\Delta L = \Delta x$ between the two blocks. The gap spacing L (typically about 300 μm) is related to the initial capacitance

$$C_0 = \frac{\epsilon_0 A}{L} \quad (3.1)$$

where A is the area of the gap where the blocks overlap. The change in capacitance when a DC voltage change (ΔV) is applied

$$\Delta C = \epsilon_0 A \left(\frac{1}{L} - \frac{1}{L + \Delta L} \right) \quad (3.2)$$

or

$$\Delta C = \frac{\epsilon_0 A}{L} \cdot \left(\frac{\Delta L}{L + \Delta L} \right) = C_0 \cdot \left(\frac{\Delta L}{L + \Delta L} \right). \quad (3.3)$$

For small changes in the block separation ($\Delta L \ll L$), equation 3.3 can be rewritten as

$$\Delta C \simeq C_0 \cdot \left(\frac{\Delta L}{L} \right) \quad (3.4)$$

or

$$\frac{\Delta C}{C_0} \simeq \frac{\Delta L}{L}. \quad (3.5)$$

Equation 3.5 can be written substituting $\Delta L = d_{15} \Delta V$

$$\frac{\Delta C}{C_0} \simeq \frac{\Delta L}{L} \simeq \frac{d_{15} \Delta V}{L}. \quad (3.6)$$

The shear piezoelectric coefficient is then

$$d_{15} = \frac{A \epsilon_0}{C_0^2} \frac{\Delta C}{\Delta V}. \quad (3.7)$$

Equation 3.7 is developed for the case of an ideal capacitor. In practice, there are two extra capacitances added to the ideal gap capacitance. One of them is the edge effect and the other is stray capacitance.

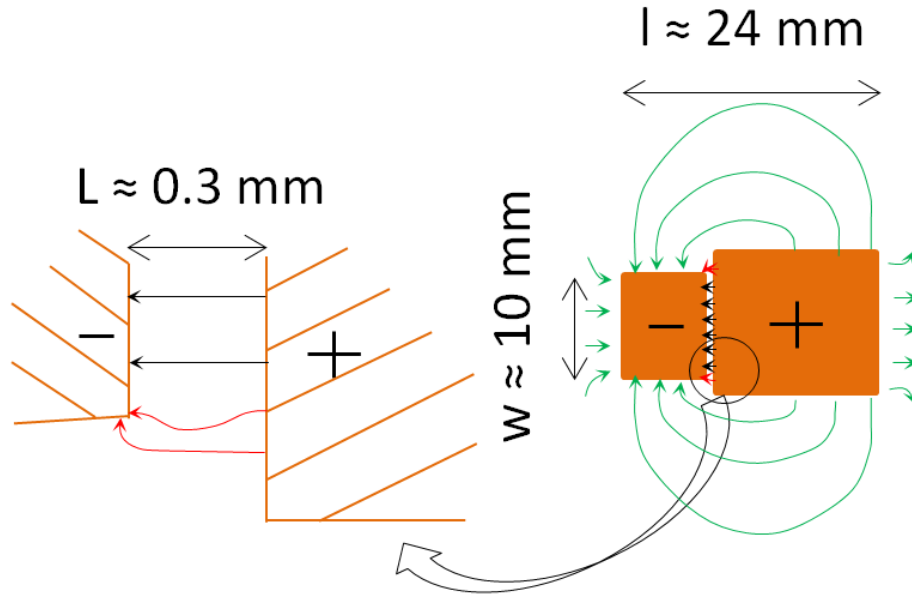


Figure 3.8: Parallel block capacitor with its electric fields. The right figure shows the strong electric fields (black arrows) inside the gap, and comparatively weak stray fields (green lines) surrounding the blocks. The small black circle blows up the fringe fields (red line) at the edges of the gap in the left figure.

An electric field is produced inside the gap of parallel blocks when a voltage difference is applied to them. Not only does this electric field exist directly between the blocks but it also extends outside, at the edges of the blocks. This is called the edge effect, and the fields at the edges are known as fringing fields. Stray capacitance occurs due to the stray electric fields surrounding the blocks and their leads and surfaces when a voltage applied to the parallel blocks. The surrounding electric fields depend on the geometry of the blocks and leads and the capacitance due to those fields is called the stray capacitance. We can assume that the stray capacitance is approximately constant for small changes in the separation of the parallel blocks since the length scale for stray capacitance ($l \approx 24$ mm) is much larger than the gap length $L \approx 0.3$ mm. Figure 3.8 illustrates the three types of electric field for our parallel blocks capacitor. The straight black arrows indicate the strong uniform electric field inside the gap and curved red arrows indicate the weak fringe fields at the edges of the gap. Together these two electric fields are responsible for the total gap capacitance (C_g), which is proportional to the effective area $A_{g(eff)}$ of the gap. The effective gap area $A_{g(eff)}$ is slightly different from the geometric area A_m . The green arrows represent the comparatively weak fields surrounding the blocks that are responsible for the stray capacitance (C_s). The relationship among the measured capacitance (C_m), gap capacitance (C_g), and stray capacitance (C_s) can be written as

$$C_m = C_g + C_s = \frac{\varepsilon_0 A_{g(eff)}}{L} + C_s \quad (3.8)$$

where the gap capacitance is $C_g = \frac{\varepsilon_0 A_{g(eff)}}{L}$, $A_{g(eff)}$ is the effective area of the parallel blocks, and L is the separation between the blocks. This is a general straight line equation, $Y = mX + c$ between the capacitance C_m and the inverse separation $\frac{1}{L}$. The slope, $m = \varepsilon_0 A_{g(eff)}$ is a constant and the intercept on the Y-axis is the stray capacitance $c = C_s$. Therefore, the intercept of C_m vs L^{-1} plot will give the desired stray capacitance and the effective gap area $A_{g(eff)}$ can be calculated from the slope of the plot.

To find the stray capacitance for our parallel blocks, the capacitance was measured with different separations (L) between the blocks. A series of 0.15 mm thick glass slides were used to set L , as shown in Figure 3.9 (a). For example, one slide was used between blocks for the first measurement, two slides for the second measurement and so on. To align the blocks parallel, we placed the glass slides between the blocks and pressed them tightly. The capacitance was measured with the glass slides in the gap and then they were pulled out gently to measure the capacitance without the glass slides. We repeated this process 2 or 3 times to make sure the capacitance values

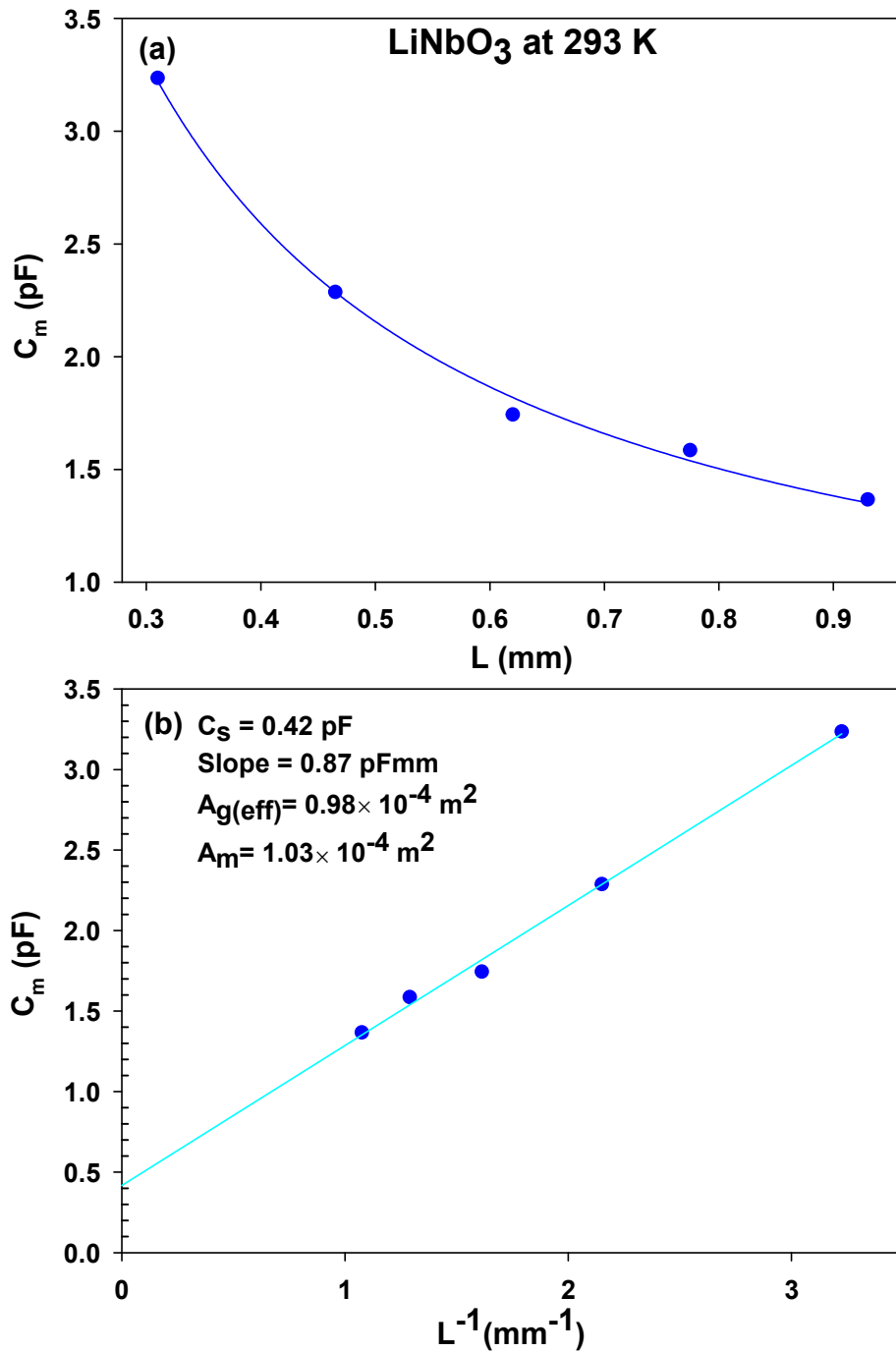


Figure 3.9: Stray capacitance calculation for the LiNbO₃ device at room temperature.

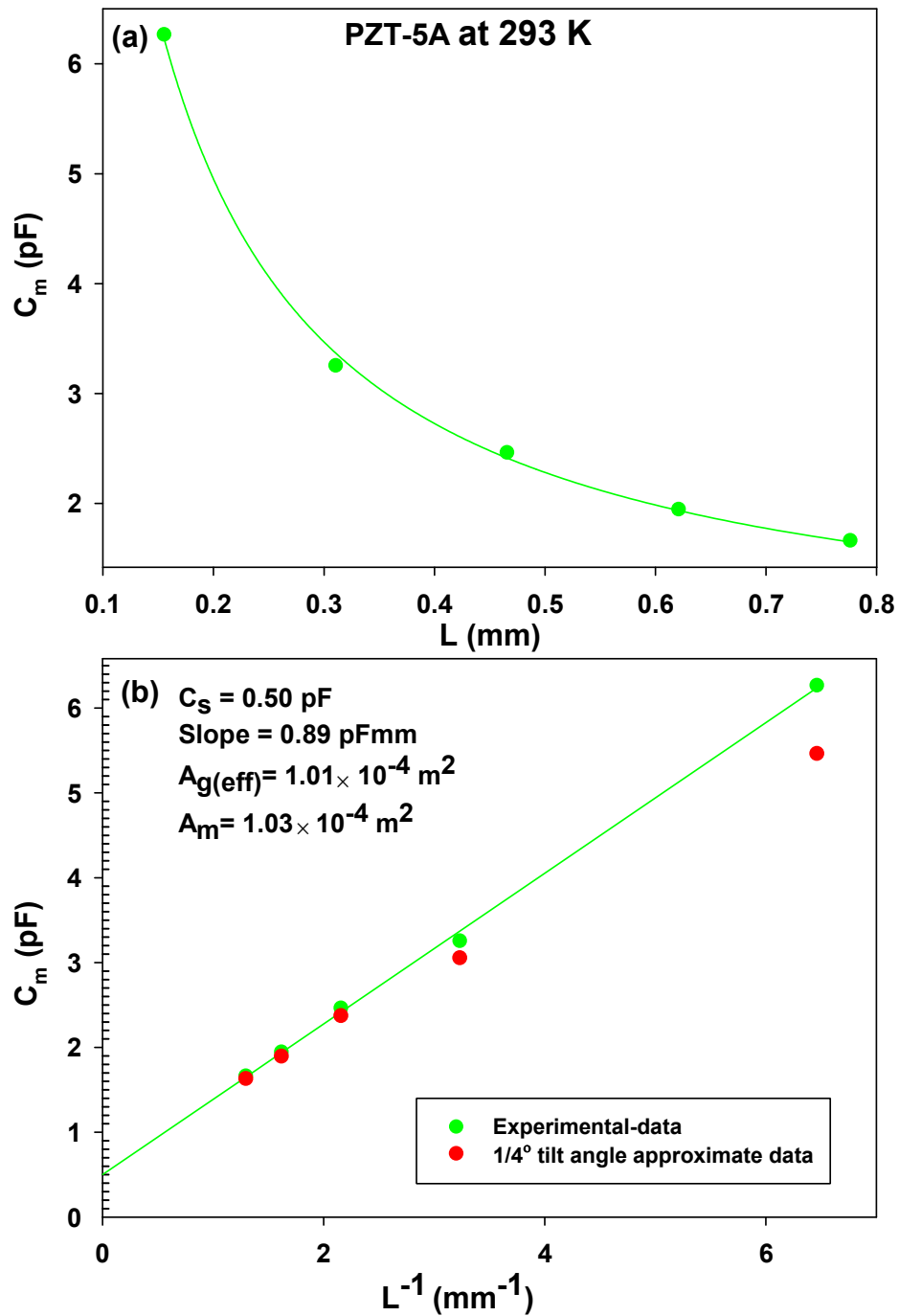


Figure 3.10: Stray capacitance calculation for the PZT-5A device at room temperature.

they were reproducible.

If the blocks are tilted slightly then the capacitance will be

$$C_m = \frac{\varepsilon_0 A_{g(eff)}}{L} \left(1 - \frac{\theta w}{2L}\right) + C_s, \quad (3.9)$$

where θ is the small tilt angle and w is the gap width at the narrowest point. Equation 3.9 is not a straight line equation.

We used two devices, one for the LiNbO₃/stack and another for the PMN-PT/PZT-5A transducers. Figures 3.9 (a) and 3.10 (a) show the capacitance measurements (C_m) with respect to separation (L) for both devices. Figures 3.9 (b) and 3.10 (b) show the same capacitance measurements (C_m) plotted with respect to the inverse separation (L^{-1}). Both devices give reasonably straight lines when plotted against L^{-1} , indicating that the blocks are approximately parallel and that the assumption of constant C_s is justified. In Figure 3.10 (b), the red dots show the effect expected for $\frac{1^\circ}{4}$ small tilt angle, which clearly deviates from the measured straight line. The stray capacitance, C_s , determined from the intercepts, is 0.42 pF for the LiNbO₃/stack device and 0.50 pF for the PZT/PMN-PT device. The effective area of the parallel blocks is calculated from the slope $\varepsilon_0 A_{g(eff)}$ giving $0.98 \times 10^{-4} \text{ m}^2$ (measured geometric area, $A_m = 1.03 \times 10^{-4} \text{ m}^2$) for the LiNbO₃/stack device and $1.01 \times 10^{-4} \text{ m}^2$ (measured area, $A_m = 1.03 \times 10^{-4} \text{ m}^2$) for the PZT-5A/PMN-PT device. The stray capacitance is then subtracted from all measured capacitance values in order to correct the d_{15} data. The thermal length contraction of the copper block $\frac{\Delta l}{l_{293}}$ at 4 K is 0.3% [75] which contract the area of the block capacitor about 0.6% which slightly affects the value of d_{15} or d_{33} .

3.2.2 Longitudinal d_{33} measurements and effects of magnetic clamping

When a voltage change (ΔV) is applied along the polarization of an unconstrained longitudinal transducer, it produces both parallel (Δt) expansion or contraction along the polarization direction and transverse (Δl), contraction or expansion perpendicular to the applied voltage displacements, as shown in Figure 3.11, where $\Delta t = d_{33}\Delta V$, $\frac{\Delta l}{l} = d_{31}\frac{\Delta V}{t}$ and t and l are the thickness and length changes of the transducer, respectively. In order to find the longitudinal piezoelectric coefficients d_{33} , we used the same capacitive displacement detection technique with a longitudinal transducer, as shown in Figure 3.12. The mathematical formalism for the longitudinal coefficient

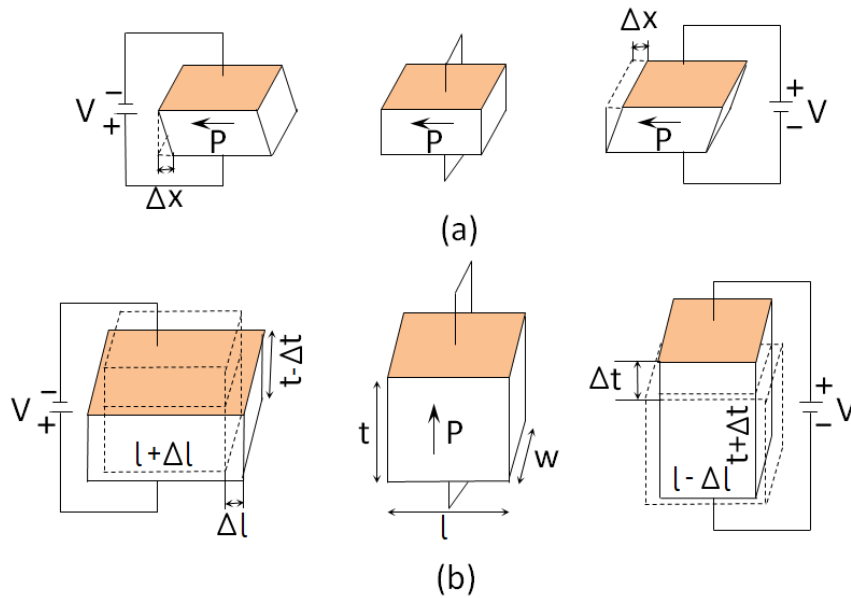


Figure 3.11: (a) Shear mode and (b) longitudinal and transverse modes of the transducers with respect to applied voltage and the polarization direction.

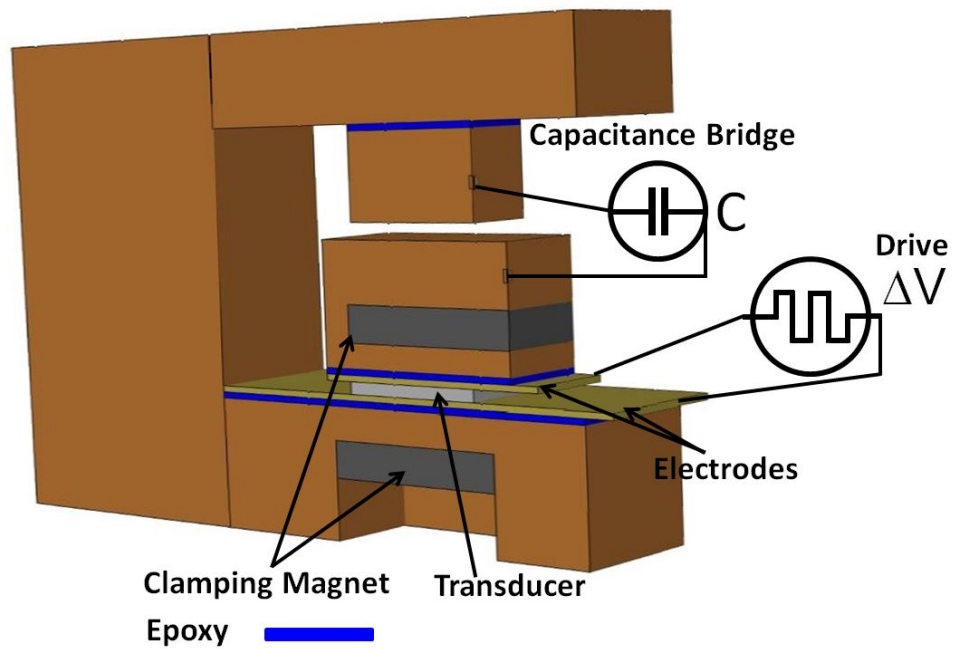


Figure 3.12: Schematic diagram of the capacitive displacement technique used to measure d_{33} of longitudinal piezoelectric transducers.

d_{33} is given below. For the longitudinal coefficient,

$$d_{33} = \frac{\Delta t}{\Delta V} \quad (3.10)$$

where the longitudinal displacement $\Delta t = \Delta L$ is the change in spacing between the two blocks. For $\Delta L \ll L$, equation 3.5 can be written as

$$\frac{\Delta C}{C_0} \simeq \frac{\Delta L}{L} \simeq \frac{d_{33}\Delta V}{L} \quad (3.11)$$

or,

$$d_{33} = \frac{A\varepsilon_0}{C_0^2} \frac{\Delta C}{\Delta V} \quad (3.12)$$

where L and A have the same meaning as in equation 3.7.

Equation 3.12 is derived for an unconstrained transducer. A limitation of the d_{33} measurement comes from the friction in the transverse direction due to the clamping. In d_{15} measurements, friction does not affect the shear displacement since there is no accompanying transverse motion. On the other hand, when a voltage is applied across a longitudinal transducer, both parallel (d_{33}) and transverse (d_{31}) displacements occur at same time and they are coupled. The transverse displacement may be limited by friction due to clamping, which will reduce the parallel displacement.

The electrical, elastic, thermal and piezoelectric properties of a crystal are expressed in matrix notation as follows [33]

$$\epsilon_m = s_{mn}^{E,T} \sigma_n + d_{im}^T E_i + \alpha_m^E \Delta T \quad (3.13)$$

$$D_i = d_{im}^T \sigma_m + \varepsilon_{ij}^{\sigma T} E_j + p_i^\sigma \Delta T \quad (3.14)$$

$$i, j = 1, 2, 3 \text{ and } m, n = 1, 2, \dots, 6$$

where ϵ , σ , E , T and ΔT are the strain, stress, electric field, temperature and change in temperature while s , d , α , ε and p are the elastic compliance (m^2N^{-1}), piezoelectric constant, the coefficients of thermal expansion, dielectric constant and coefficients of pyroelectric effect, respectively. Figure 2.5 shows the direction of the notation i , j , m , and n in terms of 1, 2, ...,6 along the axes X, Y, and Z.

Ignoring the effects of temperature, equations 3.13 and 3.14 can be reduced to

$$\epsilon_m = s_{mn}^E \sigma_n + d_{im} E_i \quad (3.15)$$

$$D_i = d_{im} \sigma_m + \varepsilon_{ij}^\sigma E_j. \quad (3.16)$$

The matrix form of equation 3.15 and 3.16 is [76]

$$\begin{pmatrix} \epsilon \\ D \end{pmatrix} = \begin{pmatrix} s^E & d^t \\ d & \epsilon^\sigma \end{pmatrix} \begin{pmatrix} \sigma \\ E \end{pmatrix} \quad (3.17)$$

where superscripts σ and E stand for the respective constants evaluated at constant stress and at constant electric field, respectively, and the superscript t denotes the transpose. Equations 3.15 and 3.16 are known as piezoelectric constitutive equations. Equation 3.17 can be expanded as [76]

$$\begin{pmatrix} \epsilon_1 \\ \epsilon_2 \\ \epsilon_3 \\ \epsilon_4 \\ \epsilon_5 \\ \epsilon_6 \\ D_1 \\ D_2 \\ D_3 \end{pmatrix} = \begin{pmatrix} s_{11}^E & s_{12}^E & s_{13}^E & 0 & 0 & 0 & 0 & 0 & d_{31} \\ s_{12}^E & s_{11}^E & s_{13}^E & 0 & 0 & 0 & 0 & 0 & d_{31} \\ s_{13}^E & s_{13}^E & s_{33}^E & 0 & 0 & 0 & 0 & 0 & d_{33} \\ 0 & 0 & 0 & s_{55}^E & 0 & 0 & 0 & d_{15} & 0 \\ 0 & 0 & 0 & 0 & s_{55}^E & 0 & d_{15} & 0 & 0 \\ 0 & 0 & 0 & 0 & 0 & s_{66}^E & 0 & 0 & 0 \\ 0 & 0 & 0 & 0 & d_{15} & 0 & \epsilon_{11}^\sigma & 0 & 0 \\ 0 & 0 & 0 & d_{15} & 0 & 0 & 0 & \epsilon_{11}^\sigma & 0 \\ d_{31} & d_{31} & d_{33} & 0 & 0 & 0 & 0 & 0 & \epsilon_{33}^\sigma \end{pmatrix} \begin{pmatrix} \sigma_1 \\ \sigma_2 \\ \sigma_3 \\ \sigma_4 \\ \sigma_5 \\ \sigma_6 \\ E_1 \\ E_2 \\ E_3 \end{pmatrix}. \quad (3.18)$$

So

$$\epsilon_1 = s_{11}^E \sigma_1 + s_{12}^E \sigma_2 + s_{13}^E \sigma_3 + d_{31} E_3 \quad (3.19)$$

$$\epsilon_3 = s_{13}^E \sigma_1 + s_{13}^E \sigma_2 + s_{33}^E \sigma_3 + d_{33} E_3. \quad (3.20)$$

Consider the case where the transducer is constrained so it can not move in the parallel direction to the applied electric field, i.e $\epsilon_3 = 0$,

$$s_{13}^E \sigma_1 + s_{13}^E \sigma_2 + s_{33}^E \sigma_3 + d_{33} E_3 = 0. \quad (3.21)$$

Assuming there is no applied stress in the X and Y axes, i.e. $\sigma_1 = \sigma_2 = 0$, only the blocking force acts along the Z direction. The blocking force is the maximum force produced by the transducer. This force is obtained when the displacement of the transducer is entirely blocked. We can then write

$$s_{33}^E \sigma_3 + d_{33} E_3 = 0. \quad (3.22)$$

With $E_3 = E = \frac{V}{t}$ the longitudinal stress is

$$\sigma_3 = -\frac{d_{33} E_3}{s_{33}^E} = -\frac{d_{33} V}{t s_{33}^E} \quad (3.23)$$

where V is the applied voltage and t is the thickness of the transducer. The blocking force along the parallel direction, F_{bz} , is

$$F_{bz} = lw \times \sigma_3 = -\frac{d_{33} V l w}{s_{33}^E t} \quad (3.24)$$

where l and w are the length and width of the piezoelectric transducer. Similarly, from equation 3.19, the blocking force along the transverse direction, F_{bx} , can be calculated as

$$F_{bx} = -\frac{d_{31}Vw}{s_{11}^E}. \quad (3.25)$$

The piezoelectric and elastic coefficients [1] required to calculate the above forces (equations 3.24 and 3.25) for a PZT-5A transducer are listed below

$$\begin{aligned} d_{33} &= 374 \times 10^{-12} \text{ m/V} \\ d_{31} &= -171 \times 10^{-12} \text{ m/V} \\ s_{11}^E &= 16.4 \times 10^{-12} \text{ m}^2/\text{N} \\ s_{12}^E &= -5.74 \times 10^{-12} \text{ m}^2/\text{N} \\ s_{13}^E &= -7.22 \times 10^{-12} \text{ m}^2/\text{N} \\ s_{33}^E &= 18.8 \times 10^{-12} \text{ m}^2/\text{N}. \end{aligned}$$

Since length $l = 12.76 \times 10^{-3}$ m, width $w = 9.56 \times 10^{-3}$ m and thickness of the transducer $t = 1.77 \times 10^{-3}$ m and the applied voltage is 40 V, the forces are

$$F_{bz} = -\frac{d_{33}Vlw}{s_{33}^E t} = 54.8 \text{ N} \quad (3.26)$$

and

$$F_{bx} = -\frac{d_{31}Vw}{s_{11}^E} = 4.2 \text{ N}. \quad (3.27)$$

For comparison, the force of gravity on the transducer from the weight of the block with magnet is $F_g = 0.2$ N, which is negligible, and the clamping force between the two magnets, F_m , was measured for our experimental set up at room temperature, giving roughly

$$F_m \cong 3 \text{ N}. \quad (3.28)$$

This magnetic force along the parallel direction ($F_m \cong 3 \text{ N} \ll F_{bz} = 54.8 \text{ N}$) is only 5% of the blocking force and does not directly have a large effect on the displacement in the longitudinal direction. However, the transverse frictional force, F_f , between the transducers gold coated surface and the brass electrode may be important. This is

$$F_f = \mu_k F_m \approx 3 \text{ N} \quad (3.29)$$

assuming the coefficient of sliding friction between gold and brass is roughly 1. Since the frictional force is comparable to the transverse blocking force, it may partially constrain the transverse motion of the transducer and, for example, cause the transducer to stick and slip when large voltages are applied.

We measured (after the stray capacitance correction) $d_{33} = 307 \times 10^{-12}$ m/V for PZT-5A at room temperature, which is 18% smaller than the manufacturer's quoted value ($d_{33} = 374 \times 10^{-12}$ m/V). We also measured $d_{33} = 1700 \times 10^{-12}$ m/V for PMN-PT at room temperature which is very close to the manufacturer's quoted value ($d_{33} = 1600 \times 10^{-12}$ m/V).

To estimate the effect of frictional clamping, consider the case of zero applied stress along the Z axes (i.e. $\sigma_3 = 0$). Equations 3.19 and 3.20 are reduced to

$$\epsilon_1 = (s_{11}^E + s_{12}^E)\sigma_1 + d_{31}E_3 \quad (3.30)$$

$$\epsilon_3 = 2s_{13}^E\sigma_1 + d_{33}E_3. \quad (3.31)$$

Assuming the transducer is perfectly clamped to base of the cell, preventing lateral movement, i.e. $\epsilon_1 = 0$, equation 3.30 can be written as

$$\frac{\sigma_1}{E_3} = -\frac{d_{31}}{(s_{11}^E + s_{12}^E)}. \quad (3.32)$$

Substituting equation 3.32 in equation 3.31, we can write

$$\frac{\epsilon_3}{E_3} = d_{33} - 2d_{31}\frac{s_{13}^E}{(s_{11}^E + s_{12}^E)}. \quad (3.33)$$

In the inverse piezoelectric effect, a voltage (V) applied across a piezoelectric produces a thickness displacement (Δt) which is related to an effective d_{33} as

$$d_{33(eff)} = \frac{\Delta t}{V}. \quad (3.34)$$

The ratio of the change in thickness Δt and the voltage (V) is equal to as the ratio of the strain and electric fields. So the effective $d_{33(eff)}$ can be written as

$$d_{33(eff)} = \frac{\Delta t}{V} = \frac{\epsilon_3}{E_3} = d_{33} - 2d_{31}\frac{s_{13}^E}{(s_{11}^E + s_{12}^E)} \quad (3.35)$$

where d_{33} and d_{31} are the unconstrained piezoelectric coefficients. Torah *et al.* [37] theoretically developed equation 3.35 to calculate an effective d_{33} for the inverse piezoelectric effect in a clamped transducer. After substituting the values for PZT-5A, the effective $d_{33(eff)}$ for a perfectly clamped longitudinal transducer is 142×10^{-12} m/V. This is a 62% reduction from the bulk d_{33} of the material. Ahmed *et al.* [77] experimentally found that the clamping effect reduced the bulk d_{33} for a thin film of PZT by 50% close to the theoretical calculation 62%. The difference may reflect differences between the piezoelectric coefficients in bulk and thin film PZT.

3.2.3 Procedure to measure piezoelectric coefficients, hysteresis and creep

A Keithley 2400-Source Meter was used to apply a DC voltage to the transducer's electrodes. Coaxial cables connected an AH capacitance bridge to a fixed copper block and to a block clamped on top of the shear or longitudinal transducer, as shown in Figures 3.7 or 3.12 . A displacement of the transducer changes the gap between the two blocks and their capacitance. A Neocera LTC-21 temperature controller was used to control the temperature. A LabVIEW program was written to measure and save the data.

In order to measure all those properties, we controlled the temperature at each point for several hours, until the temperature fluctuation was within a few mK. We set the capacitance average time exponent (averexp) of the capacitance bridge to a value of 9. At this setting, the bridge takes multiple internal readings for 4 seconds and averages them to reduce the random noise before displaying the value. We recorded the capacitance, temperature and applied voltage as functions of time.

In order to find d_{15} or d_{33} , the capacitance between the blocks was measured while applying a ± 20 V DC square wave with a period of 160 seconds to the electrodes of the transducer. Before changing the polarity of the voltage, four data points were measured with a time interval of 20 seconds between data points. Figure 3.13(a) shows the typical capacitance changes (blue line with data points) when the DC square wave (red line) was applied across a LiNbO_3 shear transducer at 6 K. To find the piezoelectric coefficients, we plotted capacitance with respect to applied voltage as shown in Figure 3.13(b). The best fit line provides the average capacitance ($C = 3.2403$ pF) and the change in capacitance ΔC (about 23 ppm) corresponding to the 40 V change in voltage. The value $d_{15} = 4.97 \times 10^{-11}$ m/V was calculated by substituting those values into equation 3.7. For these measurements, the gap separation between the blocks was $L = 0.3$ mm at room temperature.

LiNbO_3 has the smallest values of d_{ij} for the materials studied. At low temperature $d_{15} = 6.59 \times 10^{-11}$ m/V (stray capacitance corrected value) which gives a displacement $\Delta L = 2.6$ nm when the ± 20 V voltage is applied. This can be compared to the noise in capacitance in Figure 3.6. The expected noise level is $\frac{\delta C}{\Delta C} = \frac{\delta l}{\Delta L} = \frac{0.09 \text{ nm}}{2.6 \text{ nm}} = 3\%$ for a single capacitance measurement. We averaged 24 readings for positive voltage and 24 readings for negative voltage at each point to reduce the noise which is 0.7% at 30 K for LiNbO_3 .

After measuring d_{15} , the hysteresis was measured by changing the applied voltage in fixed steps over a range of ± 50 V for PMN-PT and ± 150 V for LiNbO_3 and PZT-

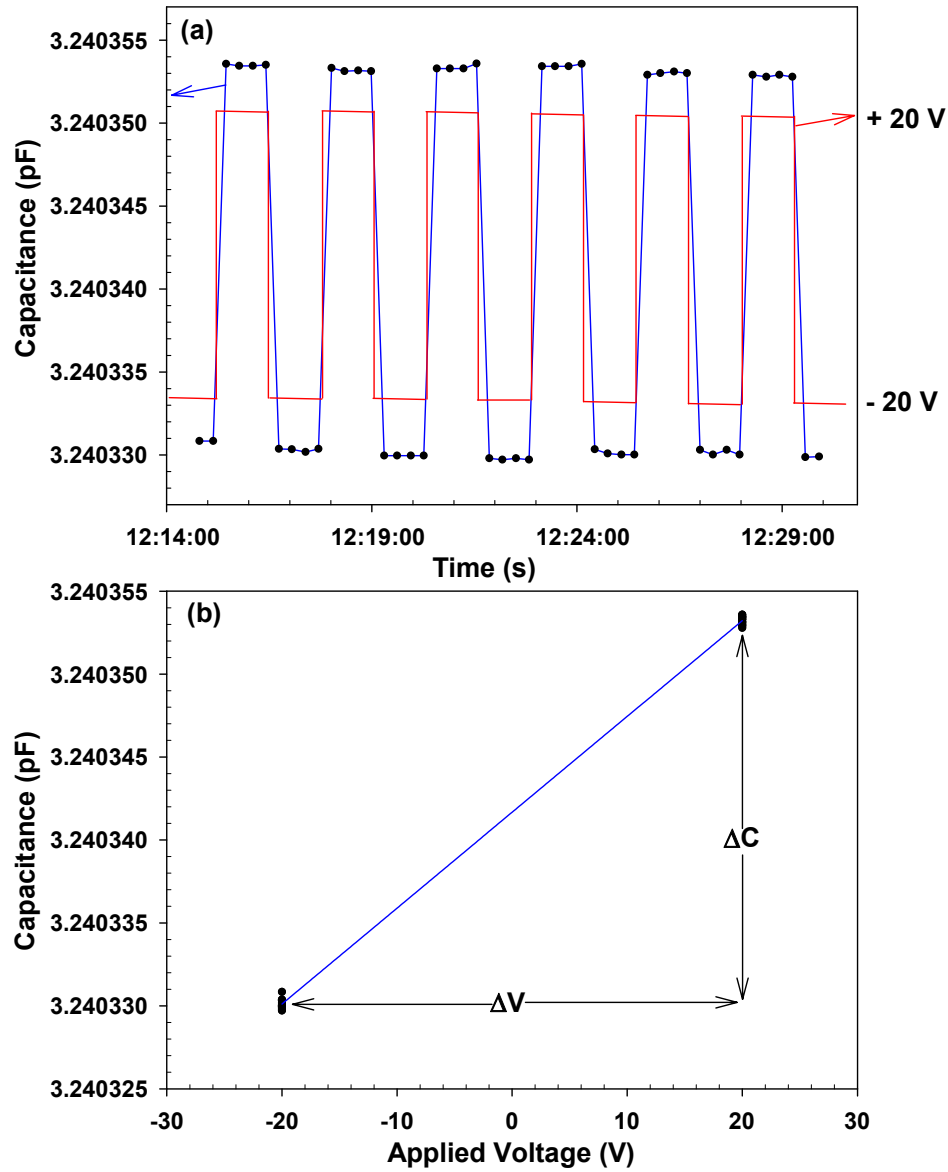


Figure 3.13: (a) Capacitance vs. time graph for a LiNbO₃ single crystal at 6 K under an applied voltage ± 20 V. (b) best fit line is to find the average capacitance and change in capacitance with respect to applied voltage.

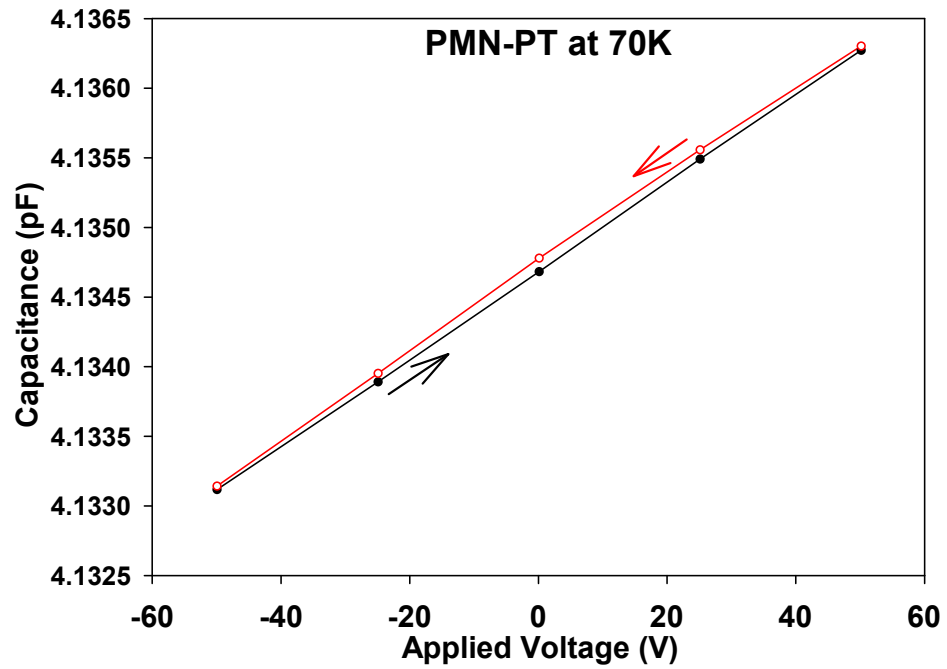


Figure 3.14: Hysteresis in a PMN-PT crystal at 70 K during cycling of the applied voltage from -50 to +50 V.

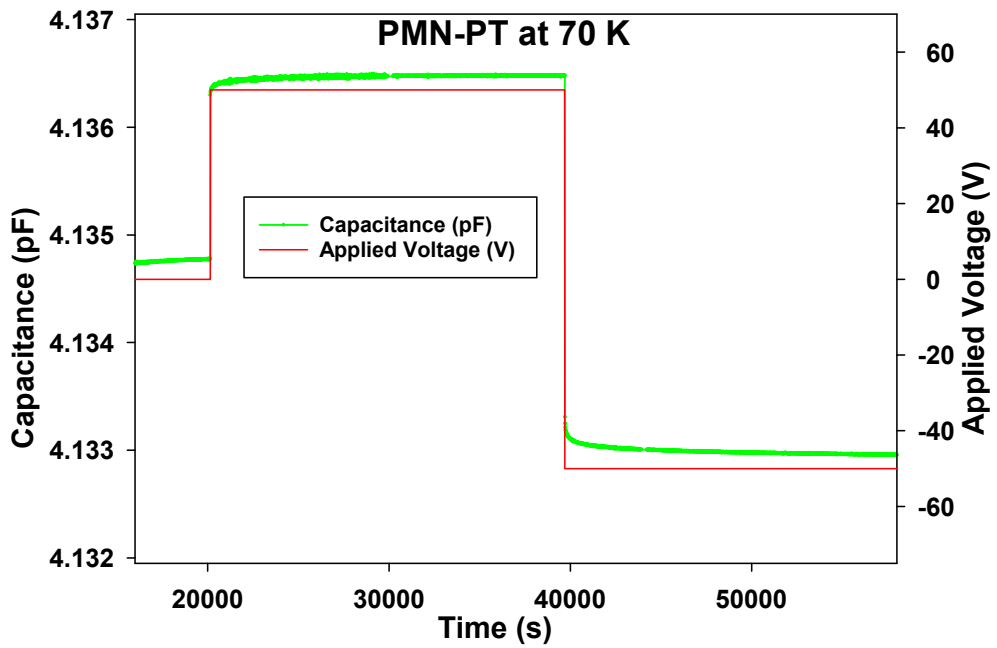


Figure 3.15: Creep for applied voltage ± 50 V at 70 K of the shear PMN-PT transducer.

5A. Figure 3.14 shows a complete hysteresis loop for PMN-PT at 70 K. The voltage step used was 25 V and each point represents a single capacitance measurements over 10 seconds. The loop began at $V = -50$ V, increased the voltage to $+50$ V, then returned to the starting point at -50 V.

In order to measure the creep properties, the capacitance was measured every 8 seconds following a voltage change. The capacitance was first measured for a few hours with no applied voltage, then the voltage was changed from 0 to $+50$ V (for PMN-PT), or from 0 to $+150$ V (for LiNbO_3 or PZT-5A). The capacitance was measured for a few hours then the voltage was changed from $+50$ V to -50 V for (PMN-PT) or $+150$ to 0 V for (LiNbO_3 or PZT-5A) and the capacitance was measured at this voltage for another few hours. Figure 3.15 shows typical creep data for a PMN-PT crystal at 70 K.

3.2.4 Piezoelectric Polarization Measurements

Polarization hysteresis loops (referred to a P-E loops) were measured for PMN-PT and PZT-5A transducers from room temperature down to 77 K. Figure 3.16 shows the experimental set-up for a P-E loop measurement, using a function generator, a high voltage transformer (output $13.8 \times$ input), a Tektronix TDS 2014B oscilloscope and a Sawyer-Tower (ST) circuit. Measurements were made using the 1 K fridge and a brass cell to hold the transducer. The cell was mounted with two thermometers and a 200Ω heater on the 1 K pot of the fridge. Two brass electrodes were attached to a brass block and a brass base, using electrically insulating epoxy. The piezoelectric transducer was magnetically clamped between the block and the base. The electrodes were connected to the ST circuit by the wires to include the sample capacitance, C_S . The ST circuit consists of two resistors in series R_1 ($10 \text{ M}\Omega$) and R_2 ($100 \text{ k}\Omega$), and two capacitors in series, the sample (C_S) and a standard reference capacitor ($C_{ref} = 1 \mu\text{F}$). The resistors work as a resistive divider to a scale down the voltage across the resistor R_2 by a factor of 100 and, since C_{ref} ($1 \mu\text{F}$) is much larger than C_S , the voltage drop (V_{ref}) across C_{ref} is much smaller than that (V_S) across C_S . The voltage (V_{ref}) drop across C_{ref} , which is proportional to the polarization of the sample, is applied to the vertical axis of the oscilloscope and the voltage drop across R_2 , V_{R2} , is applied to the horizontal axis of the oscilloscope to measure the electric field across the sample.

The mathematical analysis of the ST circuit measurements is as follows. The capacitors C_S and C_{ref} are in series so the charge $Q_S (= V_S C_S)$ is equal to the charge

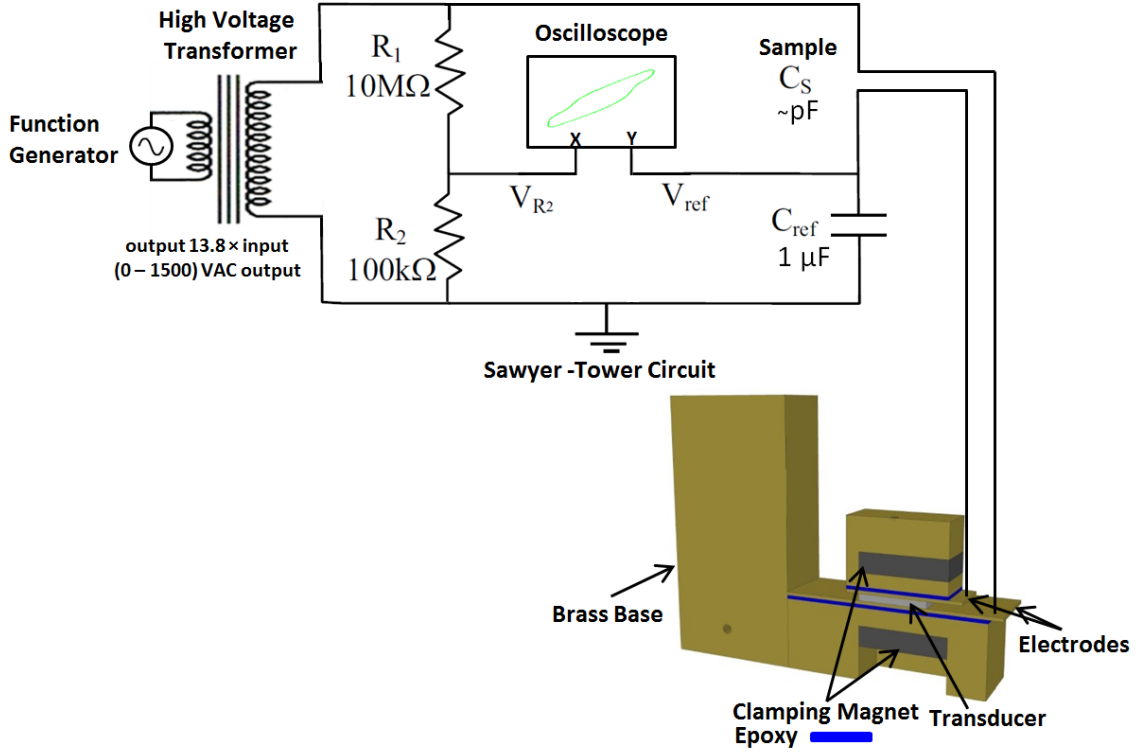


Figure 3.16: The polarization hysteresis loop measurement.

$Q_{ref} (= V_{ref}C_{ref})$. The polarization of the sample is

$$P = \frac{Q_S}{A} = \frac{Q_{ref}}{A} = \frac{V_{ref}C_{ref}}{A} \quad (3.36)$$

where $C_{ref} = 1 \mu\text{F}$ and A is the electrode area of our transducer. Or, $P \propto V_{ref}$ since $\frac{C_{ref}}{A}$ is constant. Since $C_S \ll C_{ref}$, we know that $V_S \gg V_{ref}$, so $V_S \cong V_{in}$, where V_{in} is the input voltage of the circuit. If t is the thickness of the sample, then the electric field across the sample is

$$E_S = \frac{V_S}{t} \cong \frac{V_{in}}{t}. \quad (3.37)$$

The resistive divider of the circuit gives

$$V_{in} = \left(\frac{R_1 + R_2}{R_2}\right)V_{R2} \quad (3.38)$$

where V_{R2} is the voltage drop across R_2 , so the electric field across the sample can be written as

$$E_S = \left(\frac{R_1 + R_2}{R_2}\right)\frac{V_{R2}}{t} = \left(\frac{10M\Omega + 100k\Omega}{100k\Omega}\right)\frac{V_{R2}}{t} \cong \frac{100 \times V_{R2}}{t}. \quad (3.39)$$

The measurements of V_{R2} and V_{ref} were saved for sine waves of different frequencies. The polarization (P) and electric field (E_S) of the hysteresis loop were then calculated using the known values of C_{ref} , A , t , R_1 and R_2 .

3.2.5 Experimental design and procedure to measure dielectric constant, K

In order to directly measure the dielectric constant and loss conductance, G , with high resolution and accuracy, the AH capacitance bridge was connected across the transducer with the same arrangement used to measure the P-E loops. The temperature dependent capacitance and loss conductance were measured at 1 kHz. The bridge automatically changed the applied voltage from a maximum of 15 VAC, depending on the capacitance of the transducer. The dielectric constant is

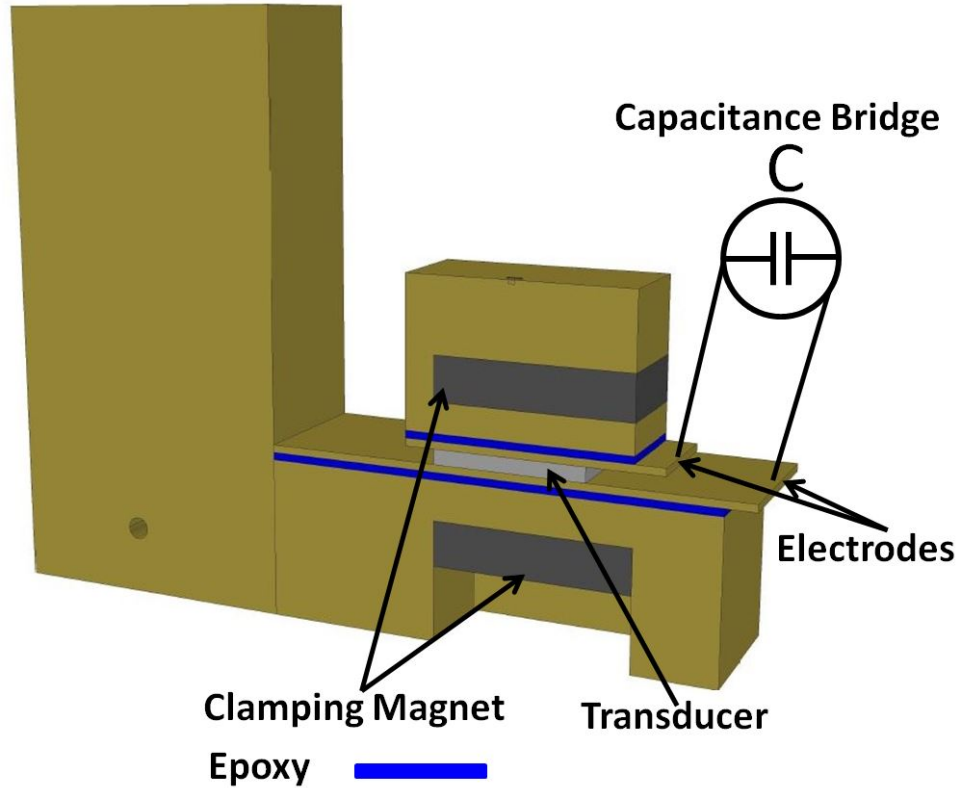


Figure 3.17: Schematic diagram for dielectric measurements.

$$K = \frac{C}{C_0} \quad (3.40)$$

where C_0 is the capacitance that would be measured if there was a vacuum between the top and bottom surfaces of the transducer

$$C_0 = \frac{\epsilon_0 A}{t}. \quad (3.41)$$

where A is the area of the top or bottom surfaces and t is the thickness of the transducer. The loss of the capacitor was measured as a conductance. The loss

tangent or dissipation factor can be obtained from equation 2.52

$$\tan \delta = \frac{G}{\omega C}. \quad (3.42)$$

The total charge (Q) on the transducer is

$$Q = CV \quad (3.43)$$

where C is the measured capacitance and V is the applied voltage across the transducer. The real part of the polarization of the transducer is simply

$$P = \frac{Q}{A}. \quad (3.44)$$

The total hysteresis loss of the P-E loop to the transducer is (recalling equation 2.57)

$$U_T = \frac{1}{2} \omega CV^2 \tan \delta. \quad (3.45)$$

The polarization hysteresis loops were measured using larger voltage and the Sawyer-Tower-Circuit [78]. The edges effect and stray capacitance did not significantly affect the P-E loop hysteresis or dielectric measurements because of the large dielectric constants of the piezoelectric materials. The room temperature dielectric constants K_{ij}^σ for the piezoelectric materials studied in this thesis are $K_{11}^\sigma = 2550$ (shear PMN-PT), $K_{33}^\sigma = 5418$ (longitudinal PMN-PT), $K_{11}^\sigma = 1590$ (shear PZT-5A), $K_{33}^\sigma = 1570$ (longitudinal PZT-5A), $K_{11}^\sigma = 88$ (shear LiNbO₃).

Chapter 4

Temperature Dependence of Piezoelectric and Dielectric Properties

4.1 Introduction

In this chapter, experimental measurements of the temperature dependence of piezoelectric and dielectric properties are presented. The fundamental piezoelectric properties of both shear and longitudinal single crystals of LiNbO_3 and PMN-PT, and ceramics of PZT-5A are investigated and analyzed as functions of temperature. The important experimental results are summarized in this introductory section.

The experimental techniques and procedures were described in section 3.2. The piezoelectric properties of LiNbO_3 transducers and a stack are presented first, followed by those of PMN-PT and PZT-5A transducers. We chose LiNbO_3 to begin because it is a single crystal with a single domain. Its piezoelectric properties are simple and are mostly the result of intrinsic contributions with little temperature dependence. We measured the temperature dependence of the shear piezoelectric coefficient, d_{15} , and the dielectric constants, K_{11}^σ for shear LiNbO_3 transducers. The room temperature d_{15} values decreased by about 7% at the lowest temperatures. If the longitudinal piezoelectric coefficient d_{33} , which is smaller than d_{15} at room temperature [19, 49], has a similar temperature dependence, then the changes in d_{33} will be comparable to the resolution of our capacitance measurements. Therefore, we did not measure the temperature dependence of d_{33} for a LiNbO_3 crystal. Next we present results for PMN-PT. Although PMN-PT is a single crystal, it is also a relaxor ferroelectric material. It has much larger d_{ij} which reflect both intrinsic and extrinsic contributions. Finally, we show results for PZT ceramics which are the most widely used piezoelectric materials. PZT's coefficients are smaller than those of PMN-PT. In PZT, one of

the major extrinsic contributions is the result of domain wall motion. There are two groups of domain walls, 180° walls and non-180° walls. Only the non-180° walls are ferro-elastic. The non ferro-elastic 180° wall motion contributes only to the dielectric property; the non-180° wall motion affects both dielectric and piezoelectric properties [29].

The motivation behind our measurements was to find suitable materials for use in cryogenic applications. The experimental results are presented in the following sequence. The shear piezoelectric coefficients (d_{15}) are presented in section 4.2. The longitudinal piezoelectric coefficients (d_{33}) are discussed in section 4.3. The dielectric constants K_{ij}^σ and loss conductance G are shown in section 4.4. The voltage constants (g_{ij}) are presented in section 4.5. All the properties are summarized in section 4.6.

4.2 The shear piezoelectric coefficient (d_{15})

4.2.1 LiNbO₃ single crystal

A square thin plate ($10 \times 10 \times 0.26 \text{ mm}^3$) of 41° X-cut (pure shear) LiNbO₃ with chrome/gold electrodes was purchased from Boston Piezo Optics, Inc. [79] to investigate the shear piezoelectric coefficient d_{15} . Figure 4.1 shows the temperature dependence of the experimentally measured (uncorrected) shear piezoelectric coefficient for a LiNbO₃ transducer, calculated from the raw data. The error bars correspond to the noise in capacitance measurements as described in section 3.2.3. To find the actual value, the measured data was corrected by subtracting the stray capacitance from the measured capacitance, as described in section 3.2.1. The corrected d_{15} is almost 1/3 higher than that of uncorrected value because d_{15} is inversely proportional to square of the capacitance. Figure 4.2 shows both the measured (black dots) and corrected data (blue dots) as functions of temperature. At room temperature, our corrected d_{15} is $69.4 \times 10^{-12} (\text{m/V})$ which is close to other published data. At room temperature, Smith *et al.* [19] and Warner *et al.* [49] measured the coefficient as $69.2 \times 10^{-12} (\text{C/N})$ and $68 \times 10^{-12} (\text{C/N})$, respectively. Yamada *et al.* [18] reported coefficient of $74 \times 10^{-12} (\text{C/N})$ for this material at 20 °C. We believe the values differ because of the different measurement techniques used, such as the resonant method. Our room temperature value decreases roughly linearly with temperature down to 100 K, where it is 5% smaller than at room temperature. Below 100 K, it is almost independent of temperature within the resolution of the measurements, so we did not extend the measurements below liquid helium temperature (4 K).

We also constructed a stack of 3 single 41° X-cut LiNbO₃ shear transducers, using

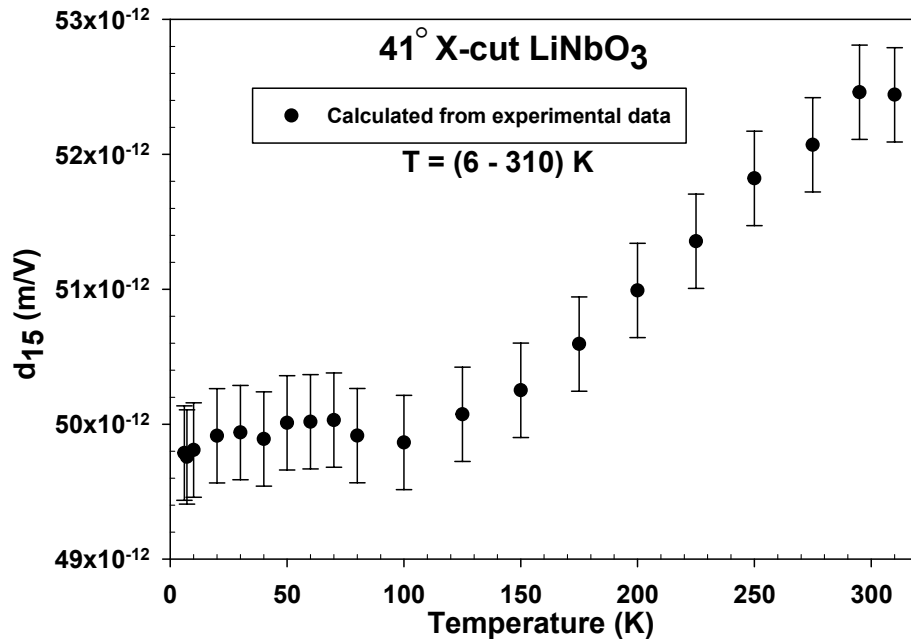


Figure 4.1: Temperature dependence of the measured (uncorrected for stray capacitance) shear piezoelectric coefficient d_{15} of a LiNbO_3 transducer.

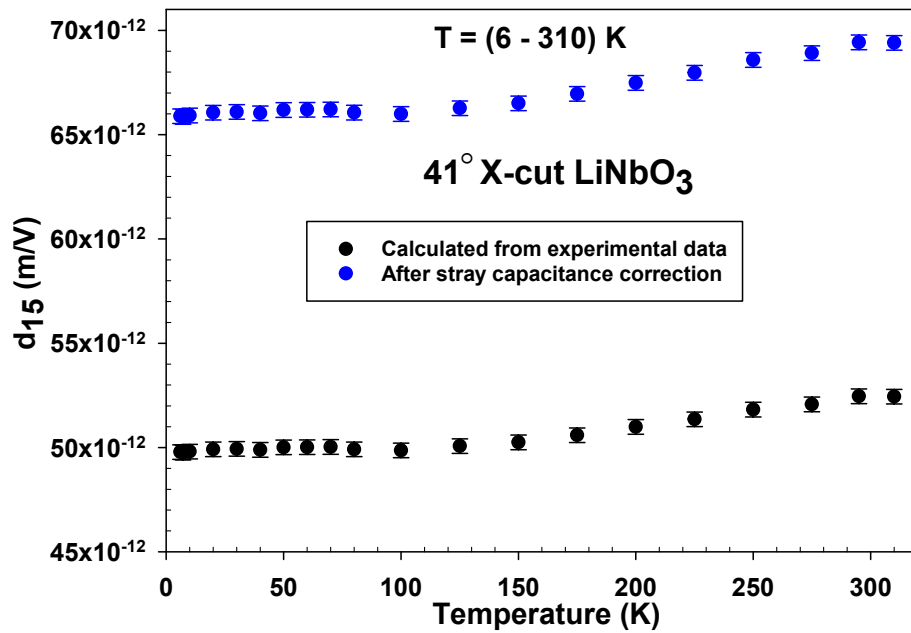


Figure 4.2: Temperature dependence of the measured uncorrected (black dots) and corrected (blue dots) shear piezoelectric coefficient d_{15} of a LiNbO_3 transducer.

silver epoxy to make the electric contact between transducers. Figure 4.3 shows the corrected d_{15} results for the single LiNbO_3 transducer (blue dots) and for the stack (open blue circles). The room temperature displacement per volt of the stack is $212.9 \times 10^{-12} \text{m/V}$, which drops by only about 7% at 50 K ($198.2 \times 10^{-12} \text{m/V}$). Below 50 K, it is nearly constant. The coefficients d_{15} of the single transducer and the stack are almost the same below LN_2 temperature and differ by about 2% at higher temperatures.

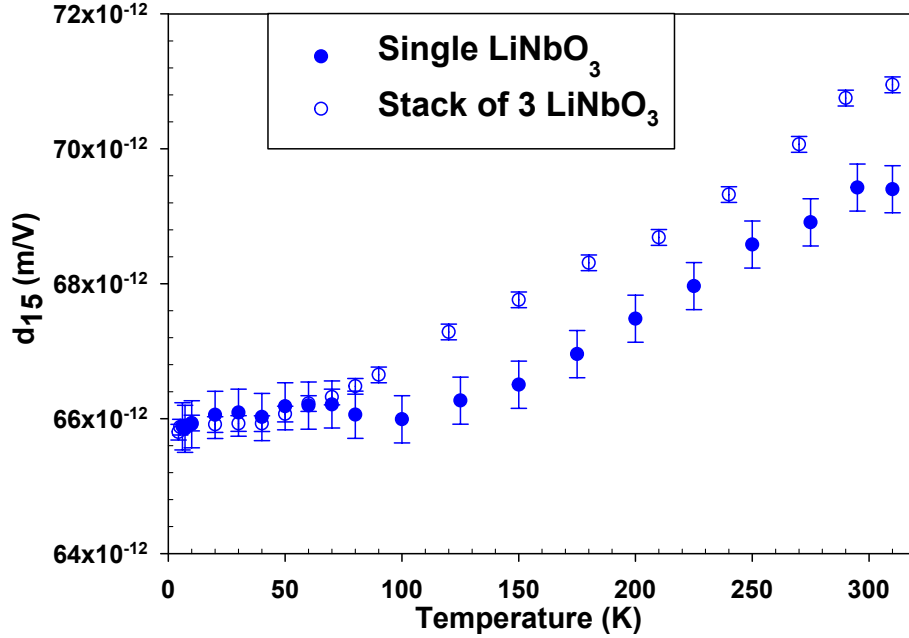


Figure 4.3: Temperature dependence of corrected d_{15} of a single LiNbO_3 transducer (blue dots) and a stack of three transducers (open blue dots).

4.2.2 PMN-PT single crystal

A square plate ($10 \times 10 \times 1 \text{ mm}^3$) of a single crystal shear PMN-PT transducer from TRS Ceramics, Inc. [80] was used to investigate the temperature dependence of the shear piezoelectric coefficient d_{15} . The crystal orientation, poling direction, and plate dimensions are given in Figure 4.4.

The temperature dependence of both the measured uncorrected (dark red dots) and corrected (red dots) piezoelectric coefficient d_{15} , is shown in Figure 4.5. The uncertainties corresponding to the resolution of our capacitance bridge are smaller than the symbol sizes. The manufacturer’s quoted d_{15} is $(2000 - 4000) \times 10^{-12} \text{ m/V}$ at room temperature. Both the measured uncorrected and the corrected room temperature d_{15} values are within this range. At room temperature, our corrected d_{15} has

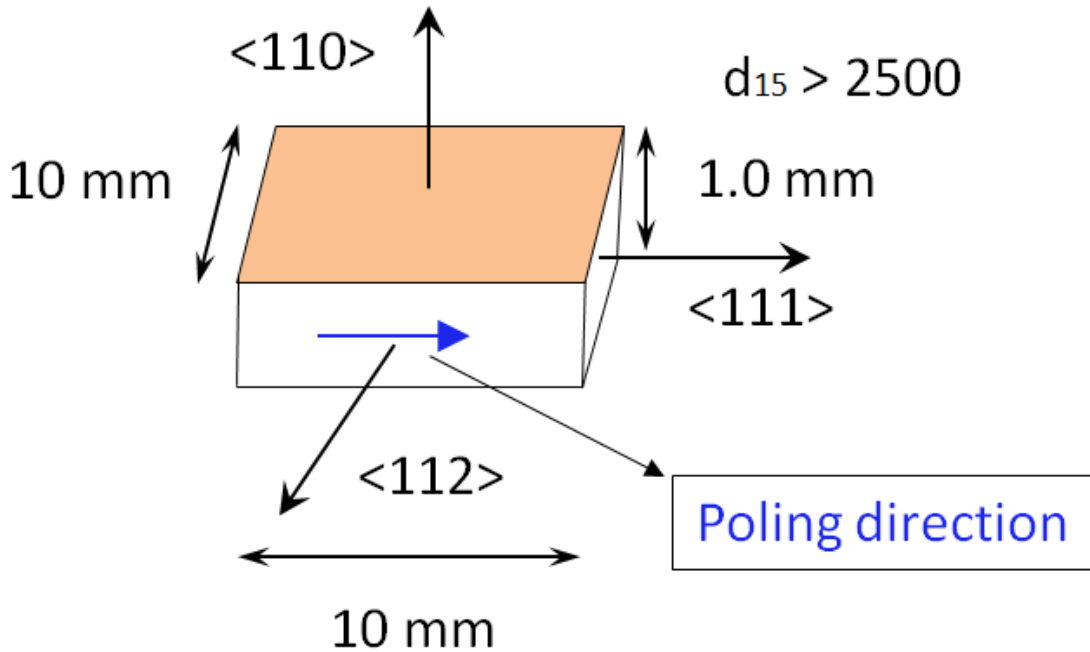


Figure 4.4: The shear PMN-PT single crystal with Cr/Au electrodes from TRS Ceramics, Inc. [80].

a value of 3200×10^{-12} m/V, and decreases with temperature, but is nearly constant (independent of temperature) between 210 and 80 K, a temperature region known as the plateau. However, below 80 K, d_{15} drops rapidly, from the plateau value of 2400×10^{-12} m/V to 315.8×10^{-12} m/V at 150 mK, a factor of 8. Wang *et al.* [14] observed a similar plateau between 225 and 78 K, but their measurements did not extend to lower temperatures. Their values of d_{15} are somewhat larger than that we measured in our transducer. This may be because of different chemical compositions and their use of a different technique, the resonant method.

Figure 4.6 shows our corrected data below 10 K for two separate runs. These two sets of data are slightly different. The two sets of data were taken 2 to 3 days apart. After taking the open red circles data down to 2 K, we warmed the fridge up to 77 K, pumped out contamination that had plugged the fridge, then cooled down the fridge back down to 150 mK and measured the solid red dot data. It is clear that d_{15} continues to decrease almost linearly to the lowest temperature 150 mK. This suggests that thermally activated effects such as domain wall motions are not frozen out completely at the lowest temperature.

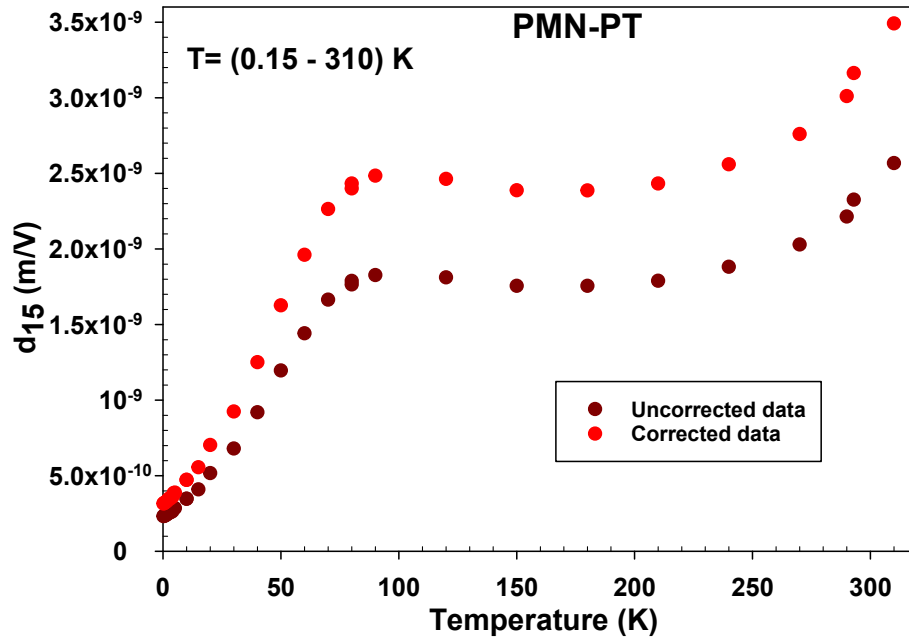


Figure 4.5: Temperature dependence of the measured uncorrected (dark red dots) and corrected (red dots) piezoelectric strain coefficient, d_{15} , for a PMN-PT single crystal.

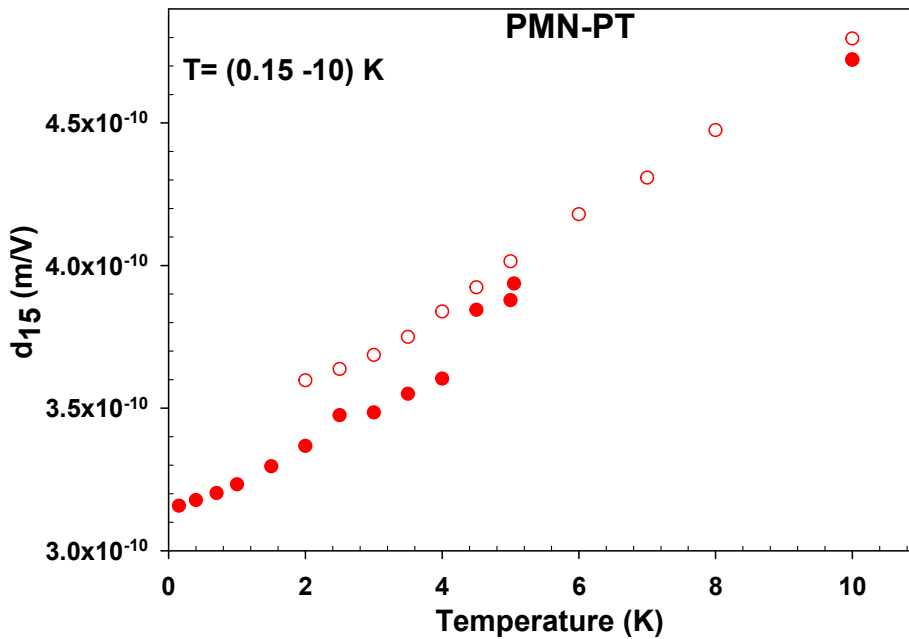


Figure 4.6: Temperature dependence of the corrected piezoelectric strain coefficient, d_{15} , below 10 K for a PMN-PT single crystal.

4.2.3 PZT-5A ceramic

A rectangular plate ($12.77 \times 9.58 \times 1.78 \text{ mm}^3$) of a ceramic shear PZT-5A transducer from Boston Piezo Optics, Inc. [81] was used to investigate the temperature dependence of the shear piezoelectric coefficient d_{15} . The temperature dependence for both the measured uncorrected (dark green dots and open circles) and corrected (green dots and open circles) piezoelectric coefficient, d_{15} is shown in Figure 4.7. The two sets of data were measured for two different transducers in separate runs a year apart. In the first run, d_{15} was measured in the temperature range from 6 to 310 K (dark green dots) and in the second run, it was measured from 78 mK to room temperature (dark green open circles). Although both transducers were from the same company their room temperature d_{15} varies by 16%.

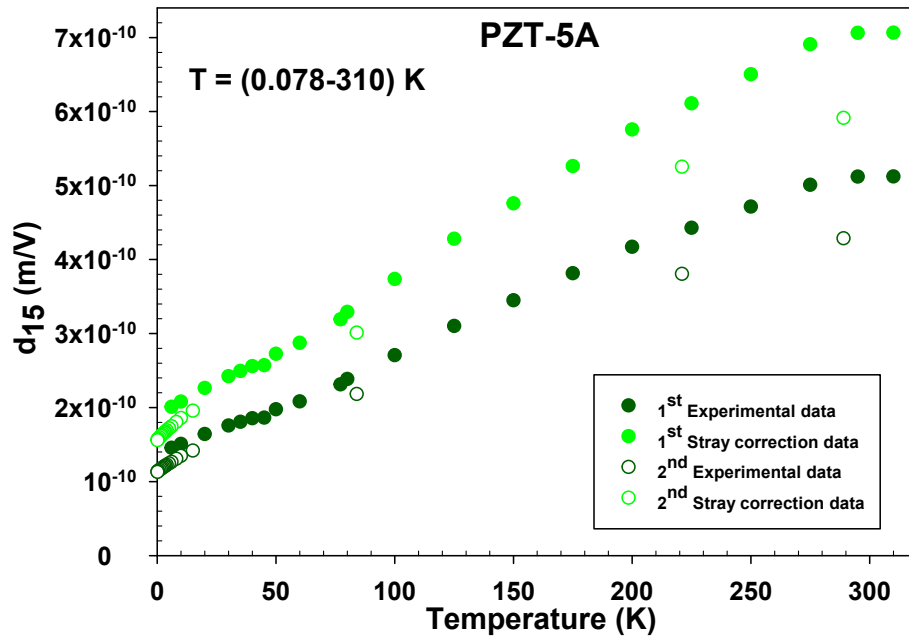


Figure 4.7: The uncorrected (dark green dots and open circles) and corrected (green dots and open circles) piezoelectric strain coefficient d_{15} of a PZT-5A ceramic.

The coefficient d_{15} decreases roughly linearly over the entire temperature range. For the second run, the corrected d_{15} decreases from $591 \times 10^{-12} \text{ m/V}$ at room temperature (close to the value quoted by the manufacturer: $585 \times 10^{-12} \text{ m/V}$) to $156 \times 10^{-12} \text{ m/V}$ at 78 mK, a 75% decrease. Figure 4.8 shows the corrected data from 78 mK to 10 K. The coefficient has a nearly linear temperature dependence in this temperature range.

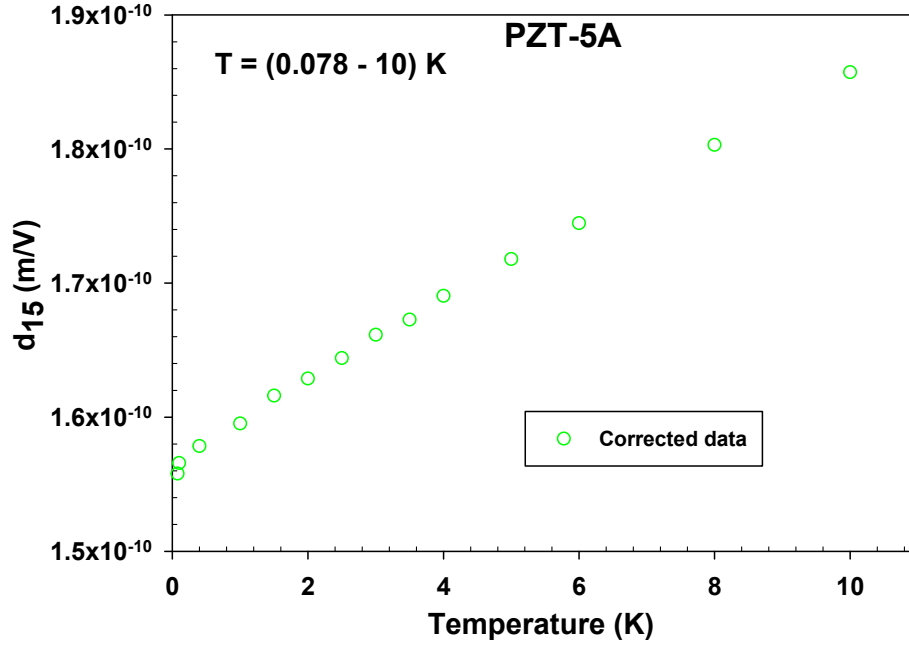


Figure 4.8: Temperature dependence of the piezoelectric coefficient d_{15} of a PZT-5A ceramic below 10 K.

4.3 The longitudinal piezoelectric coefficient (d_{33})

4.3.1 PMN-PT single crystal

A square thin plate ($10 \times 10 \times 0.140 \text{ mm}^3$) of a single crystal longitudinal PMN-PT transducer from APC International, Ltd.[82] was used to investigate the temperature dependence of the longitudinal piezoelectric coefficient, d_{33} . The temperature dependence of d_{33} is shown in Figure 4.9. The value of d_{33} decreases from a value of $1700 \times 10^{-12} \text{ m/V}$ at room temperature (manufacturer's quoted value is $1600 \times 10^{-12} \text{ m/V}$) to $96.7 \times 10^{-12} \text{ m/V}$ at 50 K, a factor of 15. However, we were unable to measure d_{33} below 50 K because we did not see displacement change due to a square wave applied voltage. The displacement change appeared again when the temperature was back at 50 K. The actual reason we do not know honestly, but we are not confident in the data below 100 K.

4.3.2 PZT-5A ceramic

A square plate ($12.7 \times 12.7 \times 0.70 \text{ mm}^3$) of a ceramic longitudinal PZT-5A transducer from Boston Piezo Optics, Inc.[81] was used to investigate the temperature dependence of the longitudinal piezoelectric coefficient d_{33} . The temperature dependence

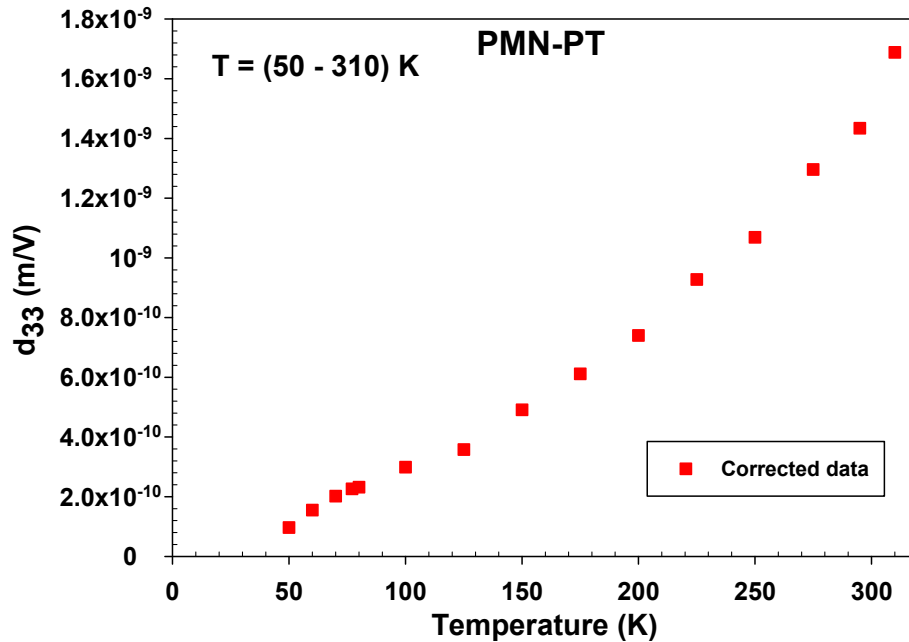


Figure 4.9: Temperature dependence of the corrected longitudinal coefficient d_{33} for a PMN-PT single crystal.

of d_{33} from 2 to 310 K is shown in Figure 4.11. It decreases roughly linearly down to 30 K, then appears to rise below 30 K. We started these measurements from 2 K and, when we were measuring the capacitance at 20 K, an experimental problem caused the applied voltage to suddenly increase from 20 V to 238 V. We then stopped the measurement and checked all the connections but could not find anything wrong. When we then restarted the measurements, d_{33} decreased down to 30 K then began to increase up to room temperature. The magnetic clamping we used might have affected the measurements, as described in section 3.2.2. We saw this behavior in both PZT-5A and PMN-PT measurements below 50 K, and therefore do not trust our d_{33} values below 50 K. We remeasured the data below 50 K and saw similar changes although their magnitudes were different.

The room temperature value of d_{33} is 307×10^{-12} m/V, which is 18% smaller than the manufacturer's quoted value for PZT-5A (374×10^{-12} m/V). The room temperature value of d_{33} drops by a factor of 5 by 30 K (66×10^{-12} m/V).

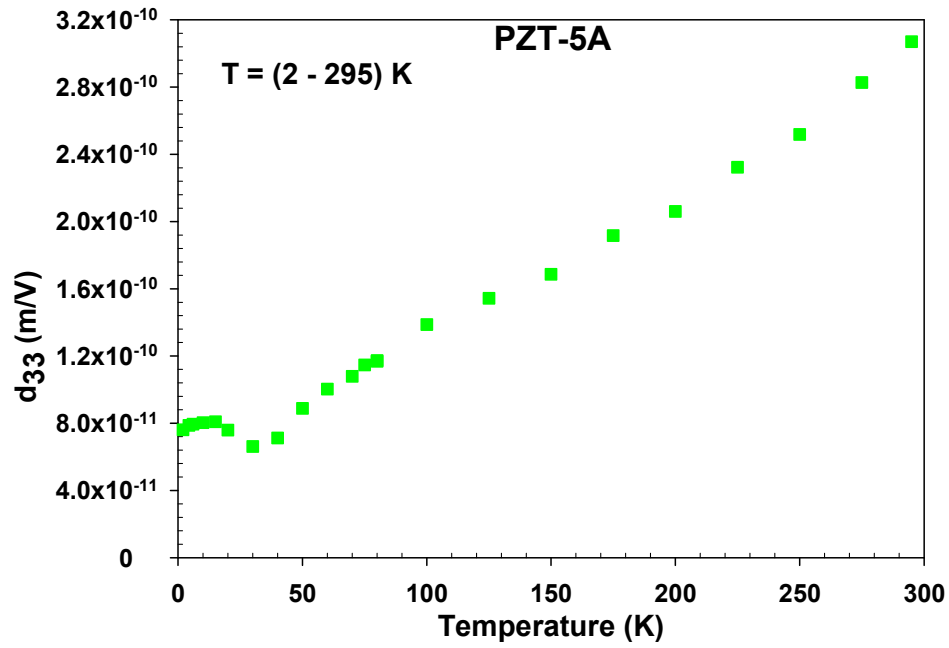


Figure 4.10: Temperature dependence of the longitudinal piezoelectric coefficient d_{33} of a PZT-5A ceramic.

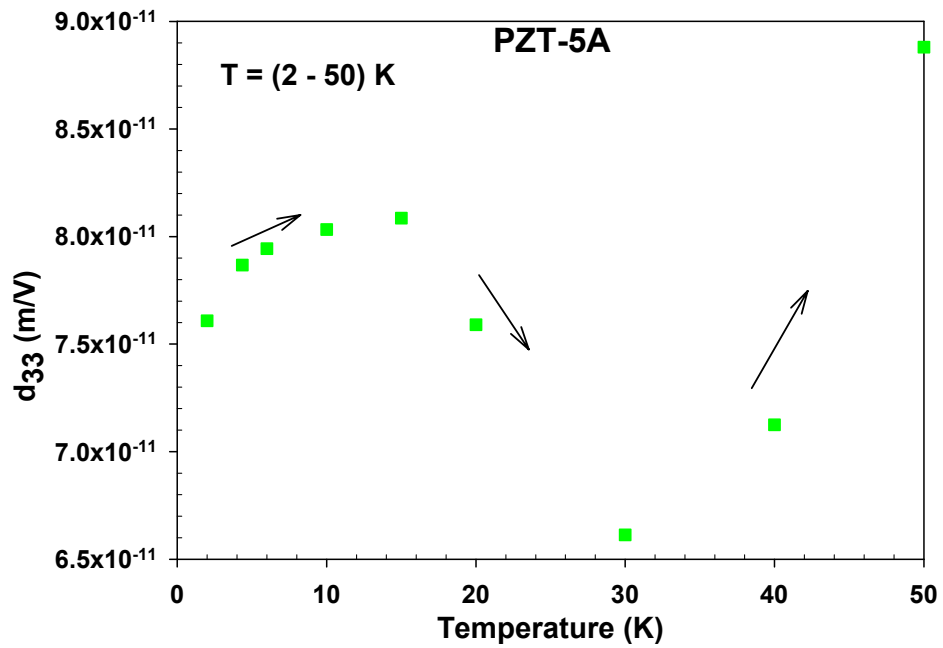


Figure 4.11: Temperature dependence of d_{33} below 50 K.

4.4 The dielectric constant and loss conductance

4.4.1 LiNbO₃ single crystal

The shear 41° X-cut (pure shear) LiNbO₃ transducer described in section 4.2.1 was used for this study. Figure 4.12 shows the temperature dependence of its dielectric constant at constant stress (K_{11}^{σ}), and loss conductance G , during cooling (black data) and warming (blue data). The entire set of cooling data was taken during 2-3 hours and the warming data was taken over 10 days. The cooling and warming rates did not affect the dielectric constant but the loss conductance is slightly different during cooling and warming. The maximum dielectric constant is 90 at 345 K and decreases down to 100 K, where it has a value of 82.8. It decreases slowly from 100 K ($K_{11}^{\sigma} = 82.8$) to 50 K ($K_{11}^{\sigma} = 82.2$) and below 50 K it is essentially constant. Over the entire temperature range it drops by about 9%, similar to the decrease for d_{15} . The room temperature dielectric constant for this material (88) is close to the value reported by Warner *et al.* [49] (85.2) and by Yamada *et al.* [18] (84.6).

The loss conductance is small and decreases gradually from the highest temperature down to 200 K and is essentially constant at lower temperatures. Data was taken above room temperature, in order to look for a relaxation peak, which may be around 360 K.

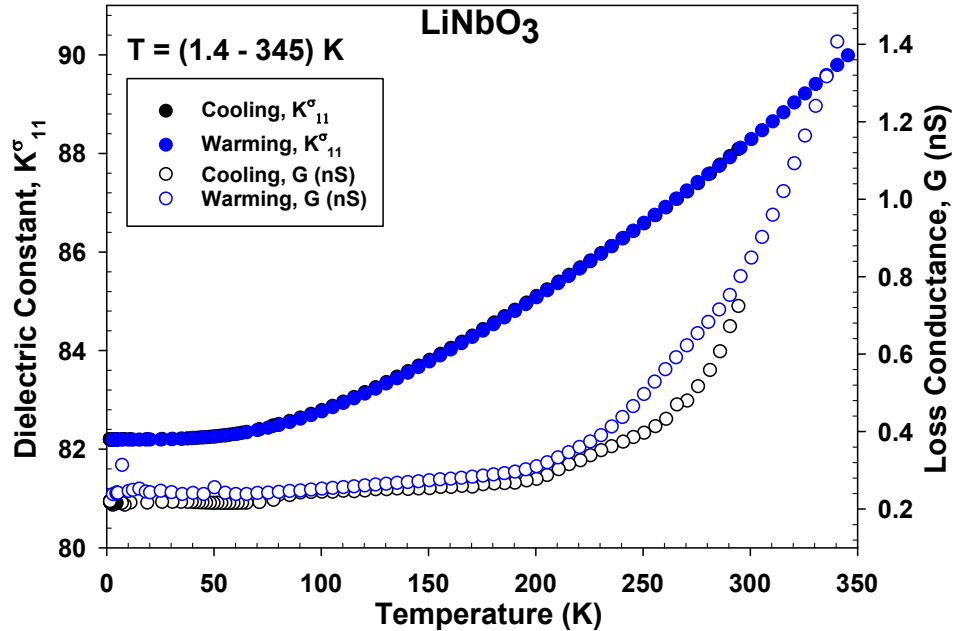


Figure 4.12: Temperature dependence of the dielectric constant and loss conductance for shear LiNbO₃.

4.4.2 PMN-PT single crystal

The PMN-PT shear transducer used for this study is described in section 4.2.2. Figure 4.13 shows the temperature dependence of its dielectric constant, K_{11}^σ , and loss conductance, G , in the temperature range from 1.58 to 293 K. The cooling rate or warming rate did not affect either the dielectric constant or the loss conductance. At room temperature K_{11}^σ is 2550 and it decreases with decreasing temperature, following a trend much like that of d_{15} described in section 4.2.2, although the plateau is not as clear as that for d_{15} . The dielectric constant drops by a factor of 10, to 254, at the lowest temperature 1.4 K. The loss conductance increases with temperature and shows a large relaxation peak around 75 K, with maximum value of 249 nS.

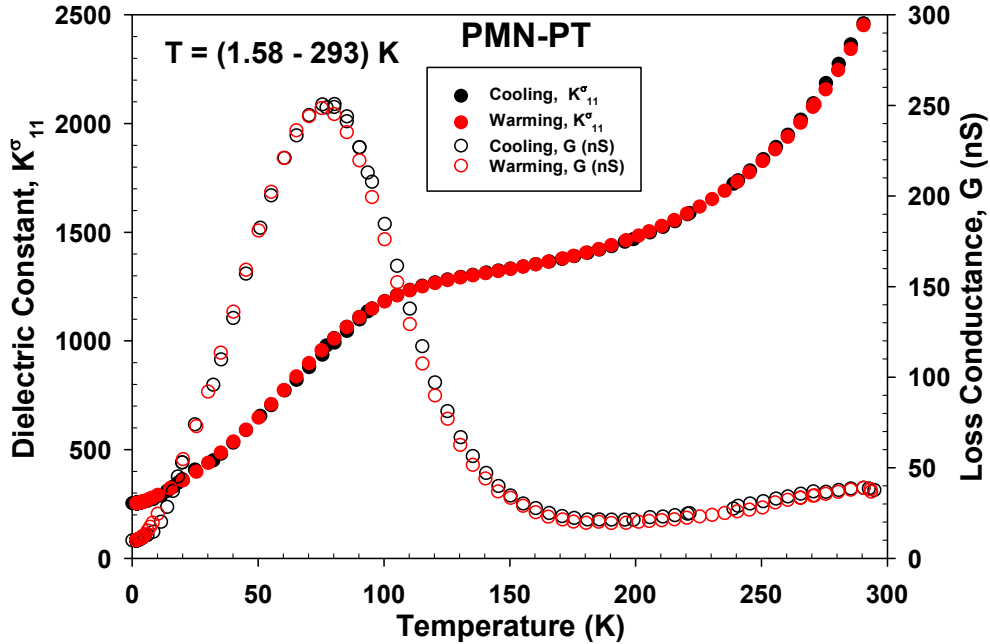


Figure 4.13: Temperature dependence of the dielectric constant and loss conductance at 1 kHz for a shear PMN-PT single crystal.

Two longitudinal PMN-PT transducers were also studied. One ($10 \times 10 \times 0.140$ mm³) was from APC International, Ltd. [82] and the other one ($10 \times 10 \times 0.30$ mm³) was from TRS Ceramics, Inc. [80]. Figures 4.14 and 4.15 show the temperature dependence of their dielectric constants and loss conductance. The cooling rate or warming rate did not affect K_{33}^σ but had a small effect on the loss conductance. The room temperature dielectric constants are 5400 for the transducer from TRS Ceramics Inc. and 4460 for the transducer from APC international Ltd. At our lowest temperature of 1.4 K, they have similar values of 401 and 360, respectively. The dif-

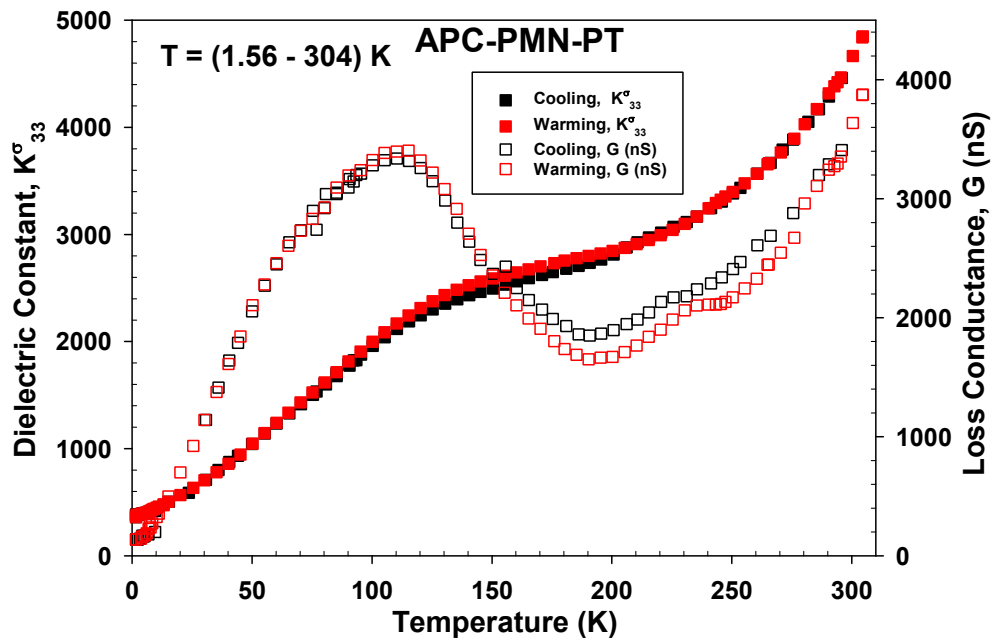


Figure 4.14: Temperature dependence of the dielectric constant and loss conductance at 1 kHz for a longitudinal PMN-PT single crystal from APC international, Ltd. [81].

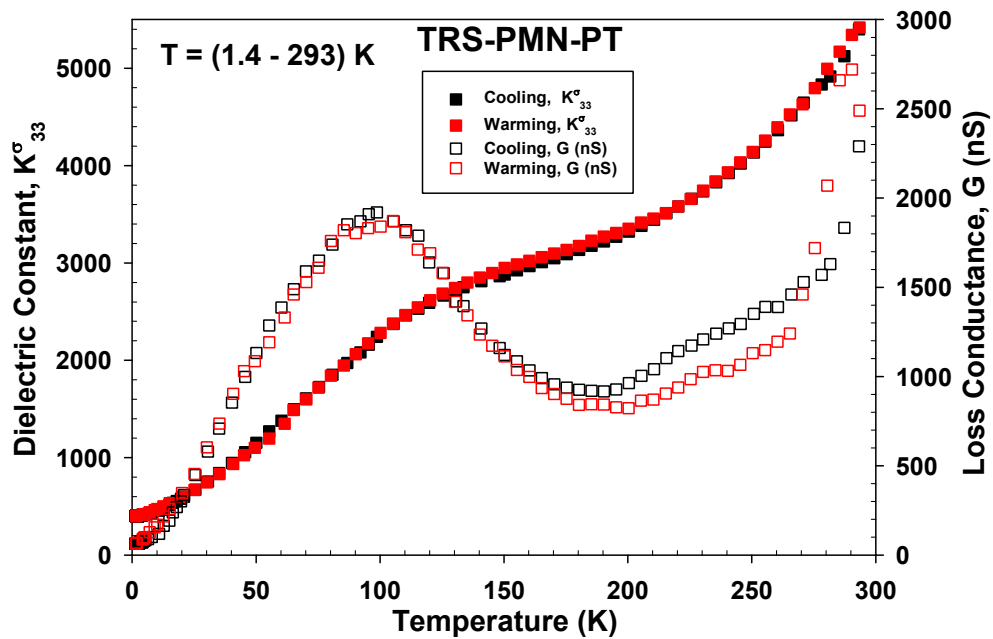


Figure 4.15: Temperature dependence of the dielectric constant and loss conductance at 1 kHz for a longitudinal PMN-PT single crystal from TRS ceramics, Inc. [80].

ference probably reflects their manufacturer’s different compositions and processing. The dielectric constants and losses have temperature dependences similar to those of the shear transducer described in the previous section, although the longitudinal values are larger.

4.4.3 PZT-5A ceramics

Two PZT-5A transducers were used for this study, a shear rectangular ($12.77 \times 9.58 \times 1.78 \text{ mm}^3$) transducer and a longitudinal (circular disc with a diameter 10.12 mm and thickness 0.42 mm) transducer from Boston Piezo Optics, Inc. [81]. Figures 4.16 and 4.17 show the temperature dependence of the dielectric constant and loss conductance for the shear and longitudinal transducers, respectively. The cooling and warming rates had a small effect on both properties above 90 K for the longitudinal transducer. The dielectric constant for both transducers decreases nearly linearly over the whole temperature range. Both transducers have two relaxation peaks over this temperature range.

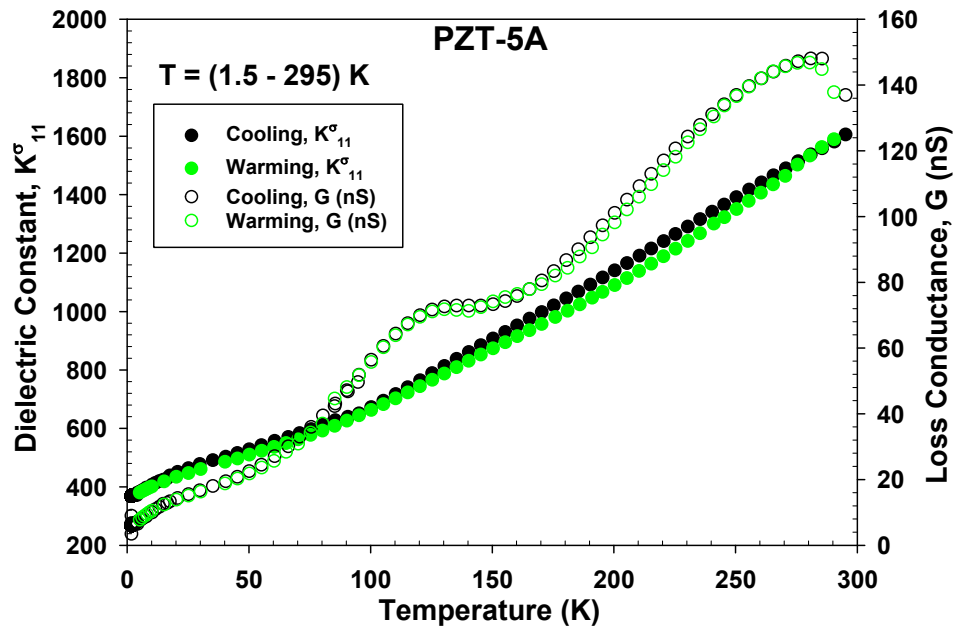


Figure 4.16: Temperature dependence of the dielectric constant and loss conductance for a shear PZT-5A crystal at 1 kHz, from room temperature to 1.4 K.

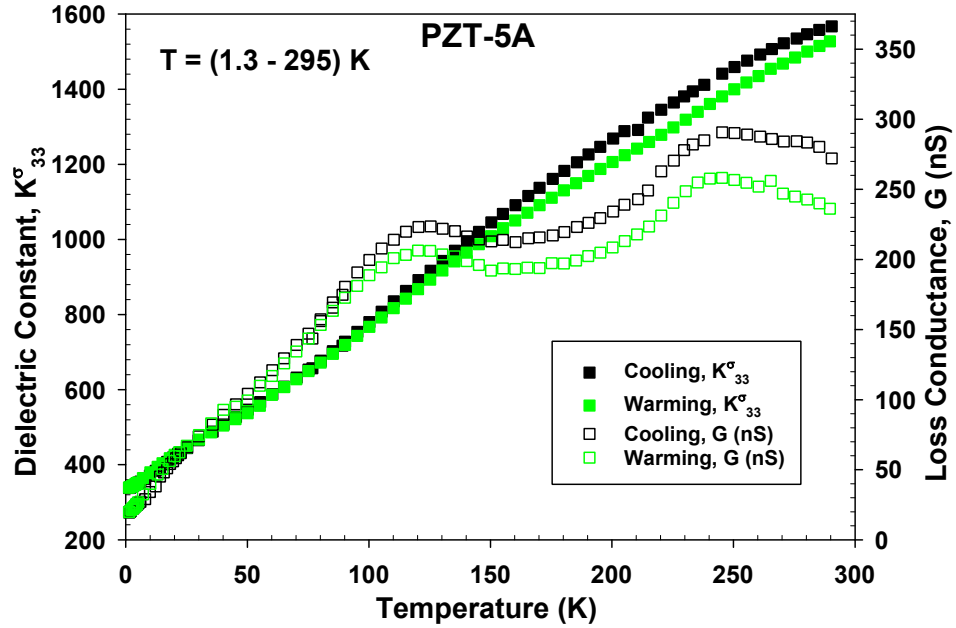


Figure 4.17: Temperature dependence of the dielectric constant and loss conductance for a longitudinal PZT-5A crystal at 1 kHz, from room temperature to 1.4 K.

4.5 The voltage constants g_{15} and g_{33}

When a mechanical stress is applied to a piezoelectric transducer, it produces an electric field, which generates a voltage across the transducer. The corresponding piezoelectric voltage constant is

$$g_{ij} = \frac{d_{ij}}{\varepsilon_0 K_{ij}}. \quad (4.1)$$

The voltage constant is useful in evaluating the suitability of a material for sensing applications [36] in which the output voltage is recorded.

4.5.1 LiNbO₃ single crystal

The shear voltage constant g_{15} of a material is calculated from shear piezoelectric coefficient d_{15} , and the dielectric constant, K_{11}^σ . This is shown for LiNbO₃ in Figure 4.18, using the d_{15} data of Figure 4.1 and the K_{11}^σ data of Figure 4.12. At room temperature, Warner *et al.* [49] calculated a shear voltage constant of 9.1×10^{-2} (mV/N), exactly the same as our value of 9.1×10^{-2} (mV/N).

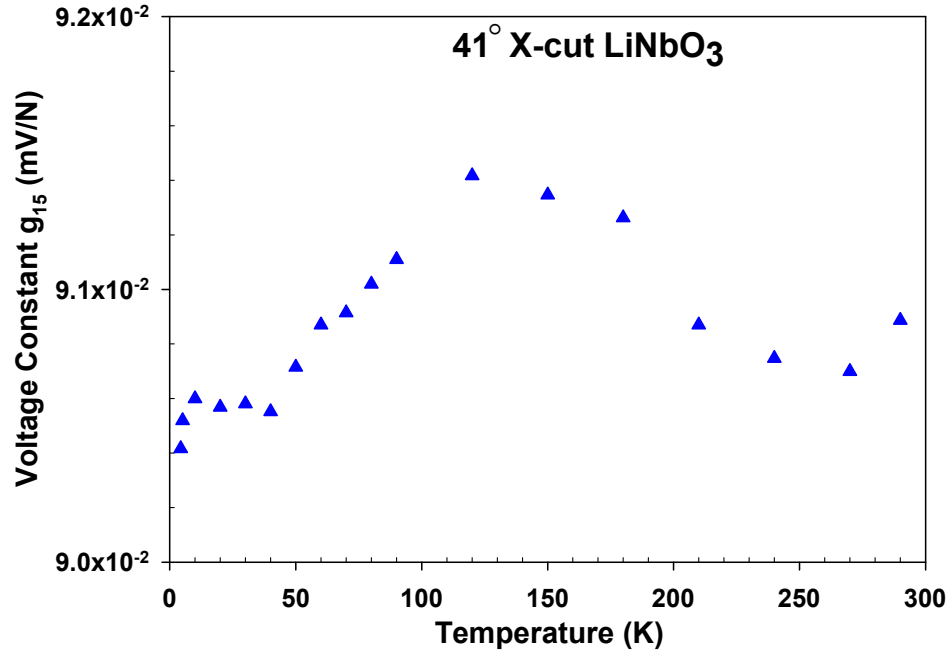


Figure 4.18: Temperature dependence of the shear piezoelectric voltage coefficient g_{15} of a LiNbO₃ transducer.

4.5.2 PMN-PT single crystal

Figures 4.5, 4.9, 4.13 and 4.15 show the temperature dependence of the shear and longitudinal piezoelectric and dielectric coefficients for PMN-PT single crystal. Figure 4.19 shows the corresponding voltage constants g_{15} and g_{33} for PMN-PT crystals. The shear voltage constant g_{15} increases from 1.5 K to 60 K and above 60 K it decreases slowly, while g_{33} increases between 50 and 310 K. The largest values of g_{15} are at temperatures of 50 to 70 K, which implies that PMN-PT may be suitable for sensing applications in this temperature range. At room temperature, our measured shear and longitudinal piezoelectric voltage constants g_{15} and g_{33} are 14.1×10^{-2} (mV/N) and 2.9×10^{-2} (mV/N), respectively.

4.5.3 PZT-5A ceramic

Figure 4.7, 4.11, 4.16 and 4.17 show the temperature dependence of the shear and longitudinal piezoelectric and dielectric coefficients of PZT-5A ceramics. Figure 4.20 shows the corresponding temperature dependence of the voltage constants g_{15} and g_{33} , which vary slightly with temperature. At room temperature, the manufacturer's quoted values of g_{15} and g_{33} are 3.82×10^{-2} mV/N and 2.48×10^{-2} mV/N, consistent with our values of 4.2×10^{-2} mV/N and 2.5×10^{-2} mV/N, respectively.

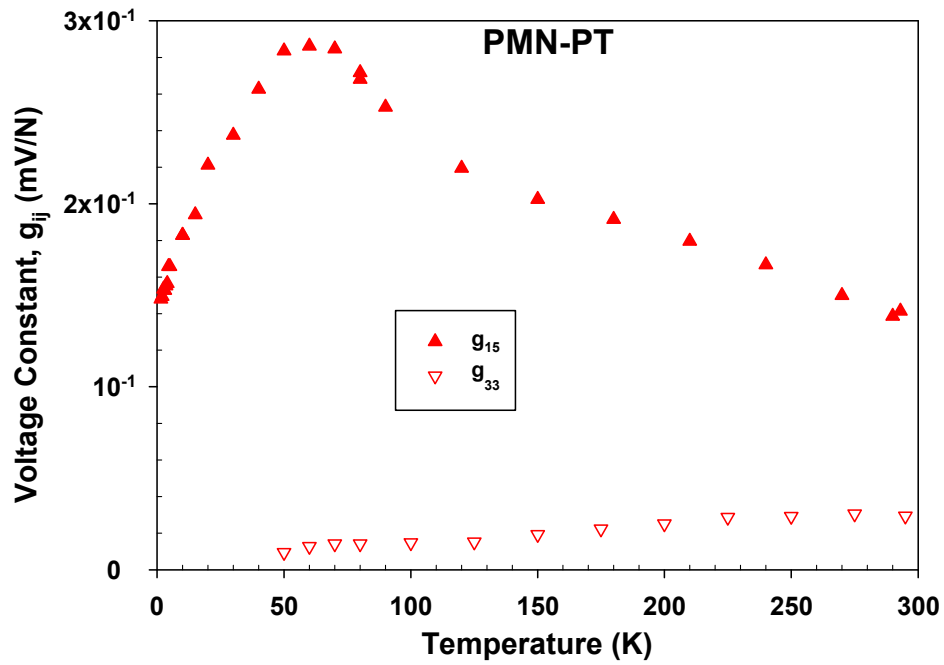


Figure 4.19: Temperature dependence of the piezoelectric voltage constants g_{15} and g_{33} of PMN-PT transducers.

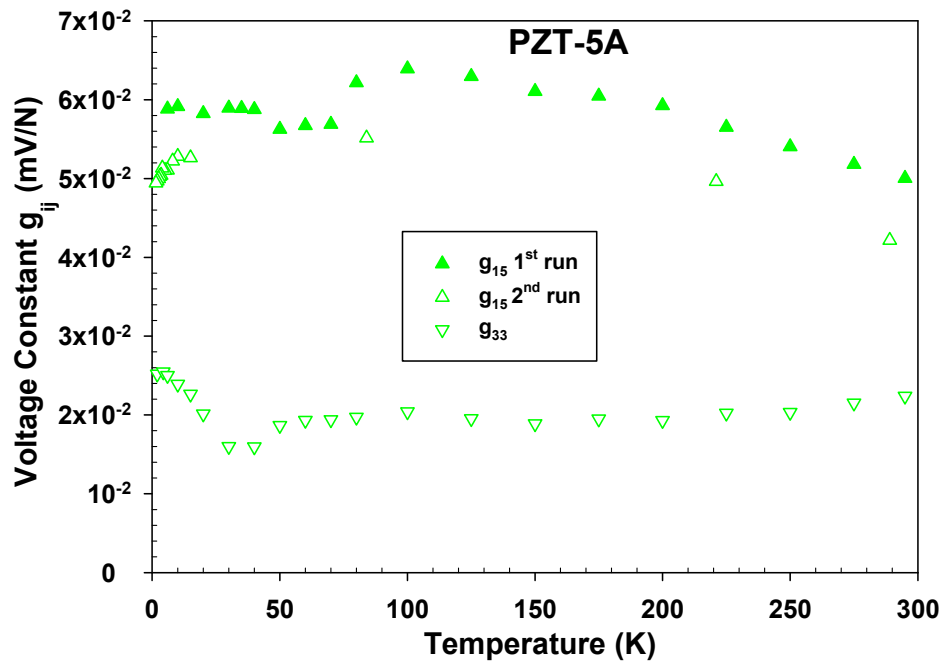


Figure 4.20: Temperature dependence of the piezoelectric voltage constants g_{15} and g_{33} of PZT-5A transducers.

4.6 Discussion

For positioning applications, the displacement range is determined by the actuator's displacement per volt ($\frac{\Delta x}{\Delta V}$) and by the maximum voltage (V_{max}) that can be applied without depoling or damaging the actuator. For a single shear transducer, $\frac{\Delta x}{\Delta V} = d_{15}$, and for the stack of three transducers $\frac{\Delta x}{\Delta V} = 3d_{15}$. Materials like PMN-PT and PZT are widely used because of their large piezoelectric coefficients, but these reflect extrinsic mechanics that freeze out at low temperatures, greatly reducing the displacement range. The piezoelectric coefficients of LiNbO_3 are much smaller, but are intrinsic and decrease only slightly at low temperatures.

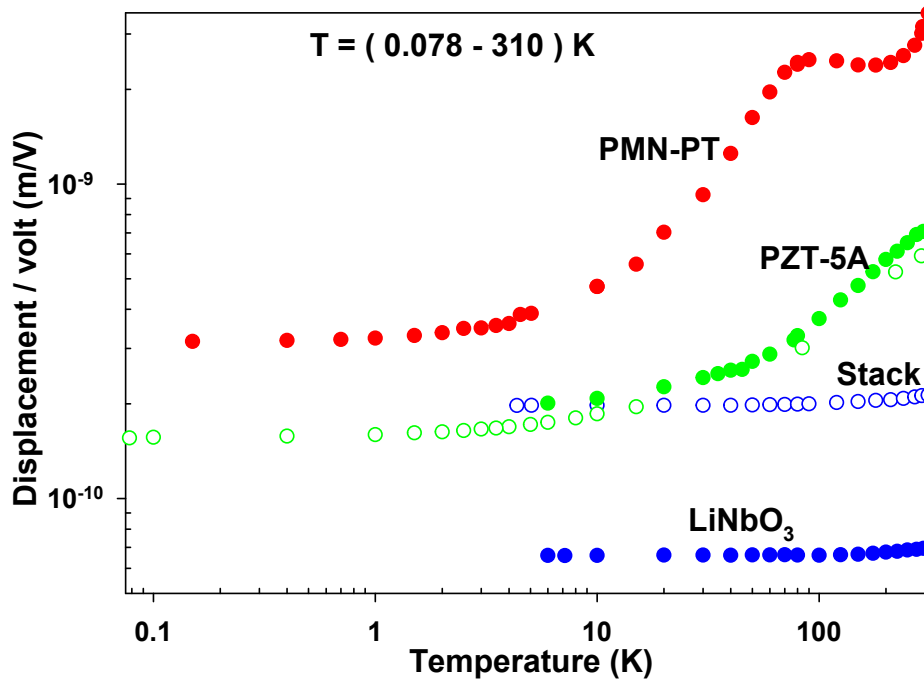


Figure 4.21: Comparison of shear piezoelectric displacement per volt for different transducers, on logarithmic scales.

Figure 4.21 compares the shear displacement per volt for PMN-PT, PZT-5A and LiNbO_3 transducers and a stack of three LiNbO_3 transducers. The data extend over a wide temperature range, from 78 mK to 310 K, and so are plotted on logarithmic temperature and displacement scales. Figure 4.22 shows the same comparison on linear scales. At room temperature, the displacement/volt of the shear transducers varies by a factor of 46, from 69.4×10^{-12} m/V for LiNbO_3 to 3200×10^{-12} m/V for PMN-PT. At the lowest temperatures, it varies by less than a factor of 5, from

65.9×10^{-12} m/V for LiNbO_3 to 315.8×10^{-12} m/V for PMN-PT. These figures clearly show that although LiNbO_3 has the smallest value at all temperatures, the differences at low temperature are small. The stack of three LiNbO_3 transducers actually has a larger displacement than a PZT-5A transducer below 20 K.

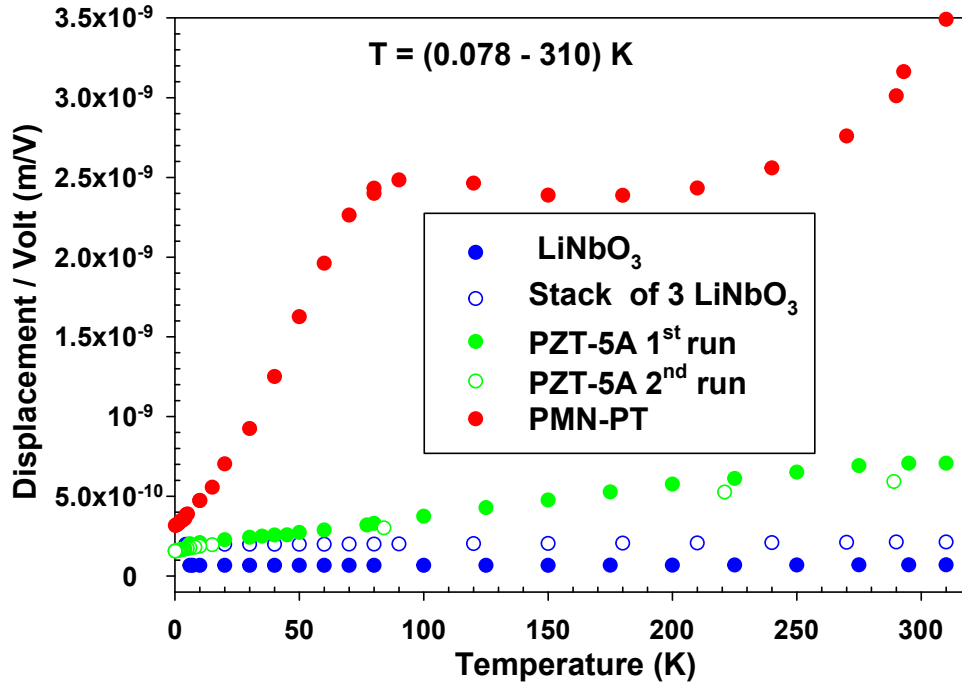


Figure 4.22: Comparison of shear piezoelectric displacement per volt for different transducers, on linear scales.

Lithium niobate (LiNbO_3) has a very high ferroelectric Curie temperature (1210 °C) and its relatively small piezoelectric coefficients (d_{ij}) and weak temperature dependence reflect the intrinsic behavior of single domain crystals [22]. The small changes in the coefficient d_{15} above 100 K may result from thermal expansion of the crystal.

In case of the other single crystals, PMN-PT, the low Curie temperature and extrinsic effects due to ferroelectric domain walls result in a strong temperature dependence. As shown in Figure 4.6, this dependence extends to temperatures as low as 150 mK. This means that extrinsic piezoelectric effects do not freeze out completely, even at 150 mK, and suggests that there must be mobile defects with a very wide range of characteristic energies. PZT-5A shows similar behavior at low temperatures (e.g. Figure 4.8) which may reflect similar extrinsic piezoelectric mechanisms.

The temperature dependence of d_{15} below 4 K has implications for precise shear stress measurements in cryogenic experiments. For example, shear modulus mea-

measurements in helium crystals between 20 mK and 2 K [11, 12] assumed that d_{15} of PZT-5A was constant, but the data in Figure 4.8 shows that it decreases by about 5% in this temperature range. In LiNbO₃, on the other hand, d_{15} is essentially constant below 10 K, making it potentially a better choice for precision applications at low temperatures.

When choosing a piezoelectric actuator, its displacement per volt is an important parameter but, if large displacements are needed, the maximum voltage that can be applied, V_{max} , is also important. This maximum voltage is chosen to avoid depolarization or other damage to the transducer. At room temperature, the manufacturers of the shear transducers studied in these experiments on LiNbO₃ gives a maximum voltage (electric field) of 250 V (1000 V/mm) for LiNbO₃. However, researchers have applied much higher fields (up to 20,000 V/mm) to LiNbO₃ without damage. For PZT-5A, the manufacturer gives maximum voltages (fields) of 400 V (250 V/mm). For PMN-PT the maximum values are 150 V (150 V/mm).

At cryogenic temperatures, domain walls and other defects that affect piezoelectric properties are much less mobile. This means that, in some materials, higher fields can be applied without depolarizing the transducer. However, on one occasion applying 150 V to PMN-PT damaged it, so we limited the voltage to lower values in all subsequent measurements.

We can estimate the maximum shear displacement of each transducer at cryogenic temperatures by assuming $V_{max} = 500$ V (LiNbO₃), 300 V (PZT) and 150 V (PMN-PT). For single transducers, this gives maximum displacements at the lowest temperatures of 33 nm (LiNbO₃), 47 nm (PZT-5A) and 47 nm (PMN-PT). It is clear that there is very little difference between the maximum displacements that can be achieved with the three materials at low temperature.

For larger shear displacements, individual transducers can be combined to make an actuator stack. The stack of three LiNbO₃ transducers described in section 4.2.1 would have a maximum displacement (at 500 V) of 99 nm, more than twice that of the PZT-5A and PMN-PT transducers. Of course these materials can also be stacked to generate large displacement, but the lengths of such actuator stacks are significantly larger because of the greater thickness (1 mm or thicker) needed to pole PZT-5A and PMN-PT shear transducers. Lithium niobate shear transducers as thin as 0.1 mm are available, allowing compact stacks with large displacements to be constructed.

Most positioning applications involve longitudinal, not shear actuators, and the temperature dependences of the longitudinal piezoelectric coefficient d_{33} of PMN-PT and PZT-5A transducers are compared in Figures 4.23 and 4.24. Their room temperature coefficients differ by almost a factor of 5, but at 50 K they are almost

the same.

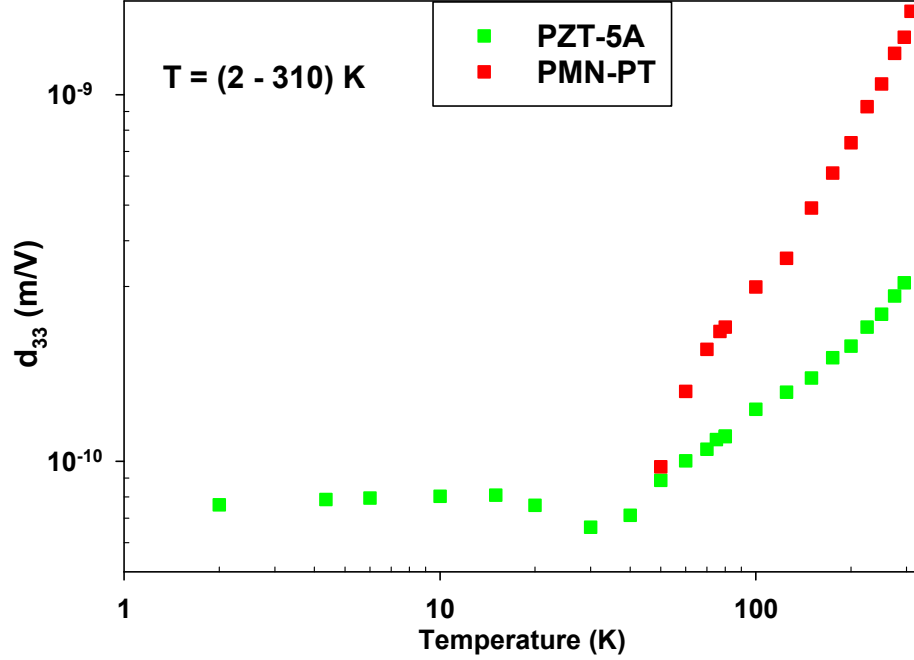


Figure 4.23: Comparison of the longitudinal piezoelectric coefficient d_{33} of PMN-PT and PZT-5A transducers on logarithmic scales.

For sensor applications in which the output signal is a voltage, the sensitivity of the sensor is determined by the piezoelectric voltage coefficients $g_{ij} = \left(\frac{mV}{N}\right)$. Because both the piezoelectric coefficients, d_{ij} , and the dielectric coefficients, K_{ij} , decrease with temperature, g_{ij} , which is proportional to the ratio $\frac{d_{ij}}{K_{ij}}$, has much weaker temperature dependence than d_{ij} , as shown in Figures 4.18 to 4.20. Figures 4.25 and 4.26 compare the values of the shear coefficients g_{15} and the longitudinal coefficients g_{33} for the different materials. PZT-5A has the lowest g_{15} value and PMN-PT has the highest g_{15} value at all temperatures. For both LiNbO_3 and PZT-5A, g_{15} is almost independent of temperature but for PMN-PT it has a maximum value around 60 K. The longitudinal voltage constant g_{33} is comparable for PMN-PT and PZT-5A, although the data at low temperature may not be reliable because of friction caused by the clamping magnets.

Figure 4.25 suggests that PMN-PT is the best choice (has the largest sensitivity) for shear cryogenic sensors, although LiNbO_3 may be preferred if a constant sensitivity is needed. The relative sensitivities of the three materials are roughly the same at the highest and lowest temperatures. For longitudinal sensors, PMN-PT and PZT-5A have comparable sensitivities.

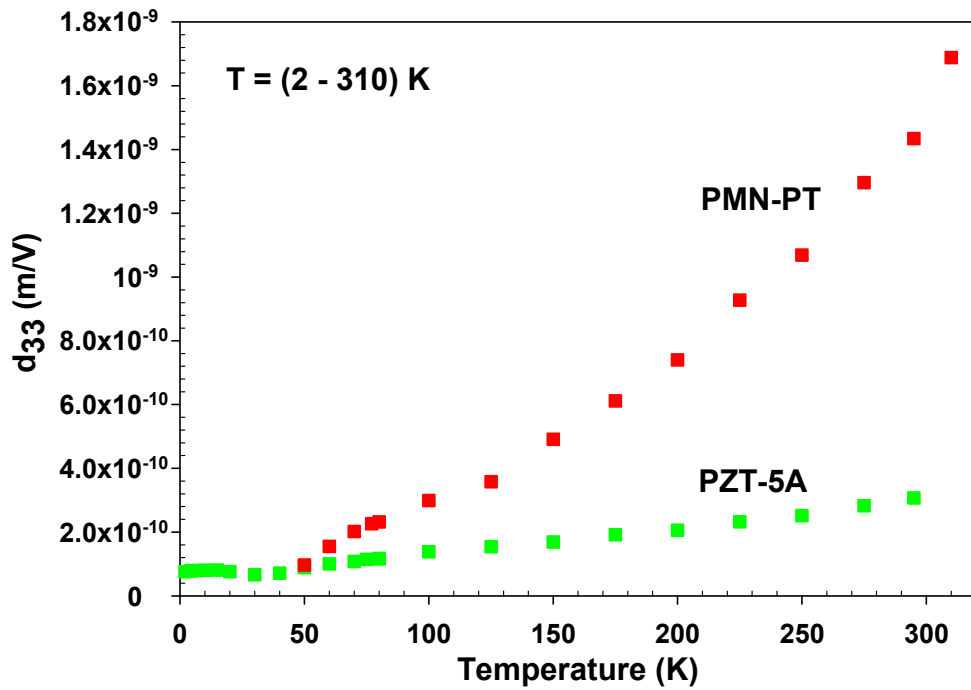


Figure 4.24: Comparison of the longitudinal piezoelectric coefficient d_{33} of PMN-PT and PZT-5A transducers on linear scales.

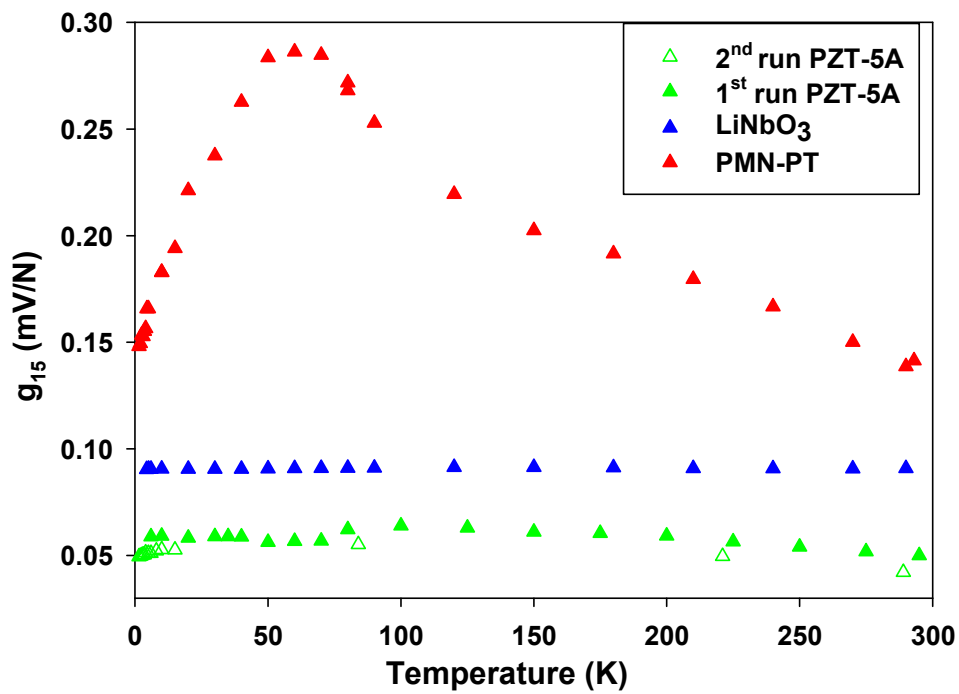


Figure 4.25: Comparison of temperature dependence of the shear piezoelectric voltage coefficient g_{15} of LiNbO₃, PMN-PT and PZT-5A transducers.

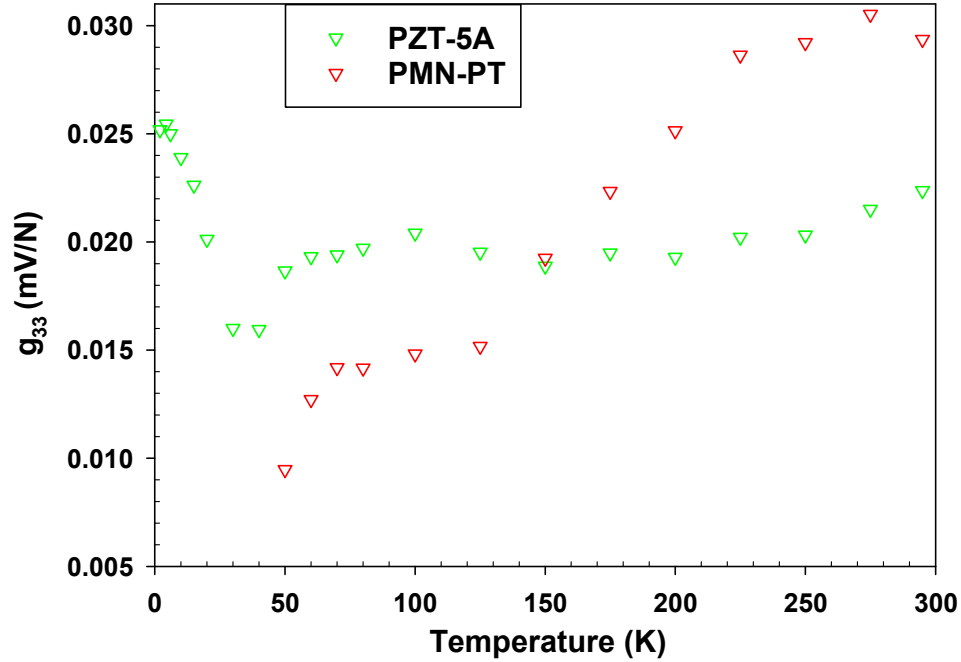


Figure 4.26: Comparison of temperature dependence of longitudinal piezoelectric voltage coefficient g_{33} of PMN-PT and PZT-5A transducers.

However, g_{15} and g_{33} give the transducer's sensitivity only if the device used to record the voltage output is ideal, i.e. has infinite input impedance R . For real devices, the input impedance is finite. For example, $R = 1 \text{ M}\Omega$ for typical oscilloscopes and $R = 50 \text{ }\Omega$ for radio frequency (RF) amplifiers used in ultrasonics. This finite impedance drains charge from the piezoelectric sensor, reducing its output voltages for long times or low frequencies. Since the transducer is basically a capacitor with $C = \frac{\epsilon_0 K A}{t}$, the relevant time constant is that for an R-C circuit, $\tau = RC$, with a corresponding characteristic frequency $\omega_c = \frac{1}{RC}$. For measurements at frequencies well above ω_c , the full voltage generated by the transducer is measured. At frequencies well below ω_c , the measured voltage is reduced by a factor of $\frac{\omega}{\omega_c} = \omega\tau$. Since τ is proportional to C , i.e. proportional to K_{ij} of the transducer, the crossover frequency ω_c will increase at low temperatures where K_{ij} is smaller, reducing the useful frequency range for piezoelectric voltage sensors.

For example, for the PMN-PT transducer at room temperature, $C = 2.2 \text{ nF}$ so the crossover frequency with an input impedance of $1 \text{ M}\Omega$ is $f_c = \frac{\omega_c}{2\pi} = 72 \text{ Hz}$. For example, an oscilloscope could be used to measure the output with full sensitivity for frequencies above 100 Hz . If a $50 \text{ }\Omega$ input amplifier was used, then $f_c = 1.4$

MHz, and the measured output would be reduced below about 2 MHz, (by a factor of more than 10,000 at 100 Hz). At the lowest temperatures, the PMN-PT transducer's capacitance is a factor of 10 smaller, so the corresponding frequencies ω_c are 10 times larger, limiting its use at low frequencies.

The corresponding frequencies for PZT transducers are similar, but for LiNbO₃ they are higher, reflecting lithium niobate's smaller dielectric constant. This can be partially compensated by using thinner transducers to increase their capacitance, something not practical for PMN-PT and PZT shear transducers. For the 41° X-cut (pure shear) LiNbO₃ transducer with thickness 0.26 mm, its capacitance is 0.29 nF, decreasing slightly to 0.27 nF at low temperature. The corresponding frequencies at room temperature are $f_c = 549$ Hz for $R = 1$ M Ω and 11 MHz for $R = 50$ Ω . These change only slightly at low temperatures, to 589 Hz and 11.8 MHz, respectively.

In choosing appropriate piezoelectric sensors, it is important to consider their dielectric constants (capacitances), the input impedance of the measurement circuit, and the frequency of the signal being measured. All three materials would be effective cryogenic ultrasonics sensors (and both PZT and LiNbO₃ have been used at low temperatures), but it would be challenging to use any of them at frequencies below 1 kHz, since a very high input impedance would be needed. Given its nearly constant sensitivity g_{15} and dielectric constant, LiNbO₃ is probably the best sensor choice for precise measurements that cover a wide temperature range.

For low frequency sensor applications, using current pre-amplifiers rather than voltage pre-amplifiers avoids such frequency issues. However, the relevant sensitivity parameter to select a suitable transducer is then the coefficient d_{ij} , not g_{ij} .

The room temperature and their lowest temperature values of the shear and longitudinal piezoelectric coefficients and voltage constants of the three materials are presented in Table 4.1.

Table 4.1: Experimental values of the shear and longitudinal piezoelectric coefficients and voltage constants of the three materials at room temperature and at their lowest temperatures

Property (unit)	Corrected value at room temperature	Corrected value at lowest temperature
Single LiNbO ₃ transducer		
d_{15} ($\times 10^{-12}$ m/V)	69.4	65.9 (6 K)
g_{15} ($\times 10^{-3}$ mV/N)	89.0	90.5 (6 K)
Stack of three LiNbO ₃ transducers		
$3 \times d_{15}$ ($\times 10^{-12}$ m/V)	212.9	197.4 (4 K)
PMN-PT transducer		
d_{15} ($\times 10^{-12}$ m/V)	3200	315.8 (150 mK)
d_{33} ($\times 10^{-12}$ m/V)	1700	96.7 (50 K)
g_{15} ($\times 10^{-3}$ mV/N)	141.4	148.1 (1.5 K)
g_{33} ($\times 10^{-3}$ mV/N)	29.4	9.5 (50 K)
PZT-5A transducer		
d_{15} ($\times 10^{-12}$ m/V)	591.2	155.8 (78 mK)
d_{33} ($\times 10^{-12}$ m/V)	307	76 (2 K)
g_{15} ($\times 10^{-3}$ mV/N)	42.2	49.4 (1.5 K)
g_{33} ($\times 10^{-3}$ mV/N)	25.2	22.4 (2 K).

The dielectric properties of the three materials have their origins in the same electric dipoles and domains that determine the piezoelectric properties. The close relationship between them is illustrated by the voltage coefficients, g_{ij} , described above. Figures 4.27 to 4.30 compare the temperature dependence of the dielectric constant, K_{11}^σ , and corresponding loss tangent, $\tan \delta$, of the three materials. Figure 4.27 shows the dielectric constant and loss tangent for the three shear transducers. The corresponding log-log plots are shown in Figure 4.28. PMN-PT has the highest dielectric constant above 40 K. Below 40 K, PZT-5A has a higher value but both are strongly temperature dependent. Lithium niobate has a much smaller, but nearly temperature independent dielectric constant.

The main feature in the loss tangent of PMN-PT is a very large loss peak around 70 K. PZT-5A appears to have two smaller loss peaks around 120 K and 270 K. Below 10 K the loss in each material approaches a small constant value, but the loss remains finite at the lowest temperatures.

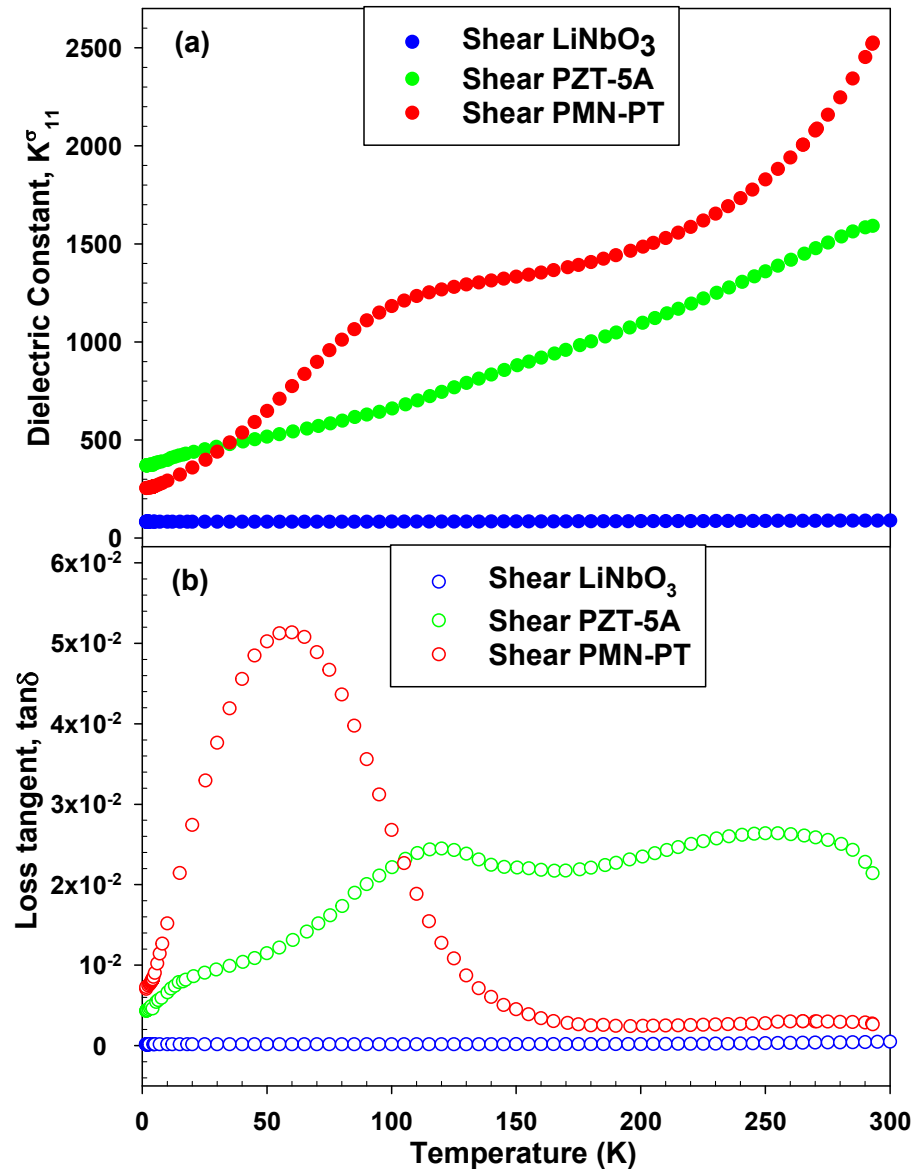


Figure 4.27: Comparison of the temperature dependence of the dielectric constant and loss tangent for shear LiNbO₃, PMN-PT and PZT-5A crystals on linear scales.

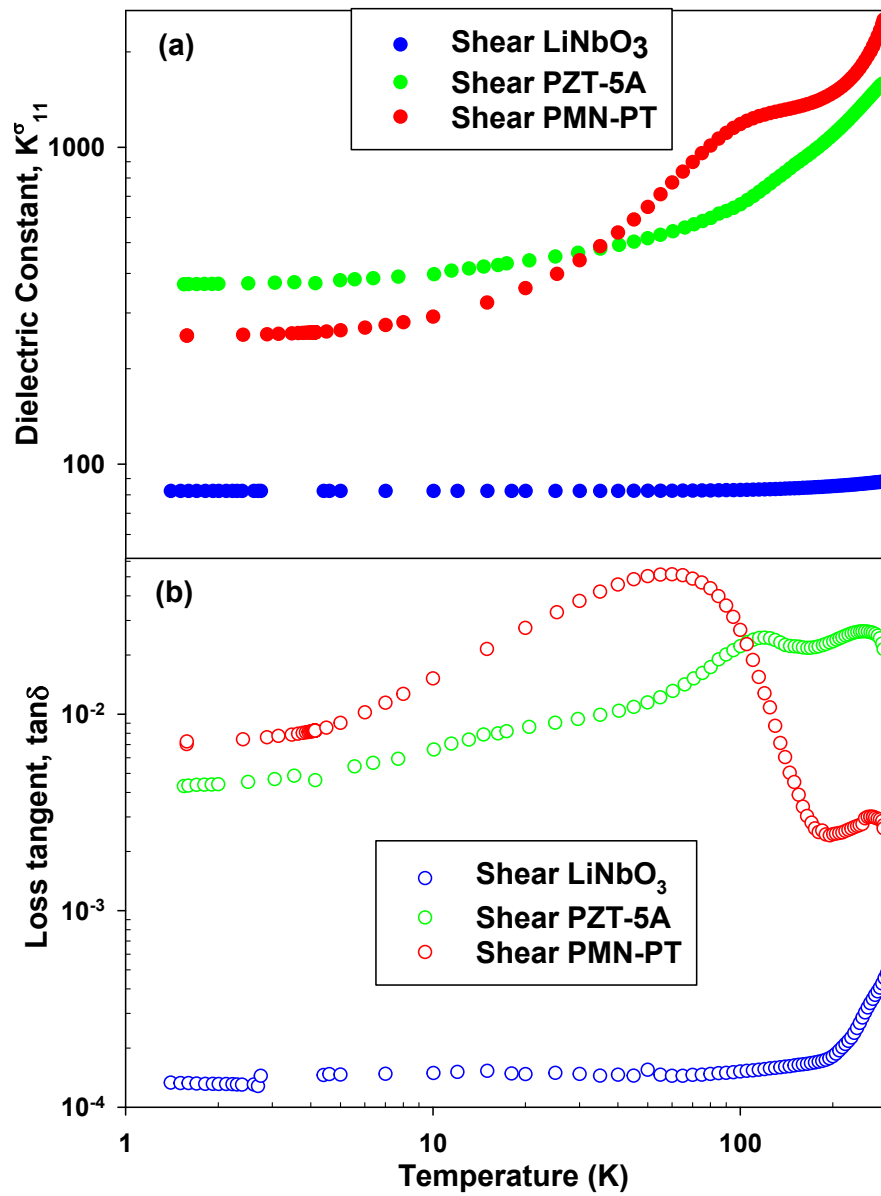


Figure 4.28: Comparison of the temperature dependence of the dielectric constant and loss tangent for shear LiNbO_3 , PMN-PT and PZT-5A crystals on logarithmic scales.

Figures 4.29 and 4.30 show the dielectric constant (K_{33}^{σ}) and loss tangent, $\tan \delta$, for PMN-PT and PZT-5A longitudinal transducers on linear and log scales. PMN-PT has the highest dielectric constant and loss tangent at all temperatures. The dielectric constants decrease with temperature for both transducers, by a factor of 14 for PMN-PT and 5 for PZT-5A at the lowest temperature. In this temperature range, PMN-PT has a single large loss peak at 90 K, and PZT-5A appears to have two smaller peaks around 120 K and 240 K. The dielectric properties of the shear and longitudinal transducers are quite similar, for both PMN-PT and PZT-5A.

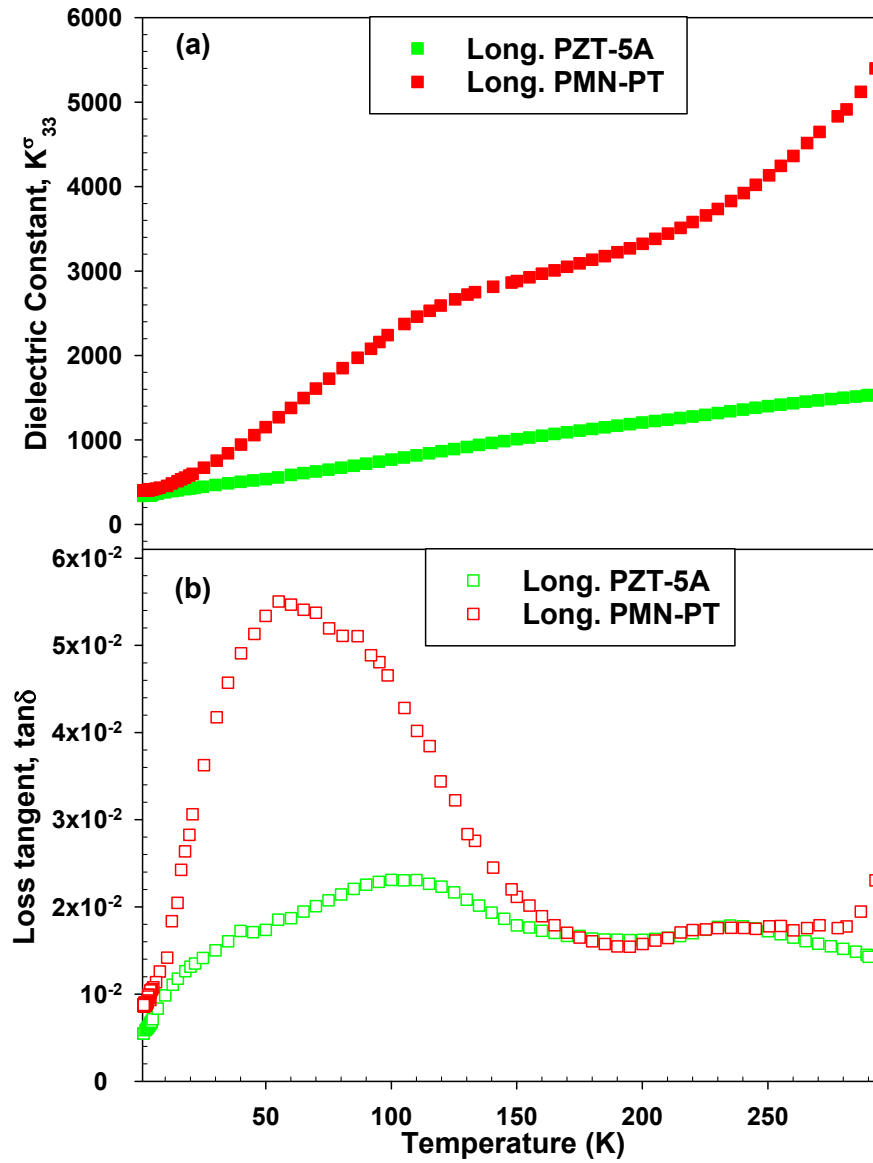


Figure 4.29: Comparison of the temperature dependence of the dielectric constant and loss tangent for longitudinal PMN-PT and PZT-5A crystals on linear scales.

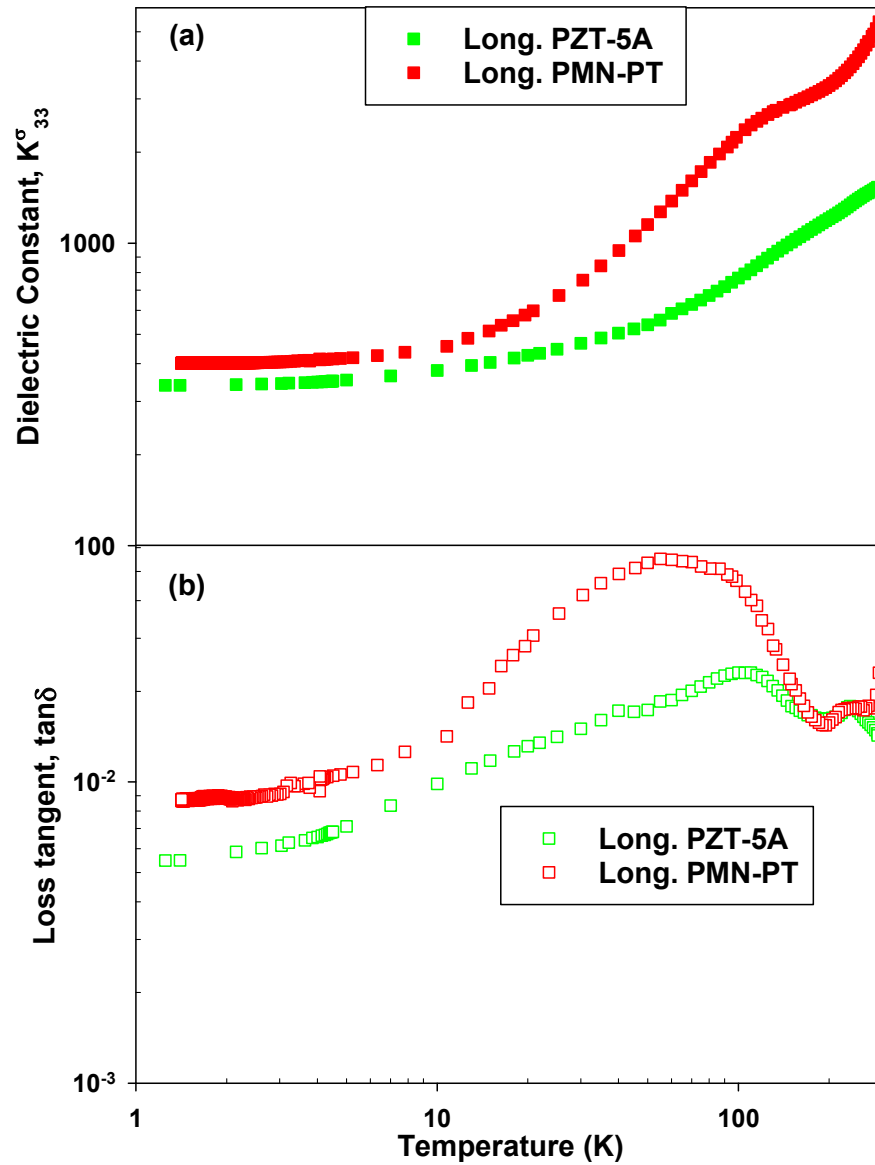


Figure 4.30: Comparison of the temperature dependence of the dielectric constant and loss tangent for longitudinal PMN-PT and PZT-5A crystals on logarithmic scales.

The largest values of the dielectric constants occur at the highest temperatures, and the smallest values are at the lowest temperatures. These are summarized in table 4.2.

Table 4.2: Experimental values of the dielectric constant of the three materials at room temperature and at their lowest temperatures

Property	value at room temperature	value at lowest temperature
Single LiNbO ₃ transducer		
K_{11}^{σ}	88	82.2 (1.4 K)
PMN-PT transducer		
K_{11}^{σ}	2550	254 (1.56 K)
K_{33}^{σ} (TRS)	5418	401 (1.4 K)
K_{33}^{σ} (APC)	4460	360 (1.56 K)
PZT-5A transducer		
K_{11}^{σ}	1590	369 (1.54 K)
K_{33}^{σ}	1570	338 (1.3 K).

Chapter 5

Hysteresis and Creep Properties of Piezoelectric Materials

5.1 Introduction

The displacement of an ideal piezoelectric actuator is linear in the applied voltage, reproducible when the voltage is cycled, and does not change with time if the voltage is held constant. Real piezoelectric actuators have non-linear responses, show hysteresis when the voltage is reversed or cycled, and exhibit time dependent creep after voltage changes. These phenomena reflect changes in polarization and motion of domain boundaries, so are expected, for example, to be smaller in an intrinsic, single domain crystal like LiNbO_3 . Defect motion freezes out at low temperatures, so hysteresis and creep may be much smaller in cryogenic applications.

Hysteresis and creep are particularly important in applications where precise and reproducible positioning is needed. In some applications, e.g. mirror positioning, creep effects can be compensated for using a feedback loop to adjust the applied voltages, but this requires an additional sensor with high resolution. In applications like scanning probe microscopy, this is not possible and images are blurred or distorted [23, 25].

This chapter presents results on the influence of temperature and voltage on the hysteresis and creep properties of piezoelectric shear LiNbO_3 and PMN-PT single crystals, and PZT-5A ceramics. The goal of these measurements was to characterize piezoelectric materials for cryogenic positioning applications.

The LiNbO_3 single crystal is discussed first because it shows no hysteresis or creep behavior. The displacement vs. voltage response is linear between -150 V and + 150 V at all temperatures. Next, the other single crystal material, PMN-PT, is described. It has strongly voltage and time-dependent properties from 5 to 310 K. Finally, results

are presented for the PZT-5A ceramic. Voltage and time-dependent behavior is also observed for this material from 35 to 310 K. The hysteresis behavior is described for all the materials before presenting creep results. Hysteresis and creep are closely related. As we show in this chapter, creep is the source of the hysteresis in PMN-PT and can be regarded as the more fundamental property.

Polarization reversal or switching (domain switching) can be induced by an electric field or a mechanical load and produce ferroelectric hysteresis [43]. When an electric or mechanical load is applied, ferroelectrics can change from one spontaneously polarized state to another [83]. This phenomenon is known as domain switching. A hysteresis loop is produced when domain-wall motion, which is crucial for polarization reversal or switching [46], is not reversible. Note that these mechanisms are usually discussed for longitudinal piezoelectric materials, where the applied voltages are parallel or anti-parallel to the polarization. All the measurements in this chapter involve shear piezoelectric materials, where applied voltages are perpendicular to the polarization and their effects on domain wall motion are less obvious.

The hysteresis loops are often assumed to be symmetric, which means the positive and negative coercive fields (E_C) and remanent polarizations (P_r) are equal. Real ferroelectric hysteresis loops may not be symmetric and can be affected by many factors, such as the thickness of the samples, material composition, thermal treatment, mechanical stresses, preparation and measurement conditions [43, 46].

The change in the displacement over time, following an initial piezoelectric displacement when the drive voltage is applied is called creep. The displacement typically changes logarithmically over time [25, 84]. The same material properties, domain reversal or switching [85], are responsible for both the hysteresis and the creep behavior [69]. Experimental results are presented in the following sequence. The hysteresis and creep behavior of LiNbO₃ and PMN-PT single crystals are presented in section 5.2 and 5.3, respectively, followed by results for the ceramic PZT-5A in section 5.4.

5.2 LiNbO₃ single crystal

The 41° X-cut (pure shear) LiNbO₃ transducer described in section 4.2.1 was used for this study.

5.2.1 Hysteresis measurements

We have investigated the voltage dependence of the piezoelectric displacement between 10 K and room temperature, to look for hysteresis in lithium niobate. Figure

5.1 shows a hysteresis measurement at 10 K. The displacement at each voltage is the same when the applied voltage is increased and when it is later decreased. The black circular dots show the displacement as the applied voltage increases from -150 V to +150 V; the red circular dots show the displacement when the applied voltage decreases from +150 V back to -150 V. The black and red arrows show the respective directions.

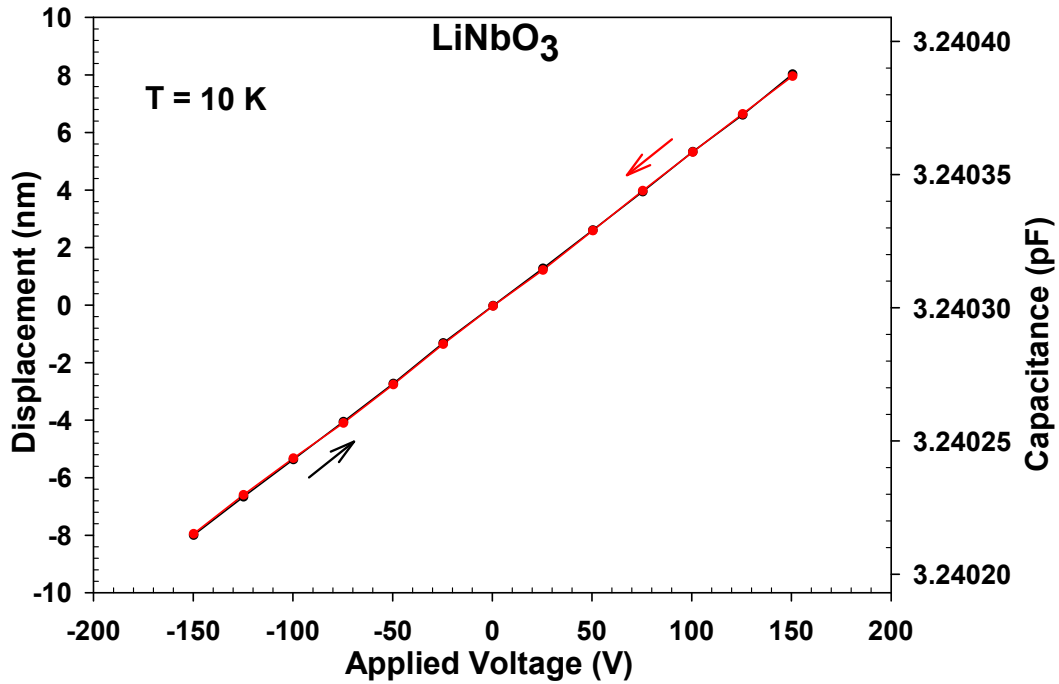


Figure 5.1: Displacement vs. applied voltage for the LiNbO_3 single crystal at 10 K. The left axis is displacement, with the corresponding measured capacitance on the right axis.

Figures 5.1 to 5.5 show the displacements with respect to applied voltage (V) for temperatures between 10 K and room temperature. The linear displacement and non-hysteretic response were observed at all temperatures. At higher temperatures, the displacement-voltage loop was measured using 5 V steps in the applied voltage (Figures 5.3 to 5.5). The total measurement time for a loop was 20 minutes and 20 seconds. Since there was no measurable hysteresis, and to save measurement time at lower temperatures, the loop times were reduced to 4 minutes 20 seconds by using 25 V steps (Figure 5.1) and to 2 minutes 20 seconds using 50 V steps (Figure 5.2). In each case, the displacement was linear and non-hysteretic. If there was thermal drift, then the displacement-voltage loops would not close, but there was no sign of such drift in these for measurements. The noise in the higher temperature displacement-

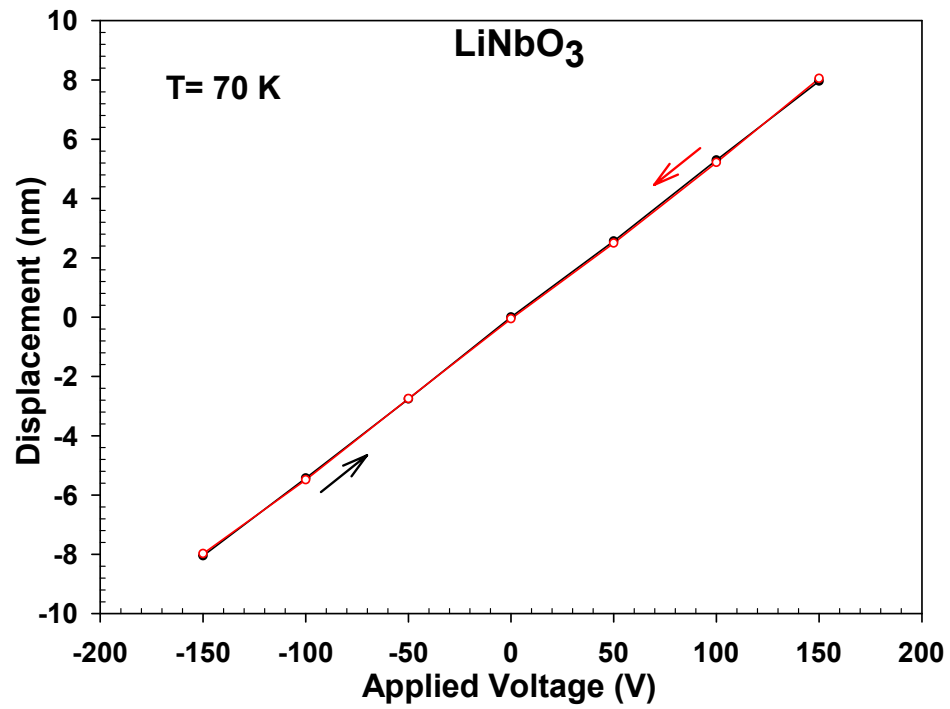


Figure 5.2: Displacement vs. applied voltage for the LiNbO₃ single crystal at 70 K.

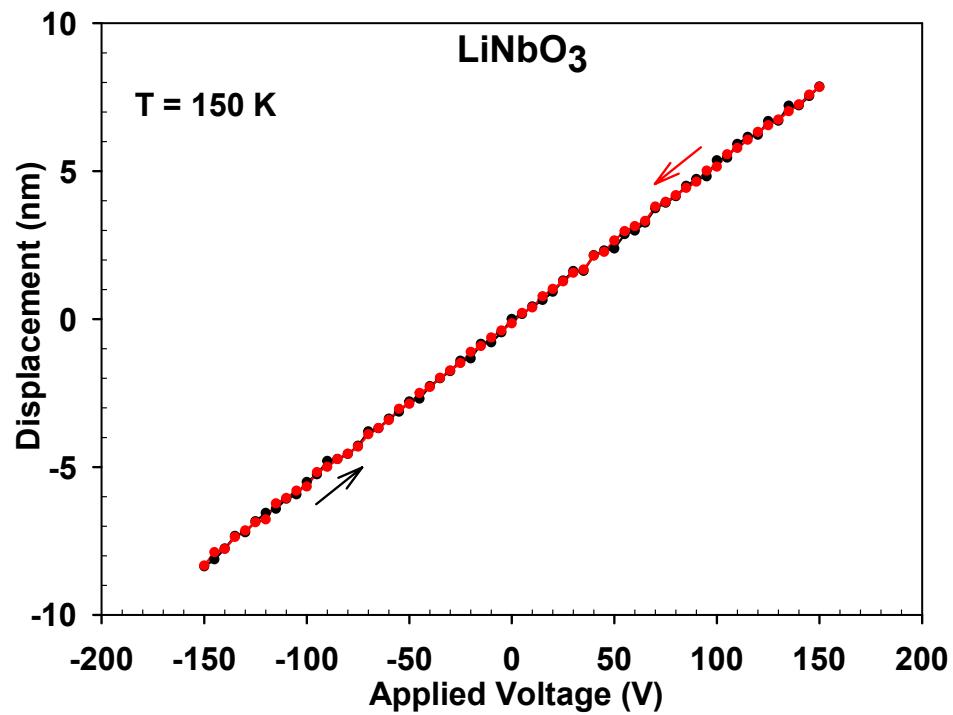


Figure 5.3: Displacement vs. applied voltage for the LiNbO₃ single crystal at 150 K.

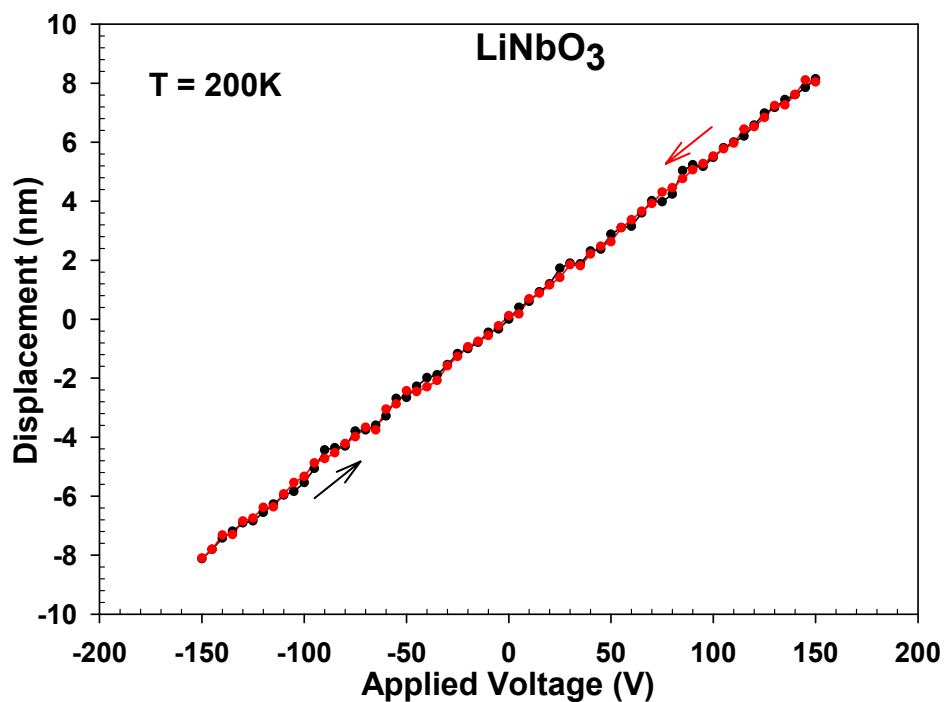


Figure 5.4: Displacement vs. applied voltage for the LiNbO₃ single crystal at 200 K.

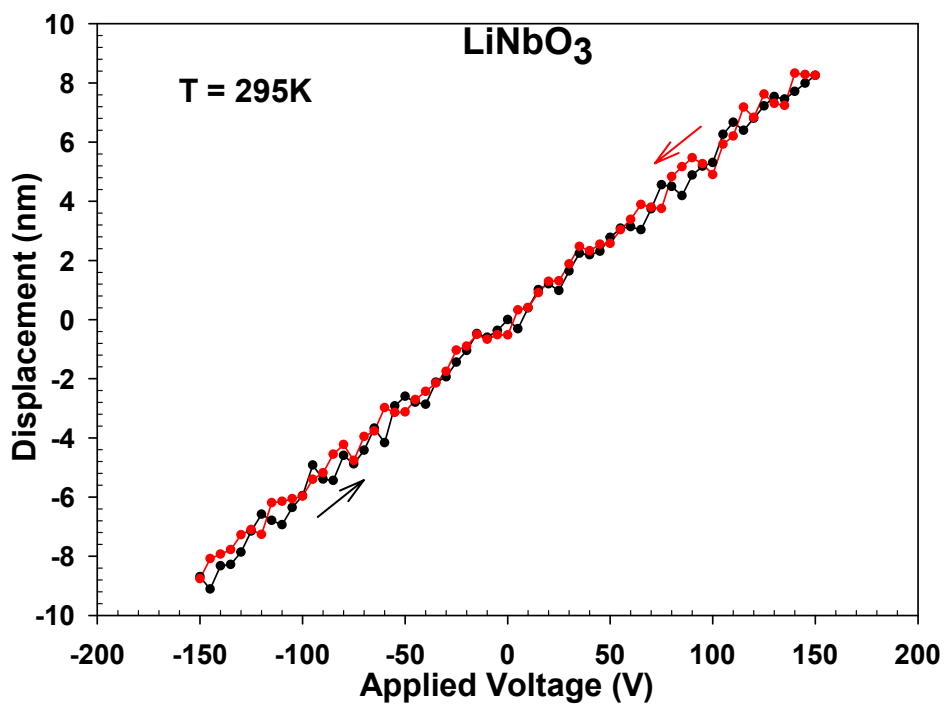


Figure 5.5: Displacement vs. applied voltage for the LiNbO₃ single crystal at 295 K.

voltage loops was due to the temperature control limitations. It did not appear at lower temperatures where the temperature control was better.

5.2.2 Creep measurements

In order to study the time-dependent behavior of the material, we also measured the displacement over time, following a change in the applied voltage from 0 to 150 V. Figures 5.6 to 5.8 show the displacements with respect to time from 10 to 150 K. At all temperatures the piezoelectric displacement was constant over the time when the applied voltage was held at 150 V. This means that there is no measurable creep in this material. The constant piezoelectric displacements in Figures 5.6 indicate there was negligible drift at 10 K. Small negative and positive thermal drift can be seen at 70 and 150 K (Figures 5.7 and 5.8) but these were not significant over 20 minutes, so the hysteresis data was not affected by thermal drift for this material.

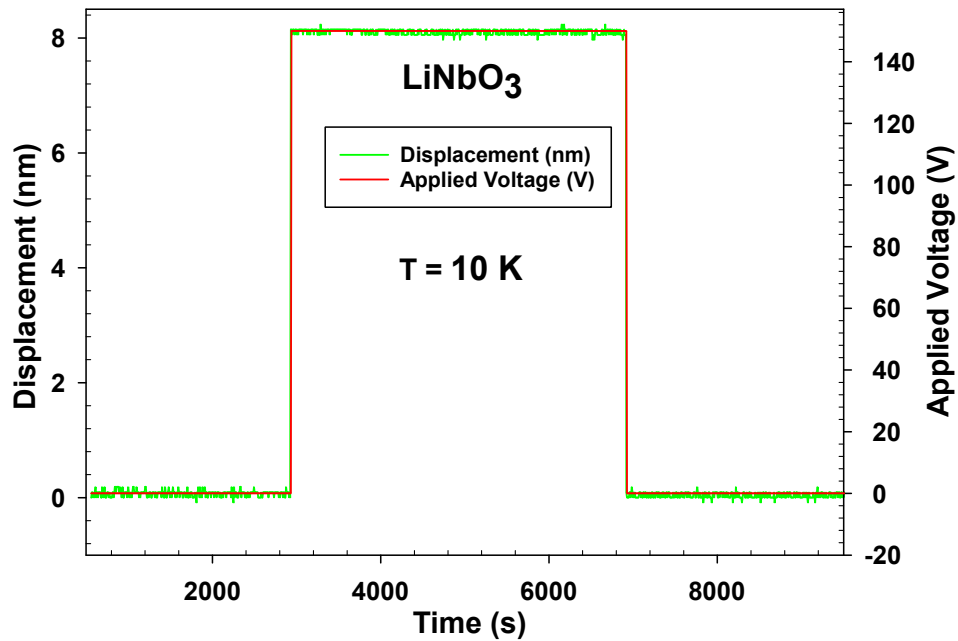


Figure 5.6: Displacement vs. time for a constant applied voltage of 150 V at 10 K.

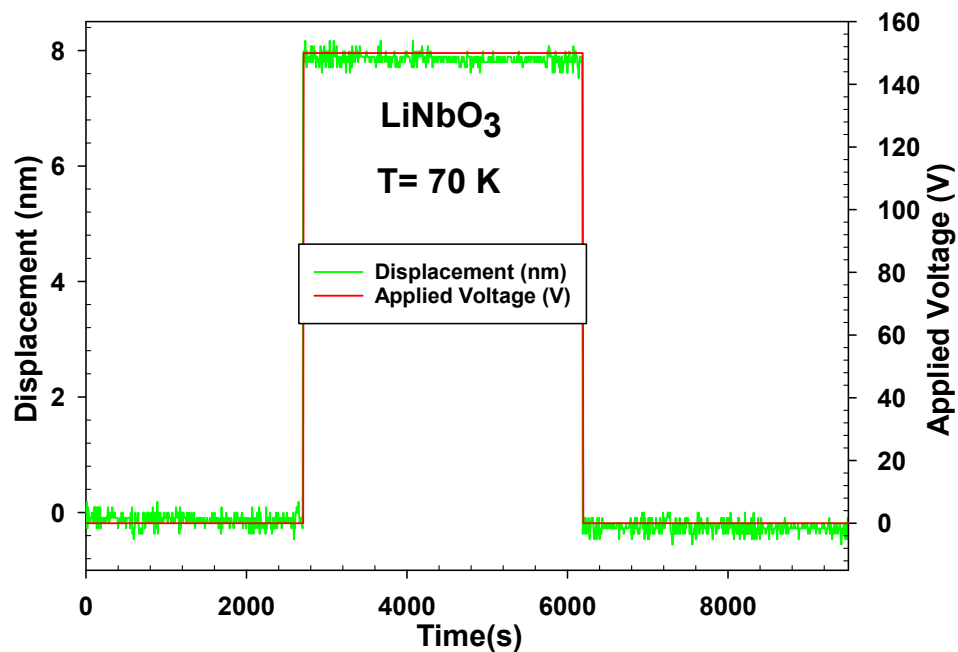


Figure 5.7: Displacement vs. time for a constant applied voltage of 150 V at 70 K. A small negative thermal drift is visible.

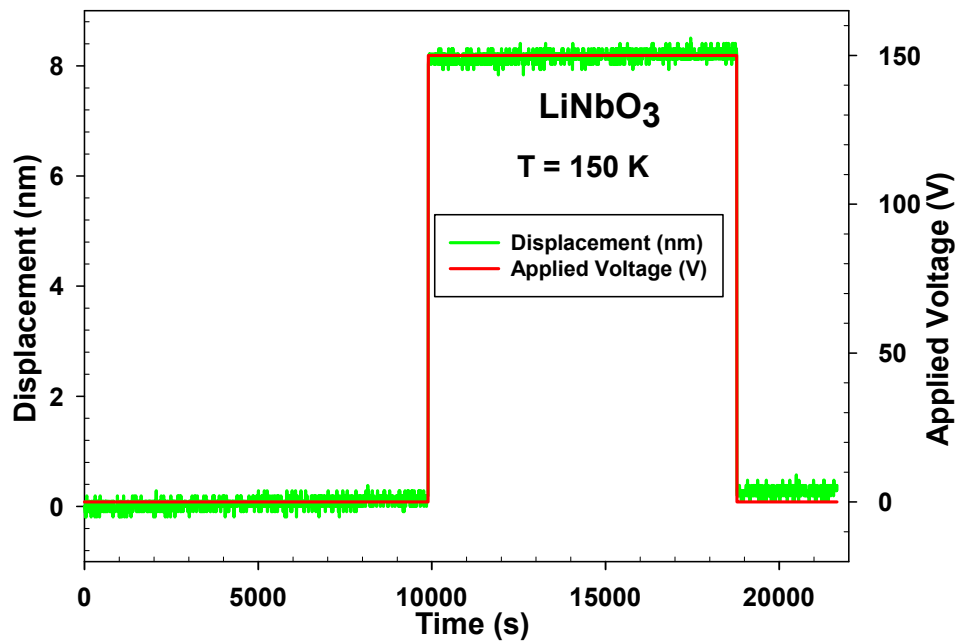


Figure 5.8: Displacement vs. time for a constant applied voltage of 150 V at 150 K. A small positive thermal drift is visible.

5.3 PMN-PT single crystal

The shear PMN-PT single crystal transducer described in section 4.2.2 was used for this study. The sequence of the creep, d_{15} and hysteresis measurements, and the timing of the voltage applied across the PMN-PT transducer at each temperature, are shown in Figure 5.9. After changing to each new temperature, the displacement was measured at 0 V for a few hours, until it was constant or showed a small, steady drift. A constant capacitance meant the transducer was in thermal equilibrium. The required wait time was a few hours but was shorter at lower temperatures, where drift and creep effects were smaller. The applied voltage was then changed from 0 to +50 V and the corresponding displacement was measured for several hours. The voltage was then changed from +50 to -50 V and the displacement was measured for another few hours. The green line in Figure 5.9 illustrates the applied voltages for creep measurements.

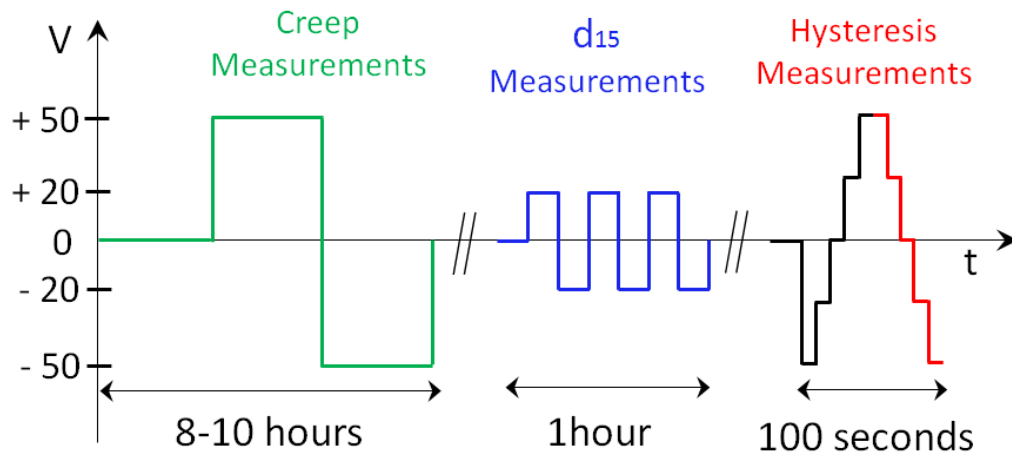


Figure 5.9: The applied voltage sequence for creep, d_{15} and hysteresis measurements on a shear PMN-PT single crystal.

After the creep measurements at this temperatures were completed, the applied voltage was set to 0 V and another program was used to apply the ± 20 V square wave used to measure d_{15} , a process that took 40 to 60 minutes (as described in section 3.2.3). The blue line in Figure 5.9 schematically shows the ± 20 V square wave used for d_{15} measurements. When the d_{15} measurements were completed, the applied voltage was set to 0 V again.

Finally, the capacitance-voltage displacement hysteresis loop was measured between -50 to +50 V at each temperature. We limited the maximum applied voltage

to ± 50 V because one of our transducers was depolarised when 150 V was applied at room temperature. To study the hysteresis, the displacement was measured at five voltages. Starting at 0 V, a voltage of -50 V was applied and measurements began. The applied voltage was changed from -50 V to a maximum positive voltage of +50 V in 25 V steps. After each change of voltage, a capacitance measurement began immediately, which involved measuring for 4 seconds and took a total of 10 seconds to complete. Once the data points were measured from -50 V to +50 V, the process was reversed to complete the hysteresis loop. The entire capacitance - voltage loop took 100 seconds. The black and red lines in Figure 5.9 show the applied voltage for capacitance-voltage hysteresis loop measurements (black for increasing voltage and red for decreasing voltage).

5.3.1 Hysteresis measurements

Figure 5.10 shows a hysteresis loop at 70 K. The hysteresis loop is traversed in the counter-clockwise (CCW) direction. This is the normal hysteresis direction or sign, which we define as positive hysteresis. Similarly, hysteresis in the clockwise (CW)

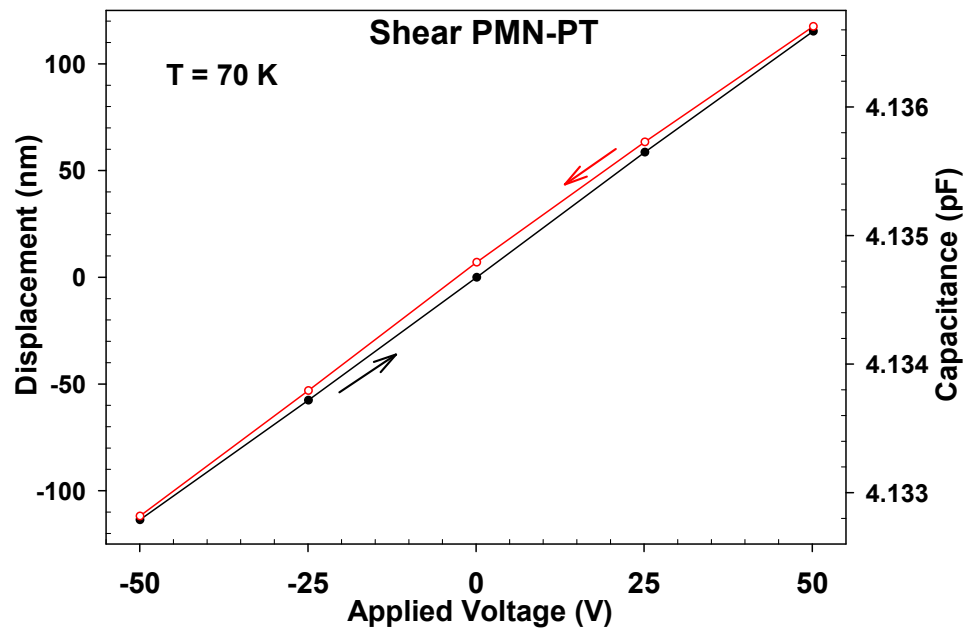


Figure 5.10: Hysteresis between displacement/capacitance and applied voltage for a PMN-PT single crystal at 70 K. Black points correspond to increasing voltages; red points to subsequent decreasing voltages.

direction is referred to as negative hysteresis. The hysteresis width is defined as the

difference between the up and down displacement curves at 0 V. It is positive for CCW loops and negative for CW loops. The loop closes at the beginning and end points (-50 V) which confirms that the thermal drift was not significant for the short period (100 s) needed to complete the measurement. Drift may still affect creep data, which acquired over a much longer time period, as described in the next section.

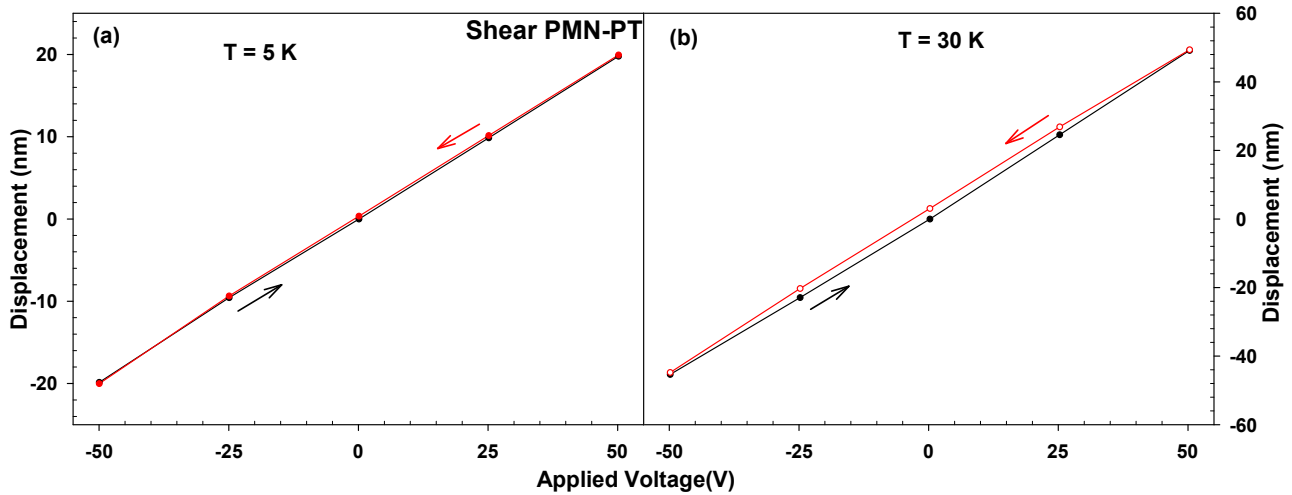


Figure 5.11: Hysteresis at 5 K (a) and 30 K (b).

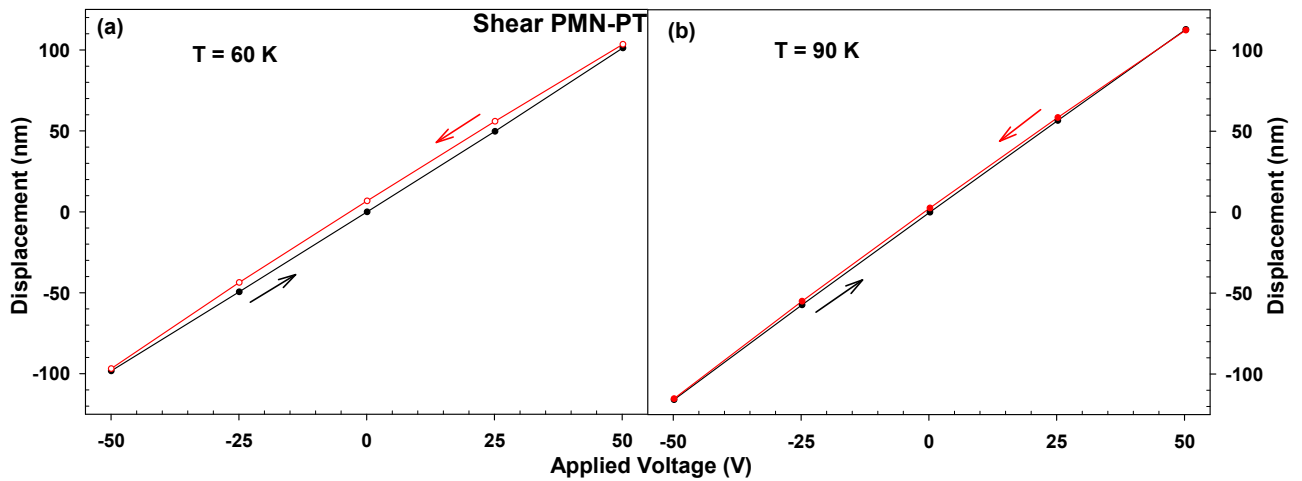


Figure 5.12: Hysteresis at 60 K (a) and 90 K (b).

In order to determine the temperature dependence of the hysteresis, loops were measured from 150 mK to 310 K. Figures 5.11 to 5.14 show hysteresis loops from 5 to 310 K. There was no hysteresis below 5 K, within the noise. The hysteresis below 150 K is CCW and its width increases with increasing temperature from 5 to 60 K. Above 60 K, the hysteresis decreases, with no measurable hysteresis at 150 K. Above

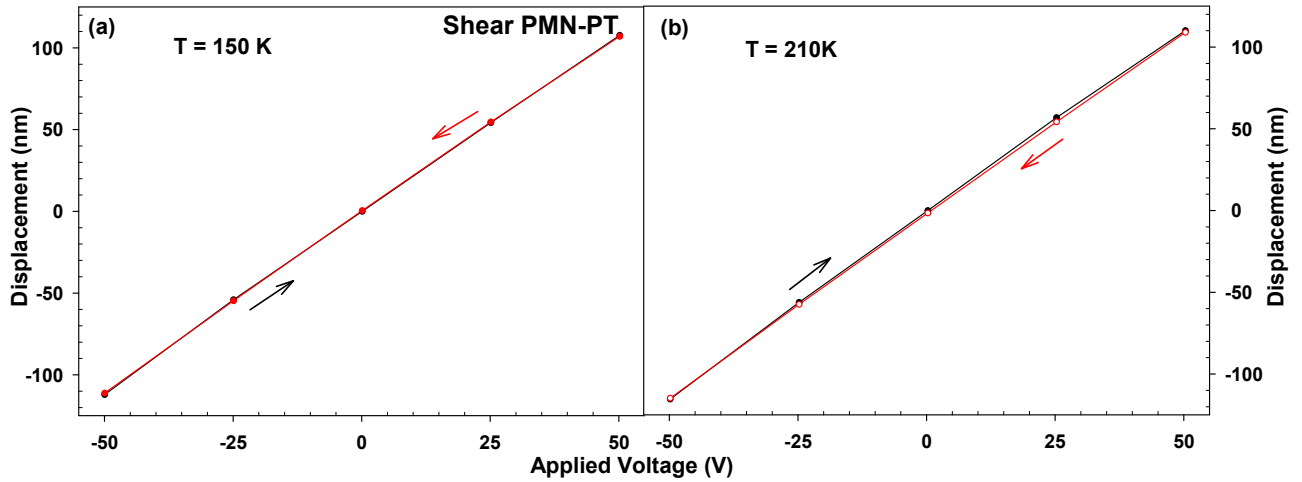


Figure 5.13: Hysteresis at 150 K (a) and 210 K (b).

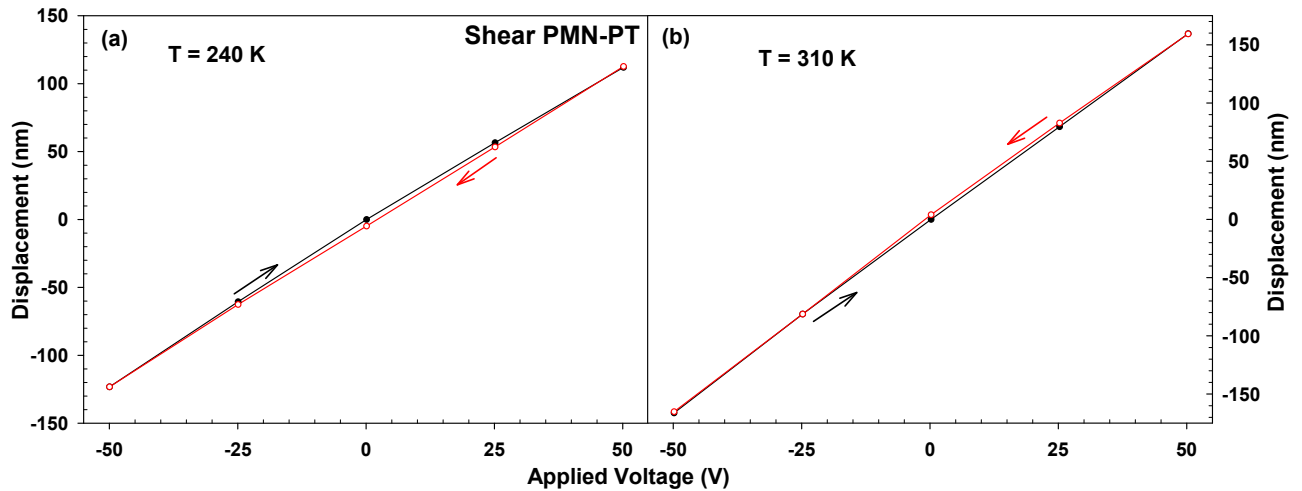


Figure 5.14: Hysteresis at 240 K (a) and 310 K (b).

150 K, the hysteresis loop becomes CW and its width increases. Above 240 K, the hysteresis width decreases, disappears around 290 K, then changes direction again (to CCW) and increases up to 310 K. The up (black) and down (red) arrows indicate the CW (negative) and CCW (positive) hysteresis directions.

Even when there is no hysteresis (e.g. at 150 K, Figure 5.13a), the displacement vs. voltage curves are not always completely linear.

Figure 5.15 shows the temperature dependence of the hysteresis widths measured in a range from 5 to 310 K. Loops were measured 3 or 4 times at each temperature and the data show scatter of about 0.5-2.0 nm, essentially the noise in the capacitance measurements. Figure 5.16 shows the average hysteresis width at each temperature. The error bars are the standard deviations corresponding to all data measured at each

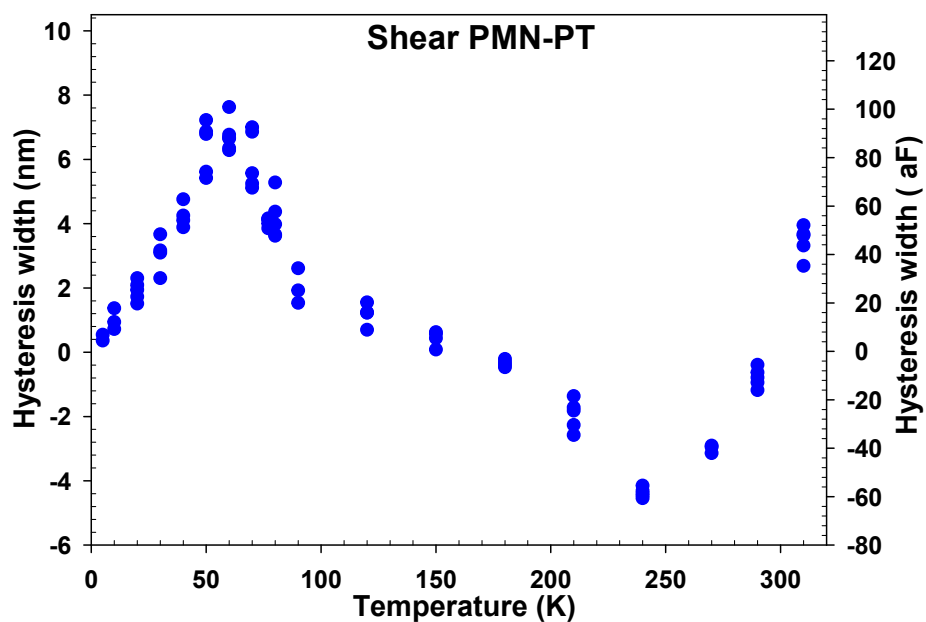


Figure 5.15: Temperature dependence of the hysteresis width determined from hysteresis loops like these in Figure 5.11 to 5.14.

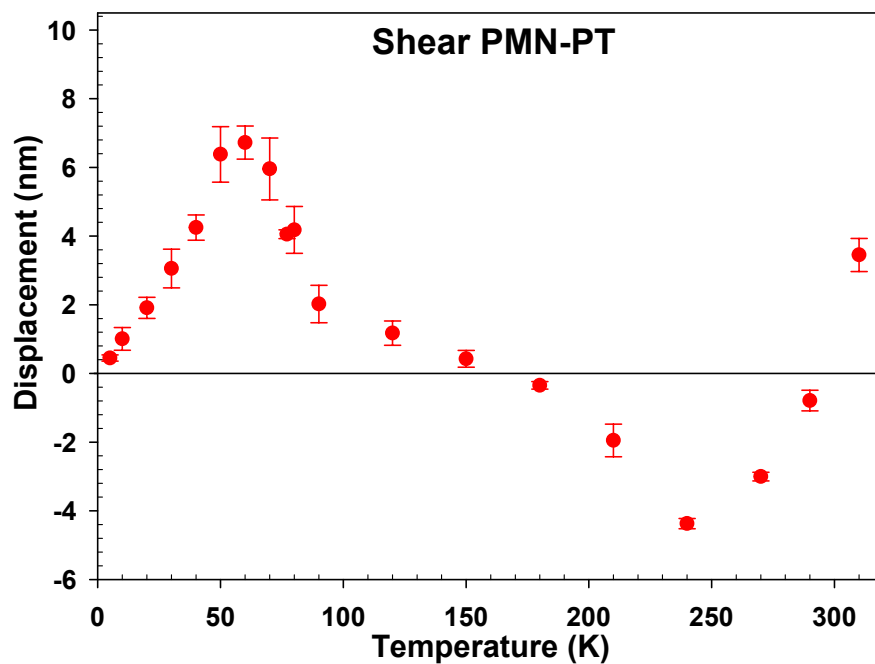


Figure 5.16: Temperature dependence of the average hysteresis width. Error bars are standard deviations of all measured data at each point.

temperature. At the lowest temperature, there is almost no hysteresis. The hysteresis width increases up to 60 K, then decreases, with a maximum negative value at 240 K. Above 240 K, it increases and becomes positive at the highest temperature (310 K).

We have also calculated the relative hysteresis width (i.e., the width normalized by the magnitude of the piezoelectric response, d_{15}) at each temperature. Figure 5.17 shows the relative hysteresis width in a temperature range from 5 to 310 K. This normalization primarily affects the shape of the curve in regions where d_{15} is changing rapidly, i.e., below 70 K and above 250 K.

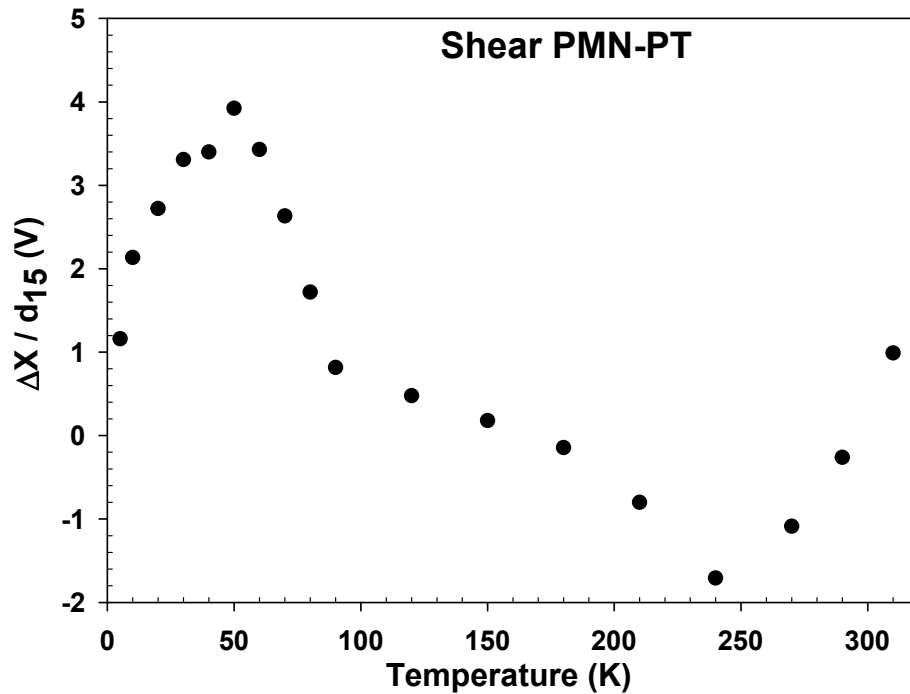


Figure 5.17: Temperature dependence of the hysteresis width normalized by d_{15} .

Hysteresis loops were also measured with maximum voltages of ± 50 , ± 75 , ± 100 and ± 150 V at 20 K. For the ± 50 and ± 75 V loops, the voltage was changed in 25 V steps. Figure 5.18 shows these loops. The ± 100 and ± 150 V loops were measured using 50 V steps, and are shown in Figure 5.19. Each data point took 10 seconds in all cases. The hysteresis loops depend on the maximum voltage, as well as on temperature. Although the slope for the minimum voltage ± 50 V is slightly larger than others, the slopes agree within 0.02 nm/V in all cases. Creep and hysteresis are most significant at the higher voltages, which is why a maximum ± 20 V square wave was used for all d_{15} measurements, to avoid creep and hysteresis effects.

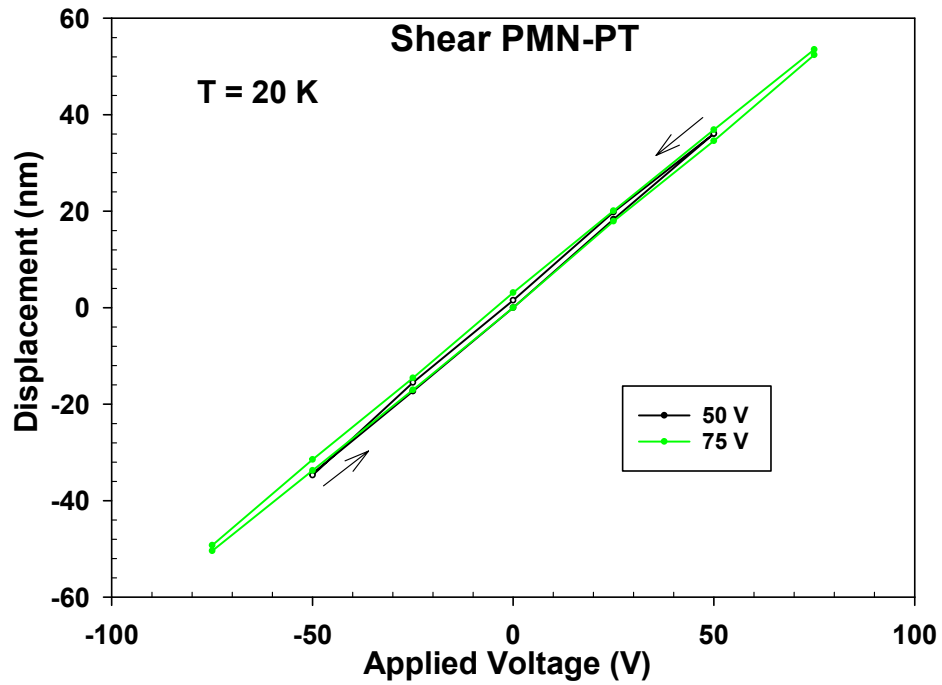


Figure 5.18: Hysteresis loops at 20 K, for ± 50 and ± 75 V maximum applied voltages.

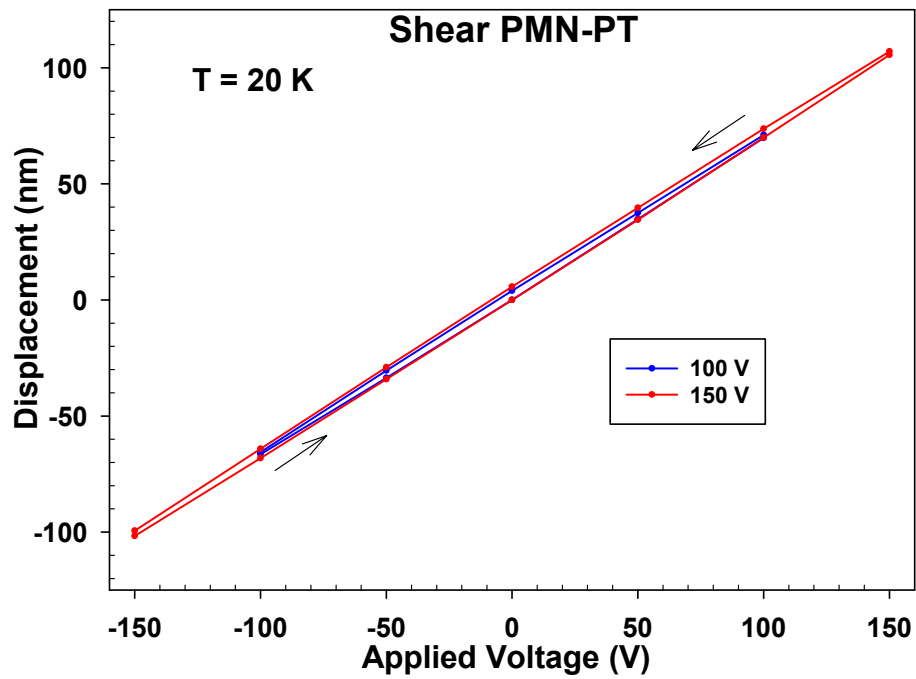


Figure 5.19: Hysteresis loops at 20 K, for ± 100 and ± 150 V maximum applied voltages.

The corresponding voltage dependence of these hysteresis widths is shown in Figure 5.20. The hysteresis width appears to vary linearly with the maximum applied voltage up to ± 150 V.

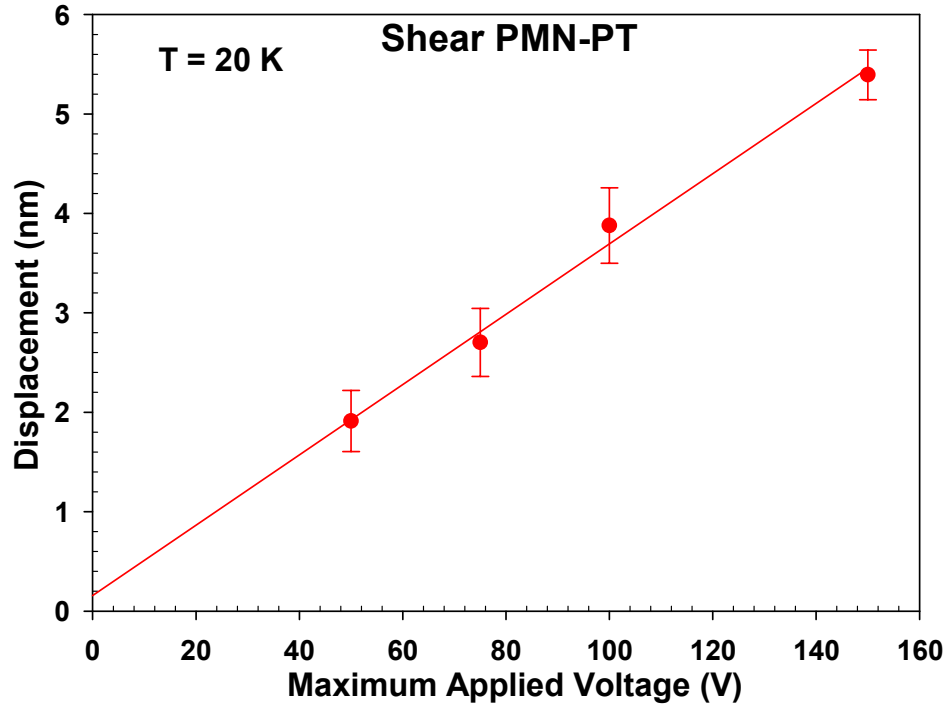


Figure 5.20: The voltage dependence of the hysteresis width for a PMN-PT single crystal at 20 K.

5.3.2 P-E hysteresis loop

Figure 5.21 shows a polarization - electric field hysteresis loop (P-E hysteresis loop) measured at 1 kHz and 295 K using a Sayer-Tower circuit [78]. The temperature dependence of the P-E hysteresis width (of the remnant polarization P_r) is shown in Figure 5.22. It has a roughly constant value between 50 and 90 K and no measurable hysteresis between 120 and 210 K. Between 210 K and room temperature, it increases rapidly. The corresponding loops for temperatures between 295 K and 53 K are shown in Figure 5.23

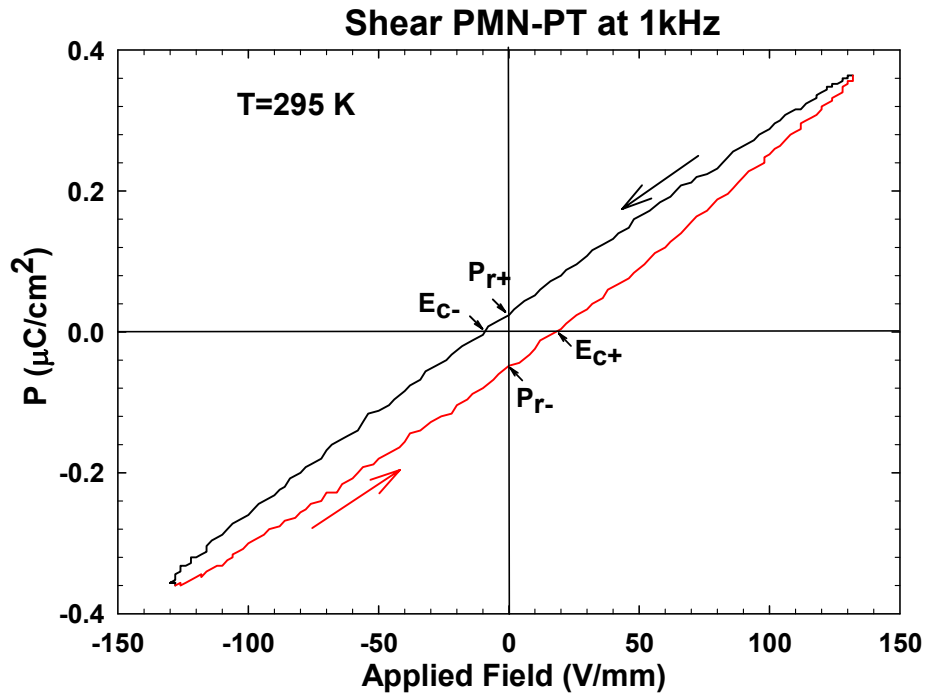


Figure 5.21: P-E hysteresis loop for a PMN-PT single crystal at 295 K.

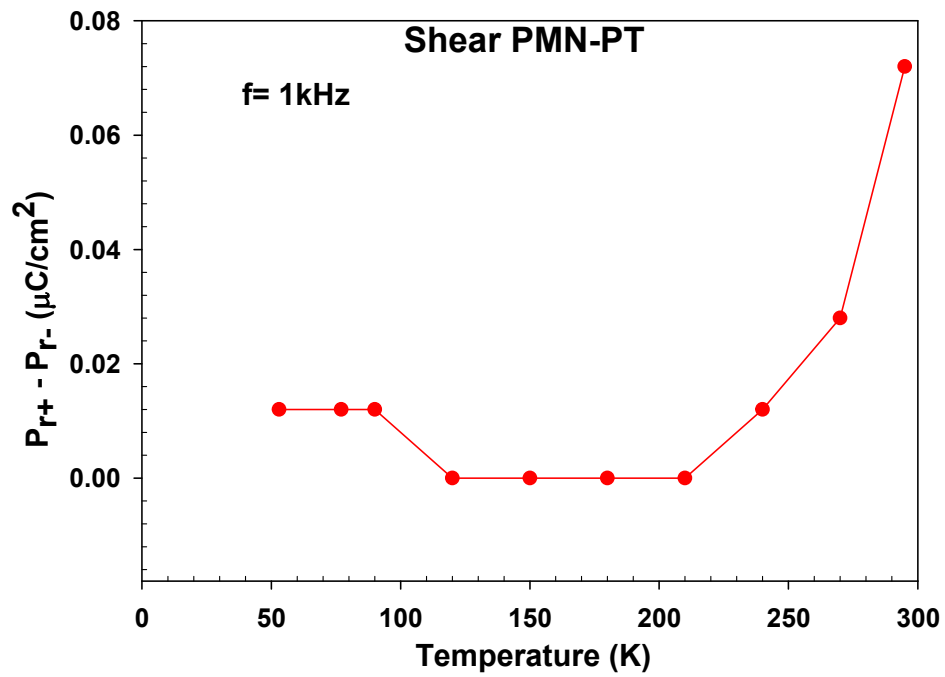


Figure 5.22: Temperature dependence of the P-E hysteresis width for a PMN-PT single crystal.

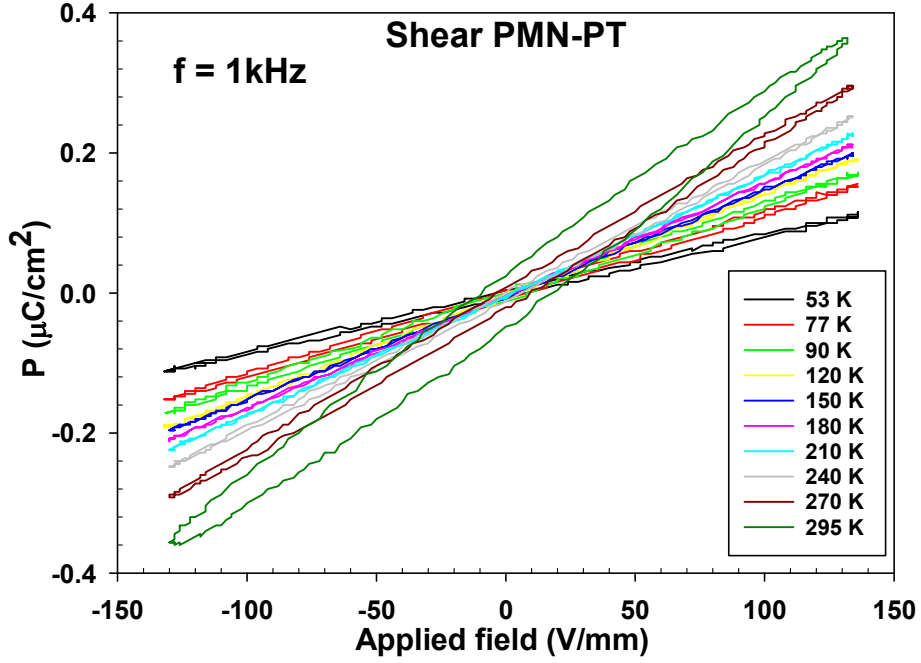


Figure 5.23: Temperature dependence of the P-E hysteresis loops for a PMN-PT single crystal measured at 1 kHz.

5.3.3 Creep measurements

Creep is an essential property of piezoelectric materials and is responsible for hysteresis. Creep displacements in piezoelectric materials usually change logarithmically over time [25], i.e. without a characteristic time constant, which means that creep and hysteresis can affect measurements over a wide range of times and frequencies.

Figure 5.24 shows the change in shear displacement (nm) with time, following changes in applied voltage (V) for a PMN-PT single crystal at 70 K. This time-dependent data shows both creep and thermal drift. The creep displacement was extracted by correcting for the thermal drift. To do this, we first linearly extrapolated the last 2000 seconds of data before a voltage was applied (the red line in Figure 5.25). We then subtracted this fit from the data after applying +50 V. Similarly, we extrapolated the last 3000 seconds of the data at +50 V (the blue line in Figure 5.25) and subtracted it from the displacements after the applied voltage was changed from +50 to -50 V. The linear fits used to correct for drift extended over 2000 or 3000 seconds, but the data actually used to analyze creep covered a smaller range, 1000 seconds, over which the creep rate was assumed to be constant. Before applying +50 V, the drift rate was $\frac{dx}{dt} = 5 \times 10^{-4}$ nm/s and before the voltage was changed to -50

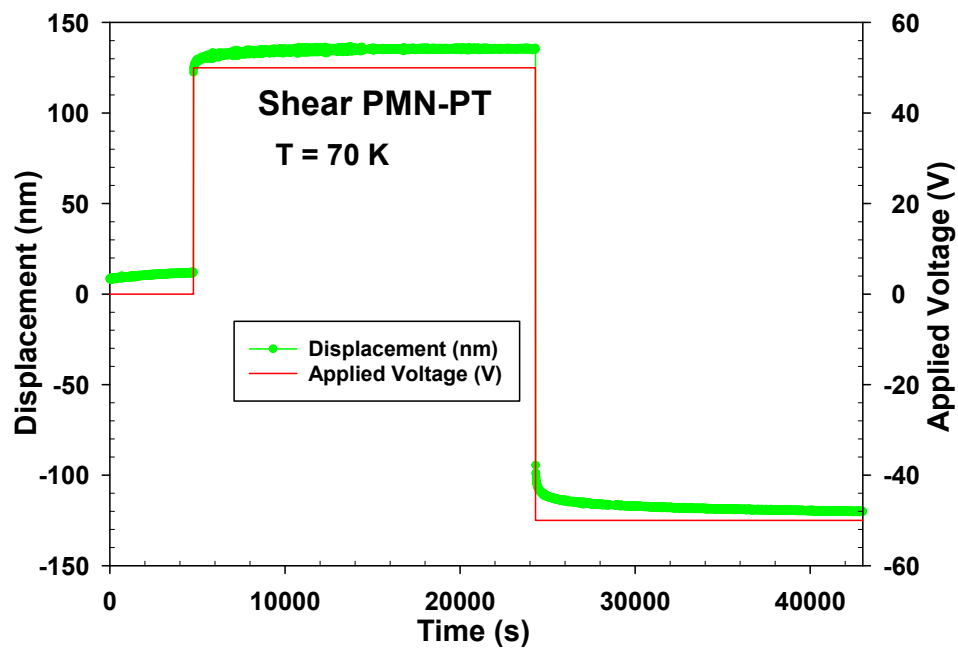


Figure 5.24: Shear displacement vs. time following changes to the applied voltage for a PMN-PT single crystal at 70 K.

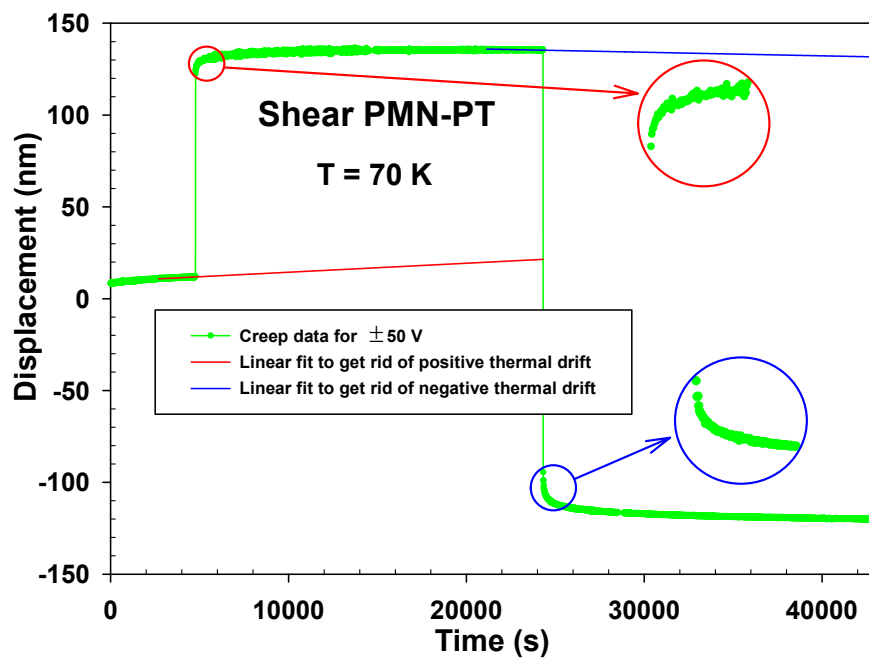


Figure 5.25: Extrapolation (red fit line) to get rid of thermal drift from the positive creep and (blue fit line) from the negative creep for PMN-PT crystal at 70 K.

V, it was $\frac{dx}{dt} = -7 \times 10^{-5}$ nm/s. During the 1000 seconds that we will analyze the creep data, the thermal drift is less than 5×10^{-1} nm, roughly the noise level in the data of Figure 5.24. Although the drift rate was not constant over for the full time of the measurement, the linear fits are sufficient to correct the creep data for shorter times. Circles in Figure 5.25 show the regions of data used to analyze the creep.

Figure 5.26 shows the creep data (after drift corrections) corresponding to a applied voltage change $\Delta V = +50$ V (0 V \rightarrow $+50$ V), at temperatures from 10 to 310 K. For this increase in voltage, positive creep is observed from 10 to 120 K and at 310 K, but the creep is negative between 180 and 270 K. There is no measurable creep at 150 K and 290 K. The negative creep region corresponds to the plateau of the d_{15} curve described in section 4.2.2. To show the positive and negative creep more clearly, we have plotted them in separate windows in Figure 5.27. The maximum positive creep occurs at 50 K and the maximum negative creep at 240 K.

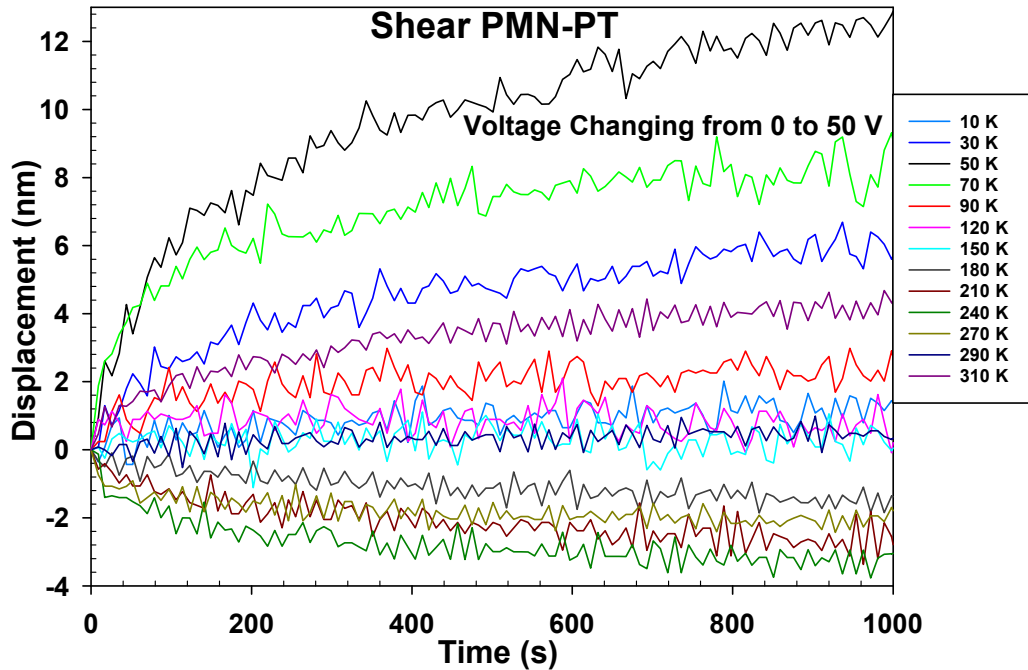


Figure 5.26: Temperature dependence of the creep following a voltage change $\Delta V = +50$ V (0 V \rightarrow $+50$ V).

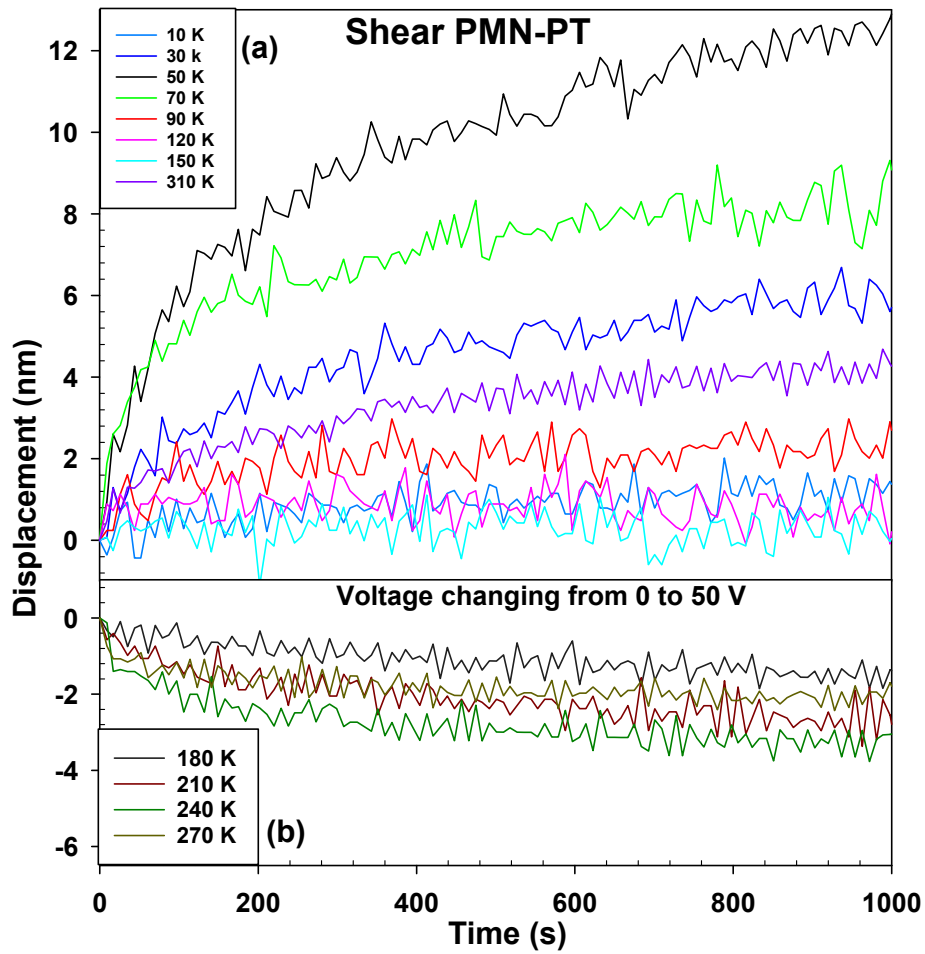


Figure 5.27: (a) Positive and (b) Negative creep following a voltage change $\Delta V = +50$ V (0 V \rightarrow $+50$ V).

Similarly, Figure 5.28 shows the positive and negative creep following a negative applied voltage change $\Delta V = -100$ V ($+50 \rightarrow -50$ V). The direction of the creep is opposite to that for a positive applied voltage change $\Delta V = +50$ V. Figure 5.29 compares the creep for the voltage changes $\Delta V = +50$ and -100 V at selected temperatures.

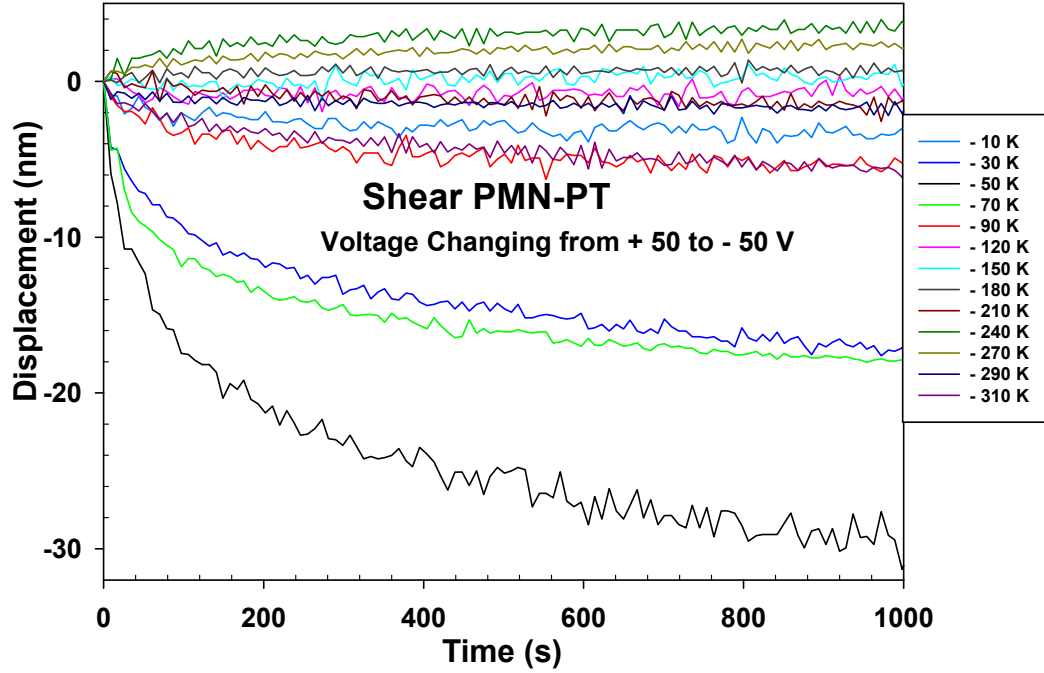


Figure 5.28: Temperature dependence of the creep following a negative voltage change $\Delta V = -100$ V (+50 \rightarrow -50 V).

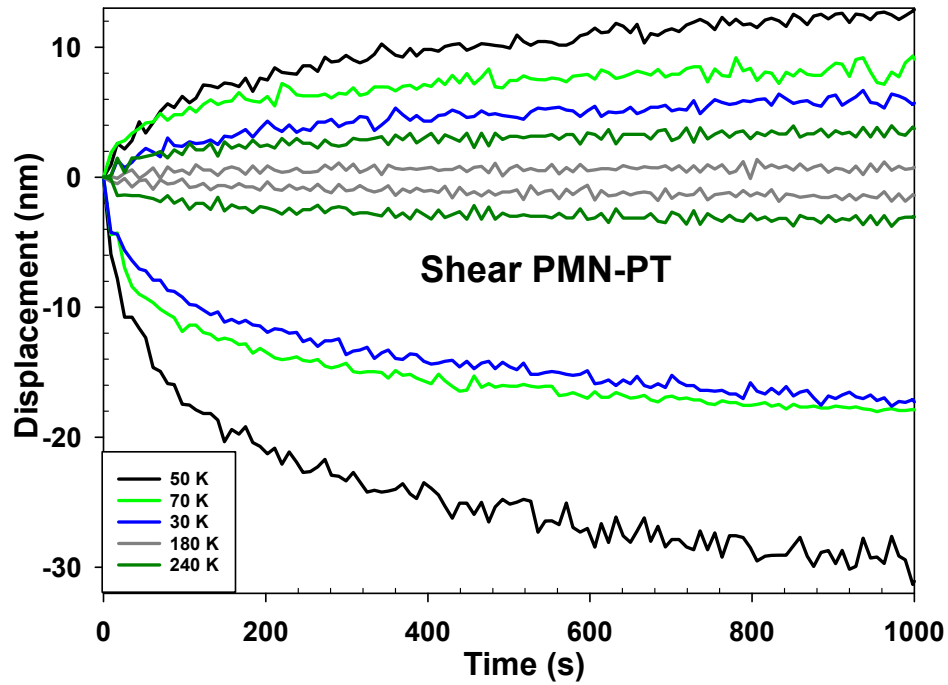


Figure 5.29: Temperature dependence of the creep for positive and negative voltage changes $\Delta V = +50$ V and $\Delta V = -100$ V.

In order to find the relationship between the creep and the applied voltage change, Figure 5.30 shows the positive and negative creep at 70 K, divided by the applied voltage changes. The black data are the creep for $\Delta V = +50$ V, divided by 50. The red data are the creep for $\Delta V = -100$ V divided by -100. They have almost same values, i.e. the negative creep for $\Delta V = -100$ V is twice as large as the the positive creep for $\Delta V = +50$ V. This proportionality between the voltage change and the creep displacement holds for temperatures below 70 K or greater than 270 K. Between 70 K and 270 K, however, this does not appear to hold, as shown in Figure 5.31 for 270 K.

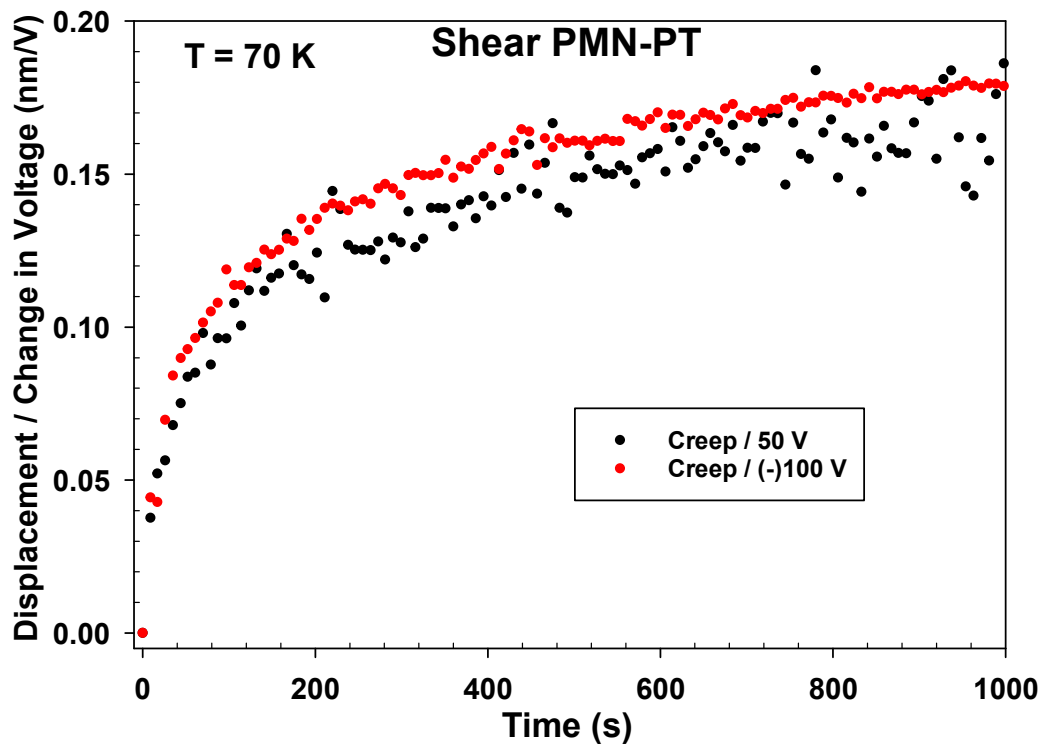


Figure 5.30: Positive (black dots) and negative (red dots) creep at 70 K, divided by the applied voltage change.

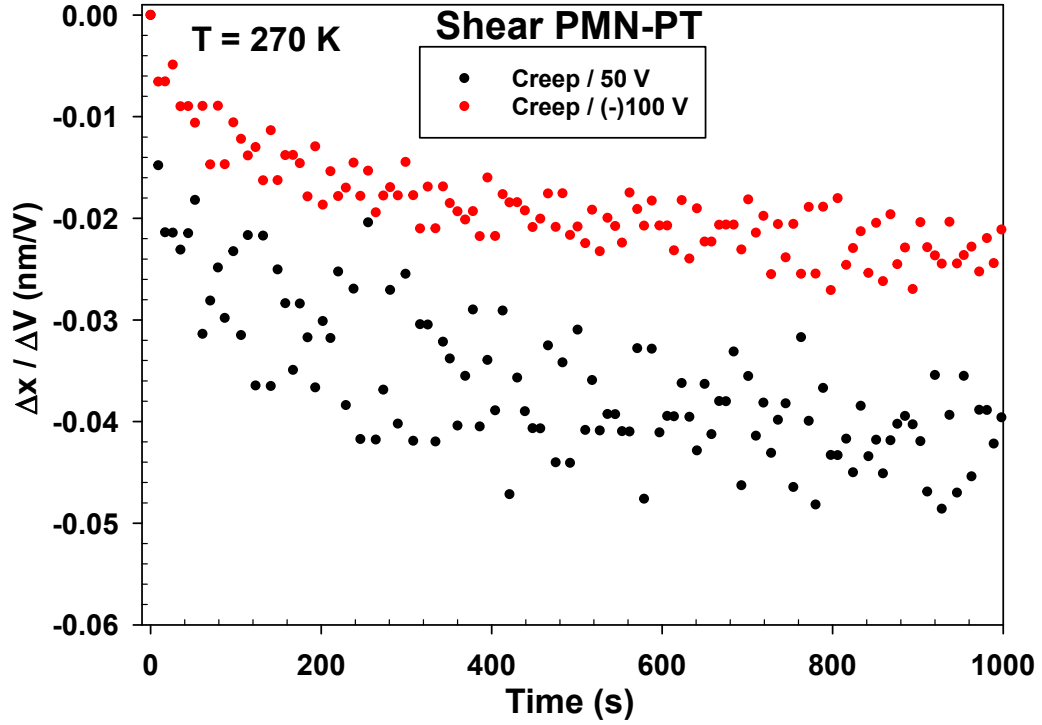


Figure 5.31: Positive (black dots) and negative (red dots) creep at 270 K, divided by the applied voltage change.

To find the time dependence of the creep, we tried to fit it to several functional forms. We first show fits to an exponential of the form

$$f(t) = y_0 + a(1 - e^{-bt}) \quad (5.1)$$

where the relaxation time constant is $\tau = 1/b$ and the parameters y_0 and a may depend on the applied voltage and temperature. Figures 5.32 and 5.33 show the exponential fit analysis at 70 K, for positive and negative creep, respectively. This equation fits the data over limited time ranges, but not over the full time range. The insert is a blow-up of the data for the first 300 seconds. The figure shows the fits for both long time (black line) and the first 300 seconds (blue line). The time constants for the fits are $\tau = 1900$ seconds (long times, black lines) and $\tau = 64$ seconds (short times, blue lines) for the positive creep, and $\tau = 3200$ seconds and $\tau = 60$ seconds, respectively for the negative creep data. The different time constants mean the long time and short time data are not consistent with a single exponential.

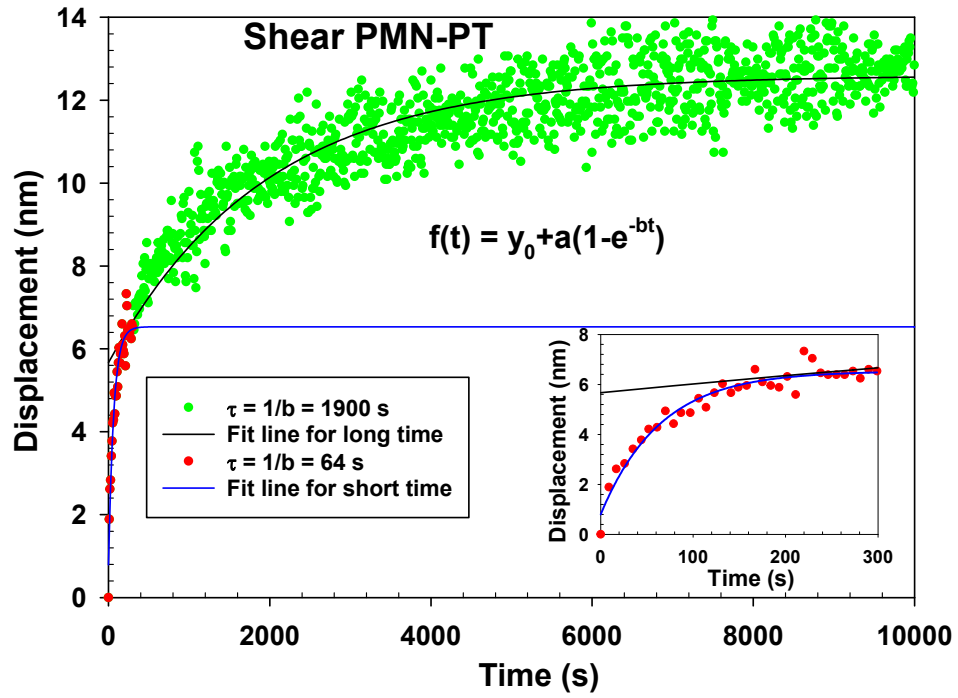


Figure 5.32: Exponential fits of the creep data after applying a voltage change $\Delta V = +50$ V. Insert shows fits of the data for the first 300 seconds.

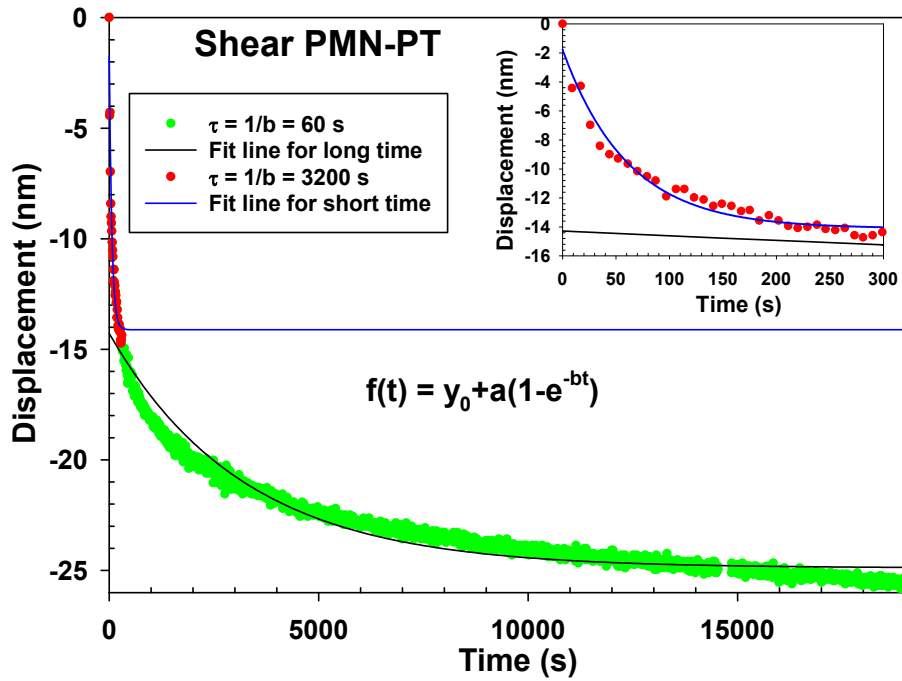


Figure 5.33: Exponential fits of the creep data after applying a negative voltage change $\Delta V = -100$ V. Insert shows fits of the data for the first 300 seconds.

Next, we fit the creep to power laws of the form

$$f(t) = y_0 + at^n, \quad (5.2)$$

where the parameters y_0 , a and n may depend on voltage and temperature. Figure 5.34 shows the power law fits for $n = 0.01, 0.1, 0.2$ and 0.5 , for an applied voltage change $\Delta V = +50$ V at 70 K. The creep is well described by a power law with a small exponent, but is not sensitive to the exact value of n , which suggests that the time dependence may be logarithmic (a logarithmic function approaches a power law t^n for $n \ll 1$).

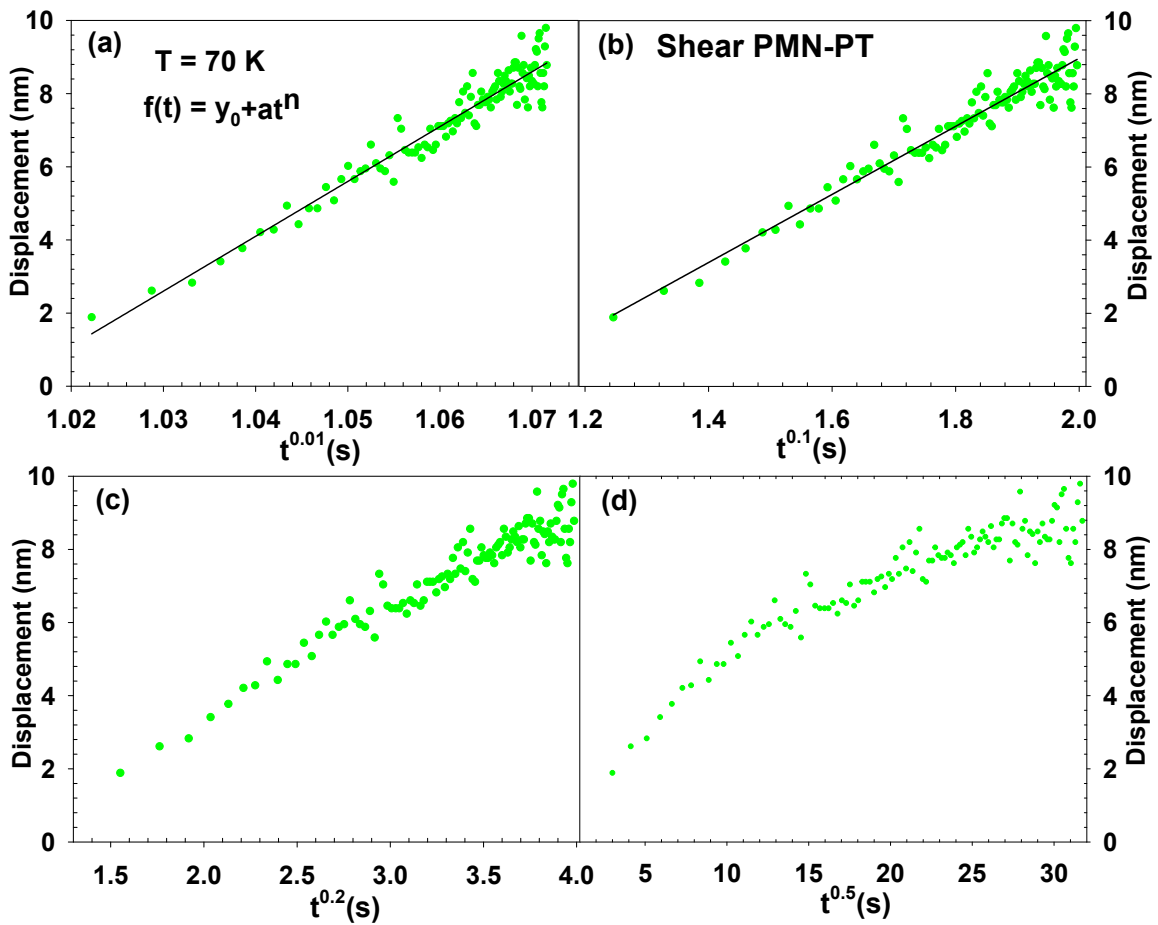


Figure 5.34: Power law analysis of positive creep data after applying a voltage $\Delta V = +50$ V. Panels (a) to (d) have logarithmic time axes corresponding to exponents n from 0.01 to 0.5.

We therefore tried a logarithmic fit of the form

$$f(t) = y_0 + a \log_{10}(t). \quad (5.3)$$

Figures 5.35 to 5.38 show logarithmic plots and fits of both positive and negative creep data for PMN-PT at 70 K. A logarithmic function fits the data well over two decades in time, from $t = 10$ seconds to 1000 seconds. This is similar to the creep behavior studied previously [25, 68, 69].

Figures 5.35 and 5.37 show the positive and negative creep data for the first 1000 seconds after the applied voltage was changed. Figures 5.36 and 5.38 show the same data over longer times, up to 10,000 and 19,000 seconds, respectively. The data appear to deviate from logarithmic behavior in Figure 5.38, but the drift correction made before plotting the creep data is not reliable at long times. The data for the first 1000 seconds (Figures 5.35 and 5.37) is more reliable and is used in the rest of the analysis in this Chapter. For example, the parameter a that characterizes the magnitude of the first 1000 seconds of creep at 70 K is about half as large for the + 50 V voltage change as for the -100 V voltage change (3.63 vs -7.01), as expected if the creep is proportional to ΔV . The values of a from fitting the long time data (Figures 5.36 and 5.38) are 3.96 and 5.95 and so are not consistent with this expected proportionality.

The first few data points (for $t \lesssim 10$ s) in each plot deviate from the straight fit line. However, the measurement time for each data point was 8 seconds, including 4 seconds of averaging by the capacitance bridge. This means the data points are not instantaneous but rather are averages over the previous 4 to 8 seconds. The horizontal red lines extending from the first few data points indicate this measurement range and explain much of the deviations.

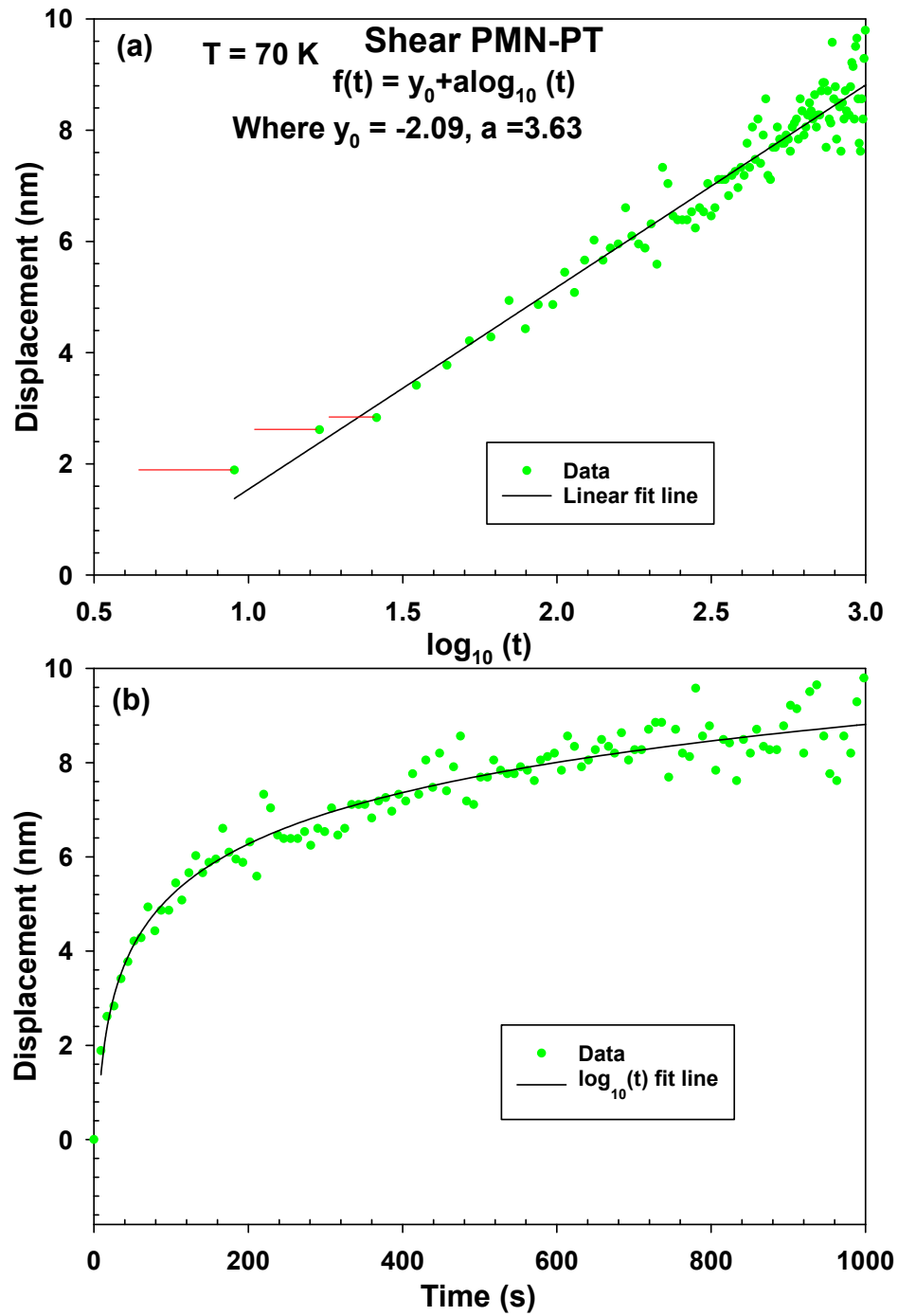


Figure 5.35: Logarithmic fit of the positive creep for 1000 seconds following an applied voltage change $\Delta V = +50 \text{ V}$.

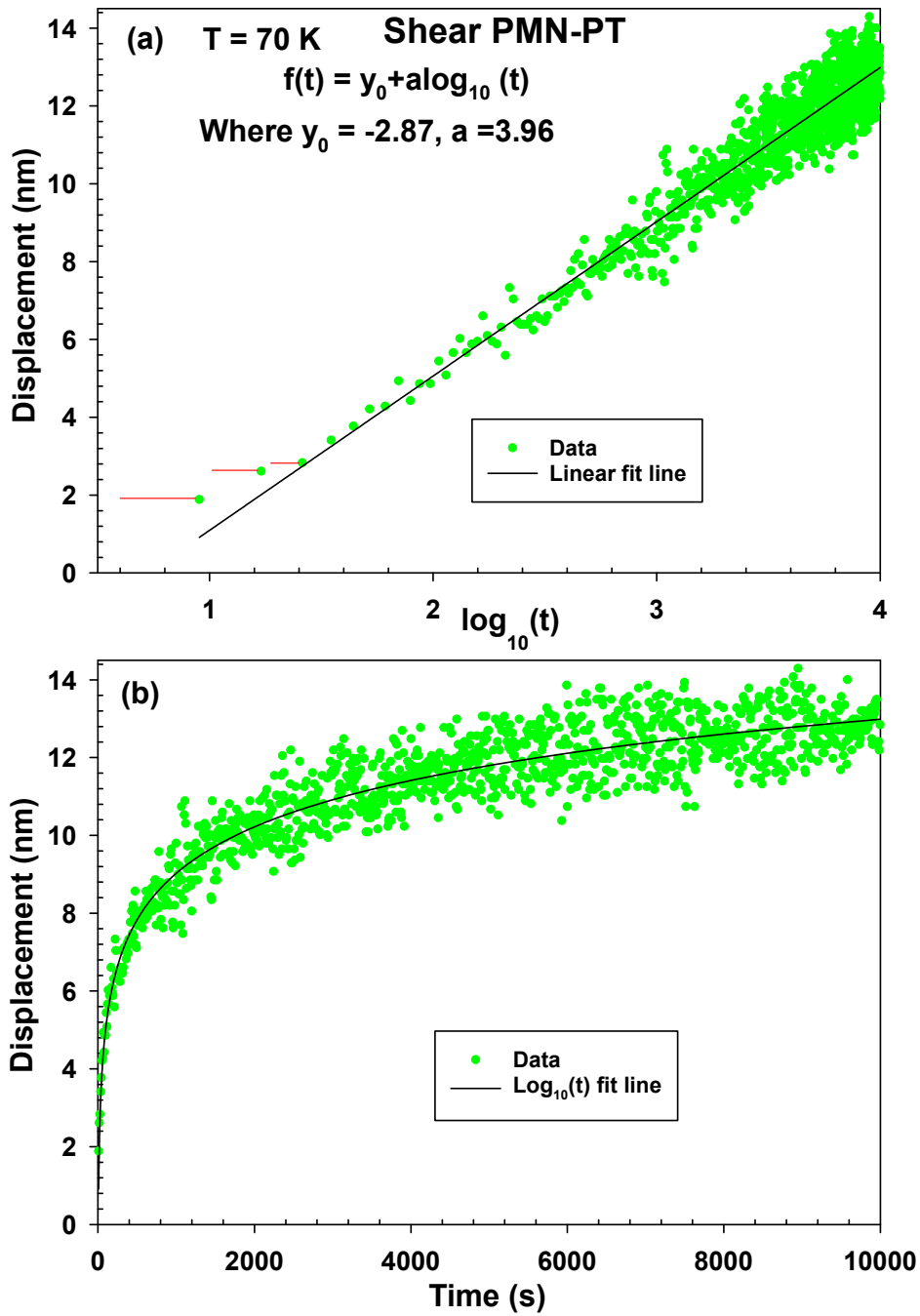


Figure 5.36: Logarithmic fit of the positive creep for 10000 seconds following an applied voltage change $\Delta V = +50 \text{ V}$.

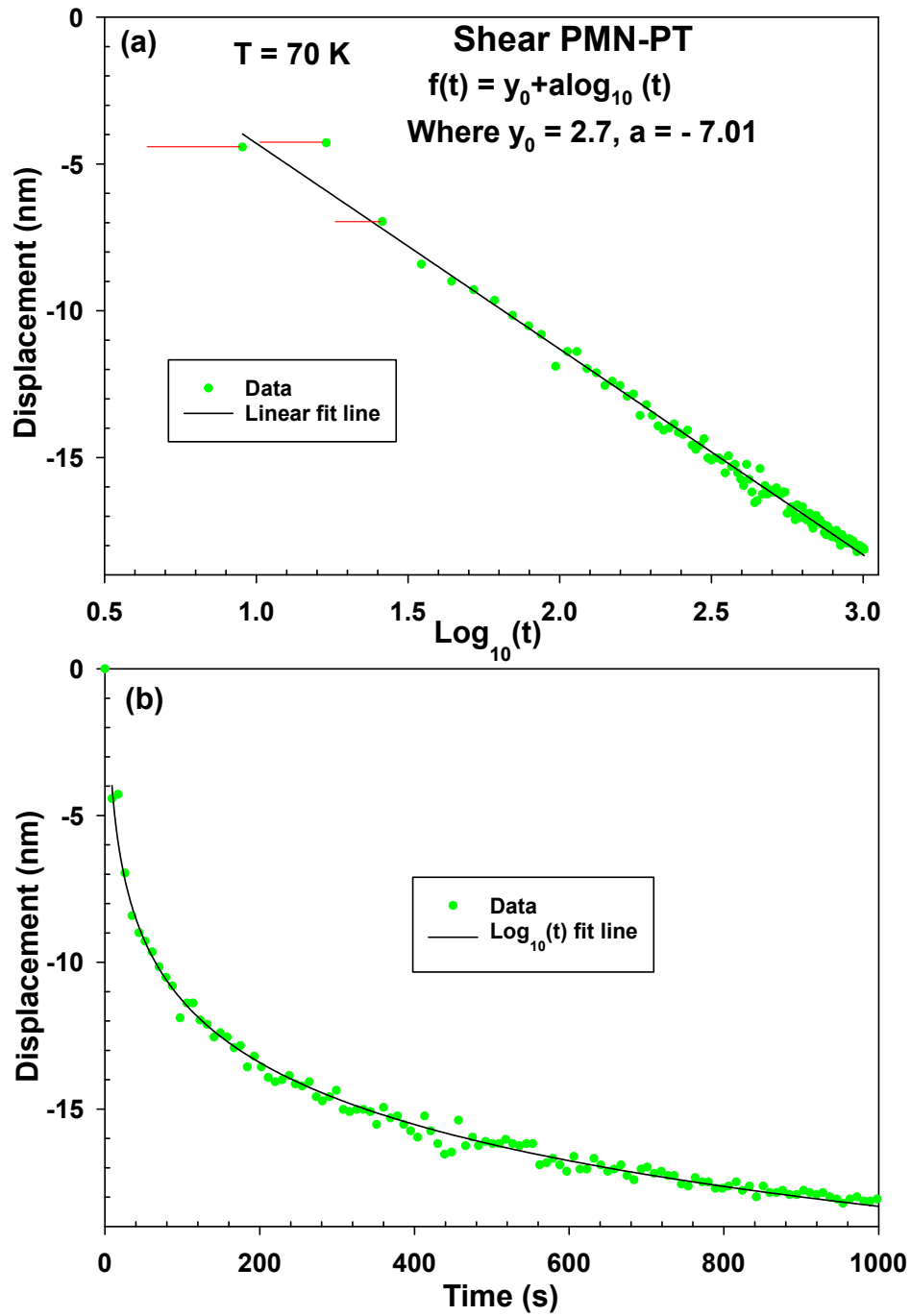


Figure 5.37: Logarithmic fit of the negative creep for 1000 seconds following an applied voltage change $\Delta V = -100 \text{ V}$.

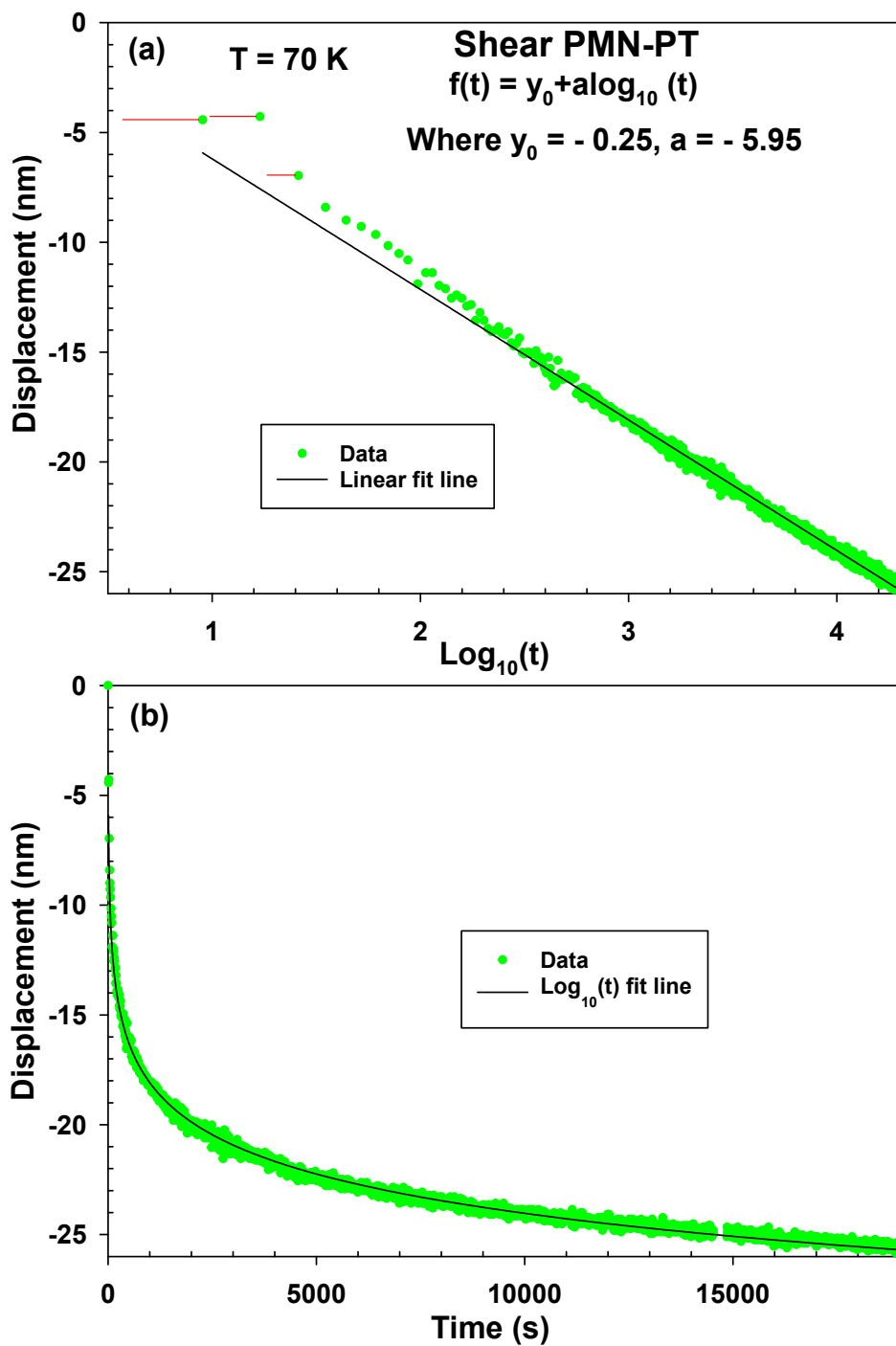


Figure 5.38: Logarithmic fit of the negative creep for 19000 seconds following an applied voltage change $\Delta V = -100$ V.

Figure 5.39 shows the positive and negative creep and their logarithmic fits at 70 K. It is known that such creep produces hysteresis in piezoelectric materials. The width of a hysteresis curve at 0 V should be comparable to the creep during the time over which the curve is measured. For example, the expected hysteresis width can be estimated from the creep during the time between the two measurements at 0 V. The inset in Figure 5.39 shows the difference in creep for $\Delta V = +50$ V and $\Delta V = -100$ V, after 20 seconds. The value, 9.1 nm, gives a rough estimate of the expected hysteresis.

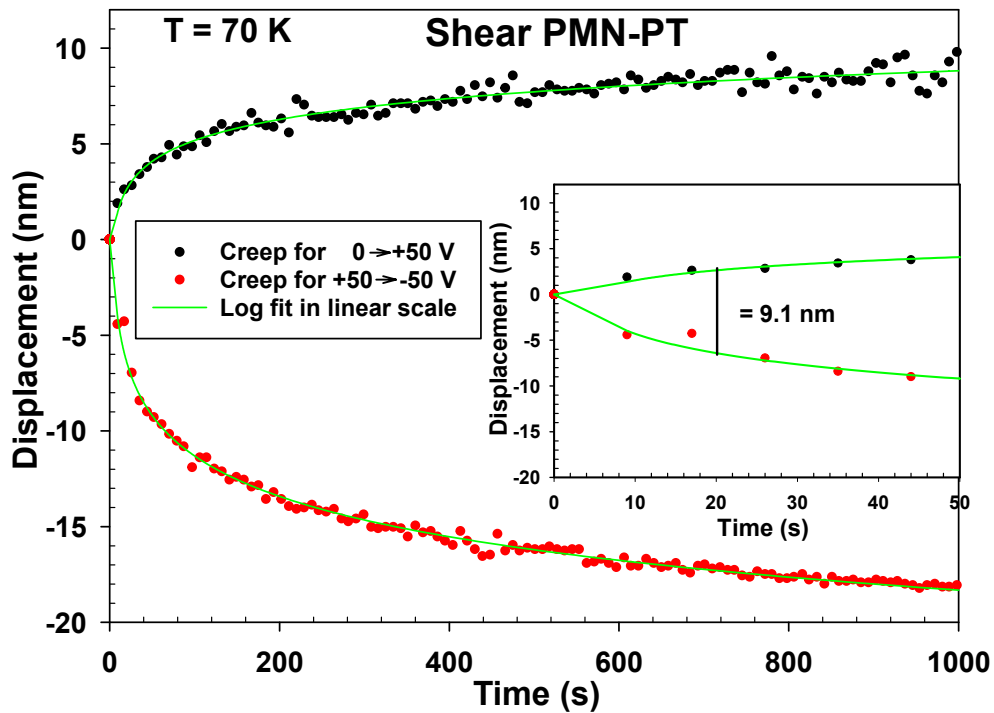


Figure 5.39: Positive and negative creep at 70 K for the shear PMN-PT single crystal. The insert shows the data for the first 50 seconds.

Another way to characterize the magnitude of the creep that is responsible for hysteresis is through the parameter c in equation 2.39, which depends on temperature but not on the voltage change (assuming the creep is proportional to ΔV).

Figure 5.40 shows the temperature dependence of the measured differences in creep (green dots, left axis) and of the creep coefficient c (dark red dots, right axis). They have similar temperature dependences, confirming that either can be used to characterize the creep. Note that the magnitude of the coefficient c is some what

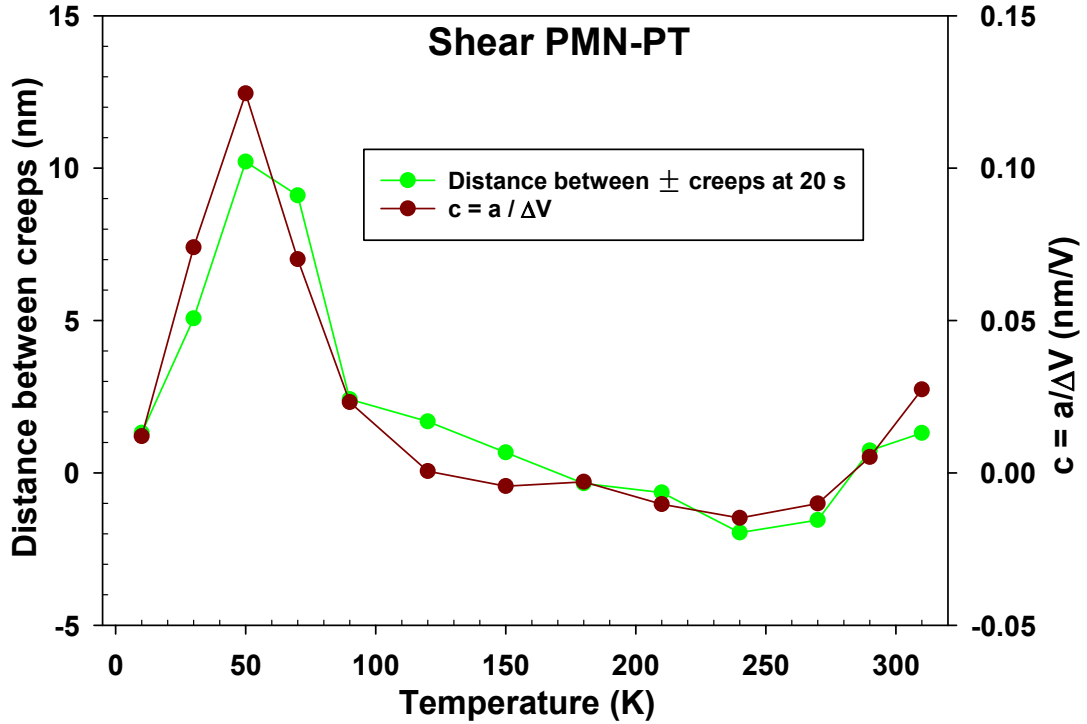


Figure 5.40: Temperature dependence of the difference between positive and negative creep displacements at 20 s (green dots left axis) and of the coefficient c (dark red dots, right axis) for the shear PMN-PT single crystal.

arbitrary since the logarithmic function in equation 5.3 should really be written as

$$f(t) = y_0 + a \log_{10}\left(\frac{t}{t_0}\right). \quad (5.4)$$

and the time t_0 is arbitrary.

5.4 Polycrystalline PZT-5A

The shear PZT-5A ceramic transducer from Boston Piezo Optics, Inc. [81] described in section (4.2.3) was used to investigate the hysteresis and creep properties.

5.4.1 Hysteresis measurements

The voltage dependence of the piezoelectric ceramic's displacement was investigated from 0 to 310 K using the same procedure as for LiNbO_3 . Voltage steps of either 25 V or 50 V were used. Figures 5.41 to 5.45 show hysteresis loops over a voltage range of ± 150 V. There was no measurable hysteresis at the lowest temperatures. Hysteresis

first appears around 35 K. The hysteresis loops were always positive (CCW) and the hysteresis width increased with increasing temperature.

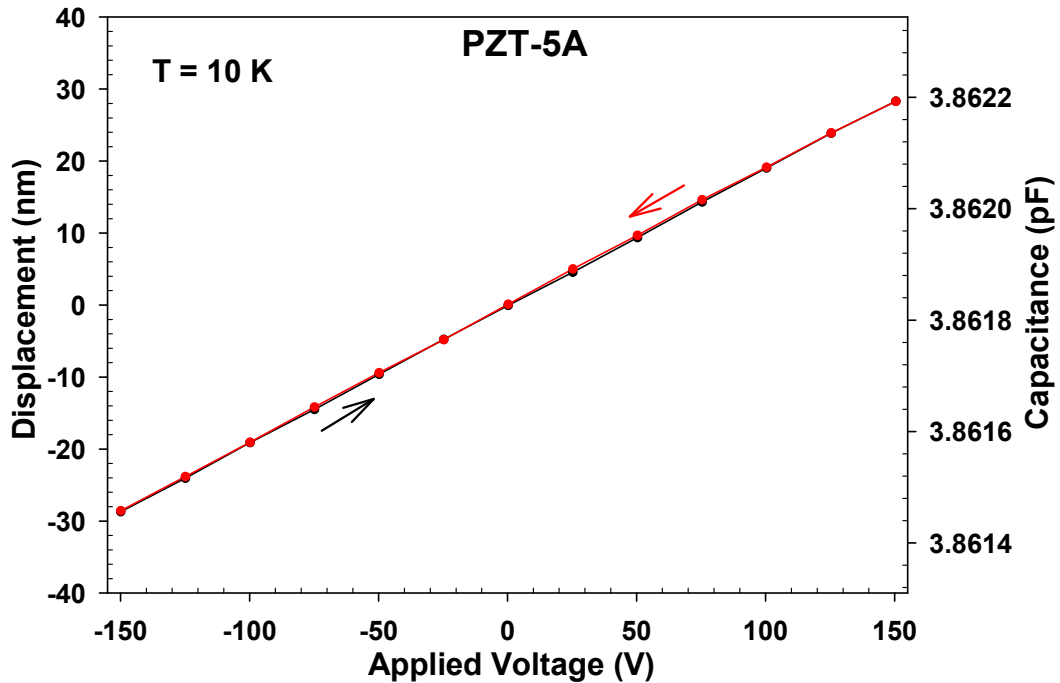


Figure 5.41: Relationship between displacement and applied voltage at 10 K for PZT-5A ceramic. Left axis is displacement with the corresponding measured capacitance on the right axis.

Figure 5.46 shows the hysteresis width in a temperature range from 0 to 310 K. It varies non-linearly with temperature for different voltage ranges. Figure 5.47 shows the dependence of the hysteresis width on the maximum applied voltage at 77 K, which is non-linear, in contrast to the linear behavior in PMN-PT shown in Figure 5.20.

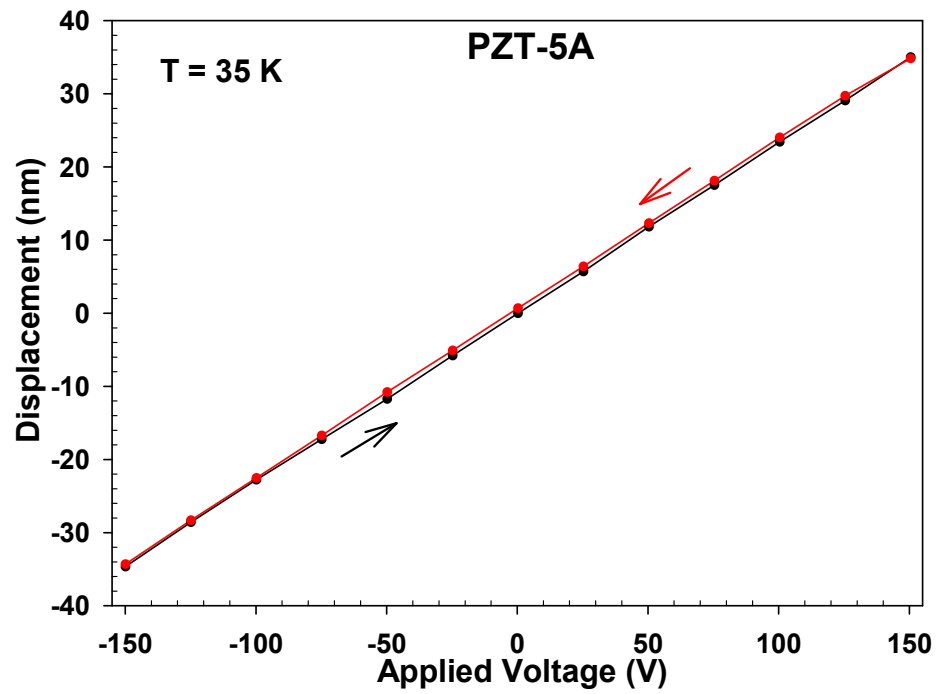


Figure 5.42: Hysteresis between displacement and applied voltage at 35 K.

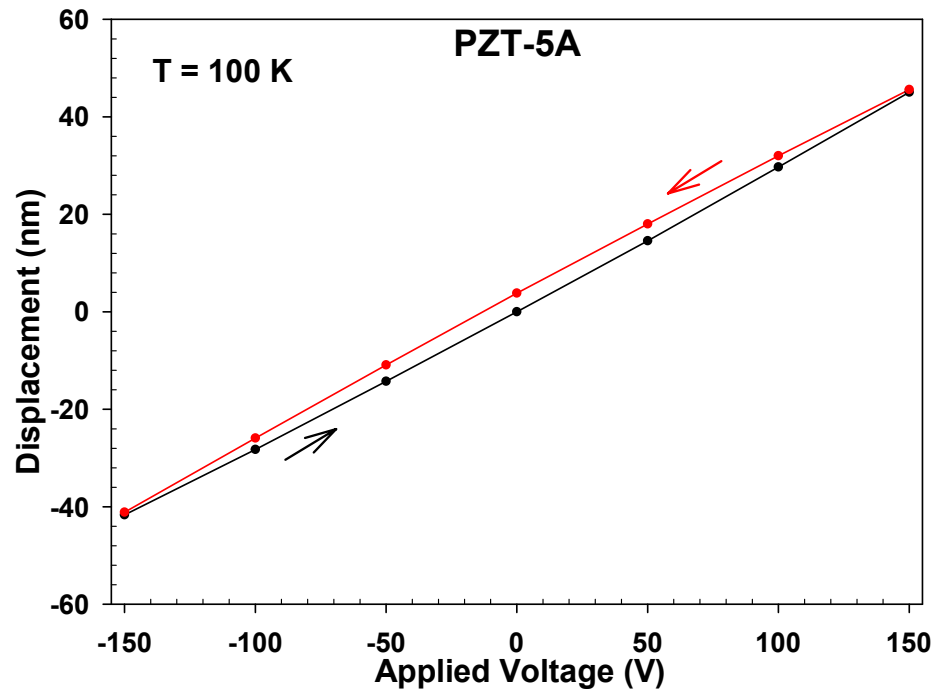


Figure 5.43: Hysteresis between displacement and applied voltage at 100 K.

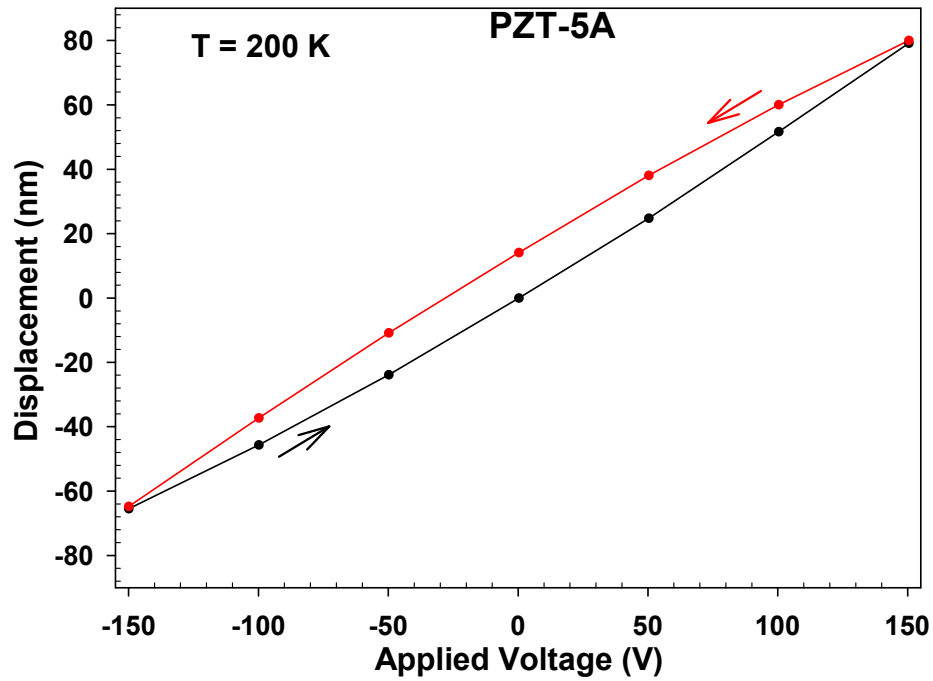


Figure 5.44: Hysteresis between displacement and applied voltage at 200 K.

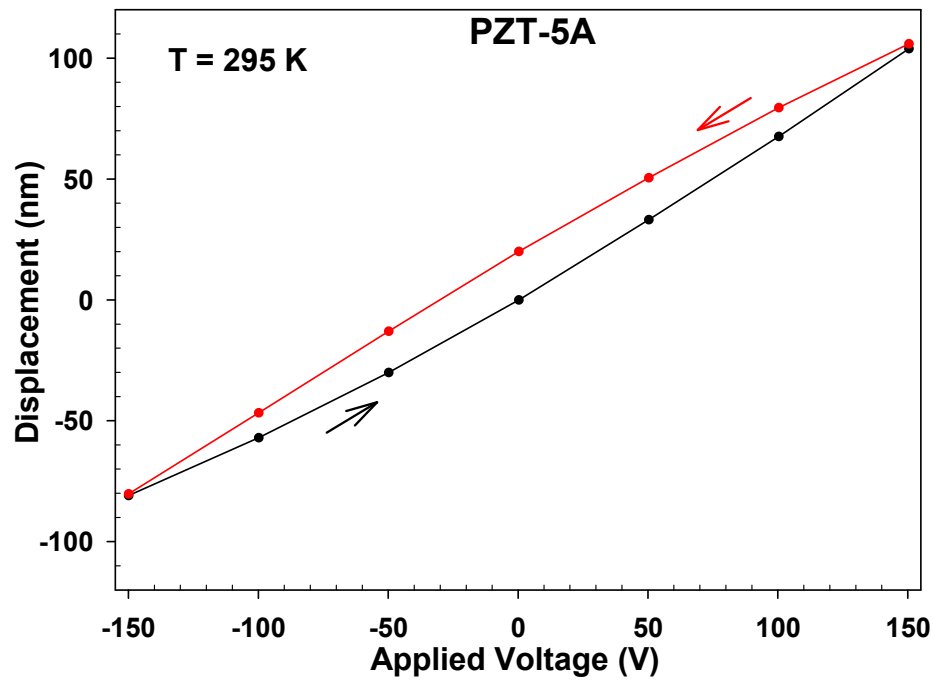


Figure 5.45: Hysteresis between displacement and applied voltage at 295 K.

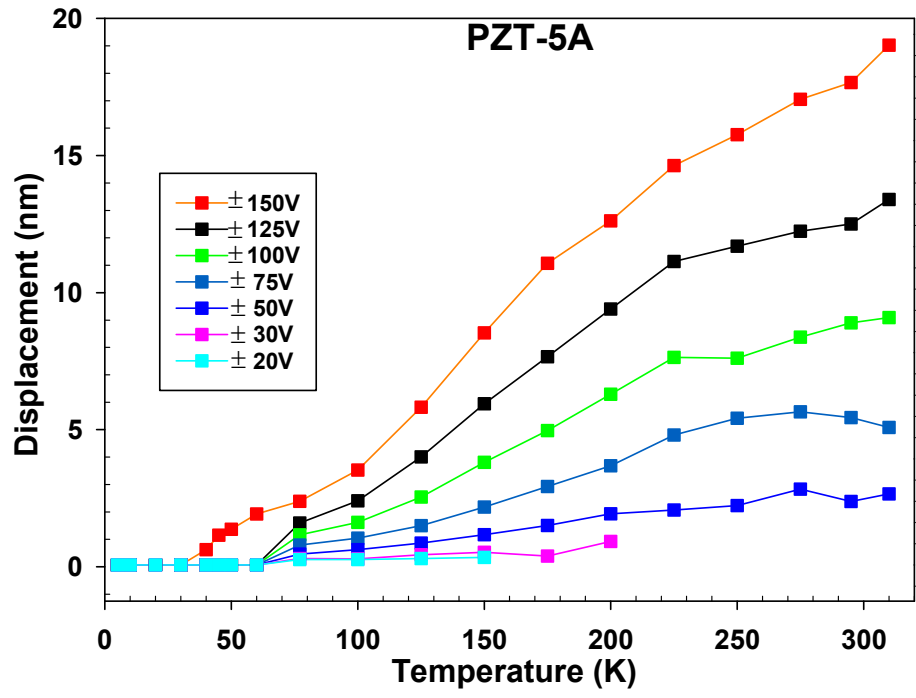


Figure 5.46: Temperature and voltage dependence of the hysteresis width of a PZT-5A ceramic.

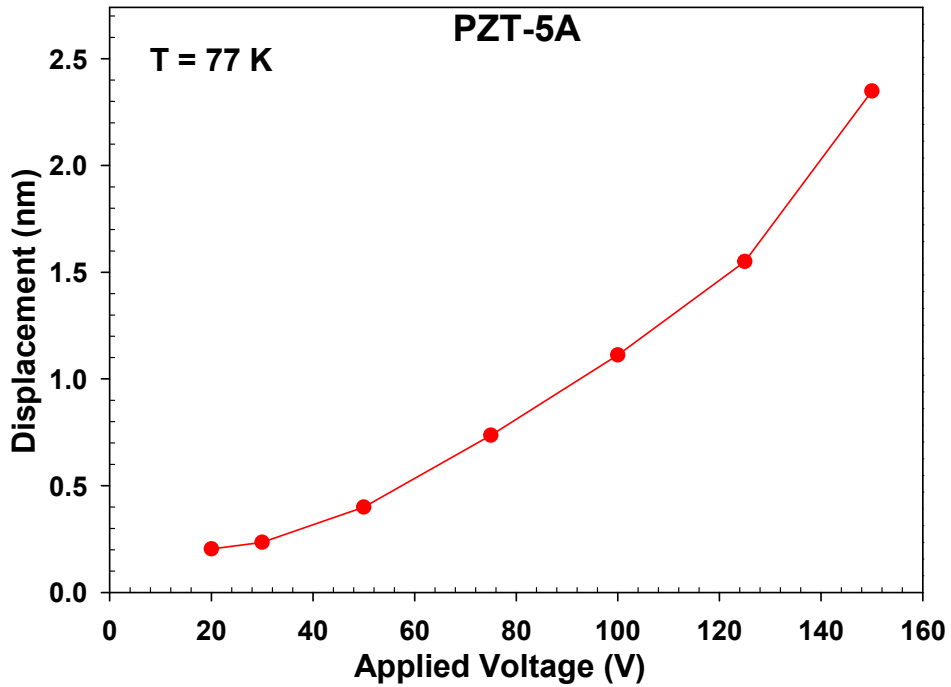


Figure 5.47: Voltage dependence hysteresis width of a PZT-5A ceramic at 77 K.

5.4.2 Creep measurements

The creep properties of PZT-5A were investigated from 10 K to 295 K. Figures 5.48 and 5.49 show the time-dependent piezoelectric displacement (nm) and applied voltage (V) at 10 and 35 K. In the 10 K data the noise level varied, but this did not reflect any changes in measurement settings. There was almost no creep at 10 K, which is consistent with the lack of hysteresis at this temperature. At 35 K, a little creep was observed, again consistent with the hysteresis data in the previous section. The creep (after subtracting any drift) is shown in Figure 5.50 for temperatures between 10 K and 295 K. It increases with temperature up to 225 K, but above 225 K the creep curves are almost the same. Figure 5.51 shows a logarithmic fit of the creep data at 77 K. Figure 5.52 shows the coefficient c that is calculated from the logarithmic fits at each temperature.

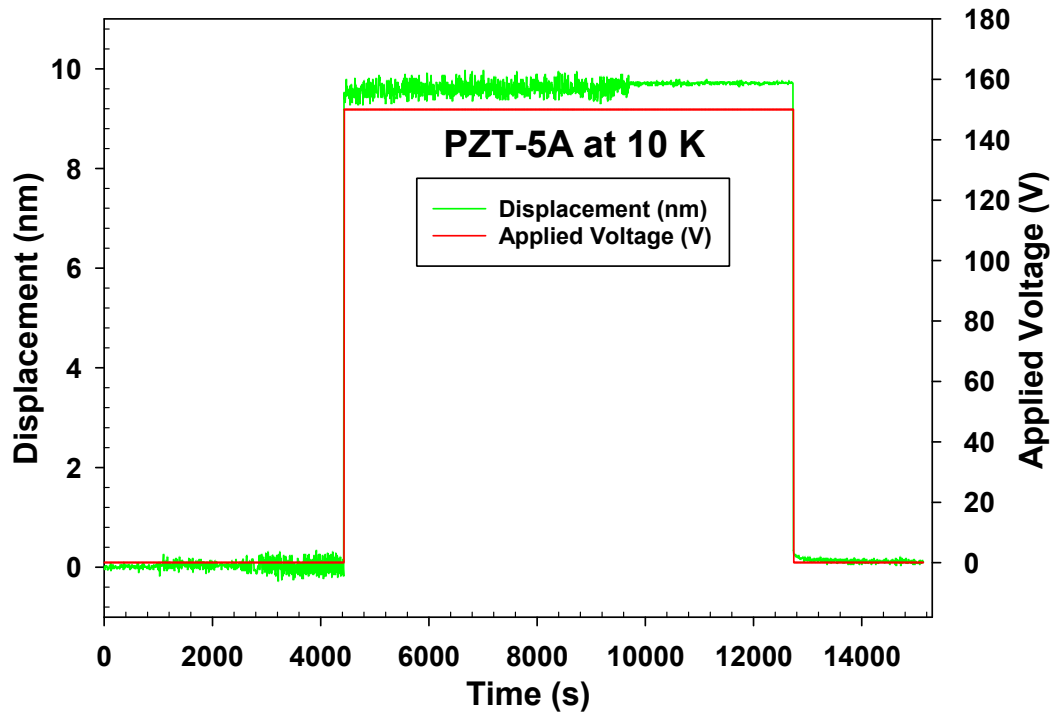


Figure 5.48: Displacement vs. time for a constant applied voltage 150 V at 10 K.

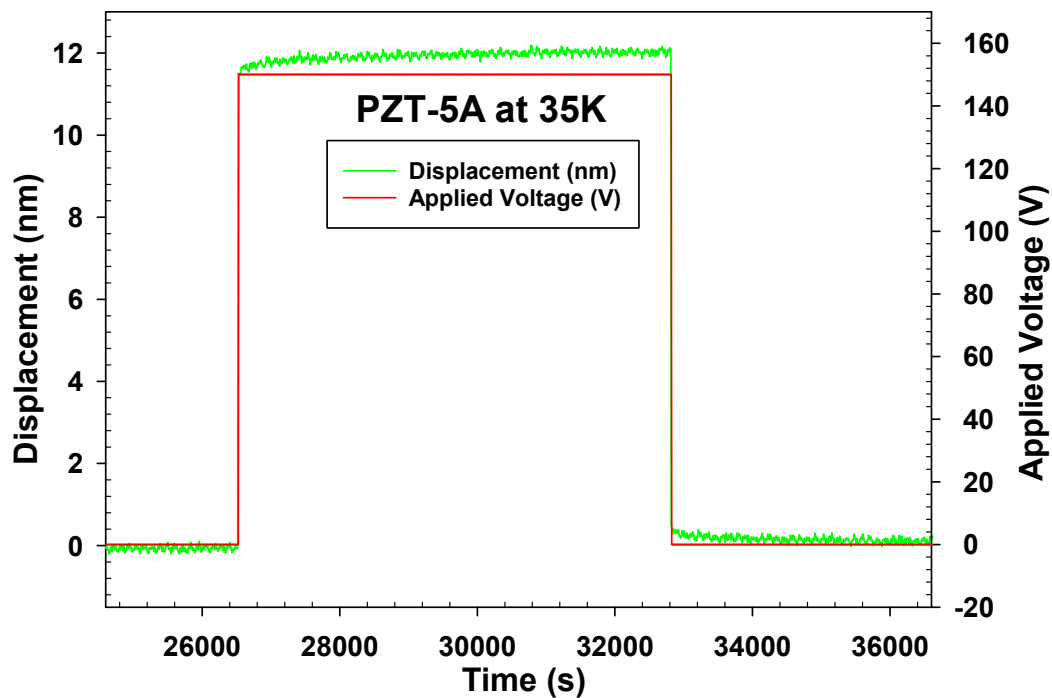


Figure 5.49: Creep of the PZT-5A ceramic at 77 K, for changes in applied voltage of 150 V.

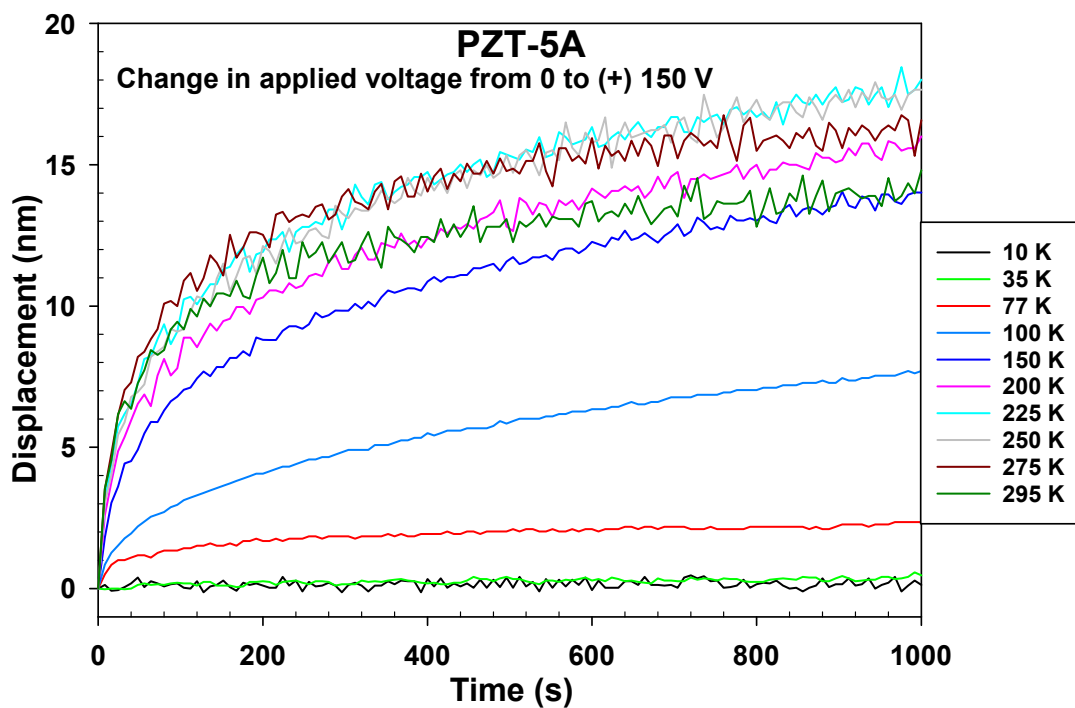


Figure 5.50: Temperature dependence of creep for the shear PZT-5A ceramic following a voltage change $\Delta V = 150 \text{ V}$ ($0 \rightarrow +150 \text{ V}$).

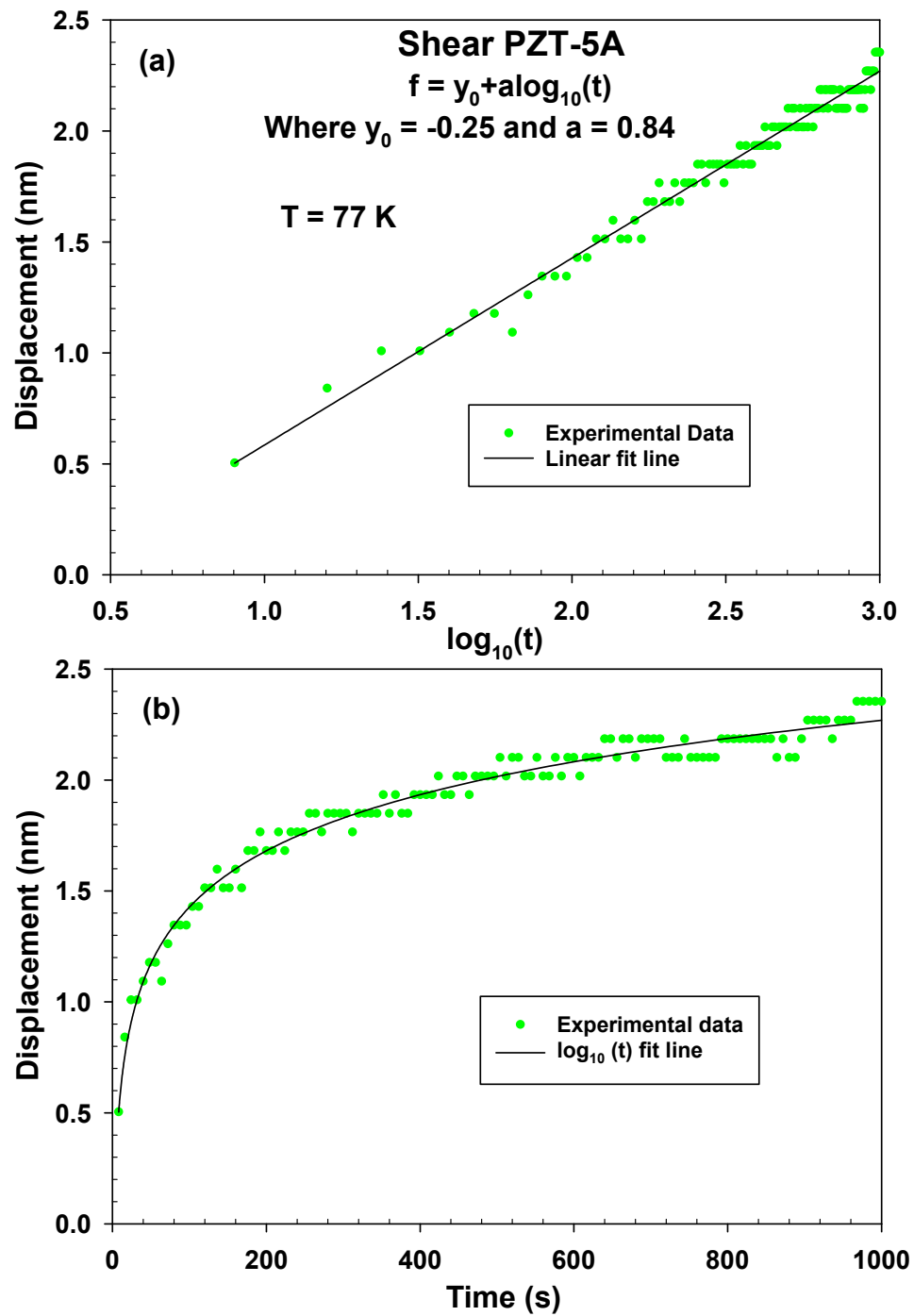


Figure 5.51: Logarithmic fit of creep data for the PZT-5A ceramic following an applied voltage change $\Delta V = 150 \text{ V}$.

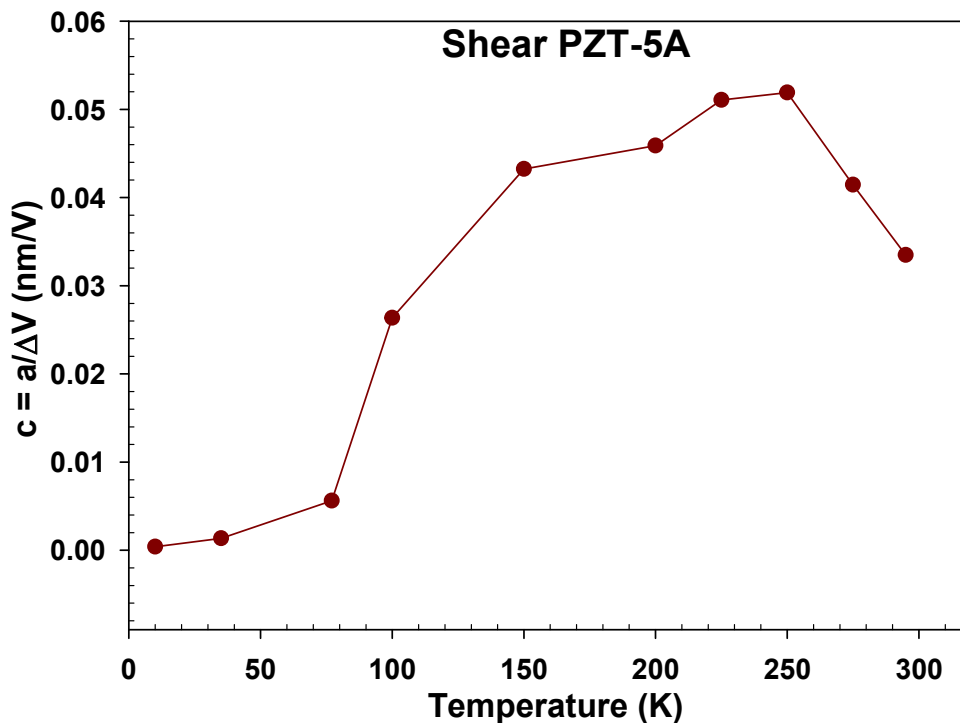


Figure 5.52: Temperature dependence of the coefficient c calculated from logarithmic fits of creep data for the PZT-5A ceramic.

5.5 Discussion

The 41° X-cut (pure shear) LiNbO_3 single crystal had no hysteresis or creep in the temperature range between 10 K and room temperature. The piezoelectric displacement increased linearly with the applied voltage. This is consistent with the behavior of a 36° Y-cut LiNbO_3 stack reported by Kawamata *et al.* [27]. The thickness (0.26 mm) of our 41° X-cut LiNbO_3 was four times thinner than the PMN-PT transducer (1 mm) and seven times thinner than the PZT-5A transducer (1.78 mm). Applying a 150 V to the LiNbO_3 transducer corresponds to a much higher electric field (E) than was used for the PMN-PT or PZT-5A transducers. The linearity and lack of hysteresis and creep at high fields at all temperature make it a very good candidate for positioning applications like STM, AFM, particularly at cryogenic temperatures.

For the shear PMN-PT crystal, the hysteresis width is comparable to the creep coefficient c in Figure 5.53. The red circular dots with error bar depict the directly measured hysteresis widths and the dark red circular dots show the creep coefficients c , respectively. Both curves show similar behavior, confirming that creep is responsible for the hysteresis. The creep and hysteresis in PMN-PT has an unusual temperature dependence. The negative creep and hysteresis seen between 150 K and 270 K appears

to be unique and has never been reported in any piezoelectric material.

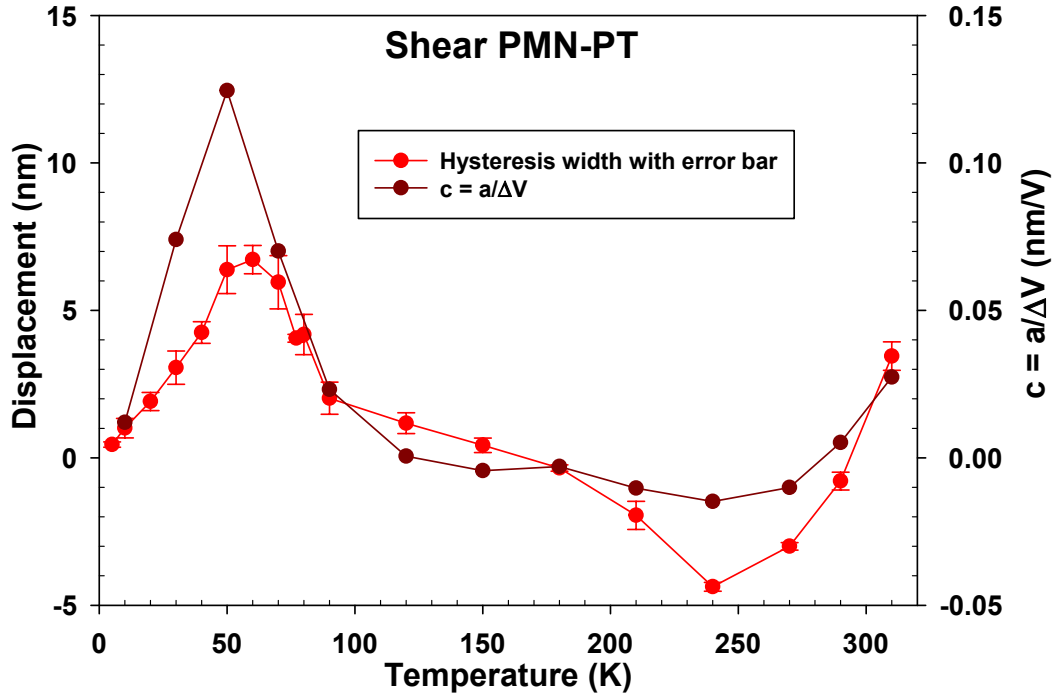


Figure 5.53: Temperature dependence of the hysteresis width (red dots) and the creep coefficients c (dark red dots) for a shear PMN-PT single crystal.

Figure 5.54 compares the piezoelectric and dielectric behavior of the shear PMN-PT transducer. The piezoelectric coefficient d_{15} and hysteresis, and the dielectric constant K_{11}^σ and loss conductance G , are strongly temperature dependent but show common features.

Both d_{15} and K_{11}^σ are smallest at low temperature and increase rapidly up to about 70 K. They are much less temperature dependent between 100 K and 200 K, the plateau region. Above 200 K, they increase more rapidly. These similarities reflect the common origin of piezoelectric and dielectric properties in crystal dipoles and ferroelectric domains.

Dielectric loss is associated with hysteresis in P-E (polarization-electric field) cycles, so can be compared to displacement hysteresis in piezoelectrics. The main features of the hysteresis width and the dielectric loss in Figure 5.54 are large peaks around 70 K. Such peaks are often associated with a temperature dependent relaxation process, for example the motion of domains walls depend on the measurement frequency. Note that the effective frequency for the hysteresis measurements ($f \approx 0.01$ Hz) is much lower than 1000 Hz used by capacitance bridge for the dielec-

tric measurements. This would shift a thermal relaxation peak to lower temperature for the low frequency hysteresis measurements, as observed. The hysteresis peak is in the region where d_{15} is changing most rapidly, as expected for a relaxation process.

However, the region of negative hysteresis between 150 K and 270 K does not have a counter part in dielectric loss data. This suggests that it does not have the same origin as the positive hysteresis peak at low temperature. It is possible that different types of domain walls are involved in the hysteresis, some of which do not contribute to the dielectric loss.

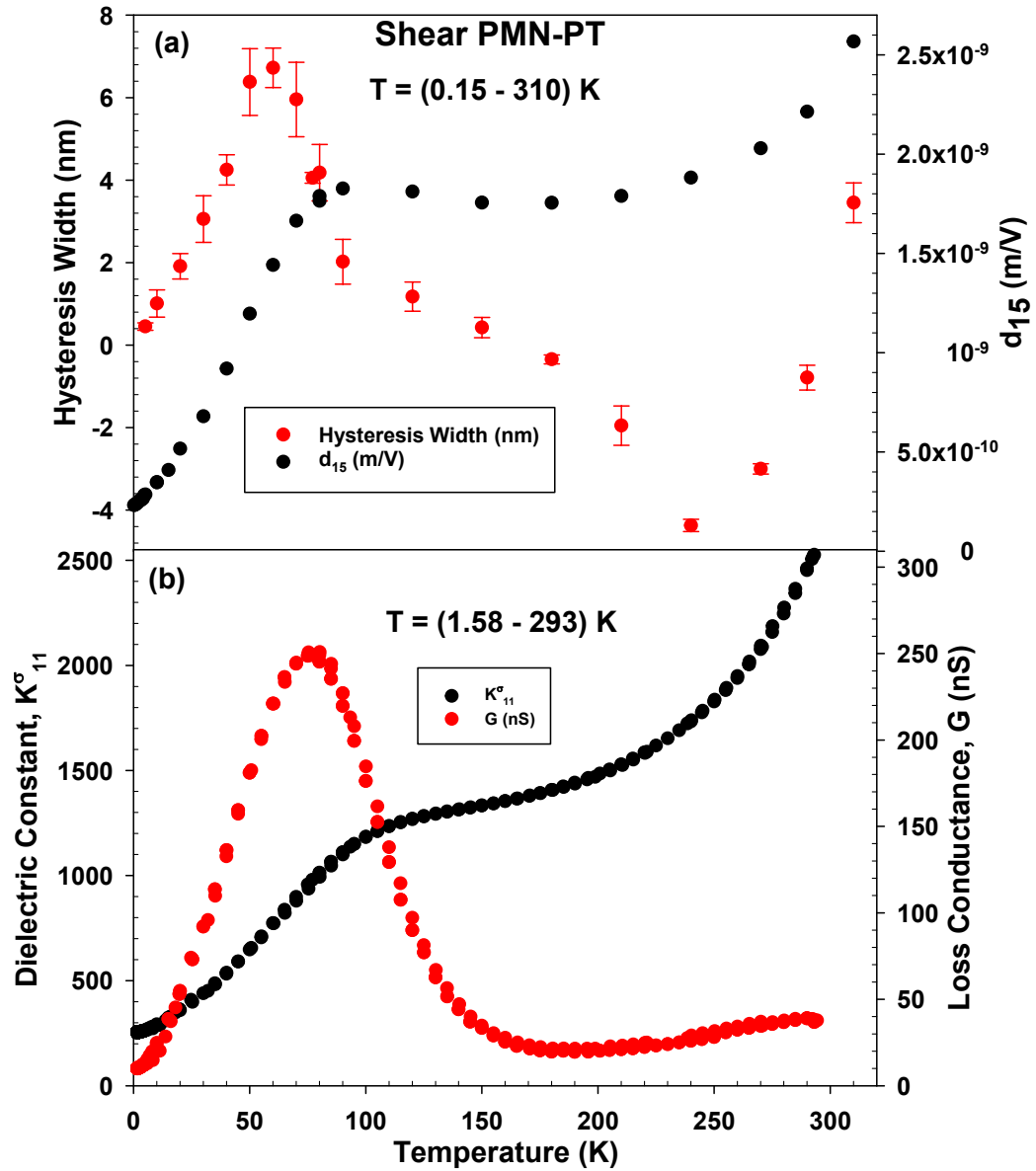


Figure 5.54: Temperature dependence of (a) d_{15} and hysteresis width and (b) dielectric constant and dielectric loss for the shear PMN-PT single crystal.

Figure 5.55 shows the hysteresis width and the creep coefficients c for the PZT-5A ceramic transducer. The creep and hysteresis are positive (CCW) at all temperatures. The hysteresis width varies monotonically with temperature but the coefficient c increases up to 250 K, then appears to decrease. It is possible that the creep data at the highest temperatures are affected by thermal drift and temperature control, but some of the hysteresis width data at same lower voltages (Figure 5.46) also show a decrease above 270 K.

Figure 5.56 compares the piezoelectric and dielectric behavior of the ceramic shear PZT-5A transducer. The piezoelectric coefficient d_{15} and hysteresis, and the dielectric constant K_{11}^σ and loss conductance G , all increase monotonically with temperature.

The behavior of PZT-5A however, is different from that shown in Figure 5.54 for the relaxor ferroelectric PMN-PT. The piezoelectric d_{15} and hysteresis width in PZT-5A have similar temperature dependences, with neither a plateau region nor a hysteresis peak. The dielectric constant K_{11}^σ has a temperature dependence to similar d_{15} . The ratios of room temperature and low temperature values are even similar: 4.5 for d_{15} and 4.0 for K_{11}^σ . The dielectric loss G for PZT-5A has a similar overall temperature dependence, although there appear to be small loss peaks around 120 K and 270 K.

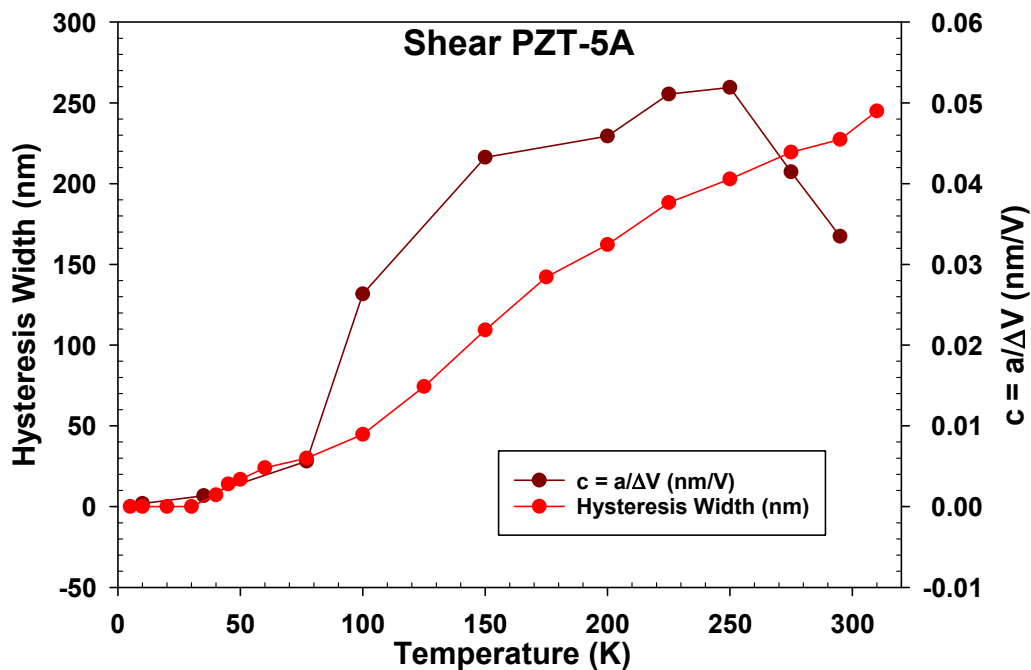


Figure 5.55: Comparison of the temperature dependence of the hysteresis width and the creep coefficient c for the PZT-5A ceramic for applied voltages between -150 and +150 V.

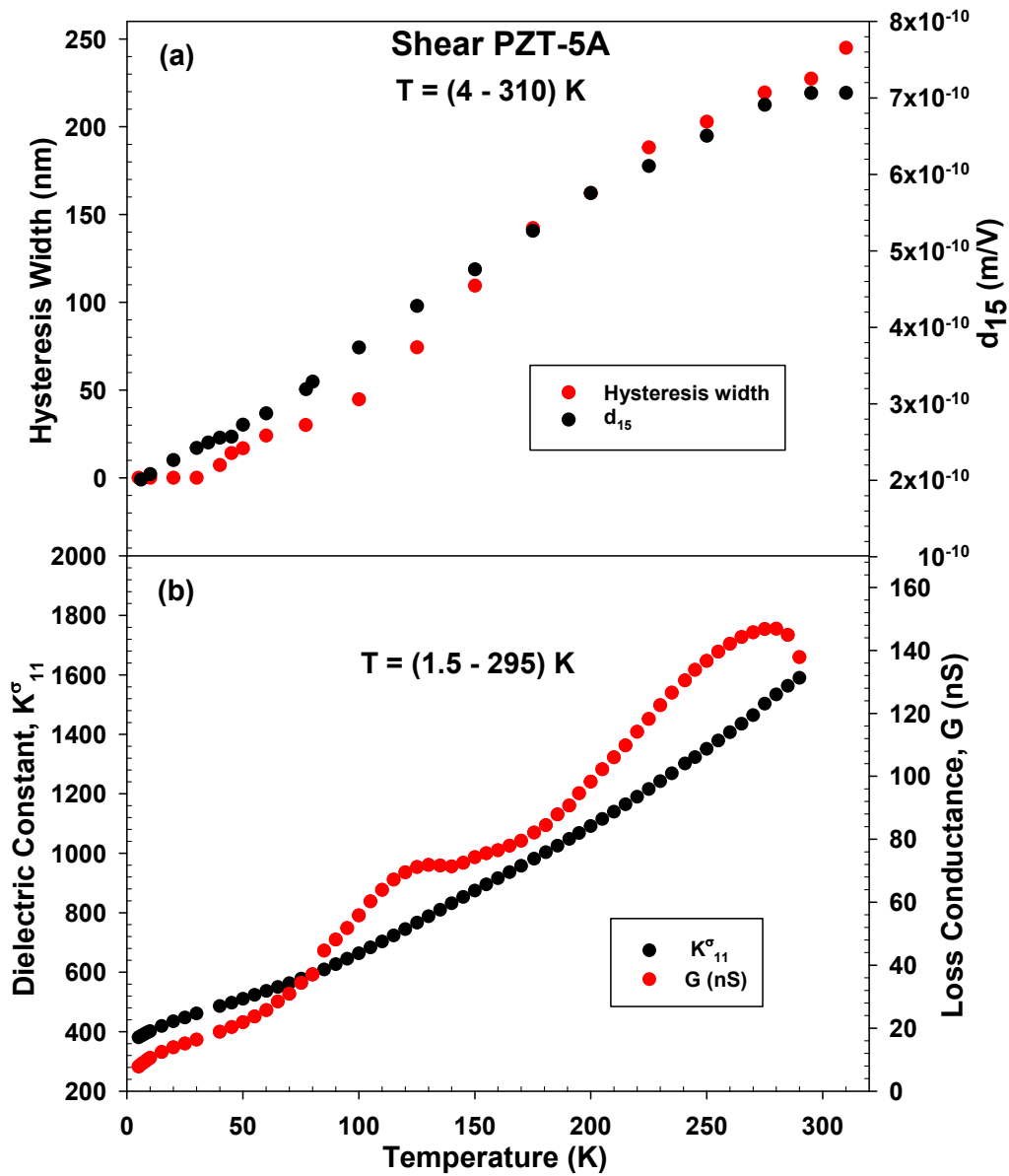


Figure 5.56: Temperature dependence of (a) d_{15} and hysteresis width for ± 150 V and (b) dielectric constant and dielectric loss for the shear PZT-5A ceramic.

Figure 5.57 compares the temperature dependence of the hysteresis width for all three materials, for the same applied voltage range -50 V and +50 V. The LiNbO_3 single crystal (blue dots) has no measurable hysteresis at any temperature. The PMN-PT single crystal (red dots) has a large and strongly temperature dependence hysteresis, including a region of negative hysteresis. The PZT-5A ceramic (green dots) has a very small hysteresis below 35 K which increases monotonically at higher temperature. Below 5 K, the response of all three materials is linear and non-hysteretic for applied voltages between -150 and +150 V.

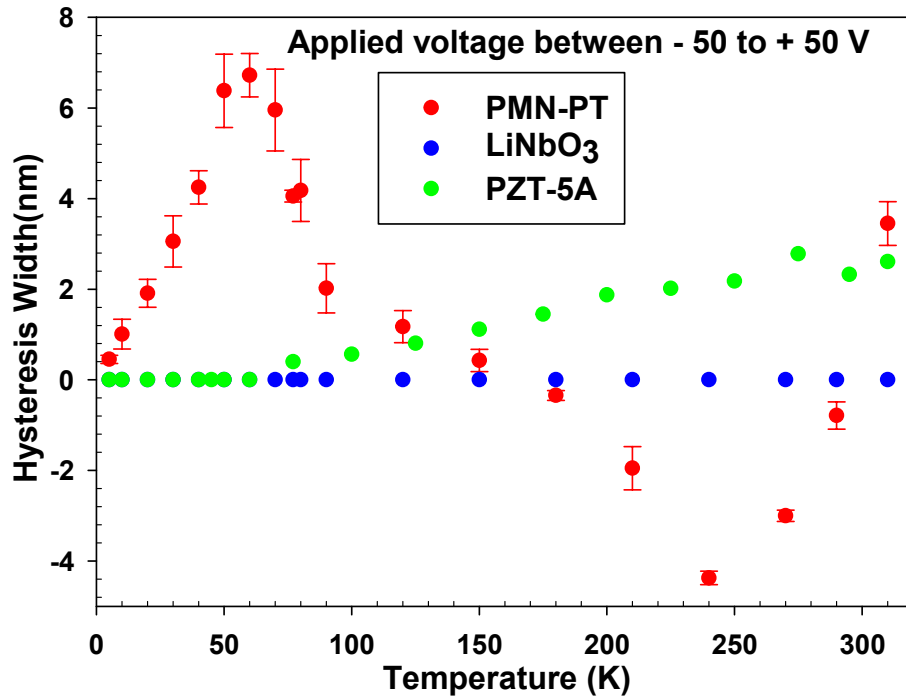


Figure 5.57: Comparison of the temperature dependence of the hysteresis width of the three materials for applied voltages between - 50 and + 50 V.

Chapter 6

Conclusion

This conclusion chapter summarizes the main results from the thesis. We have made a broad study of the piezoelectric and dielectric properties of three widely used materials, at temperatures as low as 78 mK. The materials included LiNbO₃ (a single domain, single crystal with a high Curie temperature), PMN-PT (a single crystal relaxor ferroelectric) and PZT-5A (a ceramic). Most of the measurements were done on shear polarized transducers, although longitudinal PMN-PT and PZT-5A transducers were also studied. The piezoelectric measurements included shear and longitudinal piezoelectric coefficients (d_{15} and d_{33}), displacement hysteresis and creep. The dielectric constants K_{11}^{σ} , K_{33}^{σ} and loss conductance G were measured, allowing the piezoelectric voltage coefficients (g_{15} and g_{33}) to be determined.

Shear transducers are used in ultrasonics, and in some sensors, but are not as widely used as longitudinal transducers in positioning applications. However, shear transducers have some advantages. The shear coefficient d_{15} is typically larger than the longitudinal coefficient d_{33} (by a factor of 2 more for the materials in this thesis), allowing larger displacements for the same applied voltage. Shear transducers also do not suffer from the clamping effects that can reduce d_{33} , since there are no transverse displacements associated with shear deformations.

Despite these advantages, there are few reported measurements of shear piezoelectric properties at cryogenic temperatures. Before the work reported in this thesis, there were no measurements for LiNbO₃ below room temperature, no shear measurements on PMN-PT below the plateau region that extends to 75 K, and no measurements on any of the materials in the very low temperature region below 4 K.

This thesis focusses primarily on the properties of shear piezoelectric transducers. It includes measurements of their piezoelectric coefficient d_{15} , which is important for displacement actuators, and the dielectric constant K_{11}^{σ} , which allows the voltage coefficient g_{15} to be determined for sensor applications. It also includes direct

measurements of the hysteresis and creep that limit stability and reproducibility in precise positioning applications.

The results in Chapter 4 show that LiNbO_3 has the lowest d_{15} values at all temperatures and that d_{15} is weakly temperature dependent, dropping by only about 5% at the lowest temperature. PMN-PT has the largest d_{15} at room temperature, but this advantage largely disappears at the lowest temperature where d_{15} is reduced by a factor of 10. The coefficient d_{15} of the PZT-5A ceramic is 5 times smaller than that of PMN-PT at room temperature and drops by a factor of 5 at the lowest temperature. Although the room temperature values of d_{15} for the three materials vary by a factor of 46 (from 69.4×10^{-12} m/V for LiNbO_3 to 3200×10^{-12} m/V for PMN-PT) they vary by less than a factor of 5 at the lowest temperatures (from 65.9×10^{-12} m/V for LiNbO_3 to 315.8×10^{-12} m/V for PMN-PT). Although LiNbO_3 has the smallest d_{15} value, the differences at low temperature are small and below 20 K a stack of three LiNbO_3 transducers produces a larger displacement than a PZT-5A transducer.

The dielectric constants K_{11}^σ of the three materials have temperature dependences similar to d_{15} . In LiNbO_3 , the room temperature value drops by about 7% at the lowest temperature, and the loss conductance is small. PMN-PT has the largest room temperature K_{11}^σ , which drops by a factor of 10 at the lowest temperature, and its loss conductance shows a large relaxation peak around 75 K. In PZT-5A, K_{11}^σ is smaller than that of PMN-PT at the room temperature and decreases by a factor of 5 at the lowest temperature. PZT's loss conductance decreases nearly linearly with temperature, with two small loss peaks around 120 K and 240 K. At room temperature, the materials' dielectric constants K_{11}^σ vary by a factor of 29 (from 88 for LiNbO_3 to 2550 for PMN-PT) but vary by less than a factor of 5 at the lowest temperature (from 82.2 for LiNbO_3 to 369 for PZT-5A).

The PMN-PT single crystal has the largest voltage coefficient g_{15} value and PZT-5A ceramic has the lowest g_{15} value at all temperatures. For LiNbO_3 and PZT-5A, g_{15} is almost independent of temperature but for PMN-PT it has a maximum value around 60 K. This suggests that PMN-PT is the best choice for shear cryogenic sensors (it has the largest sensitivity), although LiNbO_3 may be preferred if a constant sensitivity is needed.

However, in choosing appropriate piezoelectric sensors, it is important to consider their dielectric constants (capacitances), the input impedance of the measurements circuit, and the frequency of the signal being measured. All three materials would be effective cryogenic ultrasonics sensors (and both PZT and LiNbO_3 have been used at low temperatures), but it would be challenging to use any of them as voltage sensors at frequencies below 1 kHz, since high input impedance would be needed. Given its

nearly constant sensitivity g_{15} and dielectric constant LiNbO₃ is probably the best sensor choice for precise measurements that cover a wide temperature range. For low frequency sensor applications, using current pre-amplifiers, rather than voltage pre-amplifiers, avoids such frequency issues. However, the relevant sensitivity parameter to select a suitable transducer is then the coefficient d_{ij} , not g_{ij} .

The implication for selecting the best material for positioning actuators that need large displacement involve d_{15} . At cryogenic temperatures, one can use a LiNbO₃ transducer/stack to achieve this. Note that LiNbO₃ transducers have been used to study solidification and superfluidity of ⁴He below 1 K [60].

The origins of the temperature dependence of the piezoelectric and dielectric properties of these three materials can be summarized in terms of intrinsic and extrinsic contributions. LiNbO₃ is a single crystal with single ferroelectric domain and a very high Curie temperature. Its piezoelectric and dielectric properties have a weak temperature dependence which primarily comes from intrinsic behavior like thermal expansion of the crystal.

PMN-PT is a relaxor piezoelectric material. Like LiNbO₃, it is a single crystal, but has a multi-domain structure and a very low Curie temperature. Its large d_{ij} at room temperature and in the plateau above 100 K is due to extrinsic mechanism like domain wall motion, which freeze out at temperatures, producing the rapid drop of d_{15} below 75 K. Surprisingly the d_{ij} of PMN-PT at the lowest temperatures vary nearly linearly down to at least 0.2 K, far below the relaxation peak at 70 K. There must be a wide range of small energy scales involved in domain wall motion. One has to be aware of this temperature dependence if PMN-PT transducers are used in precise measurements below 4 K.

PZT-5A is a ceramic, with small crystallinities and domains. Its d_{ij} , g_{ij} and K_{ij}^σ , are intermediate between LiNbO₃ and PMN-PT and d_{ij} is also temperature dependent below 4 K. However, there is no large relaxation peak and no plateau region for d_{ij} and K_{ij}^σ , which may be because the motion of domain walls and defects is limited by grain boundaries.

Precise positioning actuators require reproducible and time-independent displacements, so hysteresis and creep limit their performance. Intrinsic effects (LiNbO₃) are not expected to produce hysteresis or creep. Extrinsic effects (PMN-PT and PZT) do produce hysteresis and creep but these are expected to freeze out, so hysteresis and creep may be much smaller at low temperatures.

The results in Chapter 5 showed that LiNbO₃ has no measurable creep or hysteresis in the entire temperature range, for any voltage. PMN-PT has the largest hysteresis and creep. Displacement vs. voltage measurements showed both posi-

tive (CCW) and negative (CW) hysteresis at temperatures between 5 K and 310 K. Hysteresis and creep are strongly temperature dependent, with the highest positive values around 60 K and the largest negative values at 240 K. Even below 20 K, creep is still significant. The hysteresis width and creep coefficient show similar behavior, confirming that creep is the source of the hysteresis.

PZT-5A has intermediate hysteresis and creep, which are always positive (CCW) and increase monotonically with temperature from 35 K to 310 K. Hysteresis and creep are too small to measure below 30 K.

LiNbO_3 transducers can be cut very thin and can tolerate very high voltages without depolarizing, compared to the other two. Considering their linear displacements and complete absence of creep or hysteresis, this makes them an almost ideal choice for cryogenic applications where PMN-PT and PZT no longer have the advantage of much larger values of d_{15} .

We can also relate the creep and hysteresis of these three materials to their structure. LiNbO_3 is a single crystal and a single domain, with only intrinsic behavior. As expected it shows no hysteresis or creep. PMN-PT is also a single crystal, but has multiple domains and its properties are dominated by extrinsic effects like domain wall motion, which produce large hysteresis and creep. The plateaus in d_{15} and K_{11}^σ are correlated with the hysteresis, creep and dielectric loss. The region of negative creep between 150 K and 270 K is unexpected and unique to PMN-PT. The dielectric loss G does not show a corresponding feature in this temperature range, suggesting that the negative creep mechanism does not affect the dielectric behavior. PZT's behavior is also dominated by extrinsic effects, but its creep and hysteresis are smaller than those of PMN-PT, which suggests that domain walls are less mobile, perhaps because of pinning by grain boundaries.

The hysteresis and creep in PMN-PT extend to temperatures below 10 K, which is consistent with weakly pinned domain walls. In PZT, the hysteresis disappears below 30 K, as expected if its domain walls are pinned by grain boundaries.

The results presented in this thesis provide a practical guide for selecting piezoelectric materials for cryogenic actuators and sensors. The magnitude and temperature dependence of the three materials piezoelectric properties can be understood in terms of intrinsic and extrinsic mechanisms in single crystals and ceramics. Several new features were observed, including a direct connection between creep and hysteresis, a unique region of negative creep in PMN-PT, and a surprisingly strong low temperature dependence of d_{15} for PMN-PT and PZT-5A that extends well below 1 K.

Bibliography

- [1] G. Gautschi. Piezoelectric Sensorics. Springer, 2002.
- [2] B. Jaffe. Piezoelectric ceramics, volume 3. Elsevier, 2012.
- [3] M. W. Hooker. Properties of PZT-based piezoelectric ceramics between-150 and 250 °C. 1998.
- [4] Piezo Systems Inc. PSI-5A4E piezoelectric sheets and their properties. 2011, <http://www.piezo.com>.
- [5] S. S. Rao and M. Sunar. Piezoelectricity and its use in disturbance sensing and control of flexible structures: a survey. *Applied Mechanics Reviews*, 47(4):113–123, 1994.
- [6] R. G. Loewy. Recent developments in smart structures with aeronautical applications. *Smart Materials and Structures*, 6(5):R11, 1997.
- [7] S. A. Wise. Displacement properties of RAINBOW and THUNDER piezoelectric actuators. *Sensors and Actuators A: Physical*, 69(1):33–38, 1998.
- [8] V. A. Neelakantan, G. N. Washington and N. K. Bucknor. Model predictive control of a two stage actuation system using piezoelectric actuators for controllable industrial and automotive brakes and clutches. *Journal of Intelligent Material Systems and Structures*, 19(7):845–857, 2008.
- [9] G. Schitter and M. J. Rost. Scanning probe microscopy at video-rate. *Materials Today*, 11:40–48, 2008.
- [10] Q. Zhou K. H. Lam H. Zheng, W. Qiu and K. K. Shung. Piezoelectric single crystal ultrasonic transducers for biomedical applications. *Progress in Materials Science*, 66:87–111, 2014.
- [11] J. Day and J. Beamish. Low-temperature shear modulus changes in solid ^4He and connection to supersolidity. *Nature*, 450(7171):853–856, 2007.

- [12] A. Haziot X. Rojas A. D. Fefferman, J. R. Beamish and S. Balibar. Giant plasticity of a quantum crystal. *Physical Review Letters*, 110(3):035301, 2013.
- [13] S. A. Elrod, A. L. de L.ozanne and C. F. Quate. Low-temperature vacuum tunneling microscopy. *Applied Physics Letters*, 45(11):1240–1242, 1984.
- [14] F. Wang W. Shi S. W. Or, X. Zhao and H. Luo. Cryogenic transverse and shear mode properties of $(1-x)\text{Pb}(\text{Mg}_{1/3}\text{Nb}_{2/3})\text{O}_3\text{-xPbTiO}_3$ single crystal with the optimal crystallographic direction. *Materials Chemistry and Physics*, 125(3):718–722, 2011.
- [15] B. Yurke, P. G. Kaminsky and D. M. Eigler. Cryogenic piezoelectric displacement tester. *Cryogenics*, 26(7):435–436, 1986.
- [16] S. Georges M. Ribal K. Binu, W. Ren and G. Yang. Temperature dependence of the complete material coefficients matrix of soft and hard doped piezoelectric lead zirconate titanate ceramics. *Journal of Applied Physics*, 101(6):064111, 2007.
- [17] X. L. Zhang Z. X. Chen, L. E. Cross and W. A. Schulze. Dielectric and piezoelectric properties of modified lead titanate zirconate ceramics from 4.2 to 300 K. *Journal of Materials Science*, 18(4):968–972, 1983.
- [18] N. Yamada, T. Niizeki and H. Toyoda. Piezoelectric and elastic properties of lithium niobate single crystals. *Japanese Journal of Applied Physics*, 6(2):151, 1967.
- [19] R. T. Smith and F. S. Welsh. Temperature dependence of the elastic, piezoelectric, and dielectric constants of lithium tantalate and lithium niobate. *Journal of Applied Physics*, 42(6):2219–2230, 1971.
- [20] R. S. Weis and T. K. Gaylord. Lithium niobate: summary of physical properties and crystal structure. *Applied Physics A: Materials Science & Processing*, 37(4):191–203, 1985.
- [21] F. Martin H. J. M. ter Brake L. Lebrun, S. Zhang and T. Shrout. Dielectric and piezoelectric activities in $(1-x)\text{Pb}(\text{Mg}_{1/3}\text{Nb}_{2/3})\text{O}_3\text{-xPbTiO}_3$ single crystals from 5 K to 300 K. *Journal of Applied Physics*, 111(10):104108, 2012.
- [22] S. Bukhari M. Islam, A. Haziot and J. Beamish. Shear piezoelectric coefficients of PZT, LiNbO_3 and PMN-PT at cryogenic temperatures. In *Journal of Physics: Conference Series*, volume 568, page 032004. IOP Publishing, 2014.

- [23] S. B. Jung and S. W. Kim. Improvement of scanning accuracy of PZT piezoelectric actuators by feed-forward model-reference control. *Precision Engineering*, 16(1):49–55, 1994.
- [24] K. G. Vandervoort R. K. Zasadzinski, G. G. Galicia and G. W. Crabtree. Full temperature calibration from 4 to 300 K of the voltage response of piezoelectric tube scanner PZT-5A for use in scanning tunneling microscopes. *Review of Scientific Instruments*, 64(4):896–899, 1993.
- [25] H. Jung, J. Y. Shim and D. Gweon. New open-loop actuating method of piezoelectric actuators for removing hysteresis and creep. *Review of Scientific Instruments*, 71(9):3436–3440, 2000.
- [26] M. Fouaidy G. Martinet N. Hammoudi, F. Chatelet and A. Olivier. Characterization at cryogenic temperatures of piezostacks dedicated to fast tuners for SRF cavities. In *Mixed Design of Integrated Circuits and Systems, 2007. MIXDES'07. 14th International Conference on*, pages 17–22. IEEE, 2007.
- [27] A. Kawamata, H. Hosaka and T. Morita. Non-hysteresis and perfect linear piezoelectric performance of a multilayered lithium niobate actuator. *Sensors and Actuators A: Physical*, 135(2):782–786, 2007.
- [28] W. Guo D. Jin W. Wei H. J. Maris J. Tian, X. Huang and P. Han. Low temperature piezoelectric and dielectric properties of lead magnesium niobate titanate single crystals. *Journal of Applied Physics*, 102(8):084104, 2007.
- [29] Q. M. Zhang H. Wang, N. Kim and L. E. Cross. Direct evaluation of domain-wall and intrinsic contributions to the dielectric and piezoelectric response and their temperature dependence on lead zirconate-titanate ceramics. *Journal of Applied Physics*, 75(1):454–459, 1994.
- [30] M. J. Haun E. Furman, S. J. Jang and L. E. Cross. Thermodynamic theory of the lead zirconate-titanate solid solution system, part V: theoretical calculations. *Ferroelectrics*, 99(1):63–86, 1989.
- [31] M. J. Haun E. Furman, S. J. Jang and L. E. Cross. Thermodynamic theory of the lead zirconate-titanate solid solution system, part I: phenomenology. *Ferroelectrics*, 99(1):13–25, 1989.
- [32] C. A. Randall N. Kim J. P. Kucera, W. Cao and T. R. ShROUT. Intrinsic and extrinsic size effects in fine-grained morphotropic-phase-boundary lead zirconate

- titanate ceramics. *Journal of the American Ceramic Society*, 81(3):677–688, 1998.
- [33] J. F. Nye. *Physical properties of crystals: their representation by tensors and matrices*. Oxford University Press, 1985.
- [34] G. E. Bithell. Part II Materials Science, Tensors , Course C4 (9 + 2 lectures). <https://www.scribd.com/document/372735955/Tensor-n-Examples>, 2012.
- [35] D. R. Lovett. *Tensor properties of crystals*. IOP Publishing Ltd, 1999.
- [36] APC International Ltd. *Piezoelectric ceramics: principles and applications*. APC International, 2002.
- [37] S. P. Torah, R. N. Beeby and N. M. White. Experimental investigation into the effect of substrate clamping on the piezoelectric behaviour of thick-film PZT elements. *Journal of Physics D: Applied Physics*, 37(7):1074, 2004.
- [38] R. F. Tinder. *Tensor properties of solids: phenomenological development of the tensor properties of crystals, volume 4*. Morgan & Claypool Publishers, 2008.
- [39] R. E. Newnham. *Structure-property relations, volume 2*. Springer Science & Business Media, 2012.
- [40] G. Arlt. Twinning in ferroelectric and ferroelastic ceramics: stress relief. *Journal of Materials Science*, 25(6):2655–2666, 1990.
- [41] J. C. Burfoot and G. W. Taylor. *Polar dielectrics and their applications*. University of California Press, 1979.
- [42] M. E. Lines and A. M. Glass. *Principles and applications of ferroelectrics and related materials*. Oxford University Press, 1977.
- [43] D. Damjanovic. Ferroelectric, dielectric and piezoelectric properties of ferroelectric thin films and ceramics. *Reports on Progress in Physics*, 61(9):1267, 1998.
- [44] P. R. Potnis, N. T. Tsou and J. E. Huber. A review of domain modelling and domain imaging techniques in ferroelectric crystals. *Materials*, 4(2):417–447, 2011.
- [45] S. A. M. Bukhari. Temperature dependence of the piezoelectric shear coefficient of PMN-PT, LiNbO₃ and PZT transducers, Master of Science Thesis, 2014, University of Alberta.

- [46] L. Jin, F. Li and S. Zhang. Decoding the fingerprint of ferroelectric loops: comprehension of the material properties and structures. *Journal of the American Ceramic Society*, 97(1):1–27, 2014.
- [47] J. P. Issartel. Multilayer piezoelectric actuator stack and method for its manufacture, September 21 1993. US Patent 5,245,734.
- [48] B. T. Matthias and J. P. Remeika. Ferroelectricity in the ilmenite structure. *Physical Review*, 76(12):1886, 1949.
- [49] A. W. Warner, M. Onoe and G. A. Coquin. Determination of elastic and piezoelectric constants for crystals in class (3 m). *The Journal of the Acoustical Society of America*, 42(6):1223–1231, 1967.
- [50] S. C. Abrahams, H. J. Levinstein and J. M. Reddy. Ferroelectric lithium niobate. 5. polycrystal X-ray diffraction study between 24 and 1200 C. *Journal of Physics and Chemistry of Solids*, 27(6-7):1019–1026, 1966.
- [51] T. Volk and M. Wöhlecke. *Lithium niobate: defects, photorefractive and ferroelectric switching*, volume 115. Springer Science & Business Media, 2008.
- [52] B. K. Vainshtein. *Modern crystallography. vol. 1. Fundamentals of crystals. symmetry, and methods of structural crystallography.* *Acta Cryst*, 51:234–235, 1995.
- [53] Y. Guo H. Luo D. Ling H. Xu, T. He and Z. Yin. The phase transition sequence and the location of the morphotropic phase boundary region in $(1-x)\text{Pb}(\text{Mg}_{1/3}\text{Nb}_{2/3})\text{O}_3\text{-xPbTiO}_3$ single crystal. *Journal of Physics: Condensed Matter*, 15(2):L77, 2003.
- [54] S. E. Park and T. R. Shrout. Relaxor based ferroelectric single crystals for electro-mechanical actuators. *Materials Research Innovations*, 1(1):20–25, 1997.
- [55] S. E. Park and T. R. Shrout. Ultrahigh strain and piezoelectric behavior in relaxor based ferroelectric single crystals. *Journal of Applied Physics*, 82(4):1804–1811, 1997.
- [56] M. S. Kim J. G. Fisher, S. J. L. Kang and H. Y. Lee. Grain growth control and solid-state crystal growth by $\text{Li}_2\text{O}/\text{PbO}$ addition and dislocation introduction in the PMN–35PT system. *Journal of the American Ceramic Society*, 89(4):1237–1243, 2006.

- [57] Z. G. Ye. Handbook of advanced dielectric, piezoelectric and ferroelectric materials: Synthesis, properties and applications. Elsevier, 2008.
- [58] K. Uchino. Introduction to piezoelectric actuators and transducers. Technical report, Pennsylvania State University Park, 2003.
- [59] Y. I. Sirotin and M. P. Shaskolskaya. Fundamentals of crystal physics. MIR publishers, 1982.
- [60] J. R. Beamish A. Hikata, L. Tell and C. Elbaum. Solidification and superfluidity of ^4He in porous vycor glass. *Physical Review Letters*, 50(6):425, 1983.
- [61] R. Bechmann K. Hellwege A. M. Hellwege, R. F. S. Hearmon and S. K. Kurtz. Elastic, Piezoelectric, Piezooptic, Electrooptic Constants, and Nonlinear Dielectric Susceptibilities of Crystals: Elastische, Piezoelektrische, Piezooptische, Elektrooptische Konstanten and Nichtlineare Dielektrische Suszeptibilitäten Von Kristallen. Springer Verlag, 1969.
- [62] D. Wang, Y. Fotinich and G. P. Carman. Influence of temperature on the electromechanical and fatigue behavior of piezoelectric ceramics. *Journal of Applied Physics*, 83(10):5342–5350, 1998.
- [63] A. J. Moulson and J. M. Herbert. *Electroceramics: materials, properties, applications*. John Wiley & Sons, 2003.
- [64] M. S. Senousy R. K. N. D. Rajapakse, D. Mumford and M. S. Gadala. Self-heat generation in piezoelectric stack actuators used in fuel injectors. *Smart Materials and Structures*, 18(4):045008, 2009.
- [65] K. Uchino and S. Hirose. Loss mechanisms in piezoelectrics: how to measure different losses separately. *IEEE Transactions on Ultrasonics, Ferroelectrics, and Frequency Control*, 48(1):307–321, 2001.
- [66] A. Ochi, S. Takahashi and S. Tagami. Temperature characteristics for multilayer piezoelectric ceramic actuator. *Japanese Journal of Applied Physics*, 24(S3):209, 1985.
- [67] X. Lu and S. V. Hanagud. Extended irreversible thermodynamics modeling for self-heating and dissipation in piezoelectric ceramics. *IEEE Transactions on Ultrasonics, Ferroelectrics, and Frequency Control*, 51(12):1582–1592, 2004.

- [68] S. Vieira. The behavior and calibration of some piezoelectric ceramics used in the STM. *IBM Journal of Research and Development*, 30(5):553–556, 1986.
- [69] PI Ceramic. Product information catalogue, Lindenstrabe, Germany, 2018, <https://www.piceramic.com/en/piezo-technology/fundamentals/>.
- [70] Agilent Technologies Inc. Agilent basics of measuring the dielectric properties of materials. Application Note, 2005, academy.cba.mit.edu/classes/inputdevices/meas.pdf.
- [71] M. G. Stewart, M. G. C. M. Cain and D. A. Hall. Ferroelectric hysteresis measurement and analysis. National Physical Laboratory Teddington, 1999.
- [72] F. Pobell. Matter and methods at low temperatures. Springer Science & Business Media, 2007.
- [73] Lake Shore Cryotronics. Inc., 575 McCorkle Blvd. Westerville, OH, 43082, <https://lakeshore.com/>.
- [74] AH2500 Instruction Manual Andeen-Hagerling. 1 kHz automatic capacitance bridge. <http://www.andeen-hagerling.com/>.
- [75] G. K. White and P. J. Meeson. Experimental techniques in low-temperature physics. 2002.
- [76] A. Erturk and D. J. Inman. Piezoelectric energy harvesting. John Wiley & Sons, 2011.
- [77] M. Al Ahmad, F. Coccetti and R. Plana. The effect of substrate clamping on piezoelectric thin-film parameters. In *Microwave Conference, 2007. APMC 2007. Asia-Pacific*, pages 1–4. IEEE, 2007.
- [78] C. B. Sawyer and C. H. Tower. Rochelle salt as a dielectric. *Physical Review*, 35(3):269, 1930.
- [79] Boston Piezo-Optics, Inc. Lithium niobate single crystal plates with chrome/gold electrodes, <http://www.bostonpiezooptics.com/>.
- [80] TRS Ceramics, Inc. TRS X2A single crystal lead magnesium niobate-lead titanate (PMN-PT) plates with chrome/gold electrodes, <http://www.trstechnologies.com/>.

- [81] Boston Piezo-Optics, Inc. PZT-5A ceramic plates with chrome/gold electrodes, <http://www.bostonpiezooptics.com/>.
- [82] APC International Ltd. Physical and piezoelectric properties of APC materials, 2013.
- [83] J. Y. Li R. C. Rogan, E. Üstündag and K. Bhattacharya. Domain switching in polycrystalline ferroelectric ceramics. *Nature Materials*, 4(10):776, 2005.
- [84] T. Fett and G. Thun. Determination of room-temperature tensile creep of PZT. *Journal of Materials Science Letters*, 17(22):1929–1931, 1998.
- [85] X. He D. Wang, L. Wang and R. Melnik. Modelling of creep hysteresis in ferroelectrics. *Philosophical Magazine*, 98(14):1256–1271, 2018.